

Probing Cell Signaling Networks in Microfluidic Devices

By

Jonathan David Ehrman

Dissertation

Submitted to the Faculty of the  
Graduate School of Vanderbilt University  
in partial fulfillment of the requirements

for the degree of

DOCTOR OF PHILOSOPHY

in

Physics

December, 2016

Nashville, Tennessee

Approved:

Erin C. Rericha, Ph.D

Ken S. Lau, Ph.D

John P. Wikswo, Ph.D

Shane M. Hutson, Ph.D

Copyright © [2016] by Jonathan Ehrman  
All Rights Reserved

To Erin Rericha, who taught me everything I know about experimental science

To my friends and family, for their continuous support during this trying time

And

To Claude Shannon and Isaac Asimov, who gave me a positive view of entropy

## ACKNOWLEDGEMENTS

During my graduate career, I had the pleasure of working within the Vanderbilt University department of Physics and Astronomy. The faculty and staff have been continuously willing to share their knowledge, resources, and time and have provided the most enlightening experience of my life. I would like to thank Viibre, which provided the facilities to fabricate all of the microfluidic devices used herein. I feel especially indebted to David Schaffer who trained me on all of the equipment and showed me seemingly limitless clever solutions to make fabrication easier and faster, while maintaining his friendly, sarcastic wit. I hope he continues to share his insights and brighten the halls of Stevenson 6.

The collaborative environment of Vanderbilt at large is palpable; everyone is willing to talk about one another's work regardless of how far apart they are in discipline. I feel especially privileged to be a part of the Quantitative Systems Biology Center, whose members are drawn from fourteen different departments and centers. This group hosted the Q-Bio conference at Vanderbilt which gave me an opportunity to give a talk and get critical feedback about the *D. discoideum* project. I feel especially indebted to Ken Lau and Sun Wook Kim, with whom we collaborated on the mechanosensing and autophagic flux project. Ken's relentless drive to add to our work and extensive interdisciplinary knowledge pushed the project far past where we could have gotten otherwise. Sun provided unrivaled work ethic and personal sacrifice that served as a model for excellence in any pursuit, and personal and professional advice that has shaped both my approach to science and my view of the individuals role in society.

Over the past year, I have had the great honor of joining the undergraduate research and mentoring program SyBBURE. The students within perpetually surprise me with their aptitude for learning and the team members have given me invaluable advice on my professional goals, life skills, and achieving personal fulfillment. I am indebted to Chrissy Marasco for teaching me to balance my professional and personal life and take time to enjoy myself, and giving me a creative outlet for self expression and the freedom to work on my interests with the SyBBURE students. I am undoubtedly a happier and more complete person because of my time in SyBBURE, and I look forward to continuing my involvement.

A great many people have helped me along my journey over the last five years, but none more so than my advisor, Erin Rericha. She has been continually supportive, always giving me advice on how to achieve the ever changing goals that I have had for my future throughout my time in her lab. Her ability to articulate her breadth of knowledge in simple terms is unparalleled, and she has taught me all of the presentation and writing skills that I possess. She gave me the space I needed to be independent, the direction I needed to progress, and the challenge I needed to grow. I could not have asked for an advisor whose mentoring philosophy was more aligned with my personal requirements for success. I am forever indebted to Erin for this experience.

These projects were funded by the Burroughs Welcome Fund and the Vanderbilt Department of Physics and Astronomy.

# TABLE OF CONTENTS

	Page
DEDICATION .....	iii
ACKNOWLEDGEMENTS .....	iv
LIST OF FIGURES.....	ix
Chapter	
1. Introduction .....	1
2. Literature Review: <i>Dictyostelium discoideum</i> .....	3
2.1 <i>Dictyostelium discoideum</i> .....	3
2.2 <i>D. discoideum</i> as a Model Organism.....	4
2.3 Life Cycle of <i>D. discoideum</i> .....	5
2.4 Discovery of cyclic-AMP as the Regulator of Aggregation .....	9
2.5 Adaptation and Relay .....	13
2.6 Secretion of cAMP.....	15
2.7 Reduction of Chemotaxis .....	17
2.7.1 CAR Binding and Phosphorylation.....	18
2.7.2 Minimal Transduction Machinery .....	21
2.7.3 Protein and Enzyme Localization.....	23
2.8 Models of Chemotaxis Transduction .....	25
2.8.1 Protein Networks .....	26
2.8.2 Phenomenological Models.....	28
2.8.3 Bridging the Scales.....	31
2.9 Information Theory .....	33
2.9.1 Information.....	34
2.9.2 Mutual Information .....	38
2.9.3 The Data Processing Inequality .....	41
2.9.4 The Data Processing Inequality in <i>D. discoideum</i> Signaling.....	42
2.10 Information Theoretic Models .....	42
2.10.1 Levine Model .....	43
2.10.2 Segota Model.....	48
2.10.3 Rate Distortion and LEGI.....	50
2.10.4 Filtering and Integration .....	54
2.11 Persistence .....	54
2.12 MSD .....	55
2.12.1 Connecting LEGI to Persistence: LEGI-BEN .....	56
2.13 Intention of Manuscript.....	56

3. Information Processing throughout the Early Development of <i>D. discoideum</i> .....	58
3.1 Abstract.....	58
3.2 Introduction .....	59
3.3 Materials and Methods.....	62
3.3.1 Cell Growth and Development.....	62
3.3.2 Elongation Assays .....	63
3.3.3 Dynamic Gradient Assays .....	63
3.3.4 Microfluidic Chamber .....	65
3.3.5 Microscopy .....	66
3.3.6 Calibrating cAMP Gradient .....	70
3.3.7 Image Analysis .....	74
3.3.8 Mutual Information Models .....	78
3.3.9 Receptor State over Development.....	79
3.3.10 Chemotaxis Index Calculation .....	80
3.4 Results .....	80
3.4.1 Quantification of Elongation throughout Development.....	80
3.4.2 Response to Dynamic Signals throughout Development: Persistence .....	83
3.4.3 Gradient Transduction throughout Development .....	83
3.4.4 Standard Measure: Chemotaxis Index.....	88
3.5 Discussion and Conclusion .....	88
4. Future Work: <i>D. discoideum</i> .....	93
4.1 FRET Probe .....	93
4.1.1 <i>D. discoideum</i> as an Excitable System.....	94
4.1.2 Mutual Information Accuracy .....	95
4.1.3 Secretion during Streaming .....	96
4.2 Extension of MI Bounds in LEGI Models through Development.....	97
5. Literature Review: Mechanosensing and Autophagy .....	98
5.1 Leveraging Evolutionary Conservation for Insight on Humans .....	99
5.2 Animal Studies .....	100
5.3 Culture Studies.....	102
5.4 Bridging the Gap: Organs-on-a-chip.....	103
5.4.1 Flow in OoC.....	106
5.5 Microvilli as Mechanosensors .....	107
5.6 Autophagy .....	111
5.6.1 Initiation .....	112
5.6.2 Nucleation.....	112
5.6.3 Elongation and Closure .....	113
5.6.4 Degradation and Recycling.....	114
5.7 Intention of Manuscript .....	117
6. Microvillar Sensation of Shear Stress Induces Autophagic Flux in the Intestinal Epithelium .....	118

6.1 Abstract.....	118
6.2 Introduction .....	119
6.3 Materials and Methods.....	121
6.3.1 Cell Culture.....	121
6.3.2 Microfluidic Device Fabrication .....	121
6.3.3 Live Cell Imaging with Microfluidic Control .....	122
6.3.4 Immunofluorescence Microscopy .....	122
6.3.5 Apical Surface Biotinylation .....	123
6.3.6 Histochemical Staining .....	124
6.3.7 Small Molecule Studies .....	124
6.3.8 RNA Knockdown.....	124
6.3.9 Real-Time PCR.....	125
6.3.10 Electron Microscopy .....	125
6.3.11 Analysis of Vacuole Count and Size, and Monolayer Height .....	125
6.4 Results .....	128
6.4.1 Shear Stress Induces Formation of Vacuoles.....	128
6.4.2 Vacuoles are Enriched with Extracellular Fluid from Altered Trafficking .....	135
6.4.3 Shear-Induced Vacuole Formation is Associated with Altered Flux into an Autophagic Pathway.....	139
6.4.4 Apical Shear Mechanosensation Depends on Microvillar Protrusions .....	149
6.5 Discussion.....	155
7. Future work: Mechanosensing and Autophagy in the Gut.....	160
7.1 Jamming in Gut Cells .....	160
Epilogue .....	167
Appendix	
1. Protocols .....	169
REFERENCES.....	184

## LIST OF FIGURES

	Page
2.1 Life cycle of <i>D. discoideum</i> .....	6
2.2 Morphological and cAMP regulation changes during development.....	8
2.3 Aggregating <i>D. discoideum</i> cells .....	12
2.4 Cartoon of CAR1 Receptor phosphorylation .....	20
2.5 Schematic of the minimal interactions within the chemotaxis signaling network .....	22
2.6 Fluorescent images of selected proteins from the chemotaxis pathway.....	24
2.7 Example chemotaxis signaling networks in <i>D. discoideum</i> .....	27
2.8 Comparison of observations of spirals waves <i>D. discoideum</i> motion and predicted wave patterns for excitable media.....	30
2.9 Representation of a communication channel .....	35
2.10 Information versus uniformity and number of possibilities .....	37
2.11 Mutual information over a communication channel .....	40
2.12 Cartoon of the Levine and Segota models .....	46
2.13 Collection of MI measures from literature.....	47
2.14 Mutual Information in experiment versus single and multistate receptor model bounds .....	49
2.15 Hill functions with varying Hill coefficients .....	53
3.1 Comsol flow field .....	64
3.2 Switching fluorescent gradients inside of the microfluidic chamber .....	64
3.3 Evolution of the gradient chamber via circuit analysis .....	67

3.4 Gradient chamber photolithography mask.....	68
3.5 Experimental Setup.....	69
3.6 Selection of the best simulation.....	71
3.7 Experimental and simulated chemical concentrations.....	72
3.8 Dextran and cAMP switch simulations .....	73
3.9 Cell boundary and shape identification.....	75
3.10 Local gradient directions and cellular trajectories.....	76
3.11 Persistence for individual cells .....	77
3.12 Elongation and persistence versus development time .....	82
3.13 U-turn fractions versus development time .....	86
3.14 Models and Experimental Results .....	87
5.1 Examples of organs-on-a-chip.....	105
5.2 Comparison of stereocilia and microvilli .....	109
5.3 Force on the membrane for forces applied to bundles of varying stiffness.....	110
5.4 Energy of different curvatures and lengths of double membranes .....	115
5.5 Role of the helical ATG3 in double membrane construction.....	116
6.1 Vacuole Identification .....	127
6.2 Cell monolayer height increases under shear stress.....	129
6.3 Epithelial monolayers exposed to shear stress maintain proliferation without cell death induction.....	130
6.4 Shear stress induces vacuole formation in dense Caco-2 <sub>BBE</sub> monolayers .....	131
6.5 Shear-induced vacuoles are not glycogen storage vesicles, mucin-rich granules, or liposomes .....	133

6.6 Shear-induced vacuoles are not VACs (Vacuolar Apical Compartments) .....	134
6.7 Internalized 10 kDa, but not 70 kDa, dextran, accumulates in vacuoles .....	137
6.8 Shear stress applied to cell monolayers does not induce endocytosis.....	138
6.9 Shear-induced vacuoles are associated with the autophagy machinery .....	140
6.10 Shear-induced vacuoles are associated with increased autophagy, but not endocytosis .....	141
6.11 Shear-induced vacuoles are lined with autophagy components.....	144
6.12 Chloroquine (CQ) and bafilomycin A1 (BafA) exert different effects on shear- induced vacuole formation .....	145
6.13 LC3 knockdown decreases shear-induced vacuole formation.....	146
6.14 The autophagy machinery is required for shear-induced vacuole formation. ....	148
6.15 Microvilli are required for shear-induced vacuole formation .....	151
6.16 Shear does not affect microvilli formation.....	152
6.17 Perturbing microvilli by PCDH24 knockdown suppressed vacuole formation and autophagic trafficking .....	153
6.18 Knock down of PCDH24 perturbs microvilli formation .....	154
6.19 Shear-induced vacuole formation is not triggered by increased calcium flux .....	159
7.1 Cell energy components.....	161
7.2 Identification of cell boundaries from fluorescent actin .....	165
7.3 PIV analysis of CACO-2 cells under shear.....	166

## Chapter 1

### Introduction

Signaling networks in cells enable them to respond to a wide variety of external stimuli, from chemical gradients to mechanical strain. These networks are dense (facilitated through interactions among multiple protein species and small molecules) and redundant (frequently one signal can act through multiple networks); the molecular species within the cell are frequently used in multiple signaling pathways and there are parallel and serial steps triggered by a single stimulus. Some stimuli change the rate of synthesis for proteins within these signaling networks as well as other cell components. A collection of external stimuli can drive a cell to change enough of its components to be considered a different type of cell, processes called differentiation. These processes enable a cell to optimize itself within a dynamic environment and undergo organized multistep transitions to become highly specialized, such as development of pluripotent stem cells into organ specific tissues.

When examined from a pure number of interacting components, signaling networks and developmental processes are overwhelmingly complex. The current challenge at this biology / physics interface is to find theoretical frameworks that reduce the complexity and illuminate the fundamental design and operating principles used by life. Frequently, these operating principles have analogues in non-living dynamical systems. For instance, entropy within the environment is part and parcel to developmental transitions; more variables and fluctuations can elicit more complex

response, but only if a cell has the capacity to measure such variation. Cells can additionally control some environmental parameters through, for example, chemical secretion. The relationship between the environment and the cell determines the instantiation and dynamics of both. Here we study this relationship in two projects. The first is a model developmental organism, in which the cells sense the nutrient content in the environment, secrete a chemical when the food is sparse, sense the chemical to drive phenotypic and behavioral changes, and develop into a multicellular organism from its unicellular constituents. We address the efficiency with which the cells transduce environmental chemical entropy into ordered migration during this transition. In the second project, we focus on a repurposed transduction networks response to a single controlled environmental variable, the effect of shear stress on autophagic flux in gut epithelial cells. We quantify fluid trafficking in response to mechanical stress. Both of these projects belong to the general class of emergence problems frequently found at the interface of biology and physics.

## Chapter 2

### Literature Review: *Dictyostelium discoideum*

#### 2.1 *Dictyostelium discoideum*

The social amoeba *D. discoideum* has long attracted the attention of physicists. Cells of this species are eukaryotic, and hence have frequent overlap with mammalian cell systems, but are easier to grow and manipulate in laboratory settings and amenable to quantitative study. Physicists and mathematicians have been essential to understanding aspects of the *Dictyostelium* life cycle through analogy to non-living dynamical systems, such as crystal growth and oscillating chemical reactions. Quantitative studies of *D. discoideum* frequently reveal surprises that push the bounds of expectation for a single cell. For instance, *D. discoideum* has an incredible ability to transduce external chemical cues into directed migration with only a 1-2% change in concentration across its body. In our study, we extend a theoretical model of this signal transduction through time and compare the results to our experimental measures. To contextualize this work, the following section reviews the extensive literature on *Dictyostelium's* development and chemotactic transduction network and the models created to describe it. We start with an overview of *Dictyostelium* as a model organism and its life cycle, and then focus on the life stage that we study, the transition from a unicellular to a multicellular state. We broadly describe the morphological and migratory changes that define this transition, and discuss the particulars of the chemotactic signaling network that the cells utilize to aggregate into the multicellular state. We then

describe the spatial and temporal patterns created through intercellular communication that accompanies aggregation. We briefly describe the relevant models of signaling networks that are used to describe migration at either early or late stages development, then cover the information theoretic concepts that we use in our analysis. We then cover at length the models of migration that have integrated information theory and their experimental counterparts, which our work extends through this developmental transition.

## **2.2 *D. discoideum* as a Model Organism**

*D. discoideum* has proven to be a useful model organism. It contains genes homologous to those in higher eukaryotes, including many that simpler model organisms lack<sup>1-3</sup> and its entire genome was sequenced relatively early in 2005<sup>4</sup>. Soon after sequencing, methods for genetic manipulation of *D. discoideum* were developed<sup>5</sup>, enabling rapid mapping of genes to phenotypes<sup>6-8</sup> and pathway discovery<sup>9-11</sup>. Built on these genes are common signal transduction networks that are conserved, including the phagocytosis, migration, and chemical sensing pathways<sup>12-14</sup>. These pathways are often used to infer functions in the human immune system, such as the migratory strategies of neutrophils and leukocytes<sup>15,16</sup>. Defects in transcriptional regulation controlled by signaling networks often result in disease states<sup>17,18</sup>, and direct probing of these networks is difficult in more complex organisms. Studies of these defects in *D. discoideum* generate hypotheses for disease mechanisms as well as enable discovery and early testing of potential drug targets. The life cycle of *D. discoideum* features several differentiation processes<sup>19-22</sup>, making it an ideal candidate for abstract studies

on developmental requirements such as pattern formation, cell sorting and signal-regulated gene expression.

### **2.3 Life Cycle of *D. discoideum***

*D. discoideum* undergoes several differentiation steps throughout its lifecycle. When nutrient are plentiful (Figure 2.1, state A), *D. discoideum* cells are unicellular eukaryotes and move in an amoeboid fashion up increasing concentration gradients of the bacterial metabolic bi-product, folic acid. In this state, the cells are frequently referred to as vegetative, and this condition lasts as long as food is sufficient. In the vegetative state, cells reproduce by asexual cell division roughly every 4 to 12 hours. Starvation conditions initiate a developmental transition, that is characterized by directed cell migration (state B) to form a cellular aggregate (state C) frequently termed the mound<sup>23</sup>. By state C the cells, initially monoclonal, can be separated into two differentiated cell types, and the population behaves more as a multicellular organism. Within this mound, the cells sort the two cell types into pre-stalk and pre-spore regions<sup>24</sup>. With time, the mound morphologically changes so that the front is clearly defined with a tip that continues to elongate, forming a migrating slug<sup>25</sup> (state D). The slug migrates towards heat and light and, after sufficient time, uses the stalk cells to begin growing vertically (state E). The spore cells are carried along, forming a culminant and finally a fruiting body (state F). Once all of the spore cells have travelled to the top, the fruiting body bursts and throws the cells, which distributes the spores (state G) and begins the cycle anew<sup>26</sup>. This entire process occurs in about twenty four hours in laboratory conditions.

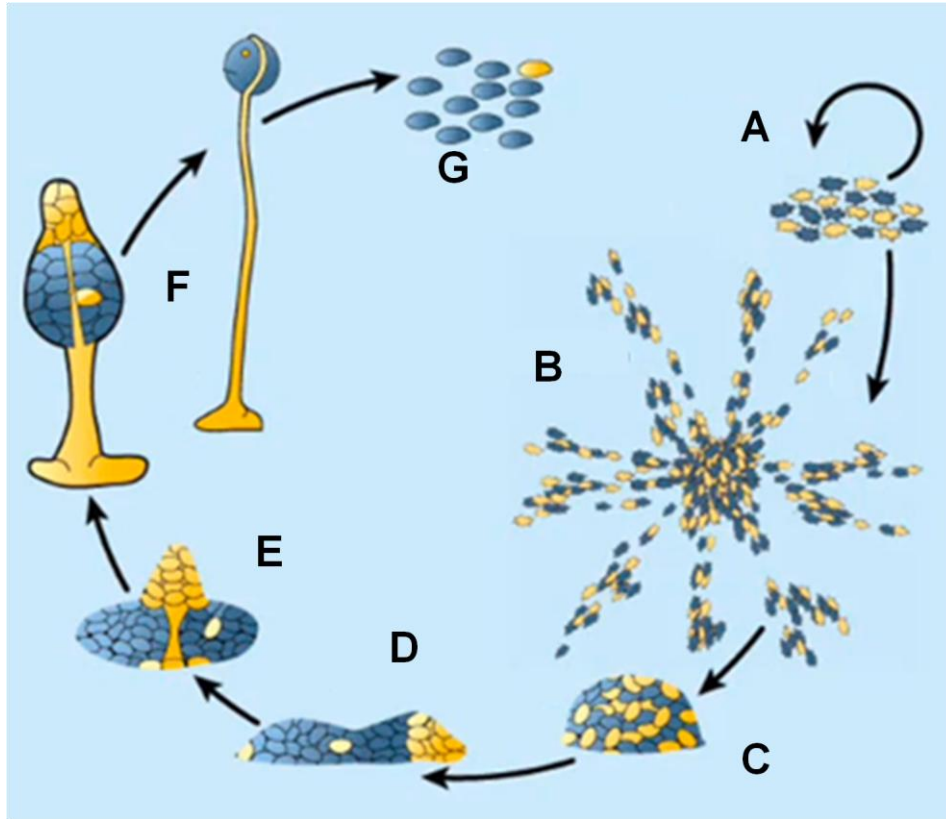


Figure 2.1 Life cycle of *D. discoideum*<sup>27</sup>. A) Cells start in the vegetative state where they hunt bacteria by sensing gradients of bacterial metabolic byproducts, primarily Folic Acid. The cells at this stage proliferate, represented by the arrow pointing from state A back to state A. B) Once the bacteria food source has been depleted, the cells begin signaling to each other by secreting cAMP and synchronize their signals. They use this signal to regulate a developmental process in which they elongate and migrate up gradients of cAMP, resulting in aggregation. C) Once the cells have aggregated, they form a mound and begin to sort themselves into pre-stalk and pre-spore regions. D) Once the cells have been sorted, the aggregate moves as a multicellular slug and looks for more food. If none is found the cells precede to state E. E) The stalk cells organize into a vertical structure while the spore cells lend support. F) The stalk cells form a solid base and vertical structure to raise the spore cells and move them to the top of the structure. G) The spores are shot from the top of the stalk to another region to begin the life cycle again. We focus on transition from state A to state B in our work.

In this work, we focus on the early stages of the life cycle (3-7 hours) – the transition from vegetative cells to cells aggregating into mounds. The multicellular mass is formed by aggregation migration of individual amoeba up a gradient of cyclic-AMP (cAMP), which is released in a synchronized pulsatile fashion by the starving cells. This extracellular cAMP binds to a transmembrane receptor, cAR1, which activates a network of signaling pathways that lead to the generation of more cAMP secreted to propagate the signal.

This transition is alternatively phrased as a transition from a unicellular population to a multicellular organism. Because of the great interest in how multicellularity evolved, this process in *D. discoideum* has been well studied both at the single cell and collective level. Here we briefly describe observations of morphological and migratory changes during development, and discuss at length discovery of the chemotaxis signal transduction network that the cells use to aggregate. We follow this with the studies of the spatial and temporal patterns that emerge during this transition. These together set up background for the development of the models of single cells and populations that are connected later.

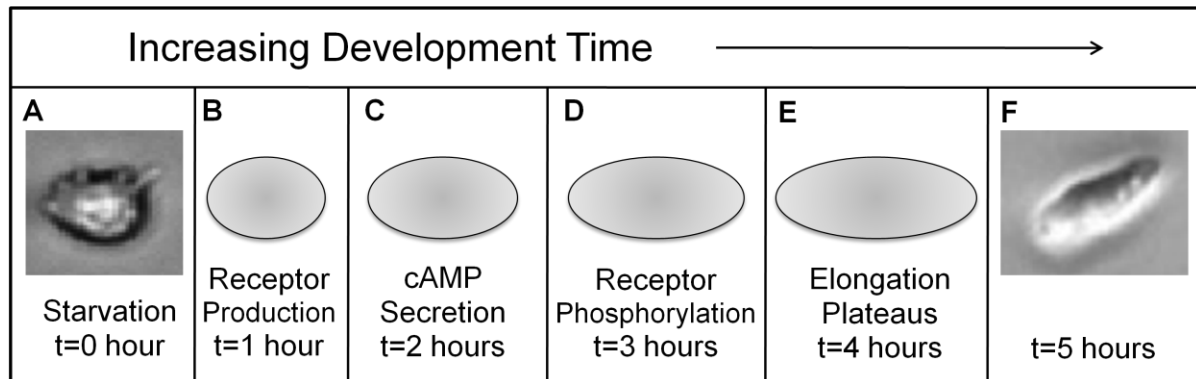


Figure 2.2 Morphological and cAMP regulation changes during development. A) Bright field image of a *D. discoideum* cell immediately after removal from its food source. The cells are round and feature protrusions at many locations on the cell membrane. B) At one hour post starvation, the cells begin to produce cAMP receptors. They maintain their rounded shape. C) At two hours post starvation, cAMP secretion begins and the cells elongate slightly. D) At three hours post starvation, the cAMP receptors begin to phosphorylate in response to cAMP binding, changing their affinity such that the signal at a frequency a factor three slower than in their non-phosphorylated state. The cells rapidly elongate. E) At four hours post starvation the cells stop elongating. F) Bright field image of a cell at five hours post starvation. The cells are more than twice as long as wide and feature protrusions almost exclusively at the front of the cell. Receptor phosphorylation reached its maximum with approximately 75% of the cAMP receptors in the slow state. We study how the receptor phosphorylation and number affect the ability of the cells to migrate up gradients of cAMP during aggregation.

## 2.4 Discovery of cAMP as the Regulator of Aggregation

The transition from the unicellular state A where the *D. discoideum* cells act independently to states C and D where they have joined into a multicellular organism has captured the interest of cell biologists and physicist for many years. An early question to be answered was 'what do the cells use to communicate? It was initially proposed that a chemical aggregation signal, first named Acrasin, was created at the center of the aggregate, and diffused outward to attract nearby cells<sup>28,29</sup>. This was tested experimentally by separating the centers from other amoeba by a semi permeable membrane through which only small chemicals could diffuse. The isolated amoeba could still orient themselves towards the centers, so it was concluded that a small molecule must mediate aggregation. The identity of Acrasin was found by removing media from aggregating cells and measuring the compounds within for approximate molecular weight, charge, and absorption. Molecular candidates with similar attributes, particularly those already known to have a biological purpose, were screened for generation of a cellular response. The common intracellular chemical messenger cAMP was the only molecule identified in the screen that attracted cells<sup>30,31</sup>.

The next question addressed was whether cAMP was generated by all or just a fraction of the cells. Key to this discovery was direct observation of cell behavior during the transition from states A and B. Cells, initially uniformly dispersed in a monolayer, migrated towards the aggregation centers in a periodic fashion, suggestive of a chemical wave in a reaction diffusion system. During the rising part of the wave, the cells would move forward up the cAMP gradient then stop moving as cAMP decreased. The absence of migration towards the gradient in the opposite direction hinted that the

cells adapted to cAMP or became incapable of detecting lower concentrations. After the wave had passed and cAMP concentrations were low in the region, the cells paused migration and became rounded. The neighboring regions “behind” would move forward, continuing the wave of migration. Studies revealed that these migration waves propagated from aggregation centers as either concentric circles or spiral waves<sup>28,32</sup>. The aggregation centers recruited cells as far as 350 $\mu$ m away<sup>33</sup>, which is farther than diffusion alone should allow, and cells oriented themselves towards an aggregate within 5-10 minutes throughout the field<sup>34</sup>. This led to the hypothesis that all cells are able to secrete cAMP and that they relay the signal to each other to increase the range and create the wave like motion. Indeed, while vegetative cells were found to be insensitive to increases in cAMP concentration, all wild type cells in the population aggregating to the mound were found capable of synthesizing and secreting cAMP.

Interestingly, the population became sensitive stochastic fashion<sup>35</sup> as the cells move out of the vegetative state<sup>36</sup>. The next major focal point of study was the creation of the large spatial structures from uniform cell populations using only stochastic processes, and the connection between cAMP signaling and cell motion.

To address the connection between cAMP and cell motion, Tomchik and Devreotes used a dilution - isotope fluorography method to record snapshots of the cAMP wave<sup>32</sup>. Briefly this technique involved aggregating cells on a filter that absorbs cAMP, then rapid placement on another filter with H<sup>3+</sup> labeled cAMP. Areas on the first filter with high concentrations of cell secreted cAMP would be locally well mixed with the H<sup>3+</sup> labeled cAMP on the second filter over about a minute. Placement on a third filter with a protein kinase that binds cAMP stopped all diffusion and effectively created a

snapshot of the concentration of cell secreted cAMP. Areas with cAMP from cells would have less labeled cAMP in the third filter. The labeled cAMP radiates detectable beta particles, thus dark regions would be high cell secreted cAMP regions. From these static snapshots, Tomchik and Devreotes could determine that cAMP concentration waves strongly correlated with the motion waves. The regions with high cAMP contained elongated cells while the low regions contained randomly oriented cells<sup>32</sup>. In addition, measurements of the snapshots produced a quantitative description of the motion. The width of the cAMP bands were between .3 and 1mm, increasing with distance from the aggregate center, and travelled at 300um/min<sup>32</sup>. Cells in a region signal between 1 and 3 minutes<sup>32</sup>. The correlation between cAMP field and motion allowed others to further quantify cAMP through migratory observations as follows. A single cell relay can propagate for 12 seconds travelling at 4.75um/s, covering 57um, and the population can relay a signal as far as 10mm. Waves of cAMP occur every 3-10 minutes, decreasing during aggregation<sup>37,38</sup>. These discoveries raised additional questions, such as what is the significance of the pulsatile motion, and how is the observed motion controlled by the cAMP wave and how do the cells control the wave.

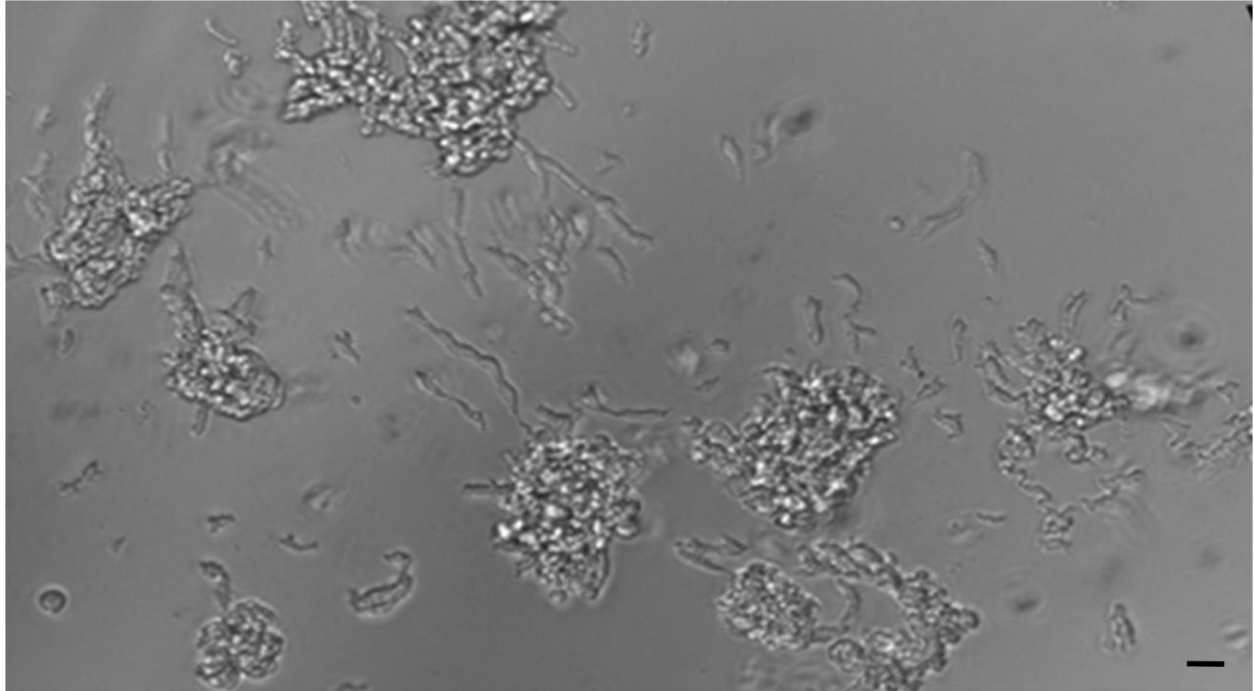


Figure 2.3 Aggregating *D. discoideum* cells. Scale bar 20um. The cells are shown in a bright field image at six hours post starvation when they have completed this early developmental cycle. The cells now stream towards aggregates, following each other in a head to tail fashion. Once the cells reach the aggregate there movement slows and they become round.

## 2.5 Adaptation and Relay

After the spatial characterization of the cAMP wave outlined above, investigation turned to quantifying the concentrations and timing of the secretions of cAMP to find the amplitude of the wave determine if there were additional regulators that modulate cAMP concentration. To measure the secreted concentrations, cells were stimulated with cAMP that exactly saturates their receptors so that all cAMP present in solution would be secreted by the cells. The intensity of isotope fluorography of the secreted cAMP was compared to intensities from known concentrations to calibrate the measurement. The cells increase their cAMP secretion from 0.2pmol (per  $10^6$  cells) at 0.5 hours to 5pmol at 7 hours<sup>39</sup>. Using optical density measurements in swirling culture at 290nm, which cAMP absorbs, the temporal characteristics were surveyed. Spikes were observed every 7 minutes, meaning that the cells secreted cAMP every 7 minutes and that it was degraded through some unknown mechanism. When the media was passed through a Millipore filter however, the solution was considerably more stable, leading to the conclusion that relatively large entities were responsible for cAMP degradation, namely enzymes<sup>34</sup>. This enzyme was later shown<sup>34</sup> to be controlled by *pdsA*, a phosphodiesterase that dephosphorylates cAMP into AMP which the cells do not sense. The spikes that result from secretion and degradation were further quantified and independent fast and slow peaks that changed over development were observed. The delay between fast and slow peaks decreases from 2 minutes to 0.8 minutes, and the ratio of the fast and slow amplitudes increases 10 fold between pre-aggregate and aggregate competent development stages<sup>40</sup>. The regular peaks of cAMP seen in the system led to the hypothesis that the cAMP secretion system is oscillatory and that the

dynamics change over development. To test if the system was oscillatory, cAMP pulses were imposed on the system at periods different than the observed peaks and caused the characteristic phase shifts of the spikes for a perturbed oscillator. To understand how this internal oscillator coupled to the external field, the role of internal and external pdsA was further explored. Mutant cells that either did not have the ability to produce pdsA or over produced the enzyme were used to probe how signal relay would function if internal and external control over cAMP was modulated, and showed that degradation within the relay mechanism increased the communication range of the cells and that the cells are able to relay directional information over long ranges only with precise control over pdsA, as both over and under production hampered relay<sup>41</sup>. The degradation of cAMP by pdsA coupled with the oscillatory behavior of cAMP both internal and external to the cell opened the question of whether signal relay was an excitable phenomenon, which seemed reasonable as the concentric and spiral waves seen in the migration are characteristic of excitable media. In order for this to be true, the cells would additionally have to adapt to signals. Adaptation refers to the process through which cells acclimate themselves to a background concentration of cAMP and set a new zero, becoming unresponsive to lower concentrations. Adaptation additionally causes cells to have a refractory period, to be unresponsive to a stimulus that occurs too rapidly after a previous stimulus. Cells were treated with artificial stimuli of cAMP at different intervals and was shown that the cells will not secrete cAMP in response to a stimulus within 7 minutes<sup>42</sup> of secretion during the early stages of aggregation, a period which drops to 2 minutes during the later stages<sup>43</sup>. Additionally, if the stimulus is never removed, the secretion rate rises geometrically but falls off to 30% after 5 minutes and is back to the

basal rate after 20 minutes<sup>37</sup>. By comparison the refractory period for movement is much shorter, with cells chemotaxing to signals as close as 12 seconds apart<sup>38</sup>, and in constant stimuli the movement stops over 80 seconds<sup>44</sup>. This suggests that secretion and migration control networks diverge downstream of the receptor, but adapt to signals so they may play a role in the excitable dynamics of signal relay. In the following sections we will outline the cascade that leads to secretion and describe the signaling network that governs chemotaxis, and then connect them with population pattern formation in excitable media.

## **2.6 Secretion of cAMP**

Over the course of development, some cells stochastically begin to secrete cAMP<sup>45,46</sup> and others begin in response. After cAMP binds to the receptor it releases proteins internally to trigger cAMP production; Adenylyl cyclase A (ACA), which catalyses the reaction of ATP into cAMP, is activated and causes internal cAMP<sup>37</sup> concentrations to rise 10-fold<sup>47</sup>; ACA activation is critical; cells without ACA did not produce cAMP<sup>37</sup>. cAMP production increases over 1-2 minutes then drops to basal levels after 3-4 minutes; the kinetics of ACA activation and the time course of cAMP production are consistent<sup>37</sup>. These results imply that ACA is the lone protein responsible for control of internal cAMP production. The measured dynamics of ATP, ACA, and cAMP within a cell allowed the relationship between the three to be described by coupled differential equations. The resulting simulations showed that the regulation of ATP and ACA are sufficient to create oscillations in cAMP with a period of 3-5 minutes<sup>48</sup>, which is similar to

the measured period of secretion of 7 minutes. Additional measurements of the internal and external cAMP concentrations showed that the internal cAMP drops more rapidly than it is secreted, which led to the conclusion that it is degraded by internal phosphodiesterase (pdsA)<sup>37</sup>. Addition of degradation of internal cAMP and secretion terms to these coupled differential equations gave insight into the possible form of secretion<sup>49</sup>, and further quantification of the secretion in shaking culture via optical density measurements would allow internal and external kinetics to be connected. The dynamics of secretion are also crucial to understand how the cells are modulating the chemical field so investigation turned towards this quantification to accomplish both tasks. In shaking culture, the optical density measurements after a stimulus provided the secretion curve shape, the secretion has a half width of 1.5 minutes and lasts 2.5 minutes<sup>50</sup>, which was consistent with the duration of spontaneous pulses when the cells are causing the stimulus rather than it being imposed<sup>38,43</sup>. To find the amplitude of response, experiments involving isotope fluorography showed that the cells secrete at rates that are an order of magnitude greater than the amplitude of the stimulus. For example, extracellular cAMP increases by 5E-7M 90seconds after 5E-8M pulse<sup>50</sup>, and the secretion rate increases proportionally as the applied cAMP concentration increases<sup>37,42</sup>. These two sets of experiments together give the secretion curves in response to a variety of stimuli, which were used to build more complete models of the internal/external regulation of cAMP that leads to spatial pattern formation. In addition to secreting cAMP after sensing it, the cells also migrate towards higher concentrations. The motion of the cAMP sources and sinks also plays a role in pattern formation, so we now turn our attention to chemotaxis.

## 2.7 Reduction of Chemotaxis

The movement of the population of cells in the aggregation phase was characterized as outlined earlier and showed wave of motion. These observations open question about individual cells within the population and how they together form the response of the group. In order to understand the motion of single cells, the focus of investigation shifted to identification of critical pieces in the signal transduction network that controls chemotaxis, a vein of research that continues today. This study started with the most upstream signaling element, the cAR receptors. The cAR1 receptors have occupation probabilities that depend on local cAMP concentrations and their inherent dissociation constants. Binding of cAR1 causes proteins to be released internally, which feed into transduction pathways that regulate internal protein concentrations and propagate the signal. These downstream protein concentrations dictate the binding and bundling kinetics of actin, a polymer that gives the cell structure and shape. The binding kinetics in turn regulates the probability of creating a pseudopod, an actin rich protrusion, by modulating the stiffness of regions near the membrane. These pseudopodia reach out and stick to the surface in the direction of migration, so the distribution and timing of pseudopodia on the cell boundary determine the direction and speed of migration. In a chemical gradient the cell receptors on the high side will have higher binding probabilities and release more proteins. The transduction machinery will thus create spatially organized distributions of proteins and enzymes that control pseudopodia production<sup>51-53</sup>, which results in preferential migration up the chemical gradient. These steps work together to control the migration of individual cells, which can be connected through signal relay to the population chemotaxis dynamics<sup>54</sup>.

### 2.7.1 CAR Binding and Phosphorylation

In order to signal to downstream protein networks, binding of cAR1 must release some agent that targets them. The search for this agent in *D. discoideum* signaling led to a discover of G-protein coupled receptors, which are transmembrane proteins with an external chemical binding site and an internal tail that comprised of several protein subunits that are disassociated when the binding site is filled. This tail also contains modification sites where phosphates can be attached following binding events, which control the re-association kinetics for the subunits and, consequently, the dissociation rate of the binding site. G-protein coupled receptors have since been found in the majority of mammals and a variety of conserved signaling pathways, and are the most common known transmembrane chemical receptor class; G-protein coupled receptors are ubiquitous in chemical signaling. In *D. discoideum*, there are four G-protein coupled cAMP receptors, named as cAR1 through cAR4<sup>55</sup>. CAR1 is receptor that controls chemotaxis during aggregation<sup>56</sup>. The G-protein in this receptor is contains several subunits,  $G_{\alpha 2}$   $G_{\beta}$  and  $G_{\gamma}$ <sup>57</sup>, which feed into downstream signaling networks once released. Upon ligand binding, cAR1 is phosphorylated at cytoplasmic residues, which changes the frequency at which the receptor can activate downstream pathways<sup>58</sup>.

Despite the correlations between cAR1 phosphorylation and adaptive kinetics of downstream pathways, some studies have suggested that receptor phosphorylation in *D. discoideum* might not attenuate G-protein signaling<sup>59,60</sup>, and that these effects are actually caused by an unknown mechanism. The connections between cAR1 phosphorylation and chemotaxis remains understudied, but the receptor state does modulate affinity and binding rates<sup>58,61</sup>.

Recently, it has been shown that a lack of phosphorylation negatively impacts persistent directional migration in late development cells<sup>58</sup>, so regardless of the explicit form of modulation, phosphorylation clearly plays a role in chemotactic ability. In our study we quantify the effects of receptor phosphorylation on the efficiency of chemotaxis throughout development and show that receptor phosphorylation is low in early development so that the receptors can signal frequently, which makes up for the relatively low receptor number to keep the environmental sampling high. Phosphorylation increases as development progresses and receptor number increases to time average signals and increase its accuracy in the transduction of stable chemical fields. These effects change the frequency of the cAR1 signaling to the protein networks downstream, but these networks remain constant throughout development and connect the receptor binding to the migratory dynamics. Here we outline a minimal set of interactions within this protein signaling network to elucidate this connection.

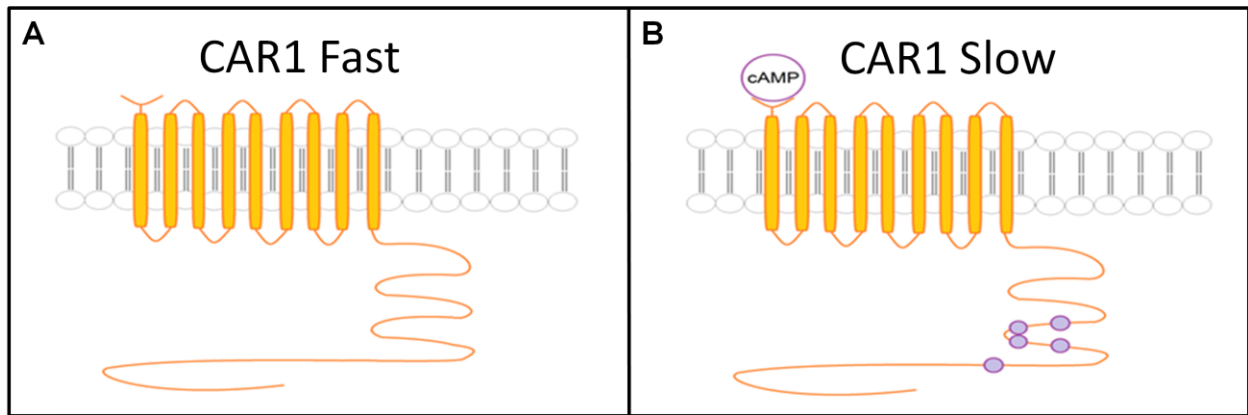


Figure 2.4 Cartoon of CAR1 receptor phosphorylation. A) The transmembrane cAMP receptor is shown in orange. The lipid bilayer membrane is represented by two sets of circles and double lines, symbolizing the hydrophilic and hydrophobic regions of the phospholipids that compose it respectively. The receptor features a cAMP binding site on the exterior (upper) side of the membrane and a long tail on the interior. The tails feature binding sites for phosphate groups. B) A cAMP molecule is shown occupying the binding site on the receptor. This promotes phosphorylation at the interior binding sites, represented by the purple circles on the tail. Phosphorylation causes the affinity of the receptor to become lower, decreasing the rate at which the receptor will bind cAMP afterwards. We study the effects of phosphorylation on gradient sensing using wild type cells and a mutant whose CAR receptors are always phosphorylated.

### 2.7.2 Minimal Transduction Machinery

The released subunit  $G_{\beta\gamma}$  binds to and activates RasG and RasC, which are small G-proteins with structure similar to the  $G_{\alpha}$  subunit that the released  $G_{\beta\gamma}$  subunit was previously bound to. In their active form, RasG and RasC have high affinity for PI3-kinases, and upon binding regulate their activity<sup>62</sup>. These kinases phosphorylate phosphatidyl inositol bisphosphate (PIP2) to produce phosphatidyl inositol triphosphate (PIP3) in the membrane<sup>63</sup>. PIP3 activates Phosphatase and Tensin homolog (PTEN), a PIP phosphatase, that dephosphorylates PIP3 back into PIP2<sup>64</sup>. The dynamics of PI3K and PTEN together control the concentration of PIP2 and PIP3, and the feedback from PIP3 to PTEN allows the cell to ignore stimulation that arose from noise. For above threshold signals, the persistent PIP3 presence activates a ribosome associated complex (RAC) that stimulates actin polymerization, which produces protrusions, and the alpha serine/threonine-protein kinase (Akt) pathway governing myosin assembly, which is responsible for cell contractions<sup>63,65,66</sup>. Together this signaling network transduces the receptor binding events into structural conformation within the cell to govern chemotaxis. This signaling network is shown in Figure 2.5. The receptors that feed into this network are bound with frequencies that mirror the external concentrations of cAMP, so in non-uniform fields this signal transduction network is non-uniformly activated. This gives rise to spatial organization of the proteins within the network, which we outline below.

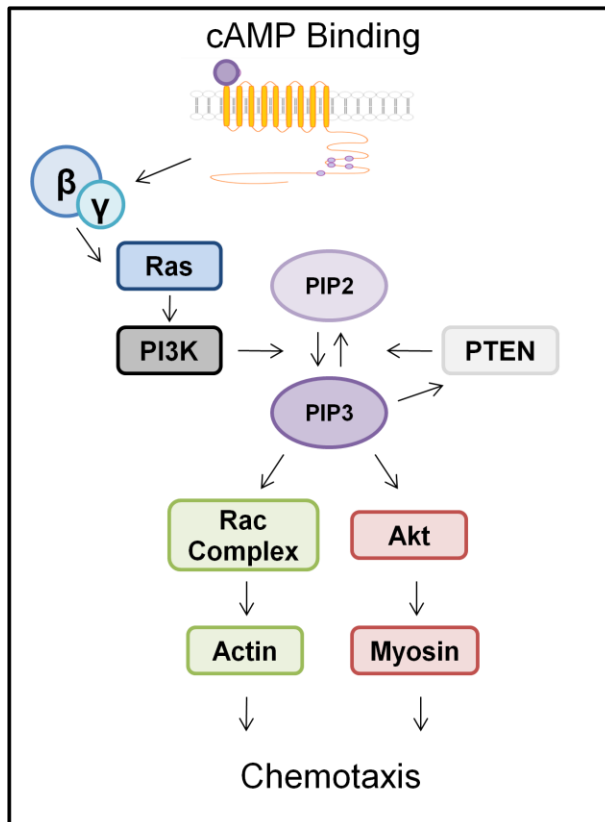


Figure 2.5 Schematic of the minimal interactions within the chemotaxis signaling network. When cAMP binds to the receptor, the Beta and gamma g-protein subunits dissociate from the interior of the cAR1 receptor. These subunits bind to and activate Ras, which in turn binds to and activates PI3K. This activation causes an increase in the rate at which PI3K phosphorylates PIP2 into PIP3. PIP3 Activates PTEN when dephosphorylates PIP3 back into PIP2 which gives a threshold for persistent PIP3 concentrations. PIP3 also activates a Rac Complex that governs the kinetics of actin polymerization that causes pseudopodia extension and activates Akt, which promotes the assembly of myosin II which contracts the cell. In tandem, these effects produce chemotaxis. The machinery outlined above is responsible for the excitable cell behavior covered in more detail in the later sections of this chapter. Adapted from<sup>51,62-64</sup>

### 2.7.3 Protein and enzyme localization

Upon cAMP stimulation, g-protein coupled subunits are released from the membrane into the cytoplasm and trigger the downstream signaling network governing chemotaxis. In a chemical gradient, the receptors on the high side of the cell are bound more frequently than the low side, yielding a front to back gradient of g-protein subunits along the membrane<sup>67</sup>. PI3K, activated by these subunits, also shows higher concentrations at the high side under stimulation<sup>68</sup>. The high concentration of PI3K phosphorylates a large number of PIP2, which creates a high concentration of PIP3. PTEN, which is uniformly distributed in the absence of signal, is concentrated at the back end, further amplifying the gradient of PIP3 through dephosphorylation of PIP3 into PIP2 at the rear<sup>69,70</sup>. PIP3 recruits Myosin I to the membrane, which polymerizes actin preferentially at the front<sup>9</sup>. The high PTEN and PIP2 concentrations on the low side of the cell create a myosin II gradient that is also high at the low side<sup>51</sup>. Myosin II is responsible for depolymerization of actin and contracts the cell by pulling on the actin filaments<sup>52</sup>. The actin polymerization at the front coupled with depolymerization at the back gives a high probability of pseudopod extension at the high side. The contraction due to myosin II activity at the back combined with the extension of pseudopods at the front drive directed migration<sup>53</sup>. The spatial distributions of PI3K, PTEN, and Myosin II are shown in Figure 2.6, with the white arrow indicating cAMP gradient direction. In order to connect chemotactic responses with these spatial distributions, modeling efforts began with the intention of creating a set of equations representing the cell which would mimic observations of chemotaxis. These efforts began both at the single cell and population levels with the intention of tying the two scales together in a unified framework.

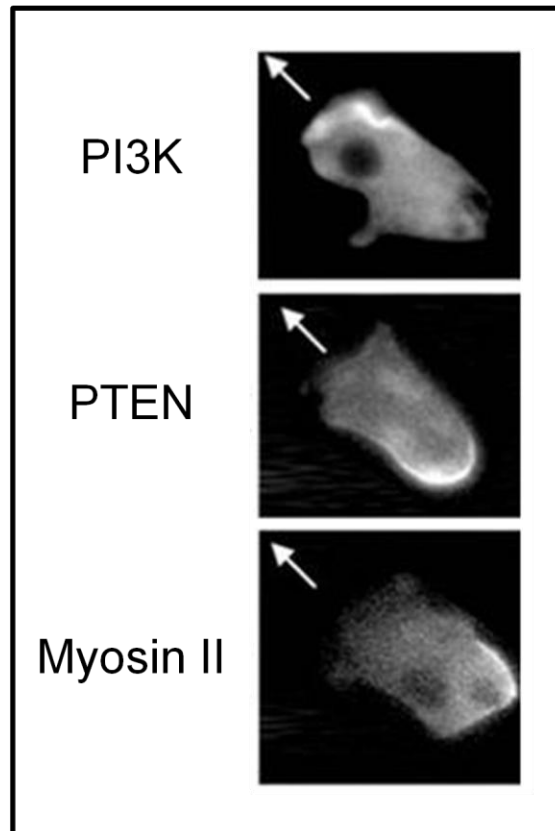


Figure 2.6 Fluorescent images of selected proteins from the chemotaxis pathway<sup>68</sup>. The white arrow denotes the direction of an applied cAMP gradient. PI3K concentrations are high at the leading edge of the cell while PTEN and Myosin II concentrations are high at the rear. The high PI3K concentration results in actin polymerization through the machinery outlined previously while high PTEN inhibits polymerization. High Myosin II contracts the cell at the rear and moves the fluid within the cell forwards such that it migrates up the cAMP gradient. The spatial organization of these proteins is crucial for chemotaxis. The receptor changes during development modulate the signaling rates at the cell membrane and in turn change the spatial distributions of these proteins and the chemotactic response<sup>71</sup>.

## 2.8 Models of Chemotaxis Transduction

The efforts to model transduction of chemical signals can be divided into two philosophical approaches: A reductionist approach identifies individual proteins and constructs them into a network that accurately simulates the salient features, and a global approach identifies and recreates spatio-temporal patterns in the population's phenomenological response. At the single cell level, a reductionist approach was taken where increasing numbers of proteins within the signaling network were discovered and their relationships with the others defined, creating large signaling maps. The kinetics of such maps were measured to populate coupled differential equation models that have been able to accurately predict chemotactic responses. This approach is limited by scale due to the increasing cost of solving larger numbers of coupled differential equations and the difficulty in interpreting high dimensional results gleaned from such models. At the population level, the well studied framework of excitable media was applied to the observations of cell motion and cAMP waves. These models allowed predictions for density dependent effects as well as predictions for pdsA activity in degrading cAMP. The two approaches were tied together by inserting an excitable signaling element within the cell transduction network models and a description of the secretion events as excitable. This unification gave insight into the connections between single cell and multi-cell responses through coupling of similar mechanisms at different size scales.

### 2.8.1 Protein Networks

A reductionist approach to identifying the transduction network elements is to disable them one at a time and quantify the phenomenological response. A combination of targeted drugs, and genetic manipulation, where the portion of the genome which encodes the specific signaling protein is removed, is used to disable specific elements. Genetic modification of *D. discoideum* has been commonplace for many years and is considered to be relatively easy<sup>72</sup>. The chemotaxis<sup>61,63,73,74</sup> and signal relay<sup>75-78</sup> pathways in *D. discoideum* were explored in this fashion, resulting in large protein transduction models. In particular, transduction maps that connect receptor binding to chemotaxis were constructed, such as the two seen in Figure 2.7, though the particulars are beyond the scope of this document. These two models have phenomena associated with specific signaling elements because when those elements are removed, the phenomenon is lost. This framework can be further exploited by disabling multiple elements to identify redundant pathways. In such cases the phenomena might be weakened in single knockdowns, but not entirely lost until several proteins are disrupted. Signaling elements are often used in multiple pathways, so this process can also elucidate key regulator proteins that control many responses if several phenomena are concurrently lost. The network maps created in this framework are readily useable to elicit a specific response, such as the removal of cAMP secretion, but are often unable to be used accurately control phenomenological responses or predict dynamic responses. In order to control a phenomenological response with a reductionist model, a large number of individual interactions would have to be controlled, and prediction of perturbations of large models requires phenomenological models to act as targets.

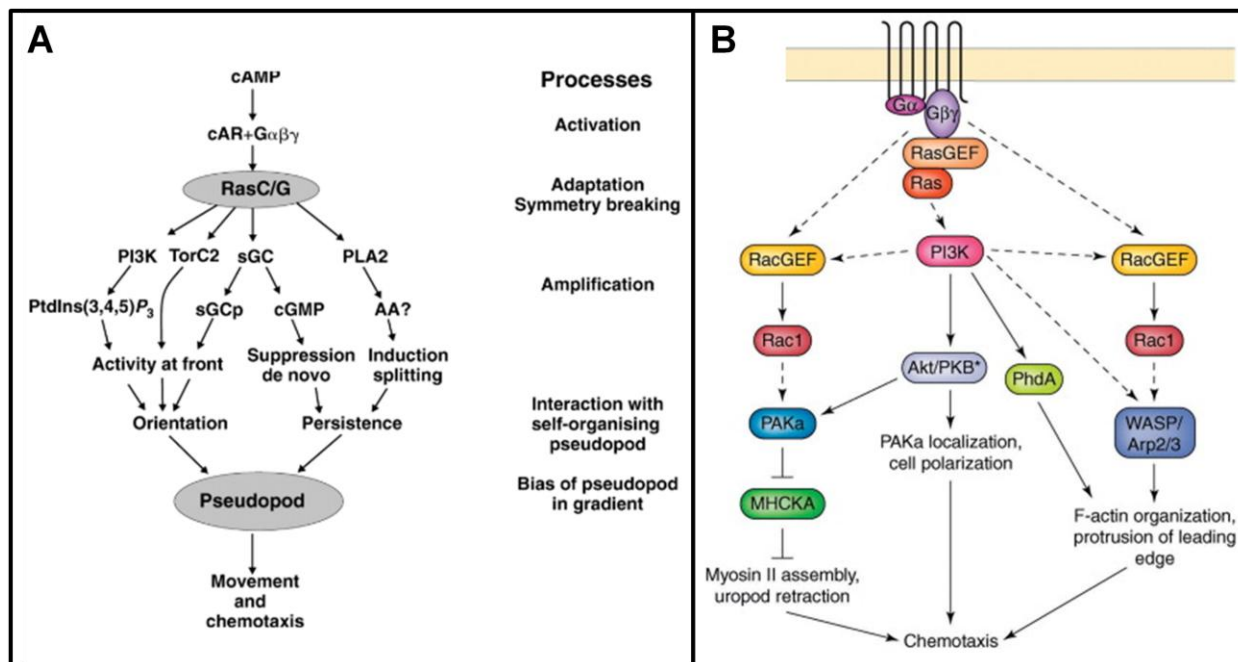


Figure 2.7 Example chemotaxis signaling networks in *D. discoideum*. A) Signaling network connecting cAMP binding and pseudopodia creation from a review connecting many studies together<sup>79</sup>. The phenomena associated with each level in the chemotaxis path are noted in the right column. Several parallel paths are responsible for these phenomena. The network is a mix of signaling proteins and descriptions of cell responses. The proteins that govern specific responses have been found through genetic knockdown studies where single elements were removed from the cells and the responses compared to wild type cells. B) Signaling network connecting g-protein subunit disassociation to chemotaxis<sup>74</sup>. The protein signaling network governing actin and myosin kinetics is outlined and connected to the phenomena at the front and back of the cell that give rise to chemotaxis. The signaling network map is of little importance to our work, but illuminates one of the methodologies employed to describe chemotaxis. We abstract the signaling network and instead connect receptor changes directly to chemotactic measures to determine the quantitative effects of receptor number and phosphorylation. Our method could be extended to each step in the transduction network to build a quantitative description of chemotaxis.

## 2.8.2 Phenomenological models

Phenomenological modeling involves observation and quantification of a systemic behavior and a subsequent discovery of the rule set that governs the creation of such patterns. Typically, the models start with the simplest, shortest set of rules that yield the most salient features of the phenomenon. The model can be made more complex and accurate with increasing difficulty. One example of a phenomenon treated in this fashion is the creation of spiral waves in excitable media, whose most basic requirements are an autocatalytic element, an inhibitory element, diffusion, and a constraint. Many systems can be described broadly by the simplest model, and individual systems can be further addressed by adding more rules to it. In the aggregation of *D. discoideum*, the cells themselves are the autocatalytic piece, secreting more cAMP when they encounter it<sup>75,80,81</sup>. They also supply the inhibitory piece, pdsA<sup>82,83</sup>, which degrades cAMP. Both molecules are subject to diffusion, and the system is constrained by the transduction networks governing chemotaxis and secretion, which change the location and timing of the release of both chemicals. The result of this configuration is spiral waves<sup>84,85</sup> in the motion of *D. discoideum* as it aggregates, which have been implicated as the method for self organization and later differentiation choices<sup>23,86</sup>. In order to understand how the transduction networks constrain the population response, additional symbols that represent the embedded interactions of the proteins that construct the networks have to be utilized and their relationships defined. This is, of course, the reductionist approach. Genetic knock out studies similar to the ones used to probe the signal transduction network were used to modulate key components of signal relay. Unperturbed cells produce both concentric waves and spiral waves<sup>87</sup> and the conditions required for each

have been investigated with such knock outs. PdsA was shown to be an important mediator of class selection, spiral or concentric, in this fashion. Populations of cells that could not produce pdsA always made concentric waves and mixed populations showed both<sup>80</sup>. Cell density was also implicated in class selection by simply titrating them before placement on the surface<sup>84,88</sup>. A comparison of the waves of motion of cell populations with variable density to the predicted waves from a model including density and pdsA degradation is shown in Figure 2.8.

Both the internal and external dynamics of the transition from unicellular to multicellular through aggregation by chemotaxis exhibit the characteristics of excitable media. In order to connect the two scales, the transduction network needed to be modeled as an excitable system and the initial efforts to do so include a black box with these dynamics inside. These early efforts had some success in describing migratory characteristics that previous models had failed to predict, specifically the ability to adapt to signals and filter noise. Such successes encouraged the continued effort to explore these models and match them to physiological agents. In doing so, the two scales were connected through the framework of excitable media.

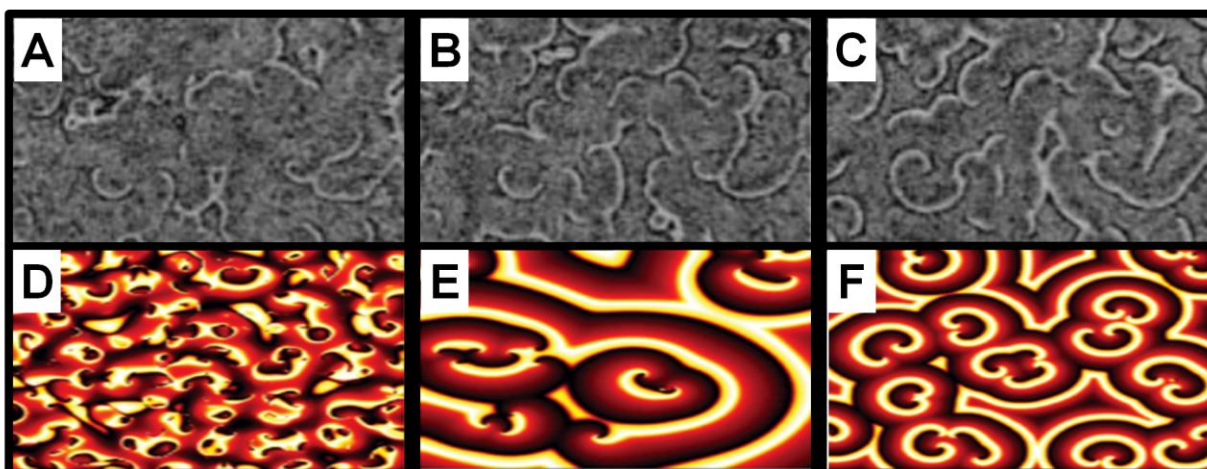


Figure 2.8 Comparison of observations of spirals waves *D. discoideum* motion and predicted wave patterns for excitable media. A-C) Visualization of spiral wave motion generated by subtracting sequential images of the cells<sup>84</sup>. Together, frames A-C show onset of pattern formation over two minutes. Frame A is the earliest, B and C are one and two minutes later respectively. D-F) Simulations of excitable media representing *D. discoideum* cells with different Camp degradation rates<sup>89</sup>. Frame D is the lowest, E and F are one and two orders of magnitude higher respectively. The model is populated with the kinetics of cAMP secretion and allows for diffusion. The observation of waves and comparison to the sizes of the different simulations allowed the degradation rate to be calculated. The phenomenological models and the reductionist protein models are distinct but can help inform each other through simulation and behavioral prediction. The protein models need to be further quantified into a predictive framework and the phenomenological models need to have their parameters informed through experimental measures. Our study offers a method for determining the validity of protein models and our future work section outlines an experimental procedure for populating the excitable parameters through observation of the cAMP field.

### 2.8.3 Bridging the Scales

The first effort to insert an excitable box into the signal transduction network of *D. discoideum* came in the form of local excitation, global inhibition (LEGI). LEGI works by having a uniformly distributed chemical species that inhibits the excitable species. This sets a signaling threshold that filters out noise. Once above this threshold, the excitable species produces more of itself and the inhibitor with some lag. This causes a rapid rise, or excitation, of the species followed by a drop back to basal levels. Once the excitable species is at its basal level, the inhibitor drops as well, resetting the threshold. Small signals when the inhibitor is high are ignored, though larger stimuli can raise the excitable species again. The LEGI models have captured chemotaxis behaviors that previous efforts have been unable to recapitulate, namely sensitivity to shallow gradients, through amplification of internal gradients by inhibiting signals at the back and becoming excited at the front, and the cytoskeleton waves that accompany migration<sup>90-93</sup>, while retaining features of simpler models such as cell shape<sup>94,95</sup>. It was later discovered that this framework describes the dynamic regulation of PIP3 through both PTEN and PI3K, where local signals drive an increase in PI3K action and a decrease in PTEN action. Both paths are excitable, so these effects are autocatalytic and rapidly increase after passing a threshold. The threshold is set by global inhibition of both paths, which also acts to cancel errant signals<sup>96</sup>. The two parallel LEGI systems act to enhance PIP2 phosphorylation (via PI3K) and reduce PIP3 dephosphorylation (via PTEN) to amplify the gradient signal directly downstream of the receptors, successfully describing a method for shallow gradient sensing. The observation of

propagating waves around the perimeter of the cell during migration<sup>97,98</sup> moved investigation towards incorporation of the actin cytoskeleton into the excitable framework. The proteins that govern pseudopod formation via polymerization and depolymerization in the actin cytoskeleton have the required properties for excitability; they are subject to diffusion and feature autocatalysis via a positive feedback loop<sup>99-101</sup>. Although the inhibitor is unknown, the polymerization features a threshold before initiation, which indicates that it exists<sup>102</sup>.

These excitable networks operate on different timescales so their connection is only possible in a framework that contains memory, which allows the different elements to proceed with respect to the past states of the other elements. To further connect the dynamic response kinetics, detection of shallow gradients, and actin waves together in a unified framework, Legi modules were connected to biased excitable network elements (BEN) whose responses depend on previous states. With the biased elements, the timescale of each response could be set by perturbing model parameters, connecting various scales of phenomena within the LEGI framework<sup>99,103</sup>. The LEGI systems in *D. discoideum* are upstream of both the migratory and chemical secretion pathways, which connects the excitable protein networks to the excitable global phenomena of spiral waves of cAMP through a single mechanism<sup>90</sup>. As the models become more complex, it takes more time to check the accuracy of all of the individual elements. In order to speed up the process determining the feasibility of models, attention turned to finding the fundamental limitations of signal transduction so that any model that violated these limitations could be quickly discarded or modified. Here we describe the abstract framework that calculates such bounds, communication or

information theory. This nonparametric framework assumes no form of the relationships between signals and their responses so any transformation or transduction system is inherently viable. Determining the feasibility of models in this framework depends solely on the content of the signals and responses, which is advantageous when the signaling networks are not fully mapped. We begin with the quantification of distributions of signals and responses, cover the metric for dependency between them, then discuss how the bounds of this dependency allow for model sorting.

## **2.9 Information theory**

The aggregation of *D. discoideum* cells relies on intercellular communication. Communication theory or Information Theory (IT) conceptualizes communication in a mathematical framework by treating the basic components of communicated media, such as words within a language, as a distribution of symbols with defined probability of being transmitted. In linguistics, the probability of a word would be based on the frequency it is used within the language. For instance, 'the' would have a relatively high probability in English while 'sporadic' might be self-descriptive. Within the context of a sentence these probabilities can change which allows for a listener to guess at the any missing content. IT aims to quantify the ability of a transmitter to send a message accurately through a communication channel to a receiver, and illuminate the effects of signal processing<sup>104</sup>. In *D. discoideum*, cells transmit chemical messages through complex internal pathways when probing their environment and through external solutions to signal to each other. The transduction networks process the inputs to

mediate cellular responses to internal and external cues. IT has been directly applied to quantify the transduction capability of cellular signaling pathways<sup>105,106</sup> and has identified the structure of several signal transduction networks<sup>107–109</sup>. Indeed, the view of *D. discoideum* as a communication channel has yielded many insights.

### **2.9.1 Information**

In his seminal work on information theory, Claude Shannon outlined the method for quantifying information and its transmission. He begins with a description of an abstract communication channel, through which any set of symbols can be conveyed, from sounds to images to binary digits. A schematic of such a channel is shown in Figure 2.9. The set of symbols can be encoded, which changes the distribution of symbols, sent through a medium such as air or a wire where it is subjected to noise, then decoded into another set of symbols. The measure that describes the distributions of symbols is called information. This measure is crucial to determine channel transmission rates, optimal encoding schemes, and uncertainty. The definition of information is analogous to entropy from statistical mechanics and denotes the amount of uncertainty in the outcome of a random process.

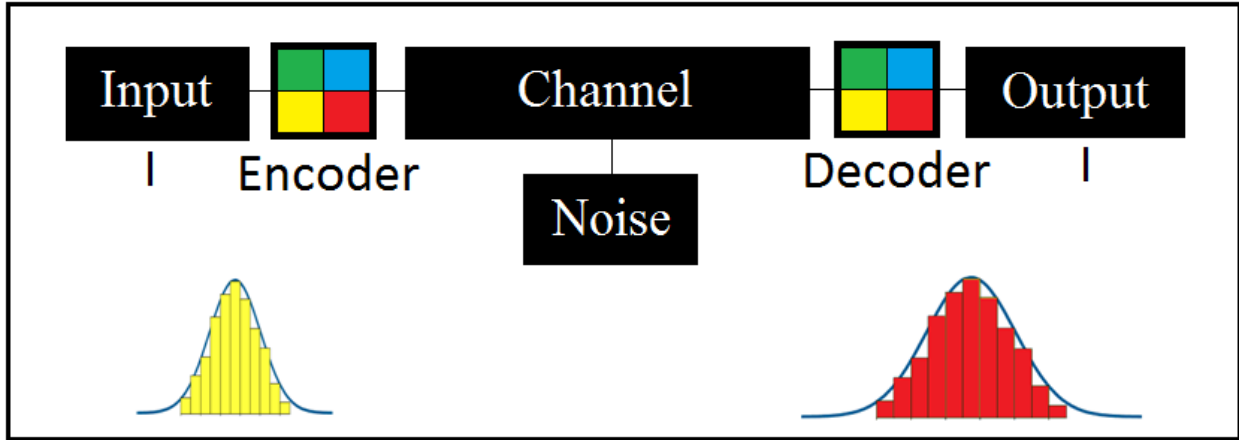


Figure 2.9 Representation of a communication channel. A distribution of input messages is shown on the left in yellow. These messages are transformed using an encoder, which changes the symbols within the input distribution. The transformed messages are sent through a medium called the communication channel, where they may be subjected to noise which obfuscates the symbols as they are transmitted. The messages are then decoded using the inverse of the encoding transformation and the resulting messages are aggregated into the output distribution. Information theory quantifies the speed and accuracy that the messages can be transmitted through the channel. In our study, the input distribution is the distribution of gradient angles within the cAMP field, the channel is the signal transduction network and the output is the distribution of cell trajectory angles.

Generally speaking, the more uniform the distribution, the higher the information, and the more possible outcomes, the higher the information as shown in Figure 2.10. The equation for calculating information is:

$$I(X) = \sum_{x \in X} p(x) \log_2(p(x)) \quad (2.1)$$

Where  $I(X)$  is the information in bits of the random variable  $X$  and  $p(x)$  is the probability of  $x$ . The base of the logarithm sets the units. A bit is the amount of information in a discrete random variable that has two equally likely outcomes, and is commonly used in computer systems which are built on binary. The base that corresponds to bits is 2, and is the base that is used throughout this document. Information theory was first used formally to describe the rate at which computer systems could reliably transmit symbols over a noisy communication channel, the channel capacity. It was quickly applied to both encryption algorithms, which obfuscate messages by increasing the number of symbols used, and compression algorithms, which shrink file sizes by decreasing the number of symbols. Similar approaches to biological systems were also developed to investigate transduction schemes by quantifying environmental variability and predictability of behaviors over time. Information theoretic approaches have been used to quantify transduction capability of cells to particular responses, to find signaling bottle necks. IT has also been used to determine the number of redundant systems required for cell decision making as well as determining the overall complexity, the number of signaling agents, in a transduction system<sup>110,111</sup>. Similar approaches have been used to create rule sets for cellular automata and sort behaviors into classes<sup>112</sup>.

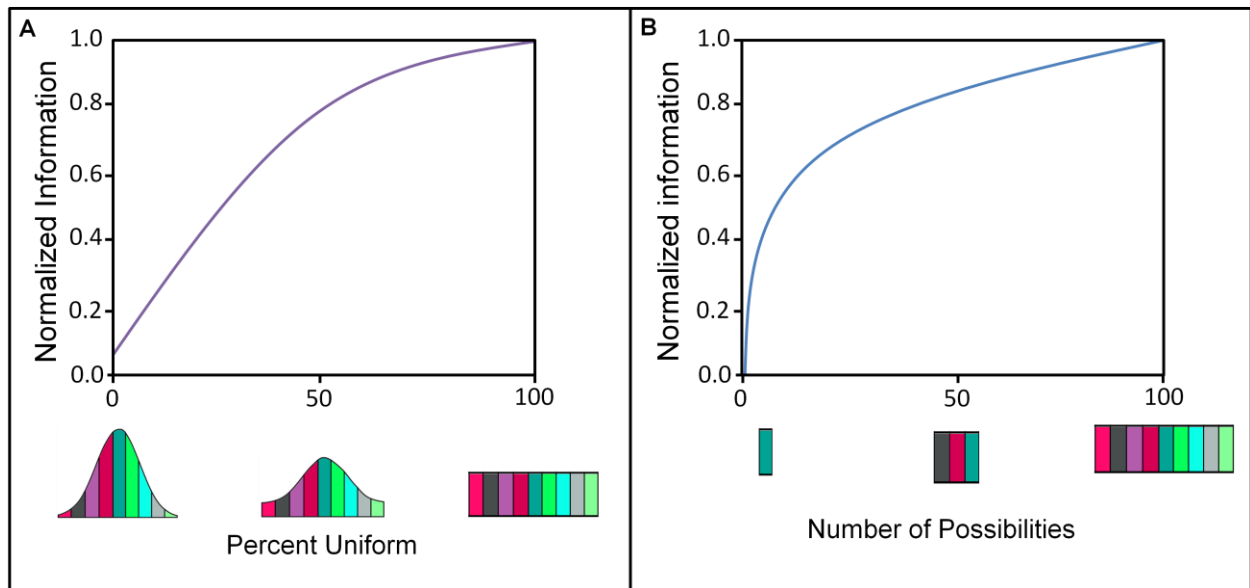


Figure 2.10 Information versus uniformity and number of possibilities. A) Uniform and Gaussian distributions are convolved to different degrees, with the far left being entirely Gaussian and the far right uniform. The distributions have identical mean and variance. The information at each level of convolution is calculated and normalized to the information of the uniform distribution. The information increases as the resulting distribution becomes more uniform. B) Uniform distributions with results drawn from increasing numbers of bins are created and their information content calculated. Information is normalized to the information of a uniform distribution with 100 bins. As the number of possible events, or bin number, increases, so does the information content. The external chemical field changes drastically during the development of *D. discoideum*. In the vegetative state, the external field is uniform with fluctuations around the bacteria that the cells hunt. During aggregation, the chemical field is often assumed to be normal, but the actual distribution is unknown. Our experiments impose a normally distributed cAMP field throughout the developmental time course, which limits the information available to be transduced, though the transduction is lower than the capacity by a factor of two.

### 2.9.2 Mutual Information

In order to quantify the efficiency or capacity of any communication channel, a metric relating the inputs and outputs is required. Mutual Information (MI) fills this role as a measure of the dependence between the input and output.

$$MI = \sum_{x \in X} \sum_{y \in Y} p(x, y) \log_2 \left( \frac{p(x, y)}{p(x)p(y)} \right) \quad (2.2)$$

Where  $X$  and  $Y$  are random variables and  $p(x, y)$  is the joint probability distribution. Since the communication channel makes no assumptions about the relationship between the input and output, it is critical that MI be nonparametric. It uses the ratio of the joint probability distribution to the marginal distributions, which is unity when  $X$  and  $Y$  are independent thanks to Bayes' law, which states that if  $X, Y$  are independent, then

$$p(x, y) = p(x)p(y) \quad (2.3)$$

Which makes MI zero for independent variables. MI is also bounded by the minimum of the information content of the two distributions independently, as you can never decrease uncertainty over a communication channel. Bayes law can also be employed to change the above MI equation into another form:

$$MI = I(Y) - I(Y|X) \quad (2.4)$$

The two equations for MI are equivalent, but are often interpreted differently. Equation 2.2 is interpreted as the entropy that is shared between two processes, similar in concept to covariance which gives the strength of a linear relationship between two

variables. This form is commonly used in phenomenological studies where individual messages are either inaccessible or meaningless. Equation 2.3 is interpreted as the average reduction in entropy in an output upon receiving a message from the input. This interpretation is commonly employed in reductionist approaches, where individual messages can be measured and their responses recorded, to make statements about the distribution of responses from particular signals. The responses are distributed instead of exact due to noise within the network. These interpretations are identical as well, accumulation of all of the individual methods will yield the full distribution and the full distribution can be sub-sampled. The advantage of having the two equivalent equations and interpretations is that the reductionist and phenomenological views can be tied together in a single value and connected in words. The two scales have yet to be connected in this fashion, but progress on both ends has been made. MI between the external chemical cue and cellular response has illuminated individual signaling pathway structures and given an upper bound for the information transduction of the network across several signal distributions<sup>113</sup>, and optimal prediction schemes for dynamics in excitable media have been established using IT<sup>114</sup>. Connecting these together requires the correct conditions within the prediction schemes which are dependent on correctly, or at least functionally, modeling the dynamics of the transduction networks. Plausibility of models can be determined using the data processing inequality, outlined below.

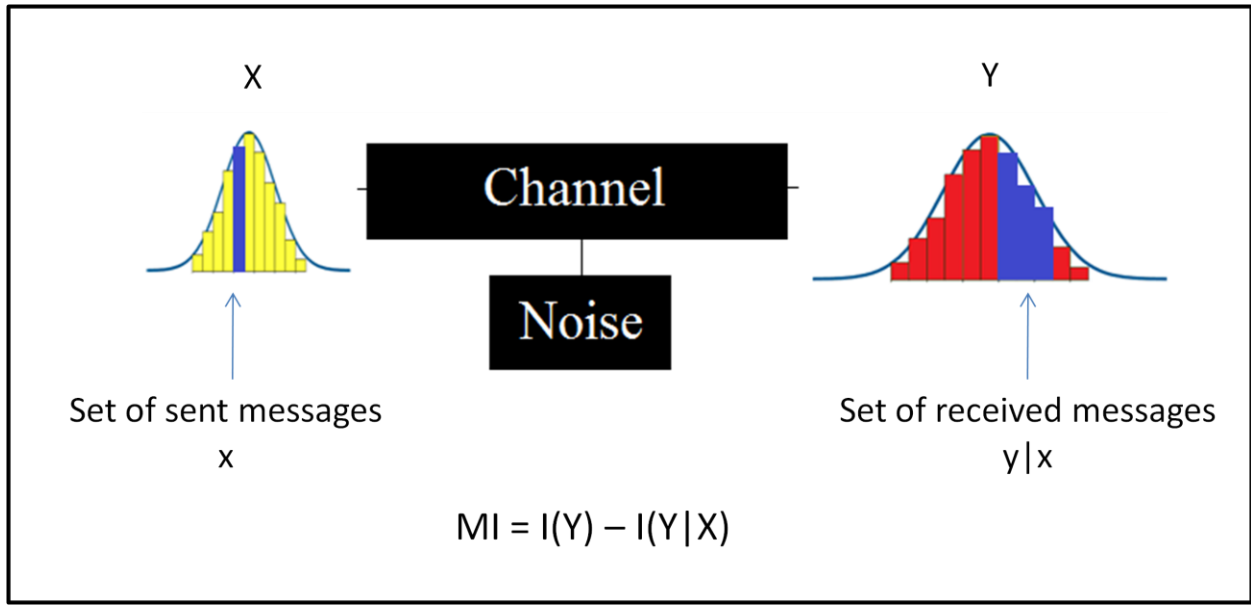


Figure 2.11 Mutual information over a communication channel. A set of messages ( $x$ ), blue bar, is drawn from the input distribution ( $X$ ) in yellow on the left. These messages are sent down a noisy communication channel and received at the output ( $Y$ ), the red distribution. The set of received messages ( $y|x$ ), blue region right, is collected in the output distribution. The Mutual information is the difference between the information of the output distribution and the information of the set of received messages when the input is known. We measure the gradient angle and the cell trajectory and calculate the MI between them. The MI value states the transduction capacity of the signaling network for the given input distribution and is used to validate chemotaxis models.

### 2.9.3 The Data Processing Inequality

The data processing inequality essentially states that information content cannot be increased through post processing. Upon transmission of signal over a noisy channel, nonnegative uncertainty is introduced and cannot be combated except through further communication. A natural extension of this concept is that in any multistep process, MI between the first and nth step is always less than or equal to the MI between the first and n-1th step. Information cannot be created through processing. This is more formally stated in the data processing inequality<sup>115</sup>.

For a markov chain

$$\begin{aligned} X &\rightarrow Y \rightarrow Z \\ MI(X, Y) &\geq MI(X, Z) \end{aligned} \tag{2.5}$$

This is a convenient rule to apply to signal transduction networks because they have many steps in the processes of communicating an event and forming a response. The steps in signal transduction all rely on the state of the previous step, so they form a Markov chain. All of the steps that are visualized and quantified can also be ordered and bottlenecks, which create the most uncertainty, can be located. Models of transduction networks are compared to these experimental measurements to check their validity and determine when knowledge is missing by using the data processing inequality.

### **2.9.4 The Data Processing Inequality in *D. discoideum* Signaling**

*D. discoideum* chemotaxis involves several transduction steps. The external chemical field probabilistically binds to receptors on the cellular membrane, which release g-protein subunits into the cytoplasm, triggering a protein-enzyme transduction pathway. These spatially distributed activations change the local protein concentrations and result in preferential pseudopodia extension at locations of higher chemical concentrations. Models of individual steps are validated by comparing their theoretical transduction capability to measurements of the upstream steps. For instance, observation of the transduction of the external chemical field, the most upstream step, to directed migration, the most downstream step, sets the bound on all of the intermediate steps. This has been used to validate theoretical receptor transduction models, which lie between the external field and directed motion. The other pieces of the transduction network can be similarly approached so that models of pieces and the whole transduction network can be validated. Several advances in the understanding of the structure of the signaling network have already been made, outlined below.

### **2.10 Information Theoretic Models**

Recapitulating all aspects of *D. discoideum* chemotaxis in a simulation has remained elusive in modeling efforts, though various models have been able to emulate some the behaviors. IT has been applied in chemotaxis modeling in an effort to elucidate whether hypothesized transduction modules were feasible through application of the data processing inequality. This method was used to show that cells leverage internal bias,

polarity, to improve chemotactic ability during intercellular signaling when external chemical gradient angles are persistent<sup>116</sup>. An application of IT has additionally confirmed that the cells must control external chemical levels through degradation to combat noise and increase the concentration range over which they can chemotax<sup>117</sup>. A key question that has been raised by such studies is how the environmental noise level attenuates the bounds for transduction. Experimental probing of this question is difficult, as changing relative noise also changes gradient strength, concentration, or both, requiring many variations on these parameters to successfully delineate their effects. Models that include gradient strength and concentration have alleviated some of this requirement by making predictions about how the bounds would change. In our work, we extend these models over development to elucidate the effects of relative noise as the cells change. We compare this extended model to experimental conditions at two gradient strengths over development to validate it. Here we outline the models that we extended.

### **2.10.1 Levine Model**

Analytical approaches to information theory models have more rapidly advanced than experimental measurement of signal transduction due to the difficulty in correctly binning data and the large amount of data points required to accurately estimate transduction. Theoretic approaches began when Levine created a geometrically simple model cell, which had receptors uniformly distributed on its surface. Each receptor has a probability of being bound at any point in time that is a function of its binding kinetics

and the local chemical concentration. The local chemical signal could be derived from any distribution, but this work focused on uniform and normal distributions of gradient angles for an ambiguous mean concentration. The transduction capacity of the spatially distributed receptors was analytically approached. The total information transduction of chemical cues into directed migration is limited by the noise at the receptors, so modeling the receptors establishes an upper bound for the whole cells transduction ability due to the data processing inequality. The upper bound for each distribution type was calculated. This work had one particularly clever step in the analytical approach that facilitated the rest of the derivations. Initially, the derivation of the transduction bound involved a difficult 2-D integration, which could only be approximated with series expansion, as had been done previously<sup>113</sup>. Levine took advantage of the simple geometry to change the spatially distributed random variables describing the receptor binding probabilities into a complex random variable vector, which was sufficient for the analytical solutions. By turning the problem into a 1-D complex integral, the analytical solution for the transduction bound was found:

$$MI(\theta; \varphi) = MI(\tilde{\mathbf{Z}}; \varphi) = \tilde{k} - \langle \ln \left[ I_0 \left( \frac{\tilde{p}\tilde{k}}{\beta v} \right) \right] \rangle \quad (2.6)$$

Where  $MI(\theta; \varphi)$  is the MI between the external gradient angle  $\theta$  and the trajectory response angle  $\varphi$ , equated to the MI between  $\varphi$  and the complex random vector  $\tilde{\mathbf{Z}}$ , which describes the probabilities of spatially distributed receptors being bound.  $\tilde{k}$  is the external noise,  $\beta$  is an amplification constant,  $p$  is the gradient steepness,  $v$  is  $p\sigma^2/2$ ,  $\sigma^2$  is the external variance, and  $I_0(\cdot)$  is the modified Bessel function of the first kind and

order zero. To test this model, experimental collection of gradient angle and cellular response needed to be collected, but the paper instead made an assumption about the mean and variance of their applied signal and showed that, if their assumption was correct, the model did not violate the data processing inequality. Direct measurements of the external signal have been made possible thanks to the availability of fluorescent proteins attached to biocompatible small molecules. There have additionally been advances in imaging technology to enable the creation of larger data sets of cell tracks and chemical signals so that experimental measurement of transduction with reasonable uncertainty is feasible. These efforts created a framework for validating models of transduction through experiments with well-defined external signals, typically linear or exponential gradients, through comparison of the predicted upper bound on transduction to experimental measures.

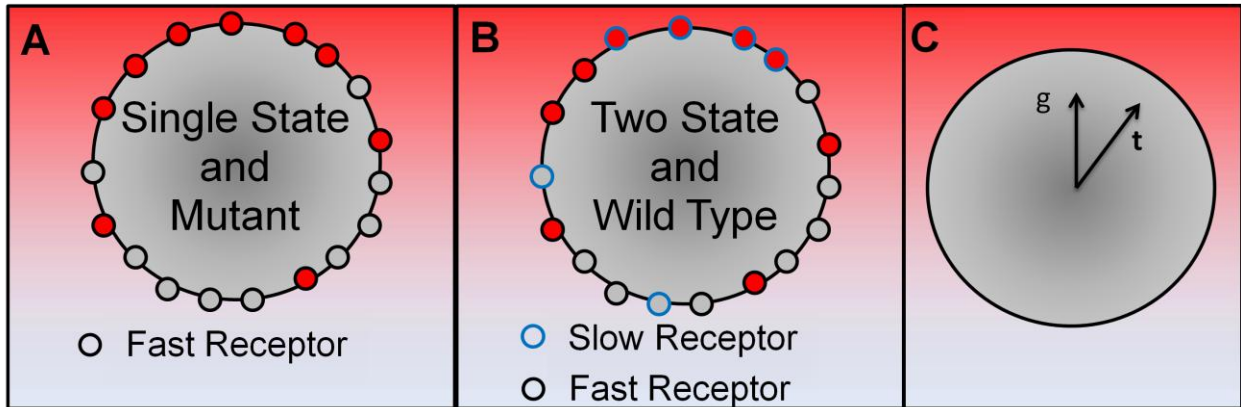


Figure 2.12 Cartoon of the Levine and Segota models. A) Representation of the single state model and mutant cell line. The cAMP concentration is shown as red intensity and the cell is represented by the gray circle. On the outer membrane the uniformly distributed receptors are the smaller circles and the red fill and gray fill are bound and unbound receptors respectively. The binding rates are a function of the dissociation constants and the local concentration, resulting in a higher probability of being bound in higher cAMP concentrations at the upper side. B) Inclusion of two states into the model, which is equivalent to the wild type cells. The two receptor states are outlined in blue and black for slow and fast respectively. C) Cartoon of the experimental data. For each observation, the gradient angle and cellular trajectory are calculated and recorded. This data is aggregated into a joint probability distribution and the MI between the gradient and trajectory is calculated. The one and two state models set the upper bound for signal transduction of the mutant and wild type observations respectively. We extend the model predictions over development by incorporating the receptor number and phosphorylation changes and experimentally validate the models by showing that the experimental measures always lie under the model predictions.

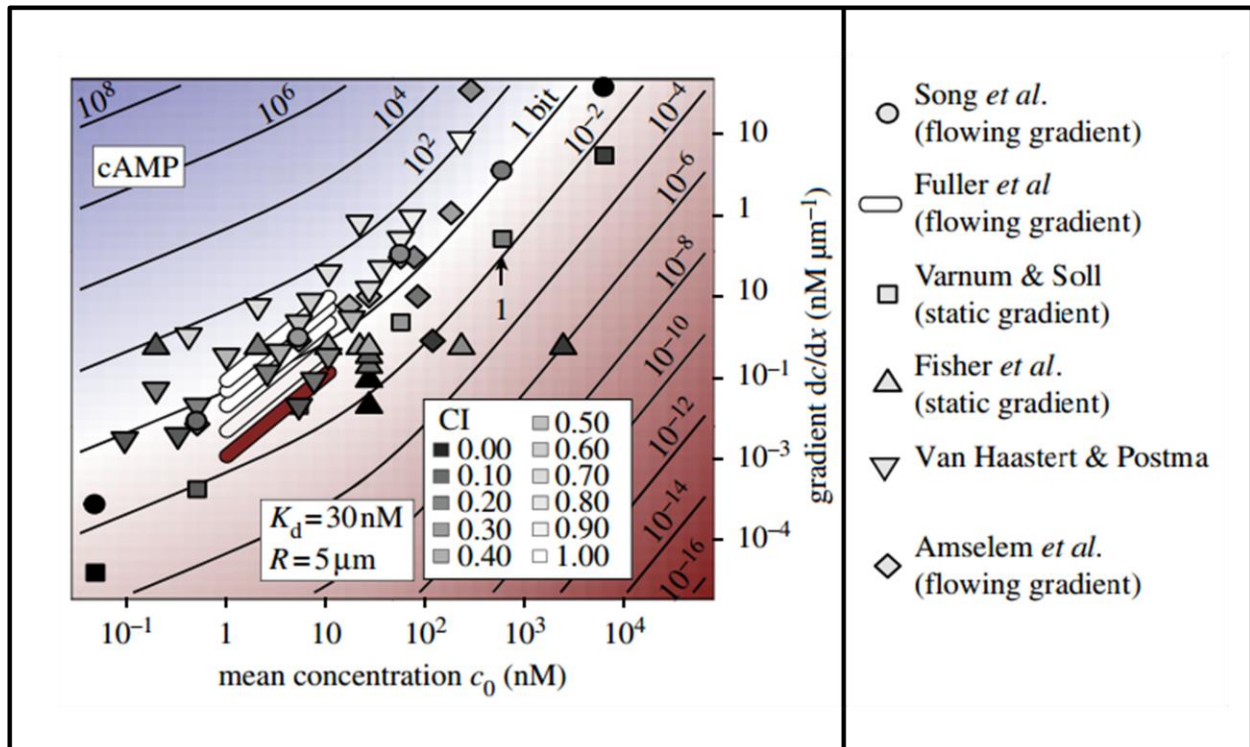


Figure 2.13 Collection of MI measures from literature<sup>117</sup>. Mean concentration and gradient strength determine the signal to noise ratio which is noted by color. The red regions have relatively high noise, while the blue regions have relatively high signal. The calculated values for the upper bound of information transduction for the gradient and concentration are plotted along constant values as solid lines. The model used to generate the information bounds is the single state Levine model for cells with a radius of five microns and receptors with 30 nana-molar dissociation constants. The experimental results are plotted in various shapes for different papers and their CIs are denoted by color with darker being smaller. The paper list is in the right side legend. The experiment with the largest violation of the data processing inequality is denoted by a 1 and this region is studied further in the following sections. We study this region over development for both the wild type cells and the mutants whose receptors are always phosphorylated to determine the effect of receptor changes on transduction.

### 2.10.2 Segota Model

After the pioneering work by Levine, Segota compared experimental measures of MI to the theoretical bound at varying mean concentrations and gradient strengths. This study scanned relative external noise under a variety of conditions to deconvolute the effects of noise, gradient strength, and average concentration. Starting with the Levine model, they found that at low to mid gradient strengths and concentrations the data processing inequality is not violated, so the model is a reasonable description (see Figure 2.14 left). At high concentrations and gradient strengths however the experimental measurement exceeds the theoretical bound; the data processing inequality is violated. The model, therefore, could not be complete. It was already known that the CAR1 receptor in *D. discoideum* changes from a fast signaling state to a slower one via phosphorylation due to a binding event, and this was added to the Levine model. They showed that models with two different receptor speeds alleviated the violation (see Figure 2.14 right).

We build on the work of Levine and Segota in our study by extending these models through development. The number of receptors and the fraction that are phosphorylated, and therefore slow, changes over the course of development. Both of these parameters are in the aforementioned models so the predicted bounds for transduction will change. Additionally, we experimentally test these new bounds by exposing cells to two different gradients at several developmental time points. We also extend the single receptor speed model over development and experimentally realize it by leveraging a mutant cell line that whose receptors are always phosphorylated. In both of these cases, the data processing inequality is not violated.

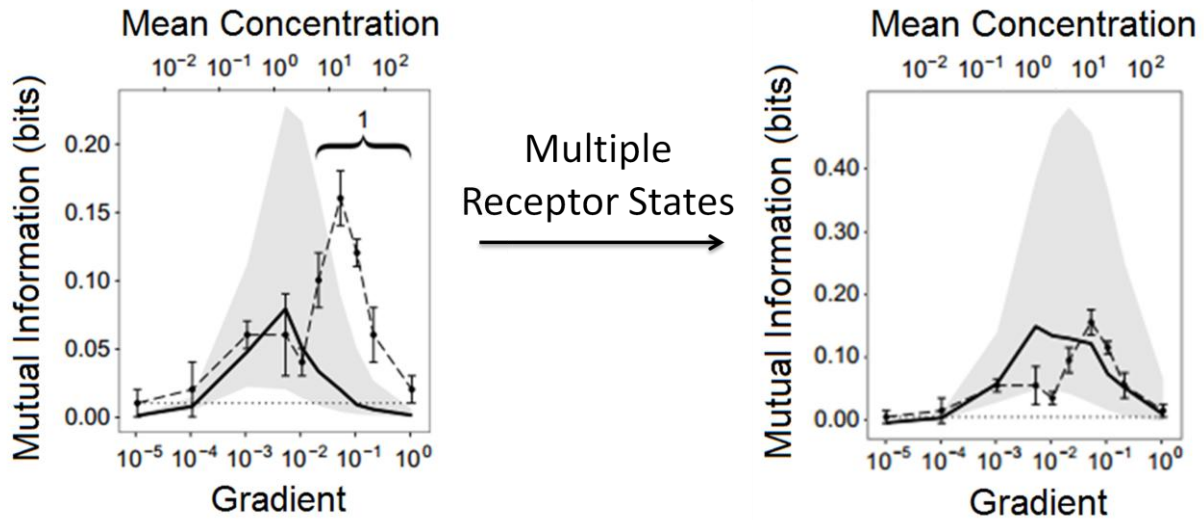


Figure 2.14 Mutual Information in experiment versus single and multistate receptor model bounds. Left) Single state predictions for MI are plotted as the solid against gradient steepness and mean concentration. The shaded region represents the model bounds for all of mean concentration inside of the gradient chamber, which changes inside of a linear gradient chamber. The experimental results are graphed as the dashed line with error bars representing the standard error. If the data processing inequality was not violated, then the experimental results would be under the top of the shaded region everywhere. This is not the case in the region denoted by a 1, and is the same region from Figure 2.13. Right) the inclusion of multiple receptor states changes the model bounds by a large enough margin such that the data processing inequality is no longer violated. We extend the model predictions over development and use a mutant cell line with a single receptor state that should follow the single state predictions to determine whether the models are valid and if the change in transduction capacity is due to multiple receptor states.

There have been several additional IT models for chemotaxis transduction, focusing largely on the dependence of transduction ability on the ratio of external noise to external signal, or the inclusion of specific transduction elements into the IT framework. Here we outline those efforts, and in our work we show qualitative agreement of our findings with the model predictions.

### **2.10.3 Rate Distortion and LEGI**

Rate distortion theory is a sub field of information theory and, where information theory aims to find the maximum rate of accurate transduction for a channel, rate distortion aims to find the speed at which symbols should be transmitted to be reconstructed with some acceptable threshold of inaccuracy. This is useful in studying signal transduction in cells because the inaccuracy can be measured and used to calculate parameters within models that would give rise to exactly that distortion. Thus, if a transduction channel is known and the bounds for transduction are calculated with information theory, the internal noise on the different elements can be used to account for the difference between the bound and the lower actual transduction capacity. Iglesias applied rate distortion theory to the LEGI model to account for such discrepancy between the LEGI bound and the measured transduction. Distortion was implemented in the LEGI model by varying the hill coefficient of the excitable element. The hill coefficient defines both the lower threshold for excitation as well as the steepness of the curve of the excitable element once past this threshold. Simply stated, it controls the

sensitivity to fluctuations in signal. This fits well into studies of the effects of environmental noise because modulating the external fluctuation magnitude and observing the responses of an excitable system allows calculation of this coefficient. The Iglesias work showed that the transduction capability could be matched by changing the internal distortion of a cell relative to the external noise levels. They thus found the distortion for vegetative and developed cells. This distortion was levied against internal bias, which weights the cell trajectory on previous movement, and compared to cell movement of the vegetative and aggregation competent cells. They found that vegetative cells had little to no bias while the developed cells incorporated bias. With the distortion and bias for both developmental stages they calculated the optimal chemical fields that the LEGI model with these parameters could transduce and found the early cells are best at transducing uniform distributions with high fluctuations and developed cells are best at exponential gradient. This is in agreement with the reality of the signals presented to those cells at those developmental stages. Early in development, the cells are primed to respond to secreted factors from uniformly distributed bacteria, which make a uniformly distributed chemical field with local fluctuations. Later in development, the cells are attracted to aggregation centers, which yield exponential gradients that are normally distributed from what is approximately a point source when far away. They conclude that the cells are indeed utilizing an optimal sensing scheme for their expected environment at different stages of development. Using a Monte Carlo method, they then compute the chemotactic efficiency, which gives the projection of cell motion in the direction of the gradient as a percentage of the total length travelled, for various values of bias and distortion and compare to analytical

calculations of MI that incorporate LEGI elements and bias into the Levine Model. They find that, in general, greater chemotactic efficiency requires greater MI and that bias increases chemotaxis efficiency. In our study, we explore bias through treatment of phosphorylation of receptors as a mechanism for integrating signals. Phosphorylation slows down the kinetics of the receptor so that g-protein subunits remain in the cytoplasm for longer after a signaling event triggering downstream signaling and receptors take longer to bind to external cAMP. The smaller frequency of sampling the environment and changing internal signaling effectively increases the time required for a cell to change its motion, biasing it towards previous trajectories. We similarly find that bias increases the accuracy of chemotaxis.

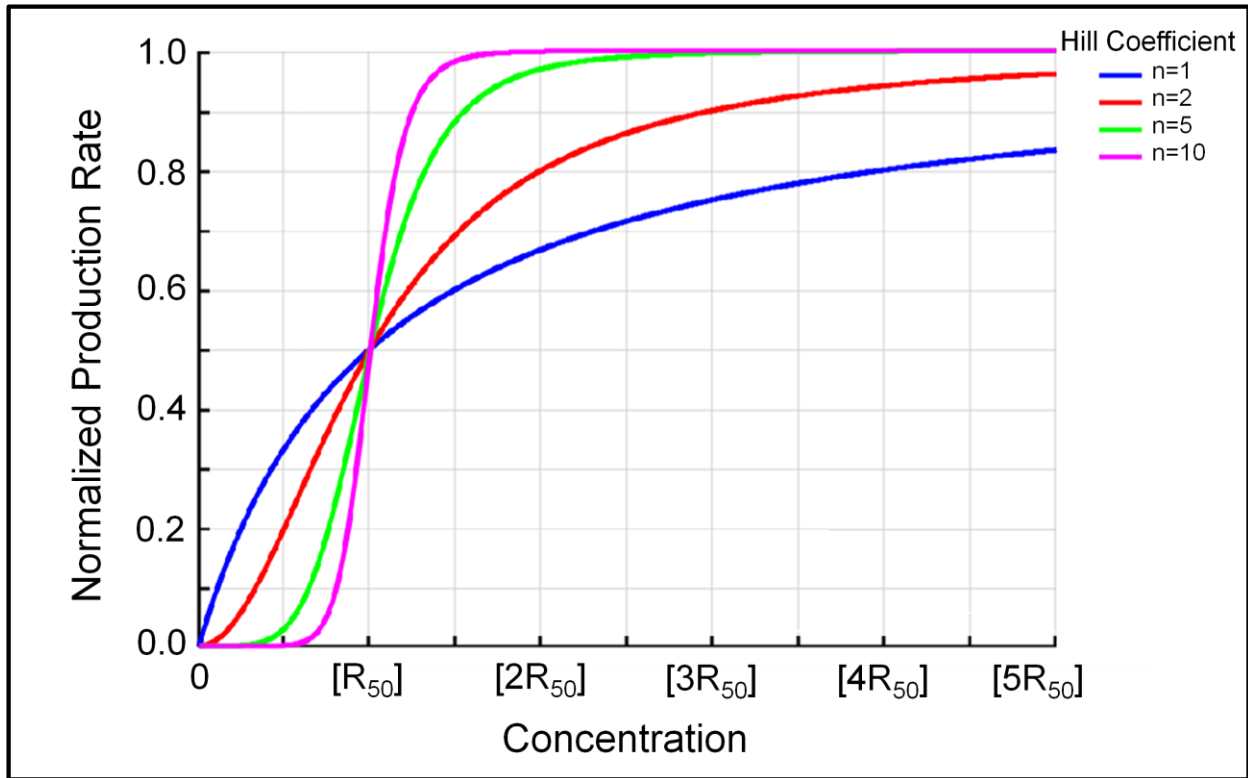


Figure 2.15 Hill functions with varying Hill coefficients. The production rate of an excitable species is plotted against concentration. The rate is normalized with respect to its maximal rate. The concentration is expressed in terms of the concentration at which the rate is half maximized. The steepness and threshold of the response of an excitable system can be matched to a Hill function by fitting the coefficient and half maximal concentration. The threshold sets the magnitude of the environmental fluctuations that the excitable system will ignore and the steepness sets how quickly it maximizes its production after passing the threshold. These two parameters were used to match the chemotactic response of *D. discoideum* to different amounts of environmental noise. In our future work section, we outline the extension of excitable information theoretic models over development. The hill coefficient may be changed as development progresses, and the thresholding that is supplies can be experimentally tested using variable relative external noise values.

#### **2.10.4 Filtering and Integration**

The Endres group studied memory schemes and their impact on signal transduction and compared the theoretical limits to experimental measures performed in a gradient chamber that could be switched in a few seconds. They also varied the gradient steepness and concentration to study the effects of relative environmental noise. Furthermore, they explored the effects of temporal correlation of environmental noise by changing how rapidly they reversed the gradient. This allowed them to determine the sensing strategy of cell in rapidly or slowly fluctuating environments. They compared two different strategies, one where the cell used prior measurements to predict the next signal (prediction), and another where the cell weighs previous and current signals to estimate the true current signal (filtering). They find that both schemes increase the signal transduction fidelity in fluctuating environments, giving a possible explanation for how the cells sense past the data processing limit of simpler models. They then compared the turning behavior of simulated cells with prediction and filtering schemes to observations in the gradient chamber and saw the cells persisting in the original direction and making a u-turn, which qualitatively agrees with the filtering simulations. These filtering schemes are equivalent to integrating signals over a larger time step, implemented biochemically as an incoherent feed forward loop.

#### **2.11 Persistence**

As a result of the integrating, averaging, and memory functions that cells employ to increase their ability to transduce external signals, they respond more slowly to dynamic

signals than simpler and less accurate sensing schemes. This is immediately evident when comparing early development cells that have less aggressive integrating strategies and shorter memories, and as a result change direction rapidly, to late development cells that employ these strategies in full and respond to changes in signals with arcing turns. The slow response, termed persistence, has been quantified using mean square displacement and folded into LEGI models using bias.

## 2.12 MSD

Cellular trajectories are easily tracked and are processed to find their randomness using mean square displacement (MSD). The slope of the log-space MSD versus delay time in measurement determines the power law relationship between the square of how far, on average, the cells move in a given time interval. For slopes near unity, the cells move like Brownian particles with their displacement growing as the square root of time. Slopes near two represent ballistic motion where displacement is proportional to time. Cells lie between Brownian and ballistic motion, and their persistence can be quantified as the transition between the two types of motion over time. Under no stimulus, developed *D. discoideum* cells will travel in a fairly straight line for about three minutes before transitioning into random motion<sup>41</sup>. These results have been used to add a stochastic fluctuation to motility models such that simulated cells have the same persistence time<sup>118</sup> and functional responses to external stimuli have been mapped using cellular observation and stochastic modeling<sup>119</sup>. These efforts set the accepted persistence time for cells in the absence of stimuli for a variety of perturbations.

### 2.12.1 Connecting LEGI to Persistence: LEGI-BEN

LEGI models of cells can predict a variety of aforementioned responses, but fail to predict how long cells will continue in a single direction, their persistence. In order to overcome this, LEGI was modified to include a biased excitable network module (BEN), which is driven by the LEGI outputs. This results in an excitable network that is filtered by the LEGI system, so that only locations where the LEGI has become excited have the potential to be excited in the downstream network<sup>103</sup>. This setup allows the bias of the system, and therefore the temporal response to dynamic signals, to be controlled by the LEGI parameters<sup>99</sup>. In tandem, these results incorporate a persistence control into the LEGI system which enabled LEGI parameters to be discovered through dynamic external field experiments and information theoretic approaches to be connected to persistence measures.

### 2.13 Intention of Manuscript

The body of literature reviewed above represents the approaches to chemical signal transduction into directed migration by *D. discoideum*, focusing on information theoretic approaches and receptor mechanisms. The literature at large is concerned with elucidating the transduction network and connecting it to the phenomenological response through a physiological framework. *D. discoideum* cells are studied primarily at either early or late developmental points, with the conserved elements between the two time points receiving considerable theoretical attention, but remaining

experimentally vacant. Modeling efforts utilizing analytical solutions to information theory measures have outpaced experimental validation as data collection on the scale required is cumbersome, especially in light of the theoretical focus on the relative noise in the environment which requires many physical perturbations to the microfluidic gradient controllers employed. The connection between persistence and chemical sensing strategies remains abstract and vague, particularly in the frame of information transduction. We aim to extend information theory predictions throughout the developmental time course by using known developmentally controlled receptor modifications in our transduction models and experimentally validating them using mutant cells that disrupt such modifications, thereby connecting early and late time points. Additionally, we use two microfluidic chambers that create gradients with different slopes to experimentally test the effects of relative environmental noise levels thought this developmental time course. Finally, we connect the transduction strategies to cellular persistence over development by observing cell responses to dynamic signals and processing them with both information theoretic and Euclidian metrics.

## Chapter 3

### Information Processing Throughout Early Development of *D. discoideum*

Manuscript submitted to the special issue of Physical Biology dedicated to

The 10<sup>th</sup> Q-Bio conference

Jonathan Ehrman, Mario Avaldi, Christopher Janetopoulos, and Erin Rericha

The manuscript presented herein would scarcely have been possible without the aid of Mario Avaldi. During his last two years at Vanderbilt, he spent countless hours in the lab collecting data and performing preliminary analysis. He showed initiative and work ethic rarely found in an undergraduate, and was always willing to debate every angle of the project (and all other topics). He also provided an opportunity for me to hone my mentoring skills while giving feedback on my approach, for which I am forever grateful.

#### 3.1 Abstract

Detection of chemical signals is critical for the function of eukaryotic cells. *D. discoideum* cells are particularly adept at responding chemical gradients, sensing single percent concentration changes across their body. *D. discoideum* has two well studied states at the beginning and end of a developmental transition, during which the cells change the number and speed of their receptors to better match their environmental conditions. Additionally, the cells elongate and become more persistent in their migration direction. Here, we measure the ability of the cells to sense gradients through this developmental transition as they change their internal machinery. Additionally, we

impair the ability of the cells to modulate the speed of the receptors and measure the effect of a single receptor state on gradient sensing over development. We compare cells from the wild type and mutants that are equally elongated to resolve any differences caused by misregulation of development in the mutants. We then extend a previous information theoretic model to include both receptor speed and number changes, and exclusively changes in number to represent both types of cells. We show that the models in each case show no violations of the data processing inequality, and are therefore reasonable descriptions of the cell responses. We compare the MI findings to the chemotaxis index of the cells to determine whether cell migration strategies skew toward instantaneous responses or integration of signal, and find that early cells respond to fluctuations while more developed cells integrate the signal. We confirmed this experimentally by exposing the cells to a switch in gradient direction and calculating the amount of time that it took the cells to turn. We then compare our findings to additional information theoretic approaches to modeling transduction and find qualitative agreement.

### **3.2 Introduction**

As the capacity for computational models has improved, more is needed from experiments to provide rigorous feedback. Recent efforts to model developmental transitions necessitate observation of cells at several time points and quantification of the dynamic relationship between environmental stimuli and the cells responses as this transition progresses. *D. discoideum* has long served as a model organism for studies for migration, signal detection, and developmental transitions. When nutrients are

plentiful cells of the social amoeba *D. discoideum* tend to be round, meander in their migration towards increasing concentrations of folic acid<sup>120,121</sup>, and react to reversals in gradient direction via internal reorganization of the cytoskeleton structure<sup>122,123</sup>, such that the front of the cells becomes the back. Upon starvation, the cells undergo a development cycle, mediated by an autocrine, paracrine feedback loop that stimulates the detection, synthesis, and secretion, of the common second messenger cyclic-AMP<sup>124,125</sup>. Later in development, the cells are elongated and respond to dynamic signals by turning their body around and retaining the cell front. These cells migrate in a single direction for longer; they are more persistent. Here we provide quantification of specific aspects of the developmental transition in order to improve the connection with computational models. In particular, we measure the changes in cell shape and persistence that accompany the first six hours of development. We find that wild type cell elongation begins at a development time of 3 hours and plateaus from 5 hours onwards. Cells early in development more rapidly change their migration direction in response to dynamic signals; persistence increases with development time.

The first six hours of the developmental transition is driven by the binding of cAMP to the CAR1 receptor, a g-protein coupled receptor, which is subsequently phosphorylated. Phosphorylation in mammalian g-protein receptors, is frequently a vital regulatory step<sup>126–128</sup>, however the role of phosphorylation for CAR1 is controversial with noted effects ranging from regulation of chemotaxis, actin distributions and signal relay, adaptation of ACA, control of developmental timing, and alteration of signal transduction rates<sup>129–133</sup>. Here we examine the impact of receptor phosphorylation on the onset of cell elongation and cell persistence using CM12345- mutant cells which

have receptors that are always phosphorylated. We find that the mutant cells, when starved under pulsing, elongate at a slower pace, with mutant cells at 4.5-6 hours resembling wild type cells at 3 hours. The mutant cells are incapable of responding to dynamic signals on the timescale of our experiment.

Here we revisit the application of information theory to *D. discoideum* chemotaxis. Seminal work by Franck and Segota<sup>134</sup> consider the mutual information between the chemokine gradient direction and the cells migratory direction and found a violation of the information inequality. The authors proposed that the data processing inequality could be resolved by considering multiple phosphorylation states. To test this hypothesis, we compare the evolution of the information transduction capacity for wild type and cells with disrupted phosphorylation states. We find, both experimentally and through modeling, that the wild type cells with multiple receptor states having a greater transduction capacity than the single state mutants. The capacity of wild type cells is greatest at 3 hours of development, corresponding with the onset of polarity, declines over several hours, and then recovers in the later stages. The mutant cells do not respond to gradients at 3 hours, and have similar transduction capacities from 4.5 hours onwards, which is consistent with the morphological measure of their development.

Finally, we explore the difference between information theoretic measures and standard chemotaxis metrics. We note that information theory uses simultaneous measurements of input and response signals while chemotaxis index, the standard efficiency measure, compares integrated inputs and responses. Thus, we have short- and long-time scale measures that we use to determine how heavily the cells rely on previous knowledge as development progresses. We find that early development cells

have little to no integration, while cells later in development rely more heavily on previous signals.

Taken together our work compliments previous efforts to find changes in protein and RNA expression<sup>135–138</sup>, receptors<sup>139,140</sup>, increased cell length, and migration persistence<sup>141</sup> by extending them over development. Additionally, our work connects information theoretic approaches involving excitable signaling networks to models of transduction in integration and filtering schemes. Our use of two gradient strengths over development corroborates the prediction of excitable network models that chemotactic efficiency is positively correlated with signal to noise ratio and inversely related to the receptor dissociation constant. Usage of CM12345- cells and dynamic gradients confirmed the prediction that integration increases fidelity but slows responses to change.

### **3.3 Materials and Methods**

#### **3.3.1 Cell growth and development**

WT *D. discoideum* Ax3 cells are grown in HL5 to  $4 \times 10^6$  cells  $\text{ml}^{-1}$ . The developmental process is initiated by washing the cells in development buffer (DB) three times and resuspending them at  $1 \times 10^7$  cells  $\text{ml}^{-1}$  in 5 ml aliquots. The solution is placed on an orbital shaker at 160 rpm. After 1 hour, 100  $\mu\text{l}$  of 4  $\mu\text{M}$  cAMP is dropped into the solution

over 5 seconds every 6 minutes. The cells are harvested and resuspended to  $2.5 \times 10^6$  cells  $\text{ml}^{-1}$  before loading into the microfluidic chamber. Adapted from<sup>141</sup>.

### **3.3.2 Elongation assays**

Cells are developed as above and sampled every 30 minutes then flowed into the cell cavity of the gradient chamber. Brightfield images are taken as in Microscopy (without fluorescent images)

### **3.3.3 Dynamic gradient assays**

Cells are developed as above and sampled every 90 minutes then flowed into the cell cavity of the gradient chamber. A fluorescent cAMP solution is prepared by mixing DB with cAMP and Alexa Fluor 568 tagged dextran (Invitrogen) to  $50 \mu\text{M}$  and  $0.44 \text{mM}$  respectively. Two peristaltic pumps (Viibre, Vanderbilt University), calibrated to  $6 \mu\text{l}/\text{hour}$  flow rate, are used to drive fluid flow through a switchable LabSmith AV202-C360 valve and into the flow cavities of the gradient chamber (see Figure 3.5B), causing a linear cAMP gradient to form across the cell cavity via diffusion. The Labsmith valve is switched after 15 minutes to flip the high and low sides of the gradient. Images are collected as in Microscopy for 75 minutes.

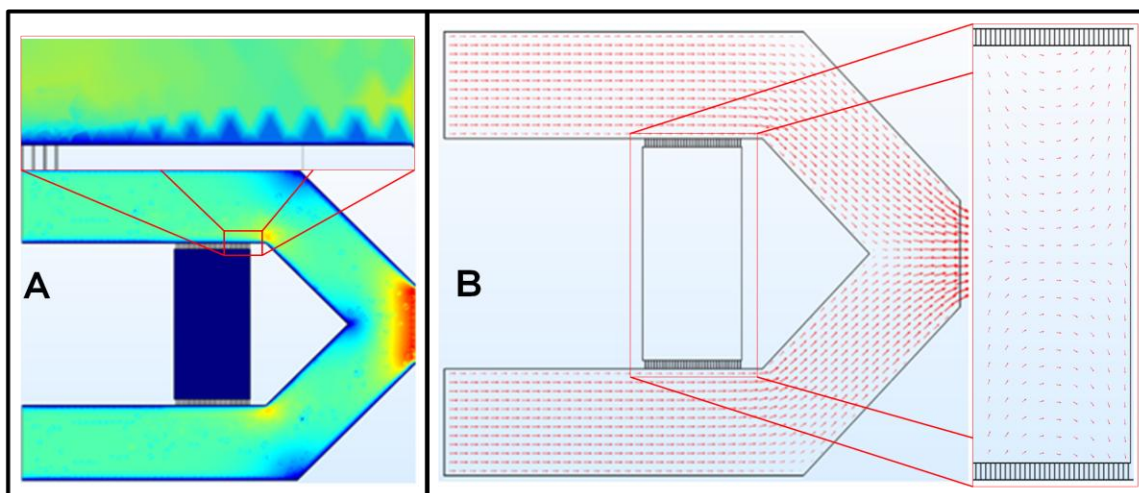


Figure 3.1 Comsol flow field. A) The Normalized flow velocity is shown by color with red representing the maximum flow and blue the minimum. The effects of the corner bend are shown (inset) with the diffusion slits far enough from the corner to prevent uneven flow. B) The red vectors represent the velocity at each location to scale. The maximum flow is 200um/second. The minimum flow occurs in the central chamber (inset) at 10nm/second. The inset vector lengths are increased by a factor of  $10^3$ . The flow rates within the central chamber are too low to cause a migratory response to shear.

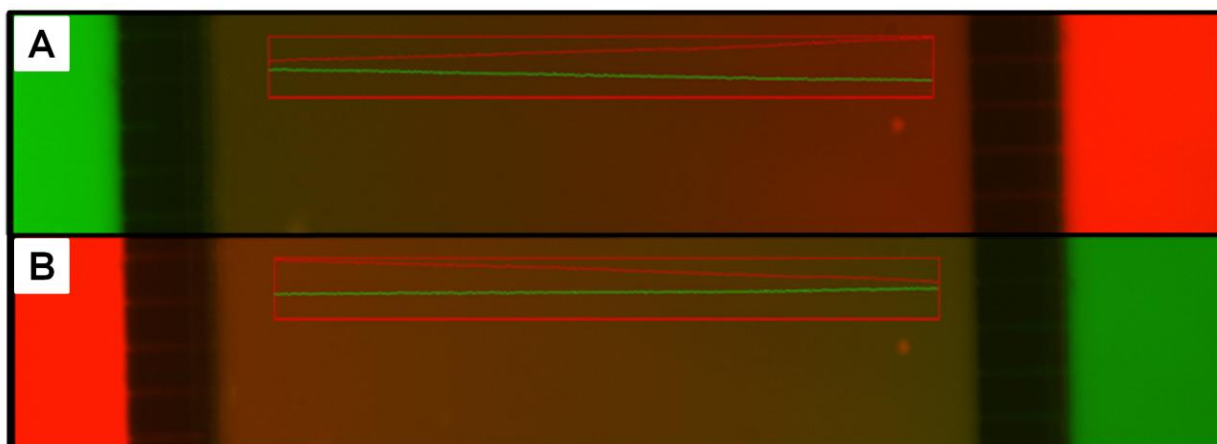


Figure 3.2 Switching fluorescent gradients inside of the microfluidic chamber. 10x fluorescent images A) Green and red fluorescent dyes flow through the outer channels, left and right, and create linear gradients. The inset red boxes have the intensity of each plotted against location, showing linear red and green gradients. B) Image taken five minutes after switching the fluids. The red and green linear gradients have switched directions. This experiment allowed us to measure the cells persistence to dynamic signals.

### 3.3.4 Microfluidic Chamber

Microfluidic chambers that create linear gradients have been designed<sup>142–144</sup>. These chambers suffer from substantial flow across the central chamber, turbulent flow, and mixing issues. We have minimized these drawbacks through simulation in Comsol (Figure 3.1), with the main improvements being larger, straight flow cavities to simplify flow and a single outlet to dampen pressure differences across the central chamber. The geometry is outlined in Figure 3.5A. Specifically, our shallow gradient chamber has a 4mm long, 1mm wide, and 100 $\mu$ m tall central cell cavity which is separated from the 6mm long, 1mm wide, and 100 $\mu$ m tall flow cavities on the top and bottom by 56 high impedance (i.e. small cross section relative to length) 80 $\mu$ m long, 2 $\mu$ m wide, and 10 $\mu$ m tall slits spaced 5 $\mu$ m apart. The slits run from 1mm to 5mm along the flow cavities to connect the central and outer cavities. At 6mm, the flow cavities are brought together at a 30° angle. The 1mm between the slits and the flow cavity angle change makes the effects of the angle change on flow profile negligible (see Supplemental Information). The steep gradient chamber is identical save for a central cell chamber that is 500 $\mu$ m wide. Gradient chambers were drawn in Adobe illustrator and made into photolithography masks by Front Range Photomask LLC. The photolithography was performed on 3 inch silicon wafers in two sequential steps according to standard procedure (MicroChem Procedures); the first step creates the 2 $\mu$ m tall gradient slits and the second overlays the flow and cell subsections onto the slits. The masters are then treated with Trichloro(1H,1H,2H,2H-perfluorooctyl)silane (Sigma) so that they are nonstick. Polydimethylsiloxane (PDMS) (Corning) is then poured onto the wafers in 10:1 base to curing agent, desiccated, and baked at 60°C for 4 hours. After removing

the PDMS from the master, holes for 150 $\mu$ m inner diameter (PEEK) and 1/16<sup>th</sup> inch inner diameter (Tygon) tubing are punched in the inlets and outlet respectively. The chambers are then sealed to a 4 well Nunc Lab-Tek chamber slide according to standard procedure<sup>145</sup> and filled with DB until used.

### **3.3.5 Microscopy**

Alexa 568 fluorescent and brightfield images are taken every 10 seconds on a Zeiss Observer.Z1 microscope with an AxioCamMR3 camera controlled by AxioVision software. All images are taken with a 20x Plan-Apochromat M27 (NA0.8) phase contrast objective. Phase contrast images allow for easy segmentation and tracking of cells while fluorescent image intensities correlate with chemical concentration.

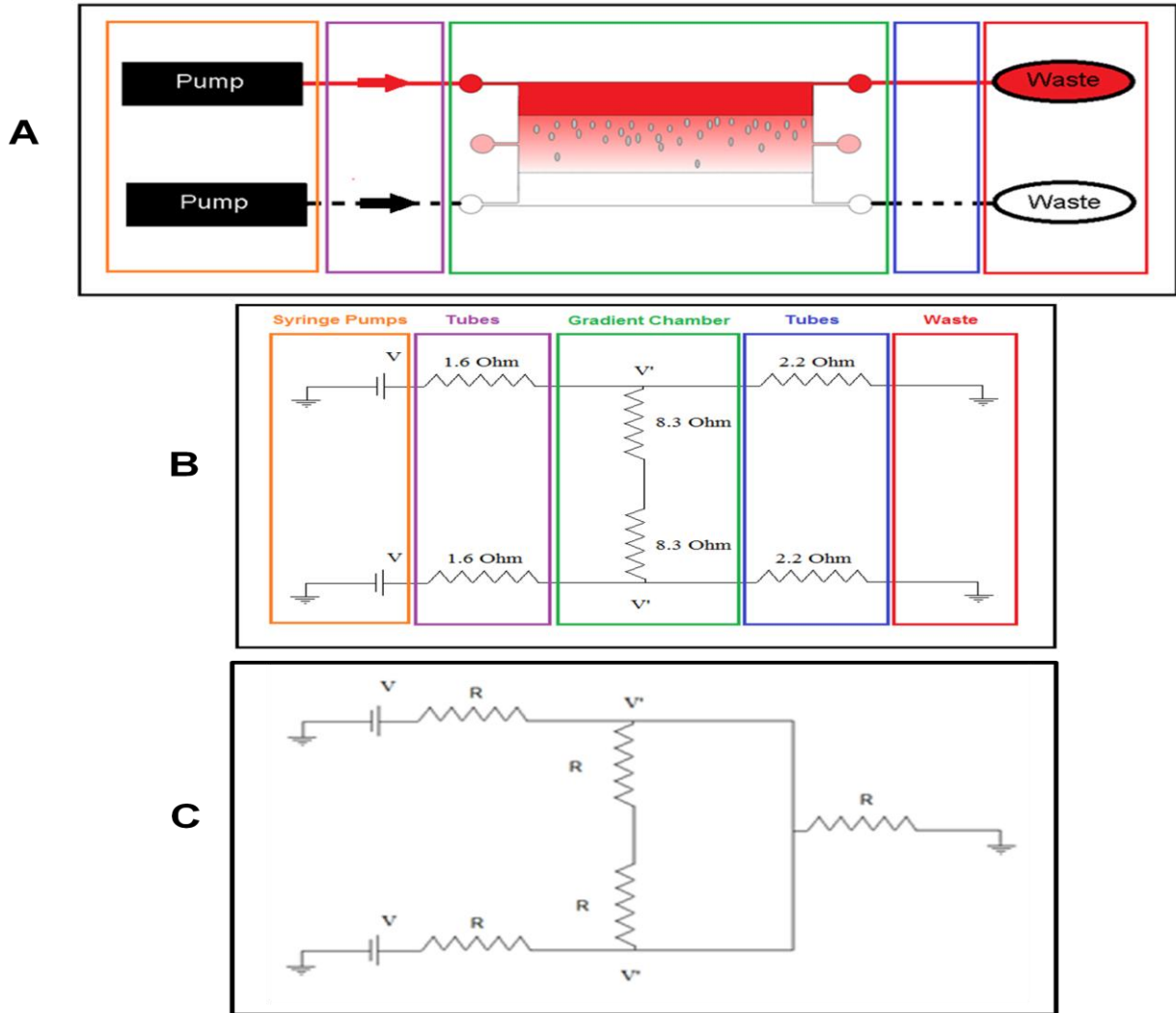


Figure 3.3 Evolution of the gradient chamber via circuit analysis. The gradient chamber was redesigned to minimize fluid flow across the central chamber. A) Drawing of original pump and tubing setup. Colored boxes match to their analogous parts in B. B) Circuit diagram of pump and valve setup. The pumps act like batteries and the tubing and diffusion slits as resistors. C) Final gradient chamber setup. Shorting the flow wires before exiting the chamber causes the voltage on each side of the central chamber to be equal, and no fluid to flow across the center. We also decreased the tubing resistances by using larger diameter tubing, thereby increasing the relative resistance of the diffusion slits. Together these changes provided a stable central chamber with low flow across the cells.

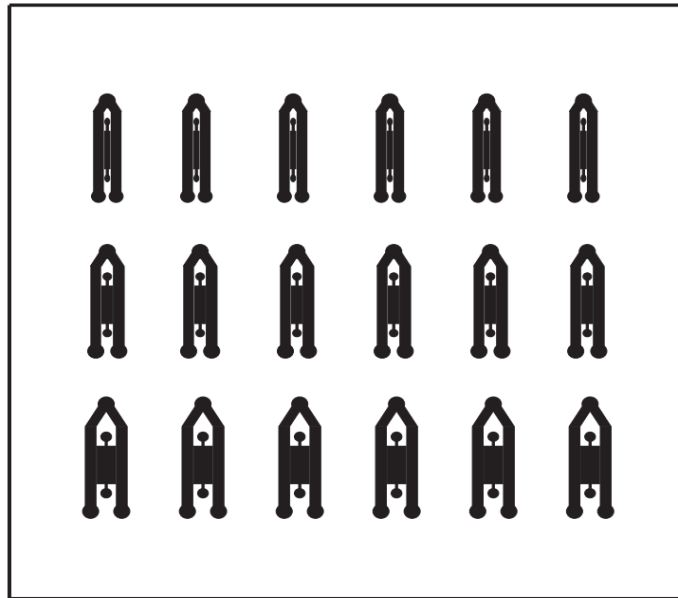


Figure 3.4 Gradient chamber photolithography mask. The varied width of the central chamber changes the gradient steepness. The bottom two chambers were used in the gradient switching experiments. The various central chamber widths were used to explore the connection between relative external noise and signal transduction.

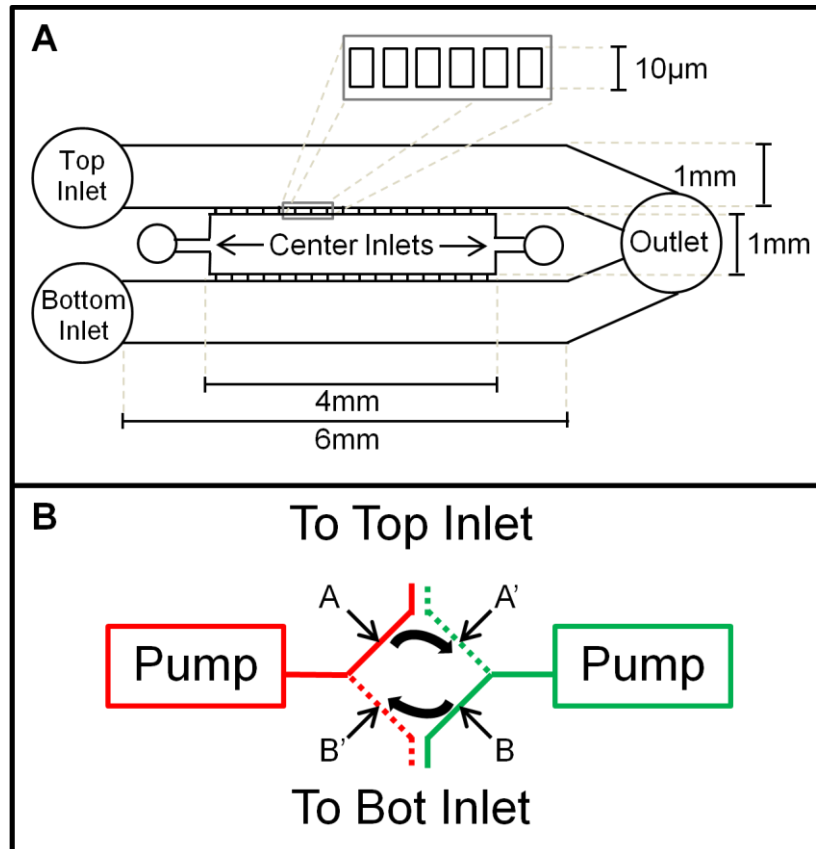


Figure 3.5 Experimental Setup. A) Over head schematic of the Microfluidic Chamber. Each device has three addressable chambers top, center and bottom. The top and bottom chambers direct flow of a cAMP solution or DB past the diffusion slits that separate them from the central chamber. The high impedance slits minimize flow across the central chamber while allowing cAMP and buffer to diffuse across them. The central chamber houses the cells during each experiment. b) Valve configuration. The fluid flow through the microfluidic gradient chamber is driven by two peristaltic pumps through a valve that reverses its outputs. In one configuration, represented by solid lines, the pump directs the red and green solutions into the top and bottom inlets respectively. The paths are labeled A and B. After switching the valve, with new paths represented by dashed lines, the red and green solutions are directed into bottom and top inlets respectively, reversing the solutions. The paths are labeled A' and B'. The gradient direction within the chamber can be switched over the period of 90 seconds, which provides a method to determine the cells response to dynamic signals and calculate their persistence.

### 3.3.6 Calibrating cAMP Gradient

Fluor 568 tagged dextran was mixed with the cAMP solution and used to infer the cAMP field. This is nontrivial as the dextran and cAMP have diffusion constants that are  $30 \text{ um}^2/\text{s}$ <sup>146</sup> and  $444 \text{ um}^2/\text{s}$ <sup>147</sup> respectively. The experiments have 5 parameters that determine the dynamics of the chemical signal: 1) the location within the chamber, the relative flow rates of the 2) top and 3) bottom channels, 4) the time of the switch, 5) the lag between the start of flow and the start of image acquisition. Comsol was used to simulate flow and diffusion of dextran and cAMP at various values of the above parameters for the entire geometry of the microfluidic chamber. The experiment covers only half the distance between the flow chambers and about 10% of the length of the cell chamber. To determine the location of the experimental data within the chamber, the mean square distance between simulation and experiment is calculated for many sections of the chamber and minimized to find the optimal simulation solution. An identical approach is used to find the following. The concentration at the low side of the image is dominated by flow at short time scales and was thusly used to find the top and bottom channel velocities. The initial concentration profile across the chamber is used to find the time lag between the start of flow and image acquisition. The edges of the simulation, being closest to the flow chambers, give an accurate depiction of the solutions within the flow chambers and are used to find the switch time (Figure 3.6).

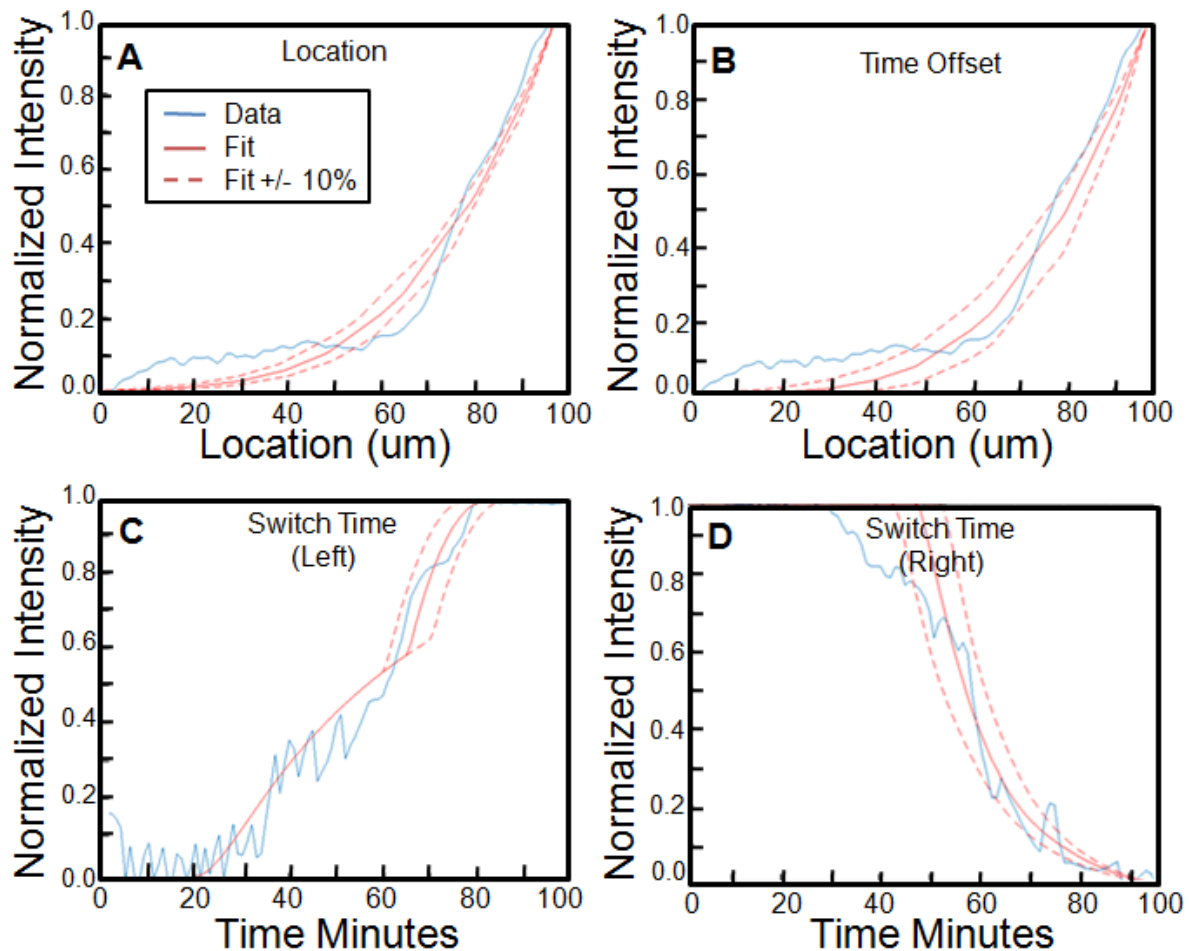


Figure 3.6 Selection of the best simulation. A) The experimental data (blue curve) is plotted over location within the chamber at the beginning of the experiment. The solid red line represents the simulated data that best fits the experimental data, with +/- 10% in the location parameter in dashed lines. B) The experimental data is plotted over location within the chamber at the beginning of the experiment. The solid red line represents the simulated data that best fits the experimental data, with +/- 10% in the time offset parameter in dashed lines. C-D) The experimental data is plotted over time at the far left (C) and right (D) of the chamber. The solid red line represents the simulated data that best fits the experimental data, with +/- 10% in the location switch time parameter in dashed lines. The best fit simulation was selected and the cAMP data was used to determine the cAMP field for the experiment. This method gives an indirect measurement of the field which is more accurate than the typical assumed distribution because large fluctuations can be measured and accounted for, but is less accurate than direct measurement. Direct measures as of yet are not available, though we outline a method for them in the future work section, Chapter 4.

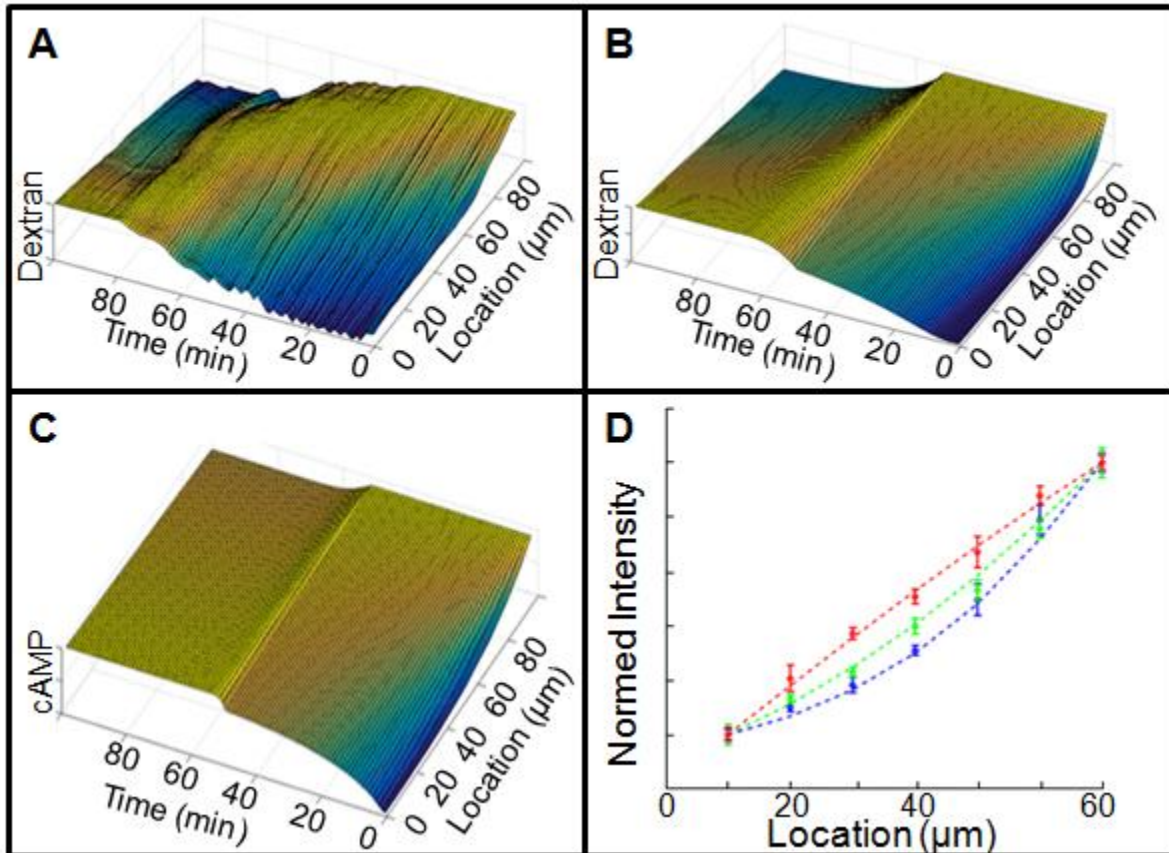


Figure 3.7 Experimental and simulated chemical concentrations. A) The Intensity of the fluorescently tagged dextran is represented by height and is plotted over location and time during a gradient switching experiment. B-C) A gradient switching experiment is simulated in Comsol with a molecule with the diffusion coefficient of the dextran molecule (B) and cAMP (C). The height represents the concentration and is plotted over location along the gradient and time. Many such surfaces were generated and the closest are plotted here. D) The simulated curves (dashed lines) and experimental measurements (points) are plotted versus location in the chamber at 5 (blue) 15 (green) and 25 (red) minutes. The error bars represent the standard error for each region. The Comsol simulations were matched to the experiments using the parameters outlined in Figure 3.6

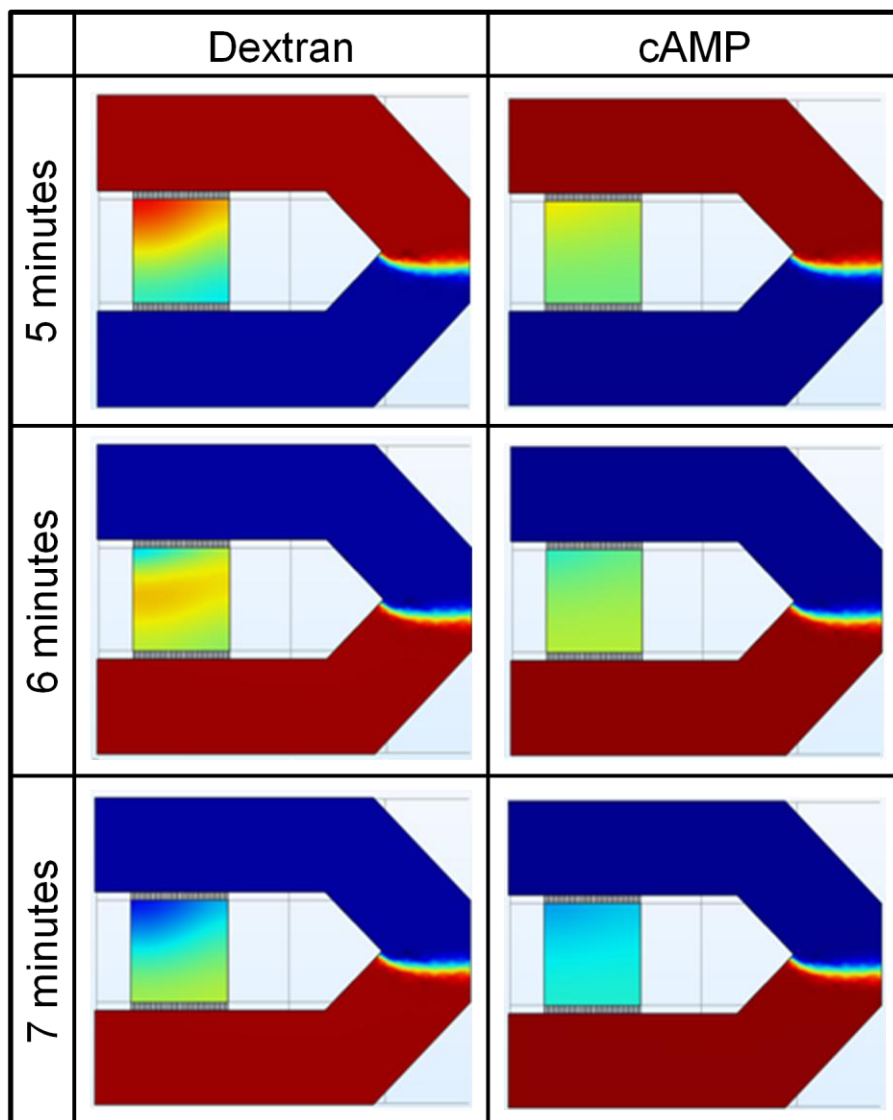


Figure 3.8 Dextran and cAMP switch simulations. The normalized concentration profiles are shown for dextran (left column) and cAMP (right column) immediately following a simulated switch at 5 minutes. The maximum concentrations are represented in red with zero in blue. The top channel velocity is 5% higher than the bottom channel to match an experimental condition. We used the difference between the timing of dextran and cAMP switches in the simulation to determine the cAMP switch timing of the experiments. The persistence measures compared the cAMP switch to the cell trajectory switch. The persistence measures and the difference between the dextran and cAMP switches are both on the order of a few minutes so the correction was critical to obtain the true value of the switches.

### 3.3.7 Image Analysis

Images are analyzed with a combination of ImageJ (NIH) and Matlab (MathWorks, Natick, MA) with the image processing toolbox. Brightfield phase contrast images have their background removed via ImageJ's background subtraction algorithm (rolling ball radius 10 pixels). The images are loaded sequentially into Matlab and binarized which, thanks to the nature of phase contrast images, gives boundaries that are accurate though sometimes not closed. To close the boundaries, the images are then essentially treated with the morphological transformation bottom hat (dilation and erosion), though the number of iterations is experiment dependant. The boundaries are then filtered by area, yielding accurate outlines of cells while ignoring imaging artifacts. The cells are tracked in subsequent frames using a nearest neighbor approach. The major (minor) axis of each cell is found by calculating the major (minor) axis of the ellipse that has the same normalized second central moments as the cell. The ratio of major axis to minor axis of each ellipse is stored as the cells elongation at a particular time. The x and y gradients at each location of the fluorescent images are approximated using the built in Matlab function. An annulus is created around each cell at each time point and the gradient values within those locations are averaged, their angle and magnitude calculated and stored. This method ensures that the effects of cells in the fluorescent channel are removed and that each cell receives a local gradient measure.

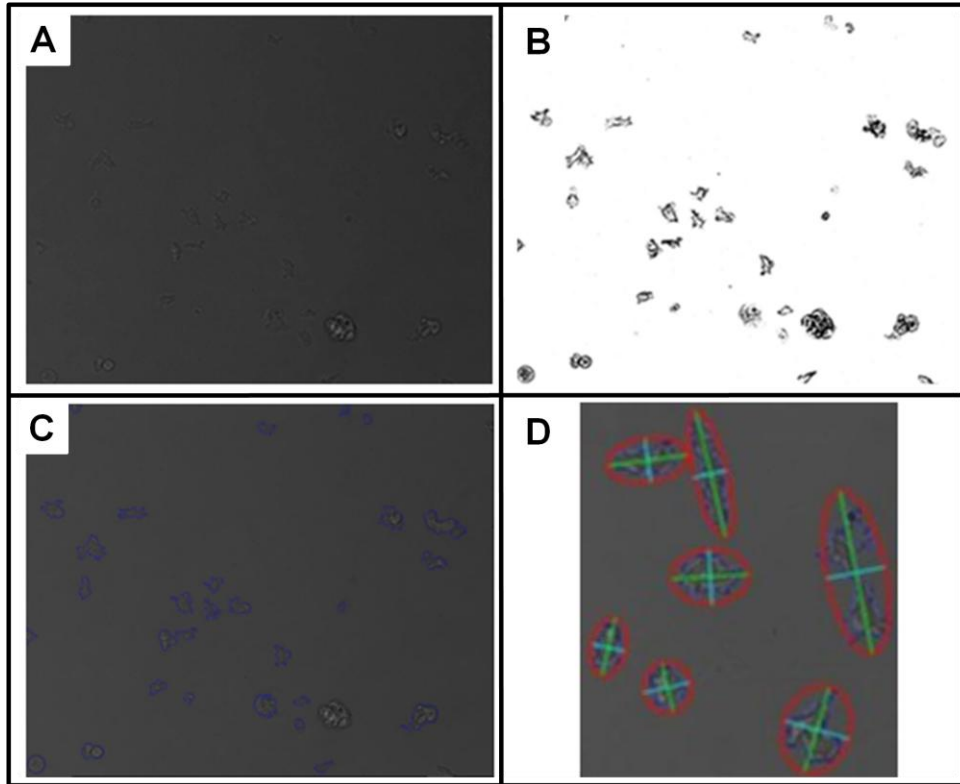


Figure 3.9 Cell boundary and shape identification. A) 10x Brightfield image of cells in the absence of cAMP. B) Binarized image after background subtraction. The images will be treated with the morphological operation 'top hat' multiple times then filled. C) The boundaries of the cells (blue) plotted on top of the Brightfield image. The boundaries have been filtered by area to remove large clumps of cells and small artifacts. D) Ellipses fit to the cell boundary are plotted. The red outline is the ellipse with the green and cyan lines the major and minor axis respectively. The axes are used to calculate the elongation ratio for each cell. This analysis was critical to determine the developmental timing of the mutant cell lines needed to compare them the wild type cells.

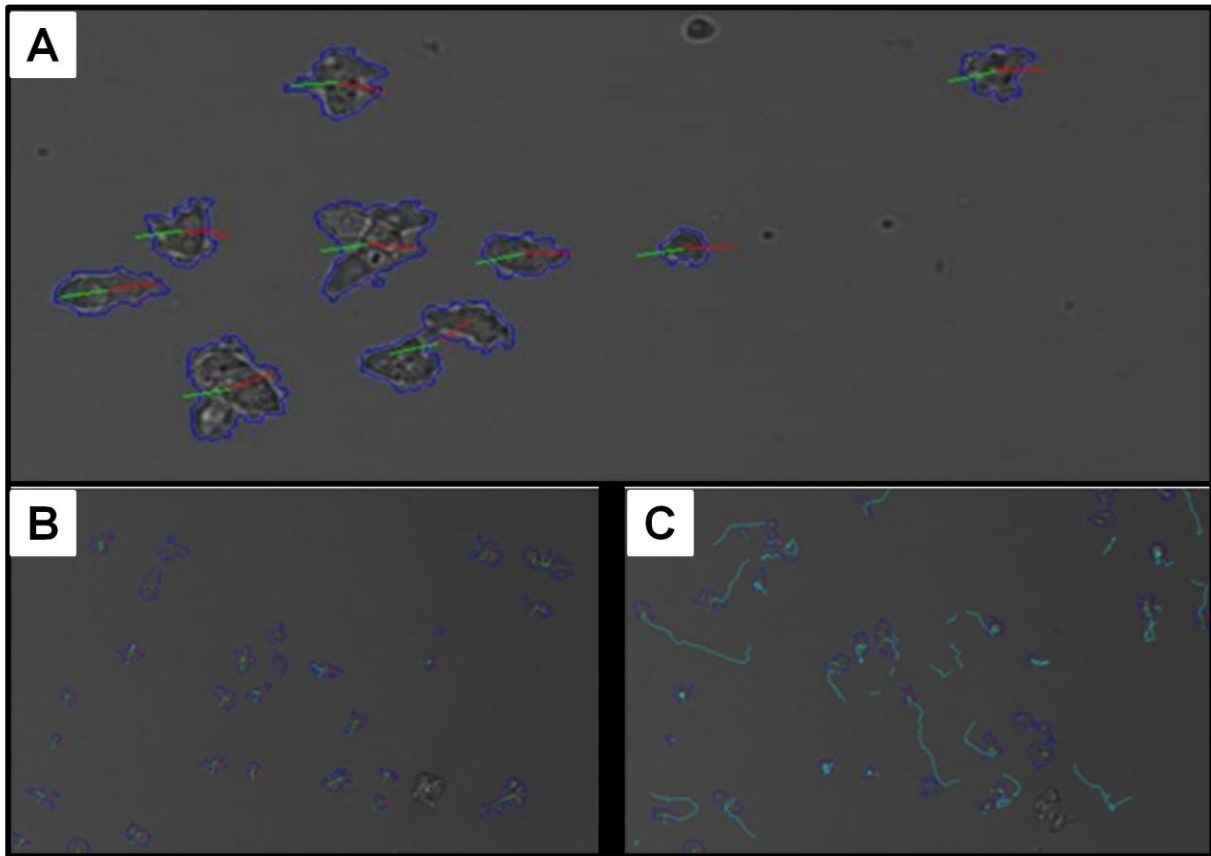


Figure 3.10 Local gradient directions and cellular trajectories. A) Analyzed brightfield image with the cell boundary in blue and the cAMP and buffer gradient directions in red and green respectively. B) Initial cell trajectory image. The trajectories are plotted in cyan. C) Trajectories after 200 seconds. The cell trajectories are plotted for each cell and each image. The simultaneously measured trajectory and gradient angles enable the calculation of the MI between them. The measures over time enable the calculation of the chemotaxis index and the persistence of the cells.

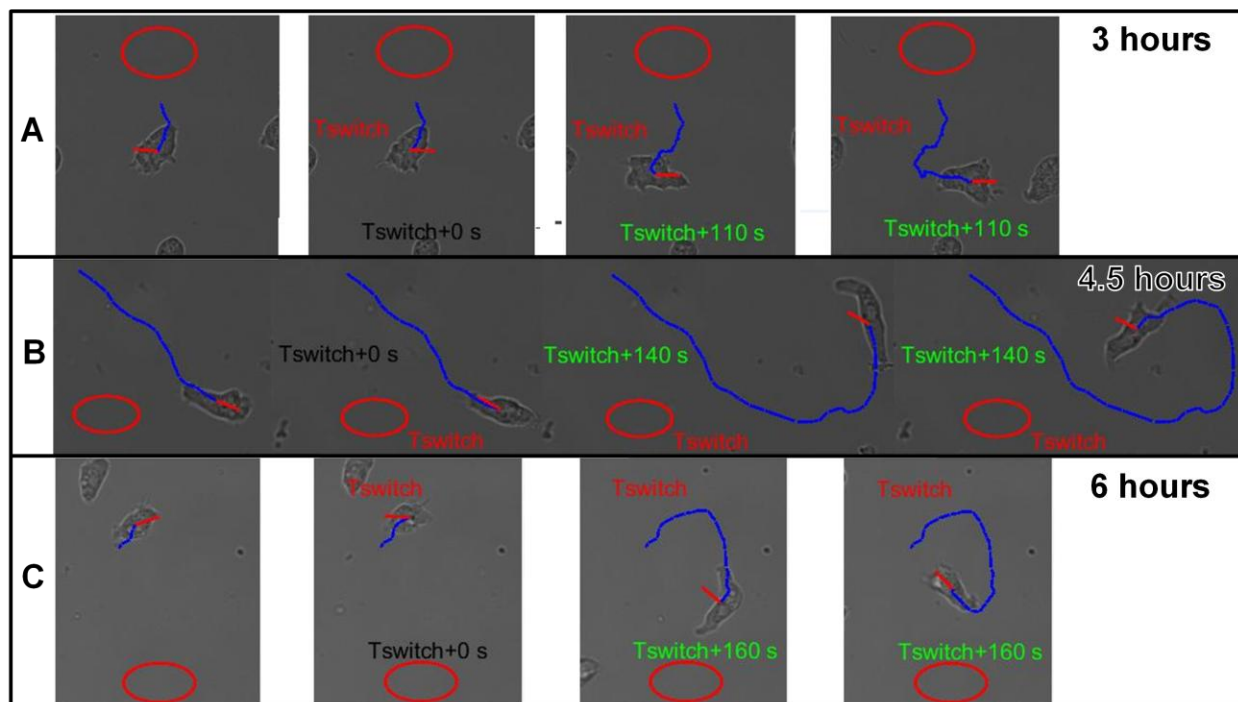


Figure 3.11 Persistence for individual cells. The cell trajectory is plotted in blue and the gradient direction in red. The red ellipse is the characteristic shape of the cell over the entire experiment. From left to right in A,B and C are the images before the gradient switch, at the gradient switch, at the trajectory switch and several frames after the trajectory switch for 3,4.5 and 6 hours post starvation. The persistence time for each cell is written in green after the trajectory switches. These images confirmed that the cell tracking and gradient algorithms were functioning as expected and that the persistence measures were accurate.

### 3.3.8 Mutual Information Models

A circular cell with  $N$  uniformly distributed receptors on its surface is divided into sectors. If the external chemical gradient has reached steady state, then we can assume that the ligand binding has reached equilibrium, so the mean fraction of bound receptors in each sector depends on the local concentration and dissociation constant of the receptors:

$$\mu_i(\theta_s) = \frac{C_i}{K_d + C_i} \quad (3.1)$$

When extended to multiple receptor states, the mean fraction of bound receptors also depends on the percent of the receptors that are in each state.

$$\mu_i(\theta_s) = \frac{P_{fast} C_i}{K_{dfast} + C_i} + \frac{P_{slow} C_i}{K_{dslow} + C_i} \quad (3.2)$$

Using the above equation, we can derive the MI bound for cells with multiple states following<sup>117</sup> to arrive at:

$$MI = \frac{(P_{fast} * N_R * [cAMP] * slope)^2}{4Log_2(2) * [cAMP] * (K_{dfast} + [cAMP])^2} + \frac{(P_{slow} * N_R * [cAMP] * slope)^2}{4Log_2(2) * [cAMP] * (K_{dslow} + [cAMP])^2} \quad (3.3)$$

This reduces to:

$$MI = \frac{(N_R * [cAMP] * slope)^2}{4Log_2(2) * [cAMP] * (K_{dslow} + [cAMP])^2} \quad (3.4)$$

if we enforce a single (slow) receptor state, representative of the mutant cells, which matches<sup>117</sup>.

### 3.3.9 Receptor State over Development

None of the receptors are in the slow state at three hours of development<sup>148</sup> and they asymptotically approach 75% in the slow state out to 6 hours. The cells are subjected to 50nM cAMP every 6 minutes during development<sup>149</sup> and the receptor dissociation constants are  $K_{dslow}=900nM$  and  $K_{dfast}=300nM$ <sup>150</sup>. We can thus write a differential equation for the fraction of receptors in each state as

$$\frac{dP_{slow}}{dt} = (1 - P_{slow}(t)) \left( \frac{[cAMP]}{[cAMP] + K_{dfast}} - C_{f \rightarrow s} \right) + P_{slow}(t) \frac{[cAMP]}{[cAMP] + K_{dslow}} \quad (3.5)$$

where  $P_{slow(fast)}$  is the fraction of the receptors in the slow (fast) state,  $K_{dslow(fast)}$  is the dissociation constant of the slow (fast) receptors,  $[cAMP]$  is the mean local concentration of cAMP, and  $C_{f \rightarrow s}$  is the rate at which the fast receptors dephosphorylate to become slow.

### 3.3.10 Chemotaxis Index Calculation

Chemotaxis index is used to measure how well a cell can track an applied gradient signal over time. It is calculate by first finding the average gradient direction over 30 seconds, finding the cell displacement vector over the same interval, then taking the cosine between them and averaging it over many cells.

$$CI = \langle \cos(\theta_g - \theta_t) \rangle \quad (3.7)$$

## 3.4 Results

### 3.4.1 Quantification of Elongation throughout Development

Qualitative descriptions state that *D. discoideum* cells elongate during their developmental transition from individual cells to aggregates, and quantitative measures have shown that the late development cells are more elongated than at early development. The timing of the transition between the two states had not previously been quantified. It has also been noted that phosphorylation plays a key role in development, so we compare our quantification of the transition in mutant and WT cells. By sampling developing WT cultures, we find that the ratio of the major to minor axis of the cells is fairly constant over the first 3 hours, at which time the ratio increases before reaching a plateau at 5 hours (Figure 3.12A, blue). The mutant cells, which cannot phosphorylate their cAMP receptors, show retarded elongation. These cells reach a ratio equivalent to the three hour WT ratio at four hours, and remain in that range before showing a slight increase at six hours (Figure 3.12A, orange). Overnight development

showed little further increase in this ratio, meaning that the cells do not proceed past this development point, though the development could be recovered by co-developing mutant and WT cells at 1:1 concentration, which shows that the mutants are viable outside of their phosphorylation handicap. This retarded development is consistent with results that show phosphorylation impacts downstream adaptation of ACA<sup>129</sup>. Adaptation in WT cells gives a prolonged period, about six minutes, where cells don't respond to signals. The cells synchronize their secretion with this refractory period, as out of phase signals are ignored. The period and synchronization of these oscillatory signals is crucial to drive development<sup>151</sup>. Due to the lack of adaptation, the CM12345-cells respond to every signal, leading to the observed continuous secretion of cAMP, which inhibits synchronization and subsequently development. We thus compare the 4.5 and 6 hour mutant cells to the WT cells at 3 hours of development and compare the 6 hour co-developed mutant cells to the 6 hour WT cells for the following measures.

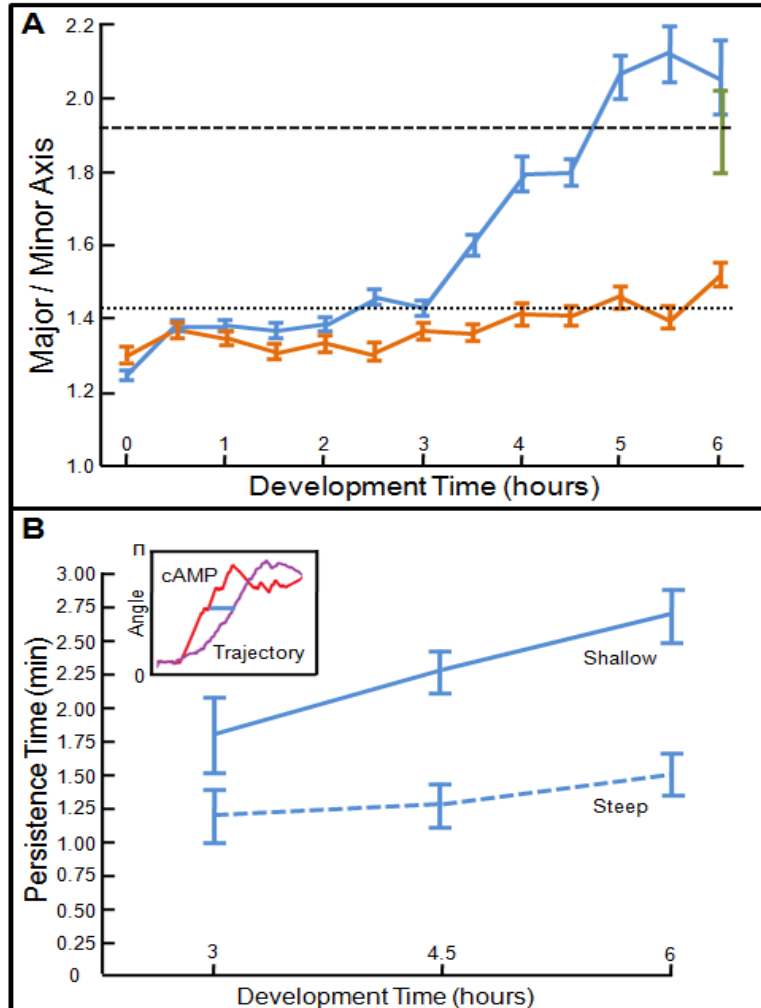


Figure 3.12 Elongation and persistence versus development time. A) Elongation versus development time. The ratio of the major and minor axes for the WT (blue) and mutant (orange) cells is plotted every thirty minutes over development. The mean for the WT cells at 3 hours is represented by a horizontal dotted line to show equivalence to the mutants at 4 hours onwards. The cells recovered by co-development are plotted in green, and their equivalence to WT 4.5-5 hours is shown with the black dashed line. The error bars represent the standard error of the ratio. This result allows us to compare cells from the wild type and mutant populations through their elongation ratios. Additionally, the recovery of the co developed cells shows that, aside from the phosphorylation state of the receptors, the mutant cells are otherwise identical to the wild type. B) Persistence versus development time. For each experiment, the time it takes each cell to turn after the gradient direction switches is recorded (inset) The red curve represents the direction of the gradient, the purple curve is the average cell angle and the blue bar represents the time between the gradient and trajectory switches. The cell averages are plotted 3, 4.5, and 6 hours and the error bars represent the standard error. This result shows that the cells respond to external signal changes more slowly as development progresses.

### 3.4.2 Response to Dynamic Signals throughout Development: Persistence

A common qualitative description of *D. discoideum* development states that undeveloped cells meander while developed cells persist in a single direction, both in the absence of a chemical signal and in an applied gradient<sup>123</sup>. We found first that a large fraction, ~75%, of cells at 3 hours of development performed u-turns in shallow gradients instead of the rapid reversals expected as shown in Figure 3.13. We sought to quantify the development of persistence over time. We found the direction of the gradient and cell trajectories as functions of time and calculated the time between the gradient flip and the trajectory flip for each cell. An example of this is shown in Figure 3.12B (inset). We found that cells respond slowly to reversals of shallow (steep) gradients, 1% (2%) change in concentration over the cell length, with the cells developed for [3, 4 and 5 hours] taking 1.83 (1.17), 2.33 (1.25), and 2.66 (1.50) minutes to flip their migration direction respectively. These results are shown in Figure 3.12B, with the WT and CM12345- cells represented by the solid and dashed lines respectively. This time scale is significantly longer than has been observed for cells responding to rapid reversals of steep exponential gradients<sup>122</sup>, however it is consistent with earlier findings of cell persistence based on MSD in the absence of chemical signals<sup>152</sup>. As expected, the CM12345- were underdeveloped did not respond to changes in the gradient direction, instead moving randomly after the switch. This is intuitively reasonable, as receptor phosphorylation is required for controlling local affinity<sup>150</sup> and adaptation to signals<sup>153</sup>. In wild type cells, the heavily phosphorylated front has slow signaling receptors, while the back has non-phosphorylated fast receptors. The sudden change in gradient direction quickly binds to the rear receptors

while the front receptors slowly stop signaling. Since the cell cannot rearrange its internal structure, it turns and realigns with the gradient. In the CM12345- cells, all of the receptors are slow signaling so the rear receptors slowly start signaling as the front slowly stop, which would make the response to the change in gradient direction take about three times as long due to the difference in affinity. This is confounded by the increase in average concentration during a gradient reversal within our device. The wild type cells utilize phosphorylation to adapt to this increase, but the CM12345- cells increase their signaling throughout the cell. The combination of these two effects substantially increase the time it for the mutant cells to reverse direction, beyond the timescale of our experiment.

### **3.4.3 Gradient Transduction throughout Development**

The multiple receptor type mutual information equation derived in the methods section has two dependencies that change over development: receptor number and the fraction of the receptors in the fast and slow states. The former was measured by Kimmel and Devreotes<sup>148</sup>; the number of receptors linearly increases from 35000 to 75000 over development hours 3 to 6, the plot of which is shown in Figure 3.14A as the dotted red line. The fraction of receptors in the slow state was calculated according to Michaelis-Menten kinetics as outlined in methods and shown in Figure 3.14A as the dashed purple line. We plot the MI surface for a shallow gradient as a function of receptor number and the percentage phosphorylated, or slow, in Figure 3.14B. We then use the dynamics of receptor number and phosphorylation described above to plot the path on

this surface for the CM12345- (orange dashed) and WT (blue dashed) as they progress through the developmental transition. From the paths generated by the MI equation we find, surprisingly, that the bound on MI will be at a maximal .78 (.9) bits at 3 hours, drop to .63 (.75) bits by 4.5 hours, and recover to .71 (.83) bits by 6 hours in the shallow (steep) gradient. The graphs of the predictions are shown Figure 3.14C in blue solid and dashed lines for shallow and steep gradients respectively. This is somewhat contradictory of the established description of chemotaxis ability over development, which implies that the cells would monotonically increase their transduction capability. The development of the CM12345- cells only changes the receptor number as the receptors are always in the slow state. The relationship between MI and development for the CM12345- is thusly linear, starting at .3 (.42) bits at 3 hours and increasing to .51 (.63) bits at six hours in the shallow (steep) gradient. This prediction is shown in Figure 3.14C as solid and dashed orange lines for shallow and steep gradients respectively. Since the MI predictions are for the upper bounds on transduction for each cell type, we expect that the experimentally measured MI values would all fall under the predicted values. Indeed, we see that taking into account the receptor states leads to no experimental violations of the data processing inequality; all the measurements fall under the bounds. Results shown in Figure 3.14C

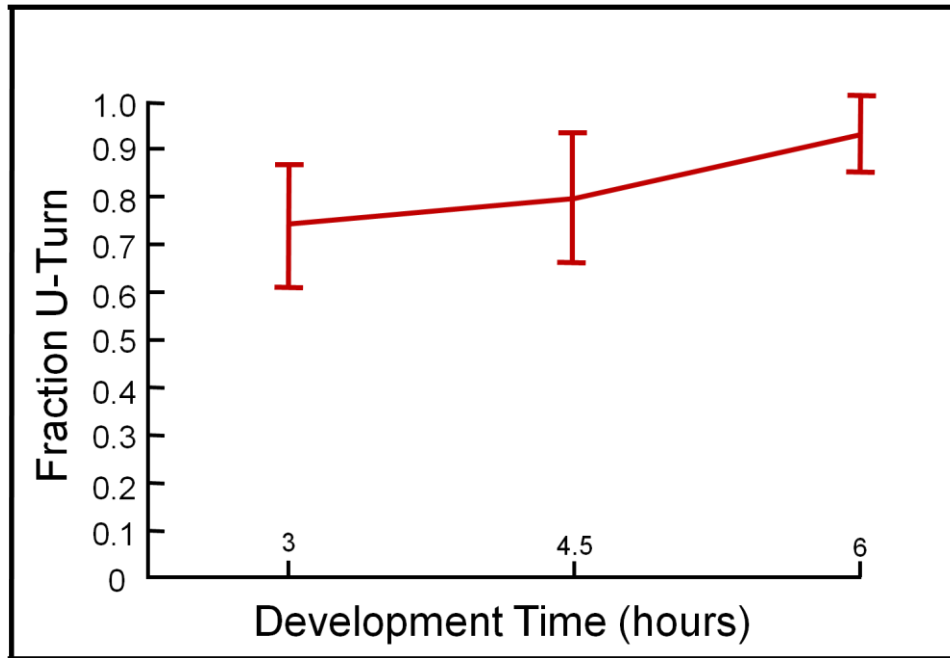


Figure 3.13 U-turn fractions versus development time. The fraction of U-turns performed in shallow gradients in response to a reversal of gradient directions is plotted against development time. The error bars represent the standard error three independent experiments at each time point. More than 30 cells were observed in each experiment. This measure was significantly different from the descriptions in literature, which state that the cells at three hours lack internal polarity and should therefore have mostly direction reversals via internal reorganization. The descriptions suggest that frequent u-turns would only happen when the cells have elongated, which we show is between 4-5 hours. This result suggests that the proteins within the cells are spatially organized early in the development process and that the cytoskeleton spatial organization that leads to elongation occurs after these proteins are already organized.

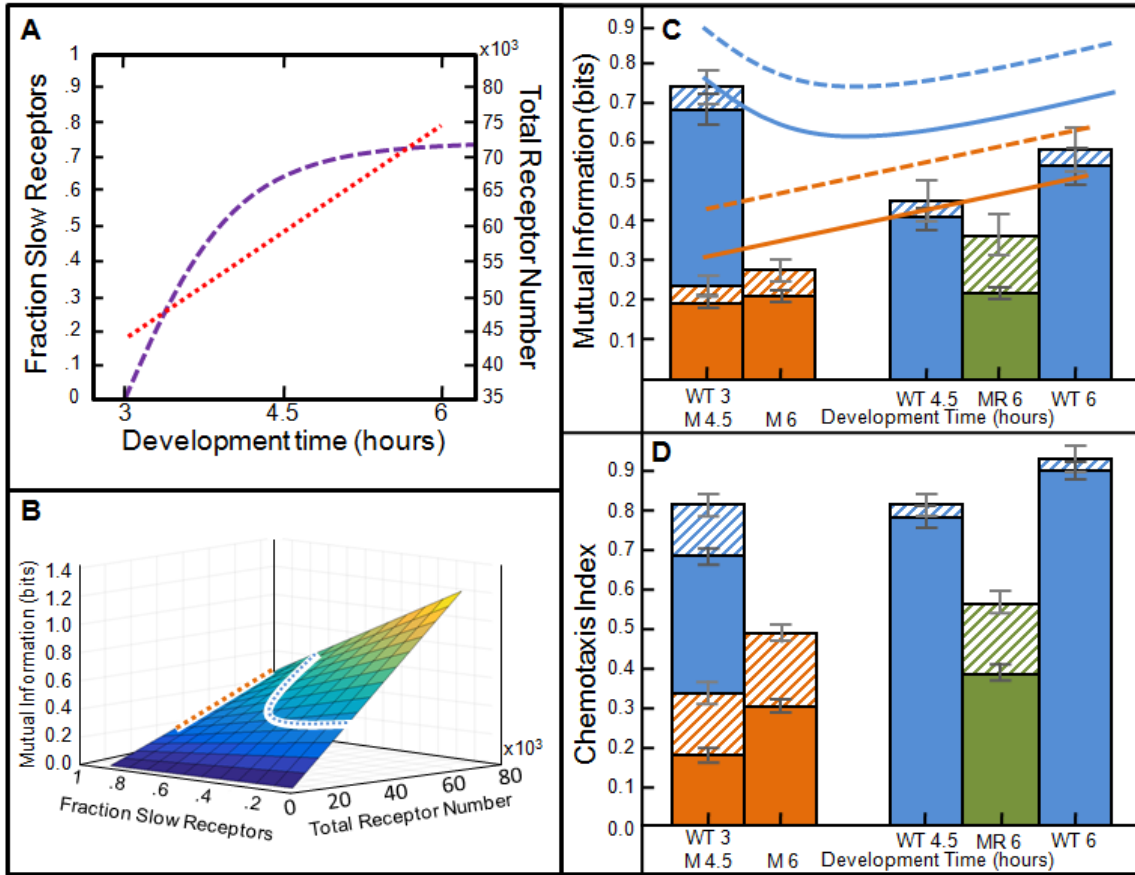


Figure 3.14 Models and Experimental Results. A) MI model inputs. The number of CAR1 receptors (blue) and the fraction of the receptors in the slow state (orange) is plotted versus development time, adapted from<sup>148</sup> and according to Equation 5 derived in methods respectively. B) The shallow gradient MI surface for the fraction of slow receptor and receptor number domain is plotted, with the WT (blue dashed) and mutant (orange dashed) developmental paths plotted on the surface. C) MI model versus experiment. The MI models are plotted against development time for WT (blue curves) and mutant (orange curves) cells. The solid and dashed lines represent the model predictions for shallow and steep gradients respectively. The experimentally measured MI for various points in development for WT (blue), mutant (orange), and rescued mutant (green) cells, with dashed and solid regions representing the shallow and steep gradients respectively. The error bars represent standard error. D) Chemotaxis index versus development time. The chemotaxis index for WT (blue), mutant (orange), and rescued mutant (green) cells are plotted over development in shallow (solid regions) and steep (dashed regions) gradients. The error bars represent the standard error for each time point. Three experimental sets for each time point were used in all plots giving ~1200 independent measurements for each bar. These results together show that the models are reasonable, since there are no violations of the data processing inequality, and that the cells trade their ability to respond to dynamic signals in the early stages of the transition (high initial MI) for long term accuracy late in the transition (high final CI) by receptor number and phosphorylation changes.

#### **3.4.4 Standard Measure: Chemotaxis Index**

Since our prediction and experimental results for MI of these cells seemed contradictory to the qualitative description of the cells over development, as well as quantitative measures at the early and late time points, we looked to the standard measure - chemotaxis index (CI) – to further quantify our experiments. The CI index of the WT cells linearly increase with development time and is higher in the steeper gradient (Figure 3.14D), which corroborates the prevailing description. Upon closer inspection of the two measures we used, MI and CI, we see that they measure fundamentally different responses to external signals. MI uses simultaneous measurements of the applied signal and response, while CI averages both the signal and trajectory over several measurements. MI and CI therefore measure chemotactic ability on different timescales, with MI giving the fast response capability and CI giving the ability of the cells to accurately integrate signals over longer times. MI and CI coupled with the response to dynamic signals (persistence) allow us to determine how the cells modulate their weight of current signals and statistics of previous measurements.

#### **3.5 Discussion and Conclusion**

We have investigated how multiple receptor states affect both developmental timing and chemotactic ability. Using information theory, we extended previous models through development to predict the ability of the cells to respond on short timescales, and found that our experimental realization of the model had no violations of the data processing inequality, which means that our model is reasonable. Using the chemotaxis index, we

investigated the cells accuracy when integrating signals. We compared the WT and mutant cells and found that both development and signal transduction are adversely effected by having only a single receptor state. Additionally, we tested the cells responses for two different gradient strengths and found qualitative agreement between the increase in MI when compared to the model predictions. Interestingly, the co-developed cells at 6 hours showed a greater increase in MI than expected. This is likely due to the heterogeneity in the development of the cells that is detrimental to their response to shallow gradients; the WT cells produce the *pdsA* required to degrade the cAMP secreted by the cells to synchronize development, and see that the cells are still less developed at 6 hours than are the WT.

Our three measures, MI, CI, and persistence, give a description of how the weighting of current and previous signals changes over development. The MI results show early cells having the highest dependence on current signals, which drops off before eventually recovering. The CI results show the cells increasing their ability to accurately integrate signals over development. The persistence results give experimental confirmation that the cells can more rapidly respond to dynamic signals earlier in the developmental process. Taken together, we conclude that the cells have high weights on current signals early, and increase the weight of previous signals as they develop. This phenomenological strategy is connected to the underlying physiological changes in the receptor number and state. Early in development, receptor numbers are relatively low, but signal frequently giving a large sample of the environment. The speed of the receptors drops more rapidly than new receptors are made, which leads to smaller samples of the environment per unit time, which is

somewhat offset by the storage of previous signals in the receptor states which produces an integrated signal. The fidelity of the transduction recovers later in development as the receptor number increases, yielding larger samples per unit time while retaining the integration of previous signals. The cells late in development are therefore the most accurate over longer timescales, but also are the slowest to respond to dynamic signals. This description is corroborated by the results of the mutant cells, which show only marginal in the MI over development time, and are significantly lower than the WT cells. Since the mutant cells exhibit retarded development, their receptor number stays low, but they still integrate the applied signal, leaving them with consistently smaller samples of the environment per unit time. This leaves them less effective than WT on both short and long time scales.

Another model focused on the receptors and their immediate downstream effects is LEGI (local excitation and global emission)<sup>103,154,155</sup>. The LEGI models have captured chemotaxis behaviors that previous efforts have been unable to recapitulate, namely sensitivity to shallow gradients and the cytoskeleton waves that accompany migration<sup>90-93</sup>, while retaining features of simpler models such as cell shape<sup>94,95</sup>. In these LEGI schemes, the cells are able to adapt to background concentrations<sup>156</sup>, though the ratio of the background concentration to the gradient still plays a role. The model predicts, at the parameters used in this work, that the chemotactic efficiency (analogous to CI) is positively correlated with background concentration and inversely related to the receptor dissociation constant<sup>157</sup>. For an information theoretic approach to LEGI modules, the receptor dissociation constant is related to transduction through the distortion constant, which essentially raises the noise in the signal through the receptor. Slow receptors

have higher distortion in this model and the more receptors in the slow state, the lower the MI between the external chemical field and the chemotactic response<sup>116</sup>. These two predictions from modeling LEGI corroborate our results, as the mutant cells have higher dissociation constants (slower receptors) and lower CI and MI; they effectively see more noise compared to the gradient strength than does the wild type, and are therefore less adept at chemotaxis at all time scales.

The information processing of *D. discoideum* can alternatively be phrased as an active filtering scheme that relies on memory to decide which signals are relevant. Biological memory based filtering schemes are commonly used to describe regulatory processes that have the ability to adapt to signals<sup>158–161</sup>, a component shared with LEGI which can use memory to create bias<sup>116</sup> and inhibit errant signals<sup>162</sup>. Active filtering schemes have been shown to effectively time-average noisy signals to improve accuracy<sup>163</sup>, just as we propose the cells do by modulating their receptor dissociation constant at the later stages of development. Furthermore, the CAR1 receptors in *D. discoideum* use phosphorylation events to both store previous signals and modulate dissociation constant<sup>132,71</sup>. Since the phosphorylation of receptors increases over development time, filtering and integration models predict that the cells would become better at tracking signals over time (CI increases) and slower to respond to dynamic signals (persistence increase) just as we see in our experiments. The mutant cell lines we used in our study could not phosphorylate their receptors, impairing the filtering mechanism by removing the memory unit and removing the integrating mechanism by forcing the dissociation to remain in their fast state. As would be postulated by such

filtering and integration schemes, these cells are worse at rapidly transducing chemical gradient information and less capable of following a gradient over time.

Our work quantifies the developmental transition of *D. discoideum* from its vegetative state to its aggregation state through morphology and persistence measures and validates multi-state receptor models through the same transition. The model states the upper bound for transduction through the chemotactic signaling network, and the experimental measures are in some cases far below it. Whether the cells are suboptimal communication channels or there are missing pieces of the model remains unclear. The external cAMP field that we measure here is not the true field, as the cells both secrete cAMP and phosphodiesterase to degrade it and the addition of these effects would undoubtedly change both the model and measurements. The environmental noise that the cells experience would also be modified by these factors. The role of noise over development and in persistence could be further investigated through use different concentrations of cAMP on each side, which would modulate the average concentration while retaining the ability to hold the slope constant.

## Chapter 4

### Future work: *D. discoideum*

#### 4.1 FRET Probe

One major concern for our approach is the assumption that the fluorescently tagged dextran follows the cAMP field. We mitigated this concern as much as we could through simulation, but direct imaging of cAMP would alleviate this concern altogether. Recent advances in imaging have enabled the detection of specific molecule concentrations through the use of a tailored pair of fluorescent proteins attached to a chemical binding site that controls the distance between the fluorophores. The fluorescent pair undergoes Förster resonance energy transfer (FRET) through coupling of their dipoles when they are close together. When chemical concentrations are low and the binding site is unoccupied, the fluorescent pair is separated by a small distance, typically about 1-10 nanometers. A laser is used to stimulate the 'donor', which both emits light and gives energy to the 'acceptor'. The acceptor will also emit photons due to this interaction, and the ratio between the intensities of light coming off the donor and acceptor fluorophores is calculated. When chemical concentrations are high, the binding protein changes conformation and increases the distance between the donor and acceptor such that the FRET interaction is lost. When the donor is stimulated, it exclusively emits photons without giving energy to the acceptor, which skews the ratio of emitted intensities towards the donor's frequency. Using known chemical concentrations, this FRET probe ratio can be calibrated and used to measure local

chemical concentrations dynamically. Furthermore, probes such as these can be attached to a glass surface to remove the effects of probe diffusion from measurements and increase resolution. A cAMP probe that works internally for a variety of cell types including *D. discoideum* has previously been invented, but one that works on the exterior has not. We made attempts to create such a probe working with the Piston lab and the CORE, and although we made some progress the probe was never completed. In our efforts, we managed to get the two fluorophores folded correctly but the binding domain was not functional and tests with cAMP had little effect on the response of the probe. Nevertheless, a probe of this nature would yield insight on several questions within *D. discoideum*. It would allow the dynamic visualization of the external cAMP field which would further the modeling efforts of *D. discoideum* as an excitable system, allow for more accurate mutual information observations both in aggregation and in an applied field, and would give insight into why cells don't chase their tails when secreting cAMP. These questions are expanded below.

#### **4.1.1 *D. discoideum* as an Excitable System**

Static visualization of cAMP by Devreotes showed the spiral waves that were seen in the motion of *D. discoideum* cells and led to the application of the excitable media framework to cAMP detection and secretion. Models of excitable media populated with parameters representative of the known features of the *D. discoideum* secretion of cAMP and pdsA and their interaction and diffusion reproduced some aspects of the pattern formation during aggregation, but the picture is still incomplete. The location

and timing of secretions of cAMP and pdsA from the cells are unknown. The cell boundaries exhibit wave like properties during migration which may play a role in the location of the secretions, but must be simulated and used as the boundary conditions for secretion as well as the external cAMP field. An external cAMP FRET probe would illuminate the secretion pattern that could then be implemented into the models of excitable media. The secretion dynamics of pdsA could be found by comparing the FRET signal due to the secretion of cAMP in wild type cells to the signal generated by pdsA null mutants. Together, this would modify the source and sink terms to more accurately reflect the cells and could increase the accuracy of the simulations.

#### **4.1.2 Mutual Information Accuracy**

We use a fluorescent protein-tagged small molecule to infer the local cAMP field around the cells. This method, in addition to requiring substantial effort to make the inference, suffers due to the cells ability to secrete and degrade cAMP. Accurate estimation of MI in *D. discoideum* chemotaxis requires accurate measurement of the chemical field that the cells are transducing, and the dynamics of the cells modulation of this field are unknown. Additionally, the models that generate transduction bounds that the experimental observations must fall under use gradient steepness and average concentration as parameters, and both of these are subject to the cells interference on the applied field. The plausibility of a model depends critically on the comparison of the experimental observations and the models predictions, both of which suffer from lack of knowledge about the actual chemical field. An external cAMP FRET probe would

enable direct measurement of the cAMP field, and the actual signal could thus be used in both the model and experimental calculation. Additionally, the error in MI calculations is limited by the bin size into which the measurements are sorted. In our setup, the bin size is set by the magnitude of the fluctuations within the fluorescent signal, which represents our certainty about the cAMP signal absent of cell effects. The direct measurement would allow smaller bin size and although this would increase the number of measurements required to decrease error, the lower limit of the certainty about the MI measurements would ultimately be lower. Taken together, these two effects enable more rigorous testing of the plausibility of models.

#### **4.1.3 Secretion during Streaming**

Towards the end of the aggregation developmental period, the cells begin to follow each other in streams to the aggregates. The cells touch each other and proceed in a head to tail fashion. The role of cAMP in this process is unknown, but it is hypothesized that the cells secrete cAMP selectively at the back to attract nearby cells into the stream. An open question during this stage is ‘why don’t isolated cells chase their tails?’ since they may secrete only at their back side. The physical contact between cells may play a role in determining the location and timing of secretion so that cells within the stream secrete cAMP differently than isolated cells. To investigate this, direct measurement of the cAMP is required. An external cAMP FRET probe would immediately elucidate this through observation of the secretion dynamics of cells included in the stream and cells in isolation.

## 4.2 Extension of MI Bounds in LEGI Models through Development

The information theoretic treatments of LEGI models revolve around the effects of varying the environmental noise relative to the signal. Phosphorylation of receptors allows the cells to integrate over signals and average out noise. The number of receptors that each cell has affects the sample size, which determines the magnitude of the effect of noise. Both the phosphorylated receptor fraction and number of receptors changes over development, and affect the bias and distortion constant of the LEGI module within the cell respectively. The effects of bias and distortion have previously been modeled and fit to experimental observations at early and late developmental time points by Iglesias<sup>116</sup>. In our work, we model the bounds of signal transduction and compare them to experiments throughout development. The difference between the bound and the measured MI is the distortion within the cells. Our measure of persistence over development is related to the bias of the cells, though some additional analysis needs to be done. The distributions of cell trajectories and gradient angles are available and can be used to create conditional probability distribution functions which, combined with the distortion, can be matched to the distributions from Iglesias to calculate the bias for each developmental time point. The exact relationships between receptor phosphorylated fraction and number and distortion and noise need to be flushed out to plug into the Iglesias work and predict the response over development and can then be compared to the experimental observations. This work gives insight into the receptor kinetics role during the transition from bacteria hunting to aggregation and gives an additional check for plausibility of the models previously developed.

## Chapter 5

### Literature Review: Mechanosensing and Autophagy in the Gut

In this section we investigate the response of CACO-2<sub>BBE</sub> human gut epithelial cells to shear force from fluid flow in a microfluidic flow chamber and make two substantial findings: microvilli in the gut act as a mechanosensor and that shear stress causes fluid flux through the autophagy pathway. To motivate the use of a microfluidic device, I outline the difficulties inherent to human studies, compare and contrast animal and culture models, and comment on the merits of using silicon flow chambers to compliment or replace both. The most accessible control in such chambers is the flow of fluid, which led us to the discovery of the two shear dependant responses presented herein. First, we find that microvilli on the apical surface of the cells act as a mechanosensor, transmitting applied force into signaling events within the cell. We compare these actin rich protrusions to the well studied mechanosensor in the cochlea of the ear, stereocilia, and report a fundamental difference in the immediate signaling strategy. Calcium ion channels are activated within the stereocilia and we demonstrate that this is not the case for microvilli. Although the immediate downstream signaling event in microvilli remains elusive, we show that the cells indeed use them as a mechanosensor through observation of fluid filled vacuole like structures that appear in response to shear and their absence when microvilli cannot bundle together, in the absence of microvilli, and in control cells without flow. The second finding is the identification of these vesicles as residing downstream of autophagosomes. This

identification was accomplished by using drugs that effect known autophagy signaling elements combined with fluorescent imaging of proteins associated with autophagosomes. This was connected to the mechanosensor by performing these observations in the presence and absence of shear in control cells, unbundled microvilli mutants, and cells without microvilli and confirming that these autophagy pathway elements were only active during shear stimulation in control experiments. In the following background section, I first outline the reasons for pursuing medical advances in microfluidic devices instead of animals, the effects of these systems on discovery focusing on responses to shear stress, and the evidence for microvilli sensing these stresses, comparing them to stereocilia. I then outline the critical steps in autophagy including the constituents that we imaged, and comment on which pieces are used during the response to shear stress. This section concludes with an outline of how our paper fits into the body of literature and connects the mechanosensing of microvilli to the increase in autophagic flux.

## **5.1 Leveraging Evolutionary Conservation for Insight on Humans**

Use of humans in scientific research is limited both by ethical concerns and fundamental bounds. The knowledge that humans feel pain and are self aware precludes studies that intentionally harm or kill us. Humans are complex and live a long time in comparison to other organisms, which make us poor candidates for basic science or genetic and evolutionary studies. Humans are required in the study of human specific attributes, such as the effect of drugs on mental activity<sup>164–166</sup> and

mental disorders<sup>167-171</sup>, a variety of psychological work, and beneficial applications of technology and substances thoroughly tested in simpler systems, such as testing of chemotherapy medication after study in animal and culture systems<sup>172-176</sup>. Often, usage of simpler animal and culture assays is merited, such as for science questions where the primary components of the system are conserved across species; the similarity between different organisms offers an opportunity to gain knowledge about many systems simultaneously while using the most cost or time efficient option. Combined with translational efforts, which bridge basic and applied sciences, leveraging of these similarities reduces the ethical cost of many efforts in the life sciences by eliminating the need for testing on humans to learn about humans. The study of organisms outside of humans additionally grants insight into the fundamental attributes of life through the discovery of conserved elements across species, which opens the door for efforts to combine humans with other organisms or biotechnology. The following two sections outline the benefits and limitations of animal studies and contrasts them cell culture systems.

## **5.2 Animal Studies**

Animals are commonly used as models for disease in biomedical and behavioral research as well as for product development and testing<sup>177-183</sup>. Animals are frequently used to test hypothesis in a wide variety of fields from drug efficacy in cancer biology, to toxicity and addiction in pharmacology, and genetic regulation, differentiation, and morphogenesis in developmental biology<sup>184-187</sup>. They see such pervasive use because

they are a whole body system with complex interactions between the parts and experience the physical and chemical stresses that are required to develop and maintain their form of life. Since mammalian life has common ancestors, animals share features with humans and perturbations of those common elements can yield insight into how the human system functions in our shared environment. Results from translational animal studies include the discovery of insulin<sup>188</sup>, testing and development of a variety of vaccinations<sup>189-191</sup> and disease treatments<sup>192-194</sup>, and development of biotechnology like pacemakers and organ replacements<sup>195-197</sup>. These results have undoubtedly spared a great deal of suffering and death for humans, and the number of animals sacrificed to increase knowledge is dwarfed by two orders of magnitude by the number consumed for sustenance so it seems an efficient and ethically permissible use of other species. Despite the cornucopia of results derived from animal studies, many concerns remain. Animals and humans are not identical so not every discovery in an animal model provides insight into humans, and not knowing what will or will not translate leads to problems such as failed clinical trials and excessive side effects in drug discovery<sup>198-201</sup>. Animals also lack some of the complexity of human systems, especially in cognition, so questions about the particulars of human dominance in this environment are inaccessible in animal models. Additionally the ethical concerns of animal studies are numerous. Inhumane treatment abounds, simply observed by the unwillingness to perform such experiments on humans and more formally shown in the violation of the regulations involving animal use<sup>202</sup>. The plethora of both positive and negative attributes causes the tension that motivates other types of study that would retain the gains provided while avoiding the pitfalls.

### **5.3 Culture Studies**

A cell culture study involves removal of cells from plants, animals, or humans, and growing them in a suitable environment that includes the nutrients, gasses, pH, and temperature necessary for their survival. Cells in these systems proliferate to confluence, total coverage of the substrate, and can be sampled and subcultured to produce large numbers of cells that are tested in a variety of perturbations to garner understanding of their construction and responses to stimuli. Cell culture studies are used in many of the same fields as animals and, in contrast to animal studies, are simple, cheap, and ethically viable. Cell culture systems are more apt for addressing basic science questions. The simplicity of culture studies gives more precise control over variables and perturbations and foregoes the complex interactions present in the body and in animal studies. Small, controlled populations of cells in isolation are suited for making single changes their signaling networks and comparing the perturbed result to the unperturbed, mapping networks of interactions by investigating them one at a time. Additionally, single cell analysis is more accessible in the simpler setup of culture. Specific cell conditions can be produced more rapidly in culture, as the gestation and development of animals is not present. The use of human cells in these systems overcomes the genetic differences between humans and animals, and the static nature of cell culture removes the physical stresses present within an animal. The ethical concerns over mistreatment of animals are not as pronounced in culture, though not entirely absent as living organisms are even more casually sacrificed due to their perceived lower value. The ability to probe individual cells within culture has yielded many insights into signal transduction, genetics, and heterogeneity. The insights gained

from culture studies include discovery and manufacture of vaccines<sup>203–206</sup>, treatment for diseases<sup>207</sup>, and pathogenesis discovery<sup>208</sup>. Culture and animal assays have attributes that are often complimentary, such as the simplicity of culture and complexity of animals. To gain further insight into the relationship between phenomenological observations from animal studies and their physiological underpinnings probed in culture studies, assays that lie somewhere between the two have been developed.

#### **5.4 Bridging the Gap: Organs-on-a-chip**

Cell culture and animal studies can be difficult to compare and integrate because they address isolated and integrated conditions respectively. In order to experimentally connect the approaches, parts from each assay were combined into hybrid systems. In one such case, the 'organ-on-a-chip' (OoC) framework adds complexity to cell culture systems by introducing physiologically relevant stresses and resources present in animal studies, while maintaining precise control over them by excluding some interactions. These microfluidic chips are typically fabricated with Polydimethylsiloxane (PDMS), an optically clear and flexible silicone. These chips include precise fluid flow control and take advantage of the flexibility of PDMS to add dynamic shear stresses matched to physiological systems. Examples of such chips are shown in Figure 5.1 for a lung that 'breathes', a gut that has periodic stress like in digestion, a brain barrier with addressable perfusion ports, and liver with nutrient flow control. Since PDMS is optically clear, the chip contents can be continuously observed under a microscope, which is difficult in animal studies though fairly common in cell culture. Chips of this

nature have also been fabricated to mimic the heart and breast, and some organs have even been connected together with a circulatory system<sup>209–212</sup>. They are populated with human cells, which can be derived from the specific organ or pluripotent stems cells that are differentiated within the chip. As such, OoC retain the direct translation of cell culture systems to medical applications and the developmental progression present in animal studies. Additionally, immediate ethical concerns are equivalent to those present in cell culture, though as the chips become more complex and connected suggestions of equivalence to animal models could be initiated. After further development when the OoC contain the minimal set of resources and stresses the assay could be compared to animal models to further explore conserved physiology among mammals and reduce the number of animals sacrificed in medical studies. OoC have already been used to grant insights into a variety of areas such as the interplay between the microbiome and epithelial cells in the gut<sup>213–215</sup>, morphological features of cells in the gut and liver<sup>216,217</sup>, chemotherapy resistance in the lung<sup>218</sup>, and drug discovery and delivery in the brain, lung, and heart<sup>219–224</sup>. These results have been achieved with minimal usage of animals and improve upon culture assays by adding complexity, including constant fluid delivery.

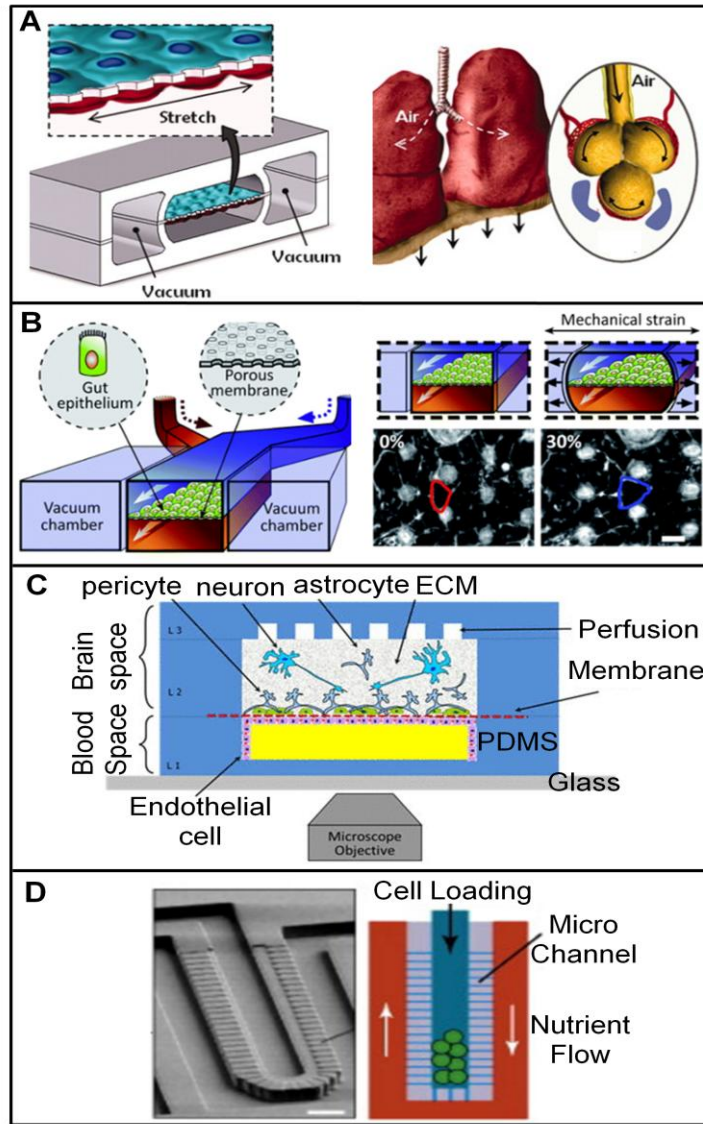


Figure 5.1 Examples of organs-on-a-chip. A) Lung-on-a-chip<sup>225</sup> that stretches lung epithelial cells that sit on a porous membrane with a vacuum to mimic breathing. The bottom chamber has fluid flow with nutrients while the top chamber is exposed to open air B) Gut-on-a-chip<sup>226</sup> stretches gut epithelial cells that sit on a porous membrane with a vacuum to mimic peristalsis in the gut. Fluid flow is present in the top and bottom channels for nutrient delivery and may be different to create gradients. C) Brain-on-a-chip<sup>227</sup> with a blood flow chamber coated in endothelial cells separated from a chamber with a variety of brain cells by a porous membrane to mimic the blood brain barrier. Perfusion channels are at the top for nutrient delivery and sampling. D) Liver-on-a-chip<sup>228</sup> with a central cell housing chamber separated from nutrient filled media by micro channels that allow diffusion and flow across them. Scale bar is 50um. OoC provide a more physiological accurate environment and maintain control over it and enable imaging of the cells during culture and over long periods.

### 5.4.1 Flow in OoC

OoC supply nutrients with constant perfusion of media across cells in contrast to the occasional media change of culture. Such flow produces shear stress on the cells. In the case of endothelial cells, such flow is a physiologically accurate addition because these cells line the interior of blood and lymphatic vessels that house moving fluid. Investigations into the addition of flow to endothelial cells show that the cells elongate and align<sup>229,230</sup> with the flow direction through mechanotransduction of the shear stress and reorganization of the actin cytoskeleton<sup>231</sup>. There are a variety of responses to shear stress in epithelial cells that have little overlap with endothelial responses. In confluent lung cells, flow drives a transition from state with high individual cell motility and frequent remodeling of cell neighbors within the sheet to a state with slower and collective motility and little remodeling<sup>232,233</sup>. The retarded timing of this transition is correlated with asthmatic airways, so regulation of responses to shear stresses is crucial in lung cells during development<sup>234</sup>. In confluent gut cells, shear stress causes out of plane polarity and height increases as well as a transition from a flat sheet to spatially repeating three dimensional structures characteristic of crypt-villi in developed gut cells<sup>225</sup>. Both of these examples transduce external shear stress into organization in a developmental transition and the mechanism in each is poorly understood. We aim to connect these responses to shear stress in a future project by investigating the jamming transition in gut cells and comparing the results to the lung cells.

## 5.5 Microvilli as Mechanosensors

Intestinal epithelial cells do not have a primary cilium, which is the predominant mechanosensor in other epithelial cells. Instead, actin rich protrusions called microvilli are located on their surface. These protrusions are similar to stereocilia, which are mechanosensors in the ear, in several ways. Both have actin containing protrusions bundled together by proteins, protocadherin<sup>235-237</sup>, as shown in Figure 5.2. In both cases, these bundles of filaments have increased elastic modulus compared to the unbundled fibers, which causes greater force on membrane<sup>238-240</sup>. This is graphed in Figure 5.3. In our study cells that have been genetically modified to be incapable of producing bundling proteins, and therefore have much lower bending stiffness, lose their mechanosensing phenotype. Second, both are present only at confluent cell densities when the cells communicate with each other physically, suggesting that they have a role in population dynamics. It has also been suggested that stereocilia developed from microvilli due to the parallels in the way that their proteins structurally organize the filaments. Additionally, the bundling proteins are connected to internal actin bundles through harmonin, shown in Figure 5.2 C on the interior of the stereocilia and microvilli, and deficiencies in harmonin are implicated in both Usher syndrome<sup>241-243</sup>, a disorder that causes deafness, and defects in microvilli assembly in the gut<sup>235,244,245</sup>. One critical difference between stereocilia and microvilli is in the signaling that occurs at the cell membrane when the protrusions are perturbed. When a sound wave travels through the spiral shaped cochlea, the membrane layers within move in relation to each other causing relative displacement of the stereocilia within each bundle and modulating the tension on the bundling proteins, or tip links<sup>246-248</sup>. These tip links

are connected to via tethers to ion channels that separate high and low concentrations. Under tension, these channels open shorting the action potential by permitting the ion concentrations to equilibrate between the sides<sup>249</sup>. We investigated whether microvilli use ion gating by manually changing calcium concentrations both up and down and saw an inverse response and no response respectively. We thus concluded that the microvilli signal through an unknown mechanism. We confirmed that they were signaling by comparing cells under shear stress that were under confluent, which would prevent them from forming microvilli<sup>235</sup>, had no bundling proteins, CACO-2 cells that have few microvilli, and CACO-2<sub>BBE</sub> cells, which have a more established brush boarder and more microvilli. We saw that BBE cells had a large number of vacuole like structures, CACO-2 cells had fewer, and cells with disrupted microvilli had almost none, confirming that the shear stress was being transduced through the microvilli.

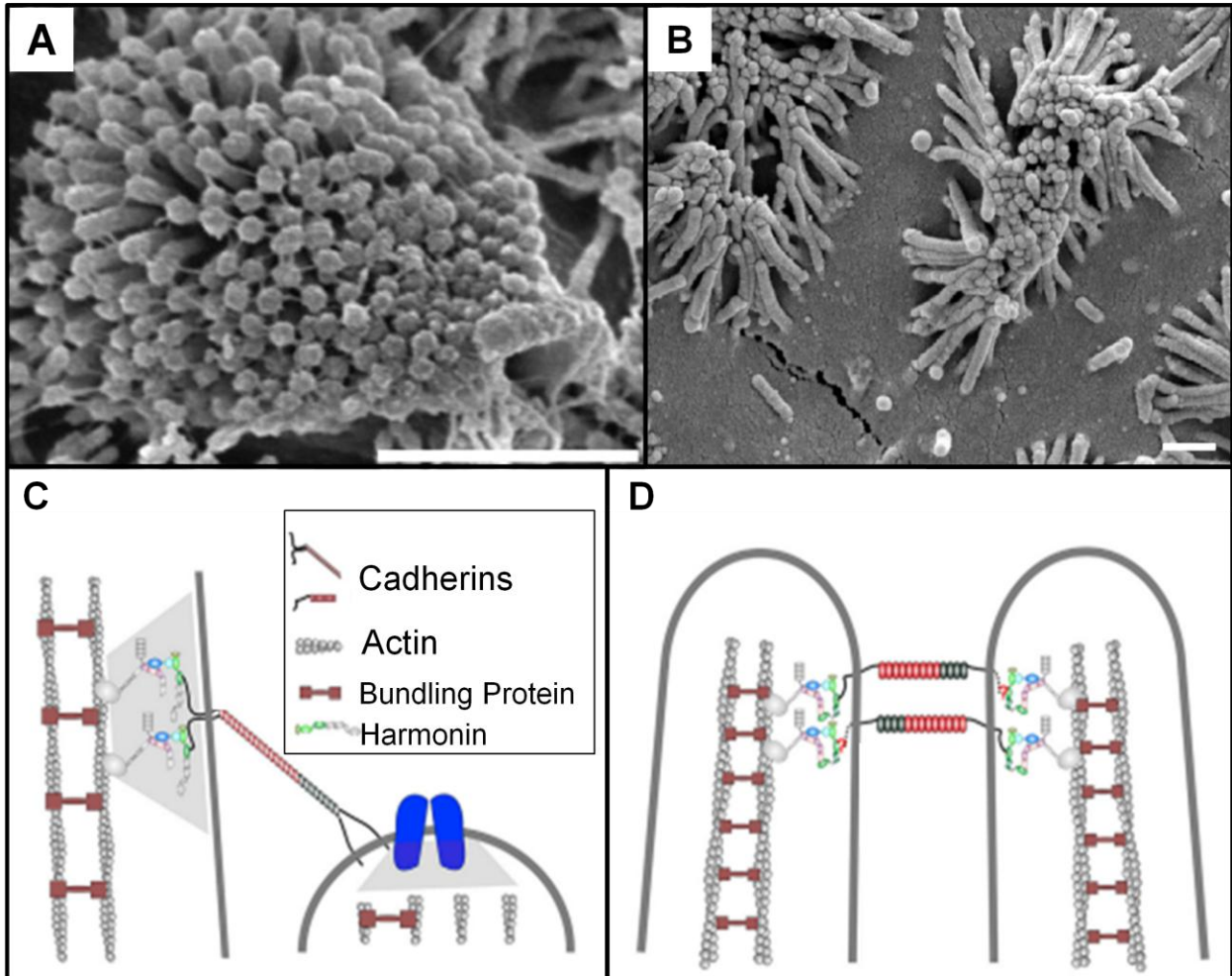


Figure 5.2 Comparison of stereocilia and microvilli. A) electron microscope images of bundled stereocilia<sup>250</sup>. Scale bar is 1 $\mu$ m. B) Electron microscope image of bundled microvilli in confluent CACO-2 cells<sup>235</sup>. Scale bar is 100nm. C) Cartoon depiction of the connection between two stereocilia<sup>245</sup>. Legend (inset) describes the main components for both stereocilia and microvilli (D). D) Cartoon depiction of the connection between two microvilli<sup>245</sup>. The visual similarity and the shared structural components between the stereocilia and the microvilli motivate the study of microvilli as mechanosensors. In the ear, shear stress on the stereocilia opens calcium channels which enable hearing. In the gut, we observe fluid filled vacuoles present under shear and absent in static conditions.

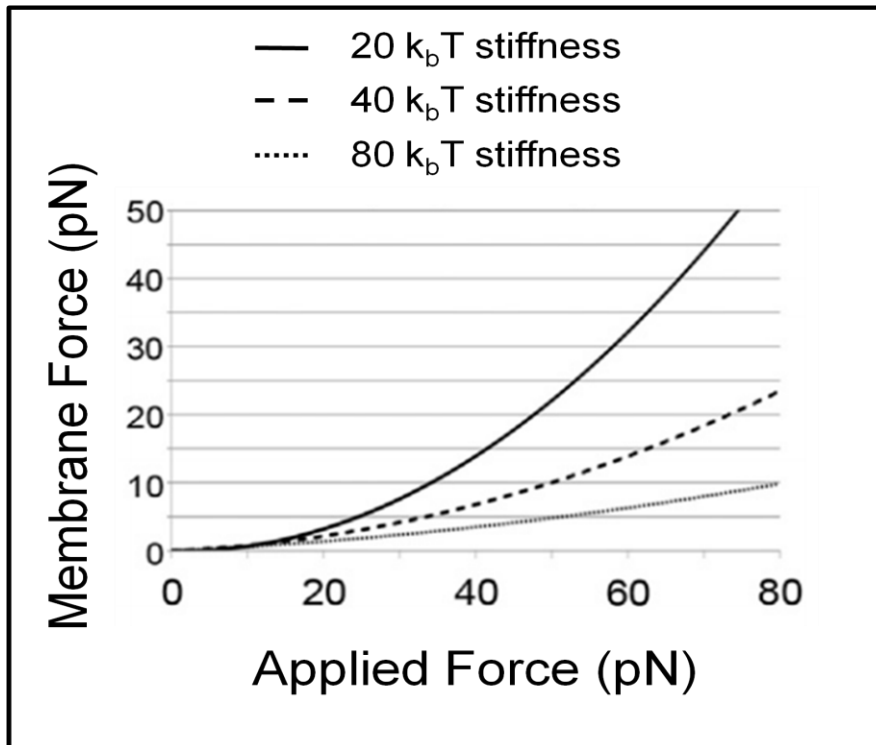


Figure 5.3 Force on the membrane for forces applied to bundles of varying stiffness<sup>248</sup>. Each curve represents the force that the cell membrane feels versus the force applied to a rod connected perpendicular to its surface. Curves are different by the bending stiffness that describes them, with  $20k_bT$  (solid),  $40k_bT$  (dashed), and  $80k_bT$  (dotted). In our study we use a genetic knockdown of the microvilli bundling protein. The bending stiffness of the unbundled microvilli is less than the bundled, as shown by comparing the dotted, dashed and solid lines. The result of this lower bending stiffness is lower force on the membrane for any applied force. We see the loss of the vacuole phenotype, meaning that there is a threshold of force on the membrane to elicit the response, and that the bundling of microvilli is crucial in this process.

## 5.6 Autophagy

After showing that microvilli act as mechanosensors, we turned our attention to the downstream signaling that led to vacuoles and probed their identity. We showed that the cells were healthy, though not developing, by staining the cells for proliferation, necrosis, and a wide variety of developmental markers. Through incidental triggering of the vacuoles in nutrient poor media while optimizing one of these markers, our attention turned to autophagy. We show that some autophagy associated proteins are used in the creation of vacuoles. Autophagy is the process of degrading and recycling cellular components. Autophagy occurs when cell constituents are damaged or in nutrient poor conditions to conserve material. It is also used to eliminate cytotoxic protein aggregates and foreign microbes. In macroautophagy, damaged organelles, subunits of cells with specific functions, are entirely surrounded by a double membrane referred to as an autophagosome. This organelle fuses with a lysosome, which reduces the pH and degrades the contents with various acid hydrolases. In microautophagy, cytoplasmic material is transported directly into lysosomes by invagination of the lysosomal membrane. We show that the vacuoles are not related to microautophagy, and are in fact related to macroautophagy through staining for the membrane proteins that accompany each. In canonical autophagy, there are four critical steps, initiation, nucleation, elongation and closure, and degradation and recycling<sup>251</sup>. The steps are outlined below.

### 5.6.1 Initiation

The first step in autophagy was discovered in yeast *Saccharomyces cerevisiae*. ATG1 (AuTophagy protein 1) is phosphorylated by AMPK in nutrient poor conditions, which activates the kinase. In nutrient rich conditions, mTOR (mechanistic target of rapamycin) phosphorylates ATG1 at different site which disrupts the interaction of AMPK and ATG1, thereby inhibiting autophagy<sup>252</sup>. An ATG1 ortholog, equivalent genes in different species, was observed in *Caenorhabditis elegans* and originally named unc-51 (UNCoordinated-51) then relabeled ATG1 when it was shown to be equivalent. Before this nomenclature change however, the human ortholog was discovered<sup>253</sup> and called ULK1 (Unc-51 Like Kinase 1) a name it retains. All of these kinases perform the same action in autophagy, interacting with AMPK and mTOR to sense the environmental nutrient level and turn autophagy on or off. Once turned on, nucleation of the phagophore occurs.

### 5.6.2 Nucleation

Nucleation of an phagophore occurs downstream of ULK1<sup>254</sup>. Upon activation, ULK1 moves to the location of autophagosome production. ULK1 phosphorylates Beclin 1, a scaffolding protein<sup>255</sup> that promotes action of VPS34-PI3K<sup>256</sup> (Vacuolar protein sorting 34) which phosphorylates lipids into phospholipids. These phospholipids have two hydrophilic tails and a hydrophilic head, so in an aqueous solution they reach a lower energy state by aligning and forming a double layer with the tails inside<sup>257</sup>, the classic

lipid bilayer. This process results in the nucleation of autophagosomes which can be built upon through further lipid organization, which elongates the membrane.

### 5.6.3 Elongation and Closure

After nucleation, the membrane pieces are elongated through lipidation of LC3 (Light Chain 3) into LC3-II<sup>258</sup> via conjugation with phosphatidylethanolamine by ATG3, a ubiquitin-like enzyme, and subsequent recruitment to the nucleated autophagosome outlined above<sup>259</sup>. The membrane grows as a double sheet<sup>260</sup> due to a physical property of the conjugation enzyme; it is an amphiphilic helix that lowers the energy of the membrane only at regions of high curvature (radius ~10nm) where packing defects caused unequal numbers of lipids on the two sheet interiors. This causes membrane expansion through LC3 recruitment at the area of high curvature, keeping the two adjacent sides close together and forming a growing double membrane sheet<sup>261</sup>. This process is outlined in Figure 5.5, starting with ATG3 action at the phagophore, and ending when the double membrane fuses together and becomes an autophagosome, excluding further action by ATG3. To explain why the entire sheet curves during elongation, eventually forming a sphere, Figure 5.4 graphs the energy of the membrane against the curvature of the sheet. The energy curve initially has three minima, two representing spherical membranes and one with the membrane flat. As the membrane continues to grow, shown by the red arrow, the curve gradually diminishes the energy boundary between the flat and spherical conformations, eventually losing the minima when the membrane is flat. This causes the membrane boundaries to come together and fuse, becoming a sphere, the conformation with the lowest energy<sup>262,263</sup>. The closure occurs through either membrane fusion<sup>264</sup>, connecting of the membrane pieces,

and/or membrane scission<sup>265</sup>, cutting of the membrane. In our study, the vacuoles get larger over time, suggesting that vesicles fuse with the vacuole after closure. The vacuoles tend to become less circular as they increase in size, which we hypothesize is due to the incorporation of the vesicle membrane into the vacuole membrane. Since the ratio of volume contained within a sphere its surface area grows proportionally to the diameter, we suggest that the excess membrane in larger vacuoles has low tension, which results in these morphological shifts.

#### **5.6.4 Degradation and Recycling**

Once the autophagosome has been formed, recycling occurs via fusion with a lysosome. Lysosomes are single membrane organelles with membranes comprised of, among other things, LAMP1 (Lysosome Associated Membrane Protein 1). The pH inside of a lysosome is typically 4.5-5, which is optimal for the class of enzymes that catalyze degradation through hydrolysis, called acidic hydrolytic enzymes, by using the excess of positively charged hydrogen atoms to promote bond cleavage of molecules through the theft of the shared electrons in a covalent bond. Once the lysosome has fused with the autophagosome, the autolysosome has both LC3 and LAMP1 incorporated in its membrane and the pH is matched to the lysosome. In our study, we see concurrent decoration of the vacuoles with LC3, the autophagosome membrane protein, and LAMP1, the lysosomal membrane protein. This suggests that the vacuoles are in fact autolysosomes and that response of the cells to shear stress flows through parts of the autophagy pathway.

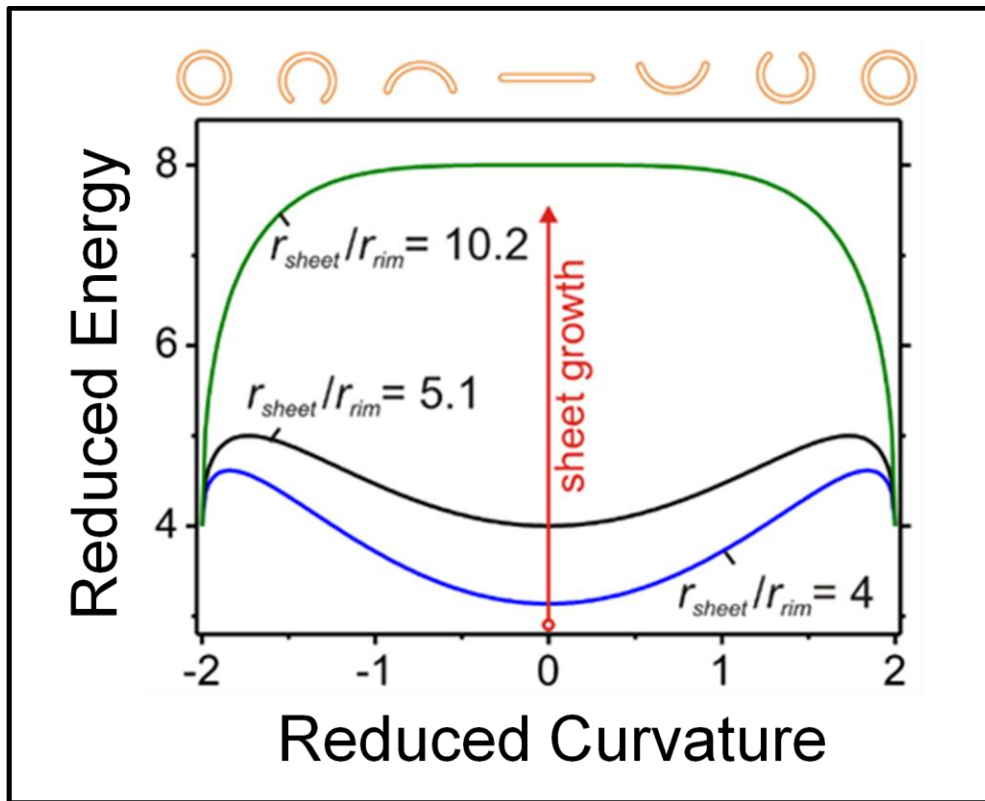


Figure 5.4 Energy of different curvatures and lengths of double membranes<sup>263</sup>. Reduced energy is plotted against reduced curvature for three different ratios of radius of the sheet ( $r_{sheet}$ ) to radius of the tip of the membrane ( $r_{rim}$ ). Energy and curvature are made dimensionless and referred to as reduced to make this graph scale free. The direction of the energy curve during sheet growth is noted by the red arrow. As the sheet grows, the energy minimum of a straight line is lost and the minima for circular membranes get deeper.

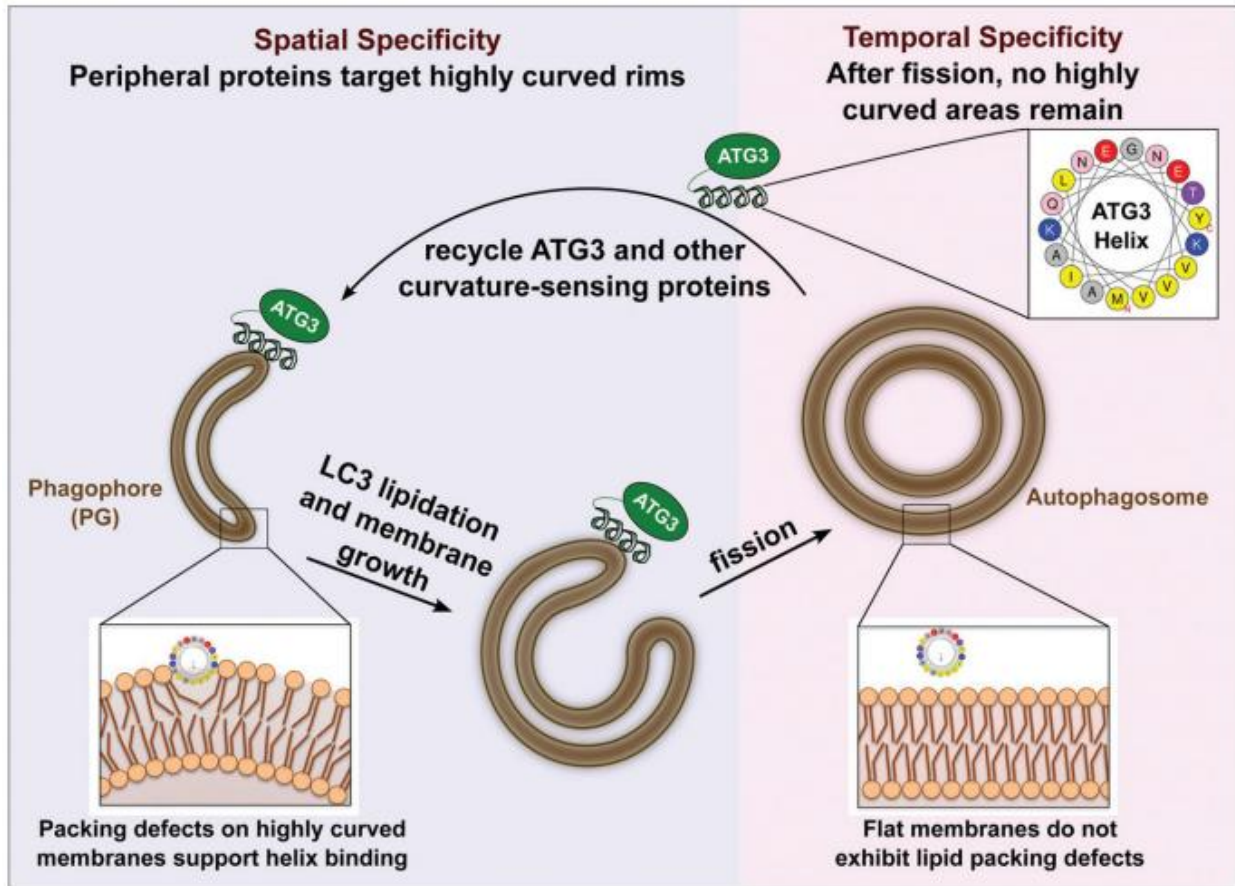


Figure 5.5 Role of the helical ATG3 in double membrane construction<sup>261</sup>. A) ATG3 targets high curvature areas in the phagophore membrane by lowering energy in these regions caused by packing defects. B) The double membrane elongates through addition of LC3-II by ATG3. C) The membrane closes through fission and becomes an autophagosome. ATG3 no longer attaches to the membrane. In our study, we show that the vacuoles are decorated with LC3-II and that knocking down LC3-II significantly lowers the number of vacuoles created. This suggests that the autophagy machinery plays a key role in the construction of the vacuoles.

## 5.7 Intention of Manuscript

The minimum to show activation of the canonical autophagy pathway includes evidence of ULK1 activation, incorporation of LC3 into autophagosomal membranes, LAMP1 and LC3 colocalization and acidification in autophagosomes. Autophagy is well studied and receiving a good deal of attention currently in studies of cancer<sup>266–268</sup>, neurological<sup>269,270</sup> and cardiovascular<sup>271,272</sup> diseases, and obesity<sup>273,274</sup>, and was the topic of the 2016 Nobel Prize in medicine or physiology. Biological systems are rarely linear and pieces of transduction networks are used in other signaling pathways creating a dense signaling network. To address this, ‘non-canonical autophagy’ was coined to describe transduction when only a fraction of this sequence is activated, and opening the door for studies of repurposed autophagy proteins and enzymes or pathways sections. In our study we replace the initiation step with signal mechanotransduced through microvilli and connect it to flux of fluid through autophagosomes. We follow this signal through merger with lysosomes via observation of the timing of the creation of vacuole like structures that are decorated with LC3, LAMP1, and are acidified under shear stress from fluid flow.

## Chapter 6

### **Microvillar Sensation of Shear Stress Induces Autophagic Flux in the Intestinal Epithelium**

Sun Wook Kim, Jonathan Ehrman, Mok-Ryeon Ahn, Scott W. Crawley,  
James R. Goldenring, Matthew J. Tyska, Erin C. Rericha, Ken S. Lau

The manuscript presented herein is a collaborative effort principally between the labs of Erin Rericha and Ken Lau. Sun Kim and I are co-first authors on this work, and working together with him multiple days a week for two years has been a great pleasure. Sun's command over biological methods and dogma coupled with his willingness to thoroughly share his knowledge greatly decreased the learning curve for this material. Sun's desire to learn the more abstract and quantitative methodologies that I provided gave me an opportunity to solidify my knowledge and allowed us to develop a common language to facilitate our cooperation. His discipline and focus was inspiring on several occasions, and pushed me and the project forward.

#### **6.1 Abstract**

We find a novel link between mechanotransduction and autophagy through the actin-rich microvillar protrusions lining the gut. These protrusions on the apical cell surface share structural similarities to the mechanosensitive stereocilia in the inner hair cells of the ear. Intestinal epithelial monolayers with microvilli, when exposed to persistent fluid

shear stress, developed large vacuoles lined with autophagy associated proteins LC3 and LAMP1. The size and number of vacuoles were suppressed by perturbations to the autophagy pathway, including small molecule inhibitors and LC3 knockdown as well as through perturbations to the microvilli. Together, our results establish a link between apical shear and autophagic trafficking in intestinal epithelial monolayers.

## 6.2 Introduction

Macro-autophagy, referred herein as autophagy, is an essential cellular process for maintaining cell physiology by removing damaged organelles and by salvaging proteins under nutrient poor conditions<sup>275</sup>. Autophagy is mediated through specialized vesicles, called autophagosomes, which fuse with lysosomes to induce protein degradation by acidic lysosomal hydrolases<sup>276</sup>. Defects in autophagy result in poor cellular response to stress and are associated with a wide range of pathologies, including neurodegeneration, cancer, and liver diseases, cardiovascular diseases, and autoimmune diseases<sup>277–283</sup>. Recently, autophagy has been linked to intestinal pathophysiology. Genome-wide association studies have identified several risk alleles to inflammatory bowel disease in autophagy-related genes (e.g., NOD2, ATG16L1, XBP1, IRGM, LRRK2)<sup>284–292</sup>. As the intestinal epithelium responds strongly to nutrient stress<sup>293,294</sup>, a role for autophagy in maintaining gut function is expected. A large body of literature focuses on the role of nutrient signaling, such as AMPK and mTOR, on the induction of autophagy<sup>295</sup>. Less work has been done on other potential autophagy modulators, an obvious candidate being mechanical stress as solid and liquid regularly

stress the apical surface of the gut. Cytoskeletal microtubules, which deform as the cell changes shape, interact with and regulate MAP-LC3 (microtubule-associated protein 1A/1B-light chain 3, herein referred to as LC3), a central component of the autophagy machinery. Microtubules also regulate the transport of various pre- and post-autophagy vesicles<sup>296</sup>. As such, a new class of microtubule-modifying drugs, such as a Flubendazole, has been identified as potent autophagy inducers<sup>297</sup>. Furthermore, a recent study reported that the primary cilium, a microtubule-rich structure, can activate autophagy in kidney epithelial cells in response to shear stress<sup>298</sup>. These observations support the role of mechanotransduction in autophagy regulation.

Here, we find that intestinal epithelial cells, when organized as a monolayer, respond to shear stress by increasing flux through the autophagic trafficking pathways. As intestinal epithelial cells lack a primary cilium, shear-stress must be transduced through another mechanical sensor. We find that actin-rich microvillar protrusions are required to trigger the shear stress response. The intermicrovillar adhesion complex (IMAC) linking adjacent microvilli resembles the complex that links stereocilia in the inner hair cells of cochlear<sup>299</sup>, which mechanically respond to sound waves<sup>300</sup>. Our findings provide the first evidence of a mechanosensing role of microvilli and propose a novel mechanically-controlled mechanism for breaking down macronutrients in the immature gut.

## **6.3 Materials and Methods**

### **6.3.1 Cell Culture**

Caco-2<sub>BBE</sub> and Caco-2 cells were cultured in DMEM (4.5 g/l glucose, Corning) in 37°C incubator supplied by 5% CO<sub>2</sub>, supplemented with 20% and 10% fetal bovine serum (FBS) (Sigma), respectively. All media were supplemented with 1% penicillin/streptomycin and 2mM L-Glutamine (Hyclone).

### **6.3.2 Microfluidic Device Fabrication**

Microfluidic devices are constructed from polydimethylsiloxane (PDMS) to the specifications below. Designs were produced in Adobe illustrator and made into photolithography masks (Front Range Photomask). Photolithography was performed on 3 inch silicon wafer according to standard procedure (MicroChem Procedures). The masters were then treated with Trichloro(1H,1H,2H,2H-perfluorooctyl)silane (Sigma) to create nonstick surfaces. PDMS (Corning) was then poured onto the wafers in 10:1 base to curing agent, desiccated, and baked at 60°C for 4 hours. After removing the PDMS from the master, holes for tubing were punched in the inlets and outlets. The chambers were then sealed to a 4 well Nunc Lab-Tek chamber slide according to standard procedure <sup>145</sup>. The chambers were then coated with a 50 µM collagen (Sigma), 300 µM Matrigel (Sigma) mixture in DMEM (Sigma). After one hour under UV light, the devices were rinsed with DMEM, covered with PBS and refrigerated until used.

### 6.3.3 Live Cell Imaging with Microfluidic Control

For shear experiments, 25 mM HEPES was added in the media when cells were seeded in the microfluidic device. Cells were seeded at a density of  $3 \times 10^7$  cells/ml to obtain dense confluency and  $7.5 \times 10^6$  cells/ml to obtain less dense confluency for microvilli perturbation experiments. After 5 hours incubation to allow monolayer formation, un-attached cells were washed off prior to the start of overnight shear experiments. Live cell imaging was performed using a Nikon A1R (Nikon) or a LSM 710 (Zeiss) fluorescent confocal microscope using a 20x objective in 30 minute intervals. At the end of the experiment, cells were fixed *in situ* with 4% paraformaldehyde (PFA) then the devices were disassembled for further cellular analysis.

To visualize the cytoskeleton and microvillar changes, Caco-2<sub>BBE</sub> cells were transfected with a GFP-UtrCH plasmid, containing the actin-binding domain of utrophin<sup>301</sup>. To study cell proliferation and cell cycle, cells were transfected with a FUCCI plasmid<sup>302</sup>. For dextran uptake assay, FITC-dextran (70 kDa, Molecular Probes) at a final concentration of 5 mg/ml, RFP-dextran (10 kDa, Molecular Probes) at a final concentration of 10 mg/ml, and/or LysoTracker (Molecular probes) at a final concentration of 50 nM were supplied continuously to the microfluidic devices for the duration of experiments. Live cell imaging was conducted and dextran positive particle (as determined by manual thresholding) count was conducted in ImageJ (NIH).

### 6.3.4 Immunofluorescence Microscopy

Fixed cells were permeabilized 0.1% Triton X and 1% bovine serum albumin (BSA) in PBS, blocked with 5% BSA (Sigma) and 5% goat serum in PBS (Jackson

ImmunoResearch) in PBS for 1h at room temperature. Cells were stained with primary antibodies diluted in the blocking buffer for 1.5~2 h, and then with fluorescent secondary antibodies (Life Technologies), Hoechst (Life technologies), and Phalloidin (Life technologies) for 1 hour. Images were taken using 20X or 60X objectives on a Nikon A1R (Nikon) or a LSM 710 (Zeiss) confocal microscope. TUNEL assay was performed according to manufacturer's specifications (Roche). For quantification, sizes of single particles were measured using custom scripts in ImageJ(NIH) after thresholding out excessively large particle clusters. Numbers of particles were estimated by the total area occupied by positively stained regions as determined by manual thresholding in ImageJ(NIH). Whole cell quantification was done by Z-maximal projection.

### **6.3.5 Apical Surface Biotinylation**

Caco-2<sub>BBE</sub> were seeded in the microfluidic device for 1 day to ensure monolayer establishment, and then were washed ice-cold PBS supplemented with 0.1 mM CaCl<sub>2</sub> and 1.0 mM MgCl<sub>2</sub> (PBS-CM). EZ-Link® Sulfo-NHS-LC-Biotin (0.5 mg/ml) (ThermoScientific) was freshly prepared in ice-cold PBS-CM, and applied to the microfluidic chamber to the apical surface of the monolayer at 4°C for two consecutive 20 min periods, after which Streptavidin-Cy3 (Sigma) was applied for 1 h at 4°C. Additional biotin was quenched with 100 mM glycine and washed prior to the start of microfluidic experiments.

### **6.3.6 Histochemical Staining**

Samples were fixed with 4% PFA for 1 h at room temperature, and then dehydrated with 60% isopropanol for 5 minutes. Samples were then stained with Oil red O solution for 10 min and imaged with brightfield microscopy (EVOS). Periodic Acid-Schiff staining was performed to manufacturer's specifications (Abcam).

### **6.3.7 Small Molecule Studies**

100 nM Bafilomycin A1 (BafA) (Sigma), 50  $\mu$ M Chloroquine (CQ) (Enzo Life Sciences), and 10  $\mu$ M BAPTA-AM (Molecular probes) were prepared in culture media from a dimethyl sulfoxide (DMSO)-based stock solution. 5 mM 3-Methyladenine (3-MA) (Sigma) and 3  $\mu$ M Ionomycin (Sigma) were dissolved directly in media. Small molecules were supplied to the microfluidic devices continuously for the duration of experiments. Control cells were treated with the DMSO vehicle.

### **6.3.8 RNA Knockdown**

siRNA against LC3 $\alpha$  (sc-106197) and LC3 $\beta$  (sc-43390) (Santa Cruz Biotechnology) were transfected into Caco-2<sub>BBE</sub> cells with PolyJet to manufacturer's specifications (SignaGen Laboratory). Cells were used 48 h later for experiments. PCDH24 shRNA was applied to Caco-2<sub>BBE</sub> cells as previously described<sup>299</sup>. Control cells were treated with scramble RNAi.

### **6.3.9 Real-Time PCR**

RNA was extracted using RNeasy kit (Qiagen), and reverse transcribed using Quantitect reverse transcription kit (Qiagen) to manufacturer's specifications. qRT-PCR was performed using ABI StepOne system (ABI) using relative quantities are calculated from Ct values using Gapdh expression as housekeeping gene.

### **6.3.10 Electron Microscopy**

Samples were prepared by washing samples with 0.1M sodium cacodylate and fixed with 2.5% glutaldehyde in sodium cacodylate for 1 h at RT, followed by post-fixation in 1% osmium tetroxide for 1 h in sodium cacodylate. After washing with 0.1 M Sodium cacodylate, samples were dehydrated with a serial dilution of ethanol, then a 50-50 mixture of ethanol and propylene oxide, and finally propylene oxide. Electron micrographs were taken by 250 ESEM (Quanta).

### **6.3.11 Analysis of Vacuole Count and Size, and Monolayer Height**

Vacuoles tend to have uniform intensity, while cells are full of contrasting features, so images were first passed through a variance filter in ImageJ (NIH), followed by further analysis in Matlab (MathWorks). Images were binarized, and morphologically transformed using "bottom hat" (dilation and erosion). Vacuolar boundaries were filtered by area and circularity, yielding outlines of vacuoles while ignoring the majority of other cell features (Figure 6.1). Vacuolar diameters were estimated by the diameters of circles with the same area as each object to negate noise of boundary identification.

Both the vacuole number and size results from this automated algorithm were initially compared to results performed manually.

To determine the height of cell monolayers, we used the highest actin signal below the dextran level as the apical boundary of the monolayer. The basal boundary was determined as the highest actin signal above the substrate, which was non-fluorescent. The difference between the top and bottom was recorded at every pixel, with errors removed and the surface smoothed.

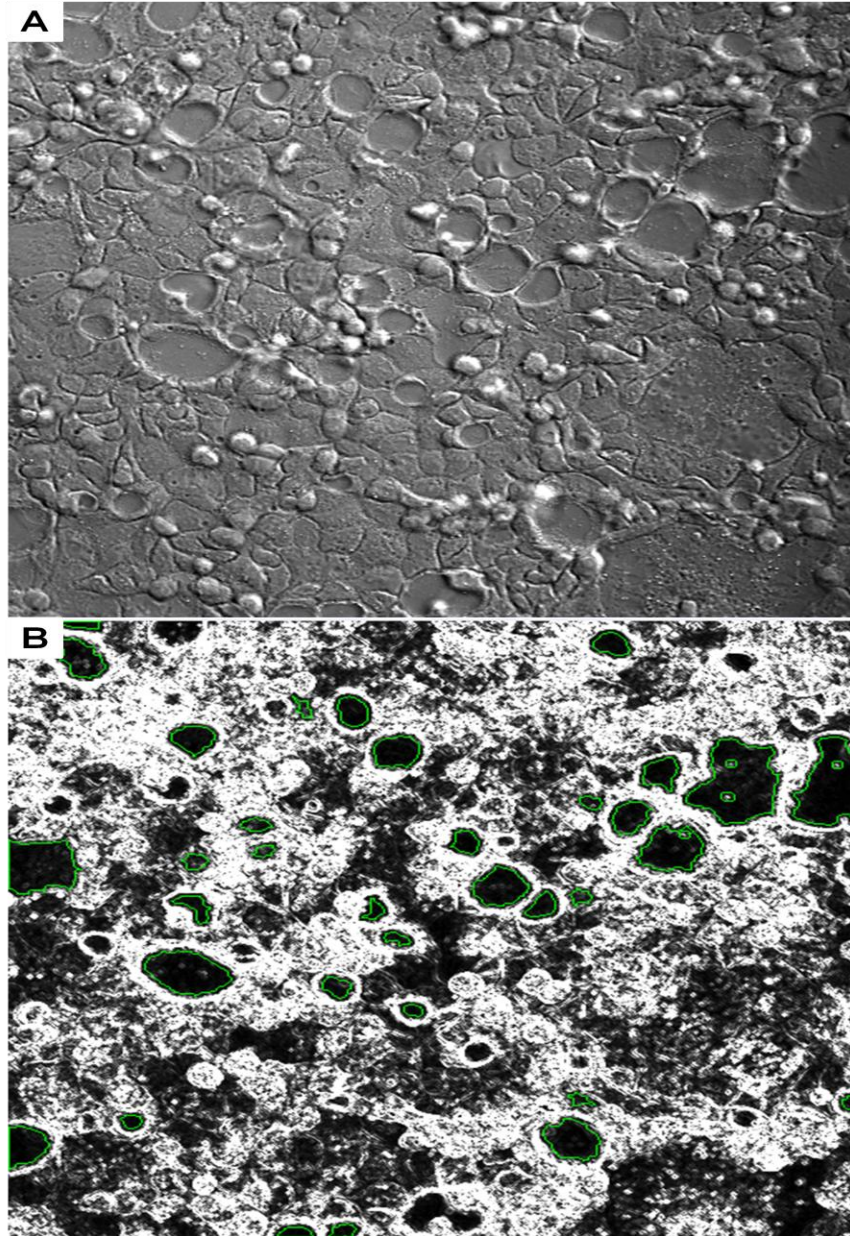


Figure 6.1 Vacuole Identification. A) Brightfield image of CACO-2 cells under shear for 10 hours. B) The brightfield images have their background removed in ImageJ, then are imported into Matlab. We then treat the images with a variance filter, then the morphological operation top hat several times to identify all objects in the image. The objects are filtered by area and circularity to select for fairly round objects. The boundaries of the identified vacuoles are overlaid in green. The area of each vacuole and total number are collected for each image to track both statistics over time. The algorithm was taught on three data sets that were also counted manually for each image. For each subsequent experiment, the output number is verified by eye for two time points and parameters varied if needed. This algorithm allowed for rapid assessment of the vacuole numbers used throughout the manuscript.

## 6.4 Results

### 6.4.1 Shear Stress Induces Formation of Vacuoles

To investigate whether intestinal cell monolayers, which lack primary cilia, respond to apical shear stress, a monolayer composed of Caco-2<sub>BBE</sub> cells was grown in a microfluidic device then subjected to the presence or absence of a fluid flow across the apical surface. A fluid shear stress of 0.025 dyne/cm<sup>2</sup> mimicking physiological luminal stress on the intestinal epithelium was applied overnight<sup>303,304</sup>. Under shear stress, the Caco-2<sub>BBE</sub> layer height increased compared to static control (Figure 6.2), corroborating earlier reports on the effects of shear flow on epithelial cell polarization<sup>305,306</sup>. Surprisingly, previously uncharacterized vacuole-like structures (termed “vacuoles” herein) appeared after 3 hours of exposure to fluid shear stress and increased in number and size until reaching a plateau after 6 hrs (Figure 6.3A-3B). These structures were observed under static control conditions, but with significantly less frequency and at much smaller sizes. Vacuoles can be indicative of cellular stress preceding cellular senescence or cell death. However, Caco-2<sub>BBE</sub> cells proliferated normally under shear stress despite vacuole formation, as shown by the fluorescence ubiquitination cell cycle indicator (FUCCI) cell cycle reporter (Figure 6.4A)<sup>307</sup>. Cell death observed by TUNEL staining was not increased by shear stress compared to control for up to 3 days of exposure (Figure 6.4B). These results demonstrated that the vacuole formation process is a normal cellular response to shear forces applied at the apical surfaces of intestinal epithelial cells.

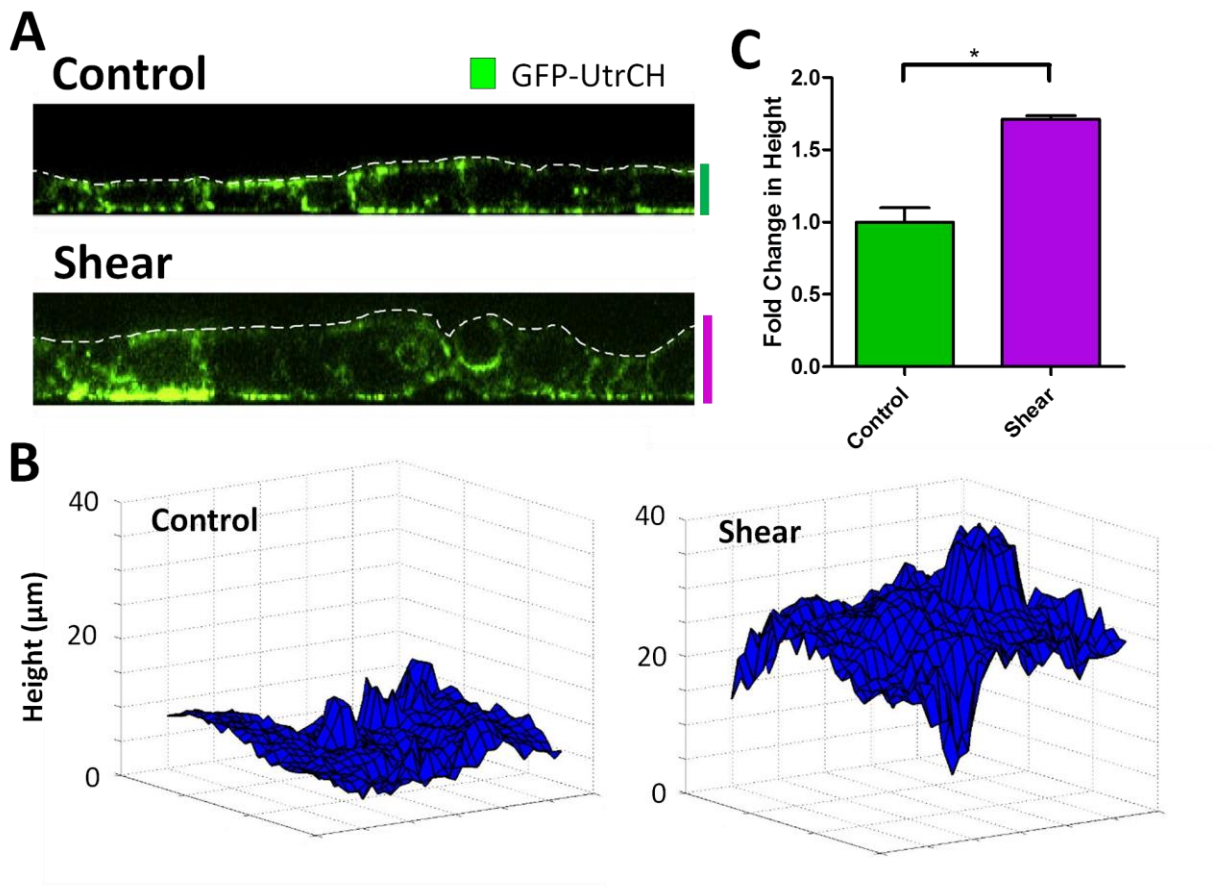


Figure 6.2 Cell monolayer height increases under shear stress. (A) Representative fluorescence images of the Z-axis view of Caco-2<sub>BBE</sub> monolayers labeled with GFP-UtrCH (green), comparing overnight shear with static control. Inset (magenta or green) bars depict average cell heights from these images. (B) Monolayer heights depicted as a surface using an image processing algorithm that detects apical cell boundaries by the location of where GFP-UtrCH meets fluorescent media. (C) Quantification of monolayer heights by considering every point on a surface depicted in B, calculated as fold change relative to static control. Error bars represent SEM from n=2 independent experiments. \*P<0.05 by t-test. These results are consistent with the literature description of gut epithelial responses to shear stress of the same magnitude.

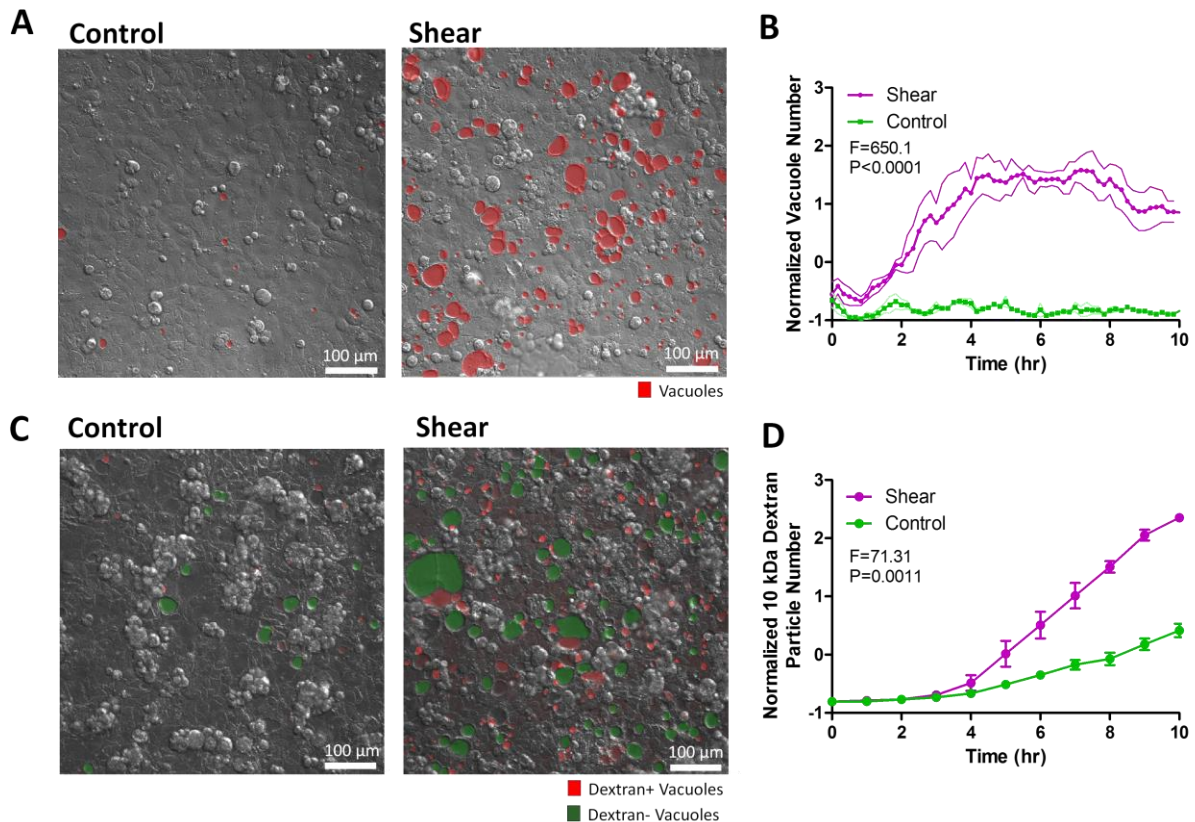


Figure 6.3 Shear stress induces vacuole formation in dense Caco-2<sub>BBE</sub> monolayers. (A) Representative DIC images of vacuole formation induced by shear overnight compared to static control. Vacuoles are highlighted in red. (B) Quantification of the number of vacuoles formed as a time course of shear induction compared to static control. Quantitative data were obtained by an image processing algorithm that segments vacuolar objects over entire time course movies, with 5 fields of view tracked and quantified per experiment. Bands represent standard error of the mean (SEM) from n=3 independent experiments. Data scales are normalized values derived from mean centering and variance scaling of each set of time course experiments. Statistical analysis was done by 2-way ANOVA. (C) Representative DIC/fluorescence image depicting 10 kDa fluorescently-labeled dextran included in vacuoles (red) and dextran-negative vacuoles (green), comparing shear overnight to static control. (D) Quantification of the number of dextran-positive vacuoles formed as a time course of shear induction compared to static control. Quantitative data were obtained by automatically counting the number of dextran particles exceeding a size threshold over the entire movie from maximum Z-projections. Data scales, error bars, and statistical analysis are the same as B. These results show that vacuole creation is dependent on shear stress due to their absence in static conditions, and that fluid flux into vacuoles is increased rather than the endocytosis rate due to the lag of dextran positive vacuoles behind vacuole creation.

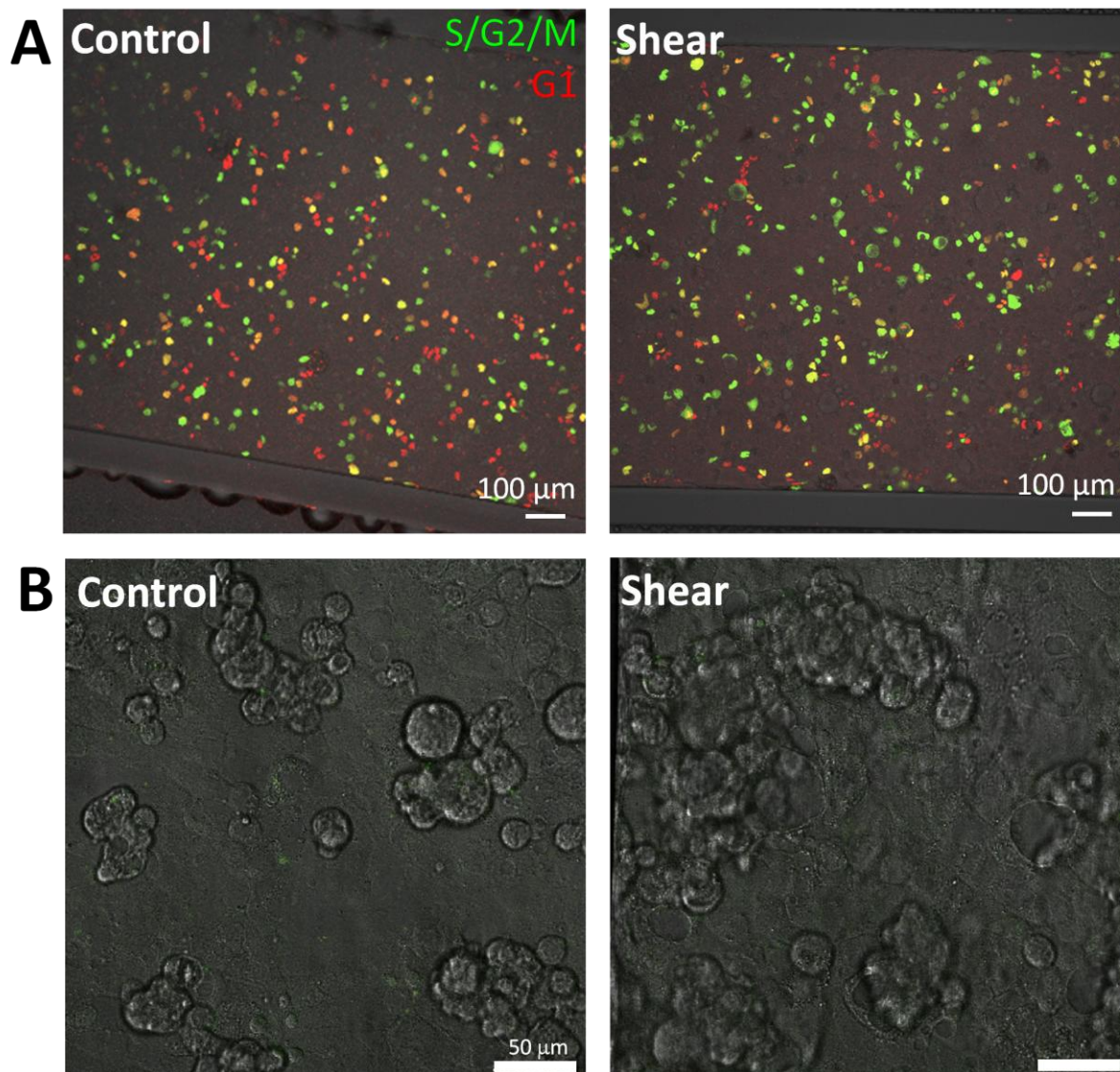


Figure 6.4 Epithelial monolayers exposed to shear stress maintain proliferation without cell death induction. (A) Representative fluorescence images of Caco-2<sub>BBE</sub> monolayers under overnight shear or static control, depicting cell cycle reporter FUCCI, Geminin (green) and Cdt1 (red). Scale bars, 100 μm (B) Representative fluorescent images depicting TUNEL (green) to assess cell death. Scale bars, 50 μm.

Next we considered whether these striking vacuolar structures were larger manifestations of known cellular entities. To determine whether shear-induced vacuoles are glycogen storage granules<sup>308</sup>, we used Periodic-Acid-Schiff (PAS) to stain for polysaccharides in cells exposed to shear stress overnight and discovered that the vacuoles were PAS negative (Figure 6.5A). Surprisingly, PAS-positive puncta were observed in control cells (Figure 6.5A), but these puncta disappeared upon shear stress induction. This experiment also excluded the possibility that vacuolated cells are goblet cells since PAS also detects acidic mucins produced by goblet cells. In addition, negative oil red staining indicated that the vacuoles are not large liposomes (Figure 6.5B). Finally, we investigated whether these intracellular vacuolar structures could be identified as vacuolar apical compartments (VACs)<sup>309,310</sup>. VACs result from macro-engulfment and subsequent invagination of apical membranes that contain actin-rich microvilli. To determine the possible apical origin of vacuolar membranes, we biotinylated the apical membrane prior to the start of shear flow, but after a monolayer with a tight barrier had formed (Figure 6.6A). The vacuoles formed after exposure to shear stress were only partially decorated with biotin (Figure 6.6B), unlike VACs that are completely labeled by biotin. Furthermore, the majority of vacuoles were not lined with actin-rich microvilli (Figure 6.6C), another hallmark of VACs. These observations excluded the possibility that shear-induced vacuoles identify with VACs and other commonly observed large, cellular structures.

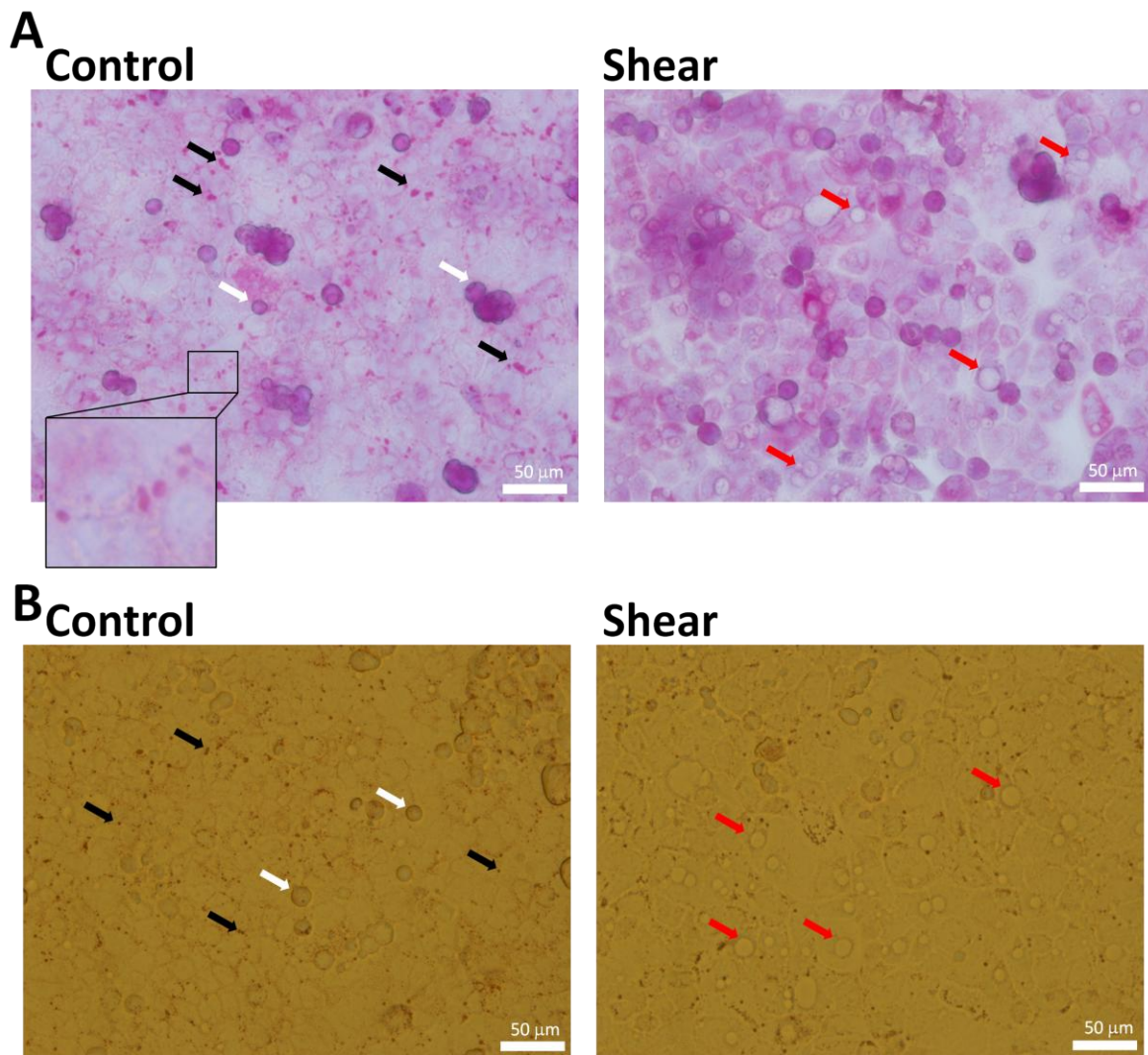


Figure 6.5 Shear-induced vacuoles are not glycogen storage vesicles, mucin-rich granules, or liposomes. (A) Representative brightfield images showing PAS staining of cell monolayers exposed to overnight shear or static control. White arrows indicate detached, rounded cells. Black arrows indicate PAS positive granules. Red arrows indicate shear-induced vacuoles. (B) Representative brightfield images showing Oil red O staining of cell monolayers exposed to overnight shear or static control. White arrows indicate detached, rounded cells. Black arrows indicate Oil red O+ granules. Red arrows indicate shear-induced vacuoles. Scale bars, 50  $\mu\text{m}$ .

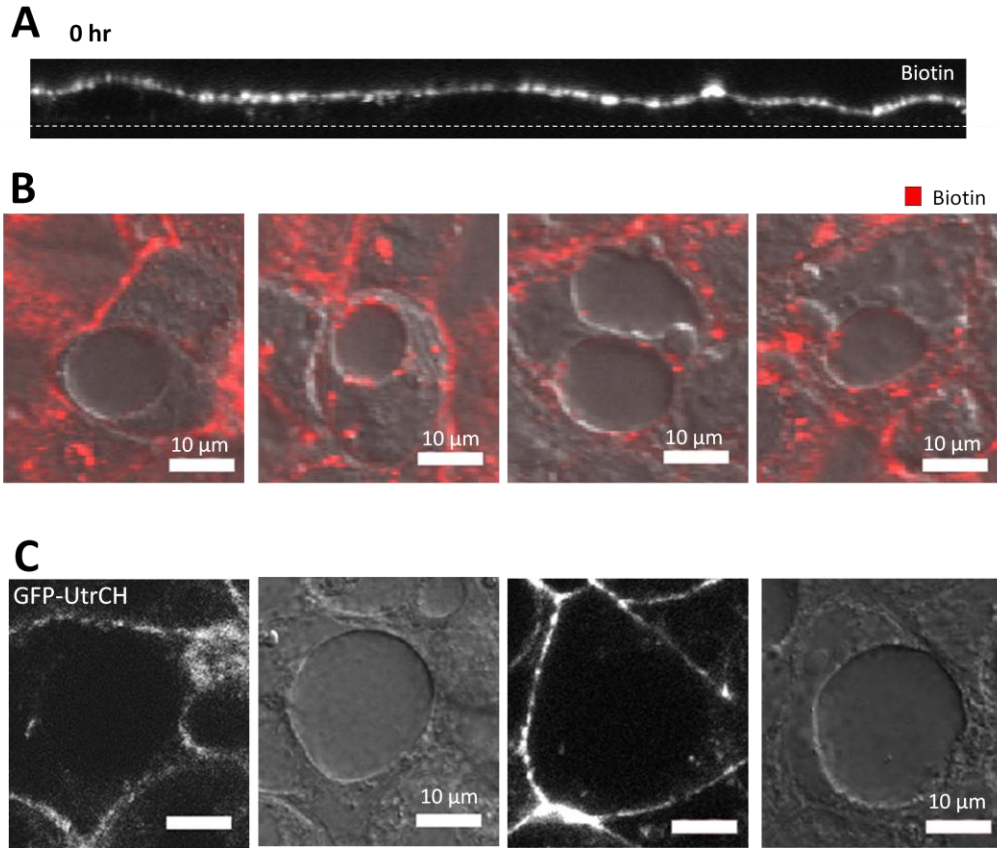


Figure 6.6 Shear-induced vacuoles are not VACs (Vacuolar Apical Compartments). (A) Representative fluorescence images of the Z-axis view of Caco-2<sub>BBE</sub> monolayers that are selectively biotinylated (red) at the apical membrane at the start of the experiment. Cells were allowed to form a monolayer overnight and biotinylated on ice prior to the experiment. (B) Representative DIC/fluorescence images (as maximum Z-projections) of biotin (red) in cell monolayers after overnight shear. Scale bars, 10  $\mu$ m. (C) Representative DIC/fluorescence images (as maximum Z-projections) of actin labeled by GFP-UtrCH in cell monolayers after overnight shear. Shear-induced vacuoles are not lined with actin (and hence, microvillar protrusions). Scale bars, 10  $\mu$ m.

#### **6.4.2 Vacuoles are Enriched with Extracellular Fluid from Altered Trafficking**

To determine whether shear-induced vacuoles formed by increased uptake of extracellular material, we supplied fluorescently-labeled dextran to the culture media in our shear experiments. Ten kDa dextran accumulated in vacuoles (Figure 6.3C), while seventy kDa dextran was excluded (Figure 6.7A). This observation indicated that the contents of vacuoles can originate from extracellular sources, but there is a size selection for contents that can be included, ruling out phagocytosis or pinocytosis-based uptake mechanisms. In addition, we confirmed that shear-induced vacuoles were intracellular by confocal microscopy, using a live-actin reporter to delineate cell borders (GFP-UtrCH)<sup>301</sup> while observing the localization of dextran-labeled vacuoles (Figure 6.7B).

Increased inclusion of extracellular material into vacuoles can result from distinct but related mechanisms, e.g., increased flux of extracellular material into the cell, and/or prolonged residence of material within the cell through altered trafficking. Prior research efforts have shown that the shuttling of internalized material among downstream routes can be controlled by cytosolic proteins and complexes such as ESCRTs, Rab GTPases, and coat proteins<sup>311</sup>. These routes include recycling back to the plasma membrane through the recycling endosome, sorting via early endosomes into the multivesicular bodies, vesicular fusion with the Golgi complex, delivery to lysosomes for degradation, and repackaging for transcytotic or exosomal release<sup>312</sup>. Redirection of these homeostatic trafficking routes by greatly increasing flux into pathways with slower out-flux could result in accumulation of extracellular material into vacuoles. We present

multiple pieces of evidence to demonstrate that shear-induced vacuoles do not result from increased endocytic uptake, and may result from this redirection mechanism. First, if vacuoles arose directly from increased uptake, all vacuoles should rapidly include dextran; instead, we observed about 30 percent of vacuoles containing dextran (Figure 6.3C). Second, dextran inclusion lagged vacuole formation, indicating that vacuoles initially arise by incorporating material already in the cell without direct uptake (Figure 6.3D). Third, we considered increased endocytosis by immunofluorescence imaging of vesicles, specifically focused on pathways that take up low molecular weight material. Clathrin-, dynamin- or caveolin- labeled vesicles were not substantially different between shear and control conditions (Figure 6.8). In addition, the early endosomal marker EEA decreased under shear compared to control (Figure 6.10A-B). These results suggest shear stress does not affect in-flux through endocytosis, but out-flux from the early endosomal compartment into downstream trafficking pathways. Hence, we investigated whether perturbations to downstream trafficking pathways altered the appearance or size of shear-induced vacuoles.

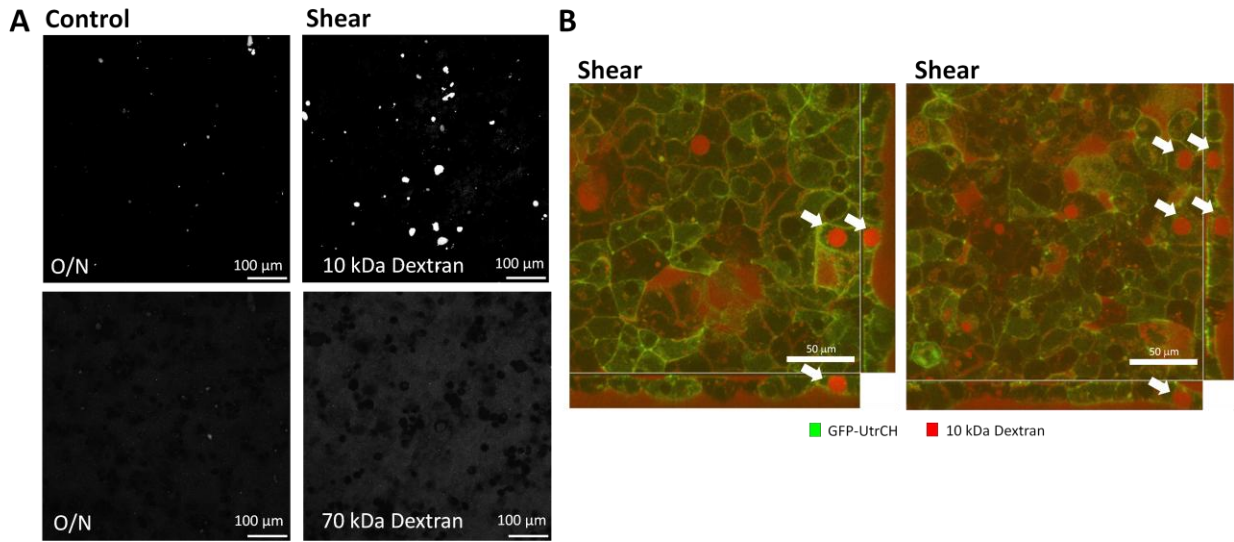


Figure 6.7 Internalized 10 kDa, but not 70 kDa, dextran, accumulates in vacuoles. (A) Representative fluorescence images of internalized 10kDa dextran (top) and 70 kDa dextran (bottom) over maximum Z-projections in overnight shear or static control groups. Scale bars, 100 μm. (B) Representative images depicting dextran-positive vacuoles (white arrows) in cells with borders marked by GFP-UtrCH under overnight shear. Two biological replicates shown. Scale bars, 50 μm. These results mean that there is a size selection in the uptake of fluid that is eventually trafficked into the vacuoles.

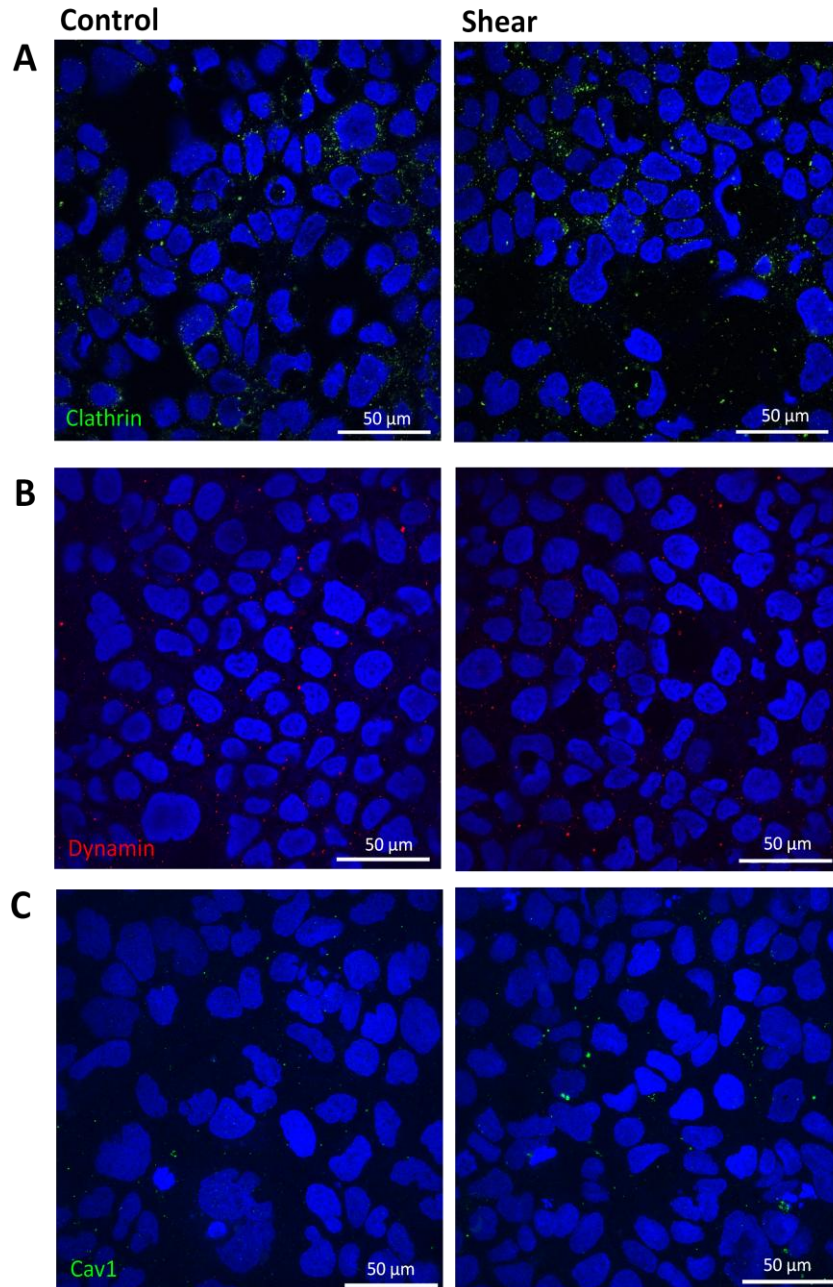


Figure 6.8 Shear stress applied to cell monolayers does not induce endocytosis. Monolayers exposed to overnight shear or static control conditions were fixed and stained with antibodies. Representative IF images depicting (A) Clathrin (green), (B) Dynamin (red) and (C) Cav2 (green). Scale bars, 50  $\mu\text{m}$ .

### **6.4.3 Shear-Induced Vacuole Formation is Associated with Altered Flux into an Autophagic Pathway**

Recent data indicated that the plasma and early endosomal membranes are possible sources of membrane for autophagosome formation, suggesting that a possible downstream fate of endosomes is processing by the autophagy machinery<sup>313,314</sup>. The partial incorporation of endocytosed, biotinylated membranes (Figure 6.15B), as well as EEA1+ membranes (Figure 6.9), into the shear-induced vacuoles was consistent with the involvement of the multiple membrane sources involved in autophagosome formation. To definitively establish an association between shear-induced vacuole formation and the autophagy machinery, we stained for LC3, a cytosolic protein that is lipidated and recruited to autophagic membranes. LC3+ puncta were markedly upregulated throughout the epithelial monolayer under shear stress (Figure 6.10C-D). Strikingly, LC3 labeled almost all vacuoles in their entirety, in contrast to partial punctate labeling of EEA1 and biotin, implicating the direct involvement of the autophagy machinery in vacuole formation and maintenance (Figure 6.10E and 6.9B).

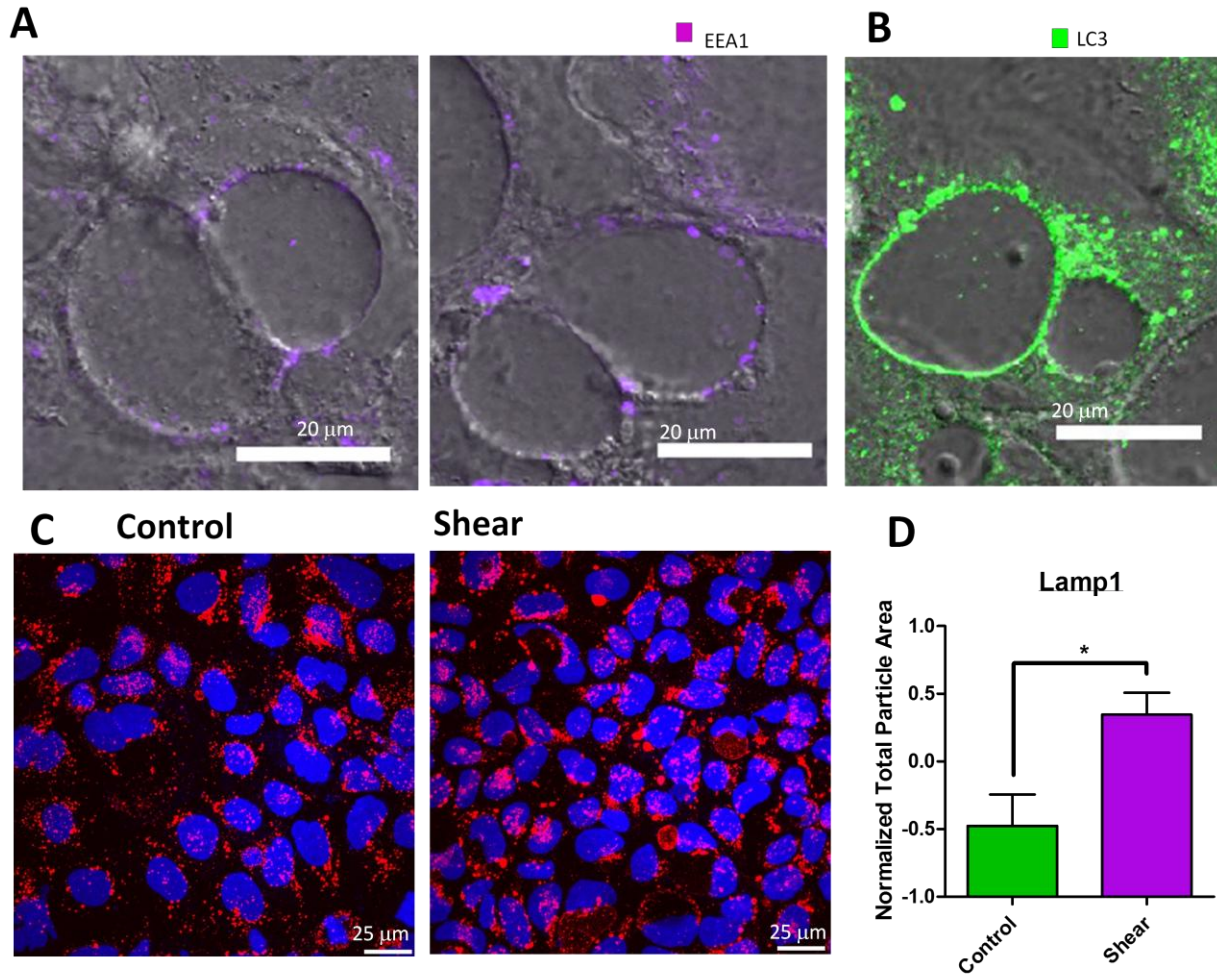


Figure 6.9 Shear-induced vacuoles are associated with the autophagy machinery. Representative DIC/IF images of (A) EEA1 (magenta) and (B) LC3 (green) and vacuoles in one confocal image section. Scale bars, 20  $\mu\text{m}$ . (C) Representative IF images (as maximum Z-projections) of LAMP1+ lysosomes (red) induced by shear overnight compared to static control. Scale bars, 25  $\mu\text{m}$ . Data scales are normalized values derived from mean centering and variance scaling of each set of experiment.

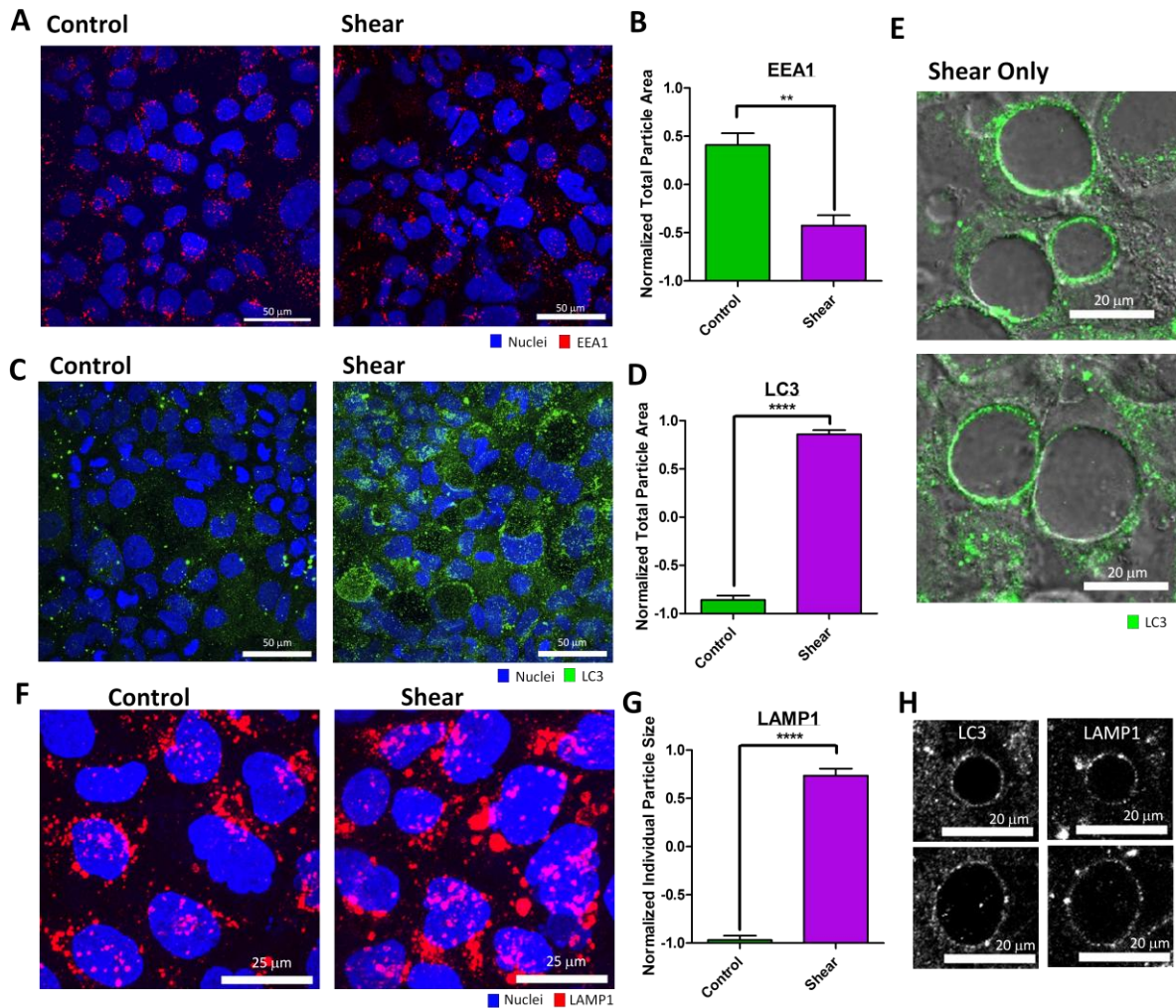


Figure 6.10 Shear-induced vacuoles are associated with increased autophagy, but not endocytosis. (A) Representative immunofluorescence (IF) images (as a maximum Z-projection) of early endosome antigen 1 (EEA1 - red) positive endosomes induced by shear overnight compared to static control. (B) Quantification of EEA1+ particles by total particle area in A. (C) Representative IF images (as a maximum Z-projection) of LC3 (green) expression induced by shear overnight compared to static control. (D) Quantification of LC3+ particles in C. (E) Representative DIC/IF images of LC3 (green) and vacuoles in one confocal image section. (F) Representative IF images (as a maximum Z-projection) of lysosomes marked by LAMP1 (red) induced by shear overnight compared to static control. (G) Quantification of the average size of individual LAMP+ puncta in F. (H) Representative IF images of LC3 and LAMP1 co-localization around shear-induced vacuoles. Error bars represent SEM from n=3 independent experiments. Data scales are normalized values derived from mean centering and variance scaling of each set of experiment. \*\*P<0.01, \*\*\*\* P<0.0001 by t-test. These results show that the vacuoles contain autophagy related membrane protein LC3 and lysosomal related membrane protein LAMP1, meaning that the vacuoles are produced in part by the autophagy machinery and fuse with lysosomes for degradation.

Autophagosomes and their contents are known to be degraded by the cell via fusion with lysosomes. To investigate the involvement of lysosomes in vacuoles, cells were stained with the lysosome marker LAMP1. While exposure to shear stress did not increase the number of LAMP1+ puncta (Figure 6.9C), the sizes of individual LAMP1+ puncta did significantly increase, signifying altered trafficking and fusion activities (Figure 6.10F-G). Moreover, colocalization of LC3 with LAMP1 was increased under shear stress, with LAMP1 lining entire vacuoles similar to LC3 (Figure 6.10H and 6.11A-B). In addition, vacuoles containing detectable dextran from the extracellular fluid colocalized with lysotracker, a fluorescent acidotropic probe for tracking lysosomes in living cells (Figure 6.11C). Taken together, these results demonstrated that fluid shear stress results in an increase in vacuole formation associated with the autophagy machinery downstream of extracellular uptake.

Having established an association between shear stress and the autophagy machinery, we pharmacologically perturbed different steps of the autophagy pathway and measured the impact on shear-induced vacuole formation. Treatment with chloroquine (CQ), a well-known lysosomotropic agent that inhibits autophagy, suppressed shear-induced vacuole formation, implying a causal role of the autophagy pathway in this phenomenon (Figure 6.14A-B). CQ inhibits steps downstream of autophagosome formation, resulting in the accumulation of LC3 puncta that cannot turnover<sup>297,315-317</sup>, as we also observed in the context of shear stress (Figure 6.12A-B). Treatment with 3-Methyladenine (3-MA), another well-established autophagy inhibitor that targets PI3K, also suppressed the shear-induced vacuoles (Figure 6.14A-C). However, treatment with Bafilomycin A (BafA) did not impact shear-induced vacuole

number (Figure 6.14D), but instead led to significantly larger vacuole sizes (Figure 6.14E-F). While CQ is a general lysosomotropic agent that can affect acidification and hence fusion of all endosomes as well as perturb the Golgi<sup>318</sup>, BafA inhibits V-ATPase and acidification of only lysosomes and vacuoles<sup>319</sup>. The consequent rise in pH due to BafA may render acidic hydrolases non-functional, leading to accumulation of vacuolar contents and larger vacuole sizes. Consistent with this notion, colocalization of dextran (marking vacuolar content) and lysotracker (marking acidic pH) was decreased by BafA in the context of shear stress (Figure 6.12C-D). In addition, we observed a slight decrease in LC3 puncta under BafA treatment (Figure 6.12E), due to its trafficking into and turnover by shear-induced vacuoles. To definitively support the role of the autophagy machinery in shear-induced vacuole formation, we knocked down LC3 using siRNA, as performed previously<sup>320,321</sup>. Downregulation of either isoforms of LC3 reduced vacuole formation in response to shear (Figure 6.14G-H and 6.13). These results suggested that shear stress may activate a non-canonical pathway involving the autophagy machinery, where CQ acts on an additional step of autophagosome-endosome fusion into vacuoles, and BafA inhibits turnover of vacuolar contents.

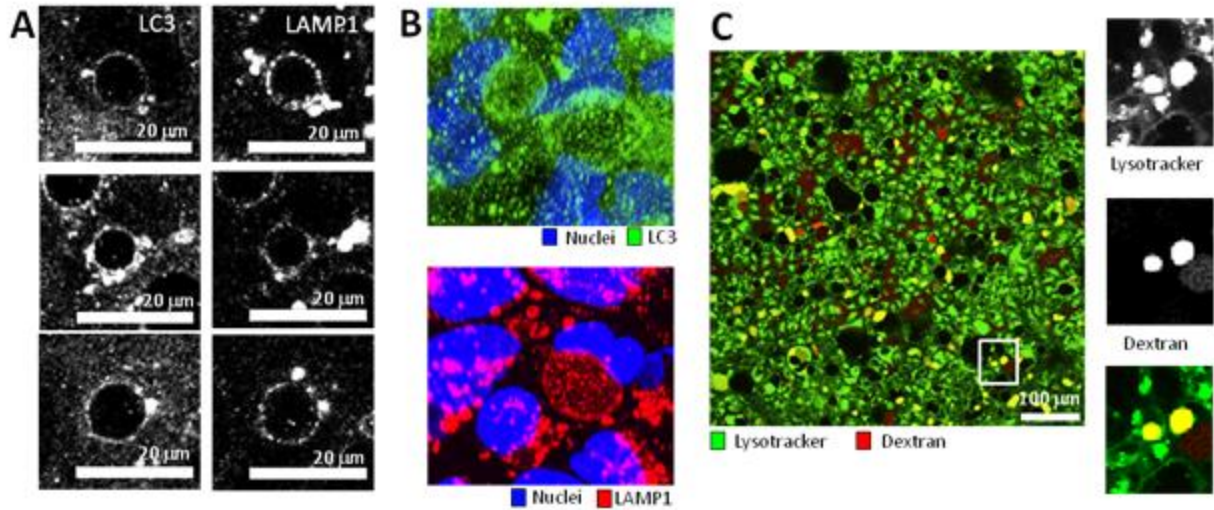


Figure 6.11 Shear-induced vacuoles are lined with autophagy components. (A) Representative IF images of LC3 and LAMP1 co-localization around shear-induced vacuoles. Scale bars, 20 μm. (B) Three dimensional reconstruction of confocal imaging stacks depicting LC3 (green) and LAMP1 (red) lining spherical shear-induced vacuoles. (C) Representative fluorescence image of colocalization of 10 kDa dextran (red) with the lysosomal marker LysoTracker (green) in vacuoles after overnight shear induction. Scale bar, 100 μm. Insets depict localization of red and green (yellow) in two vacuoles.

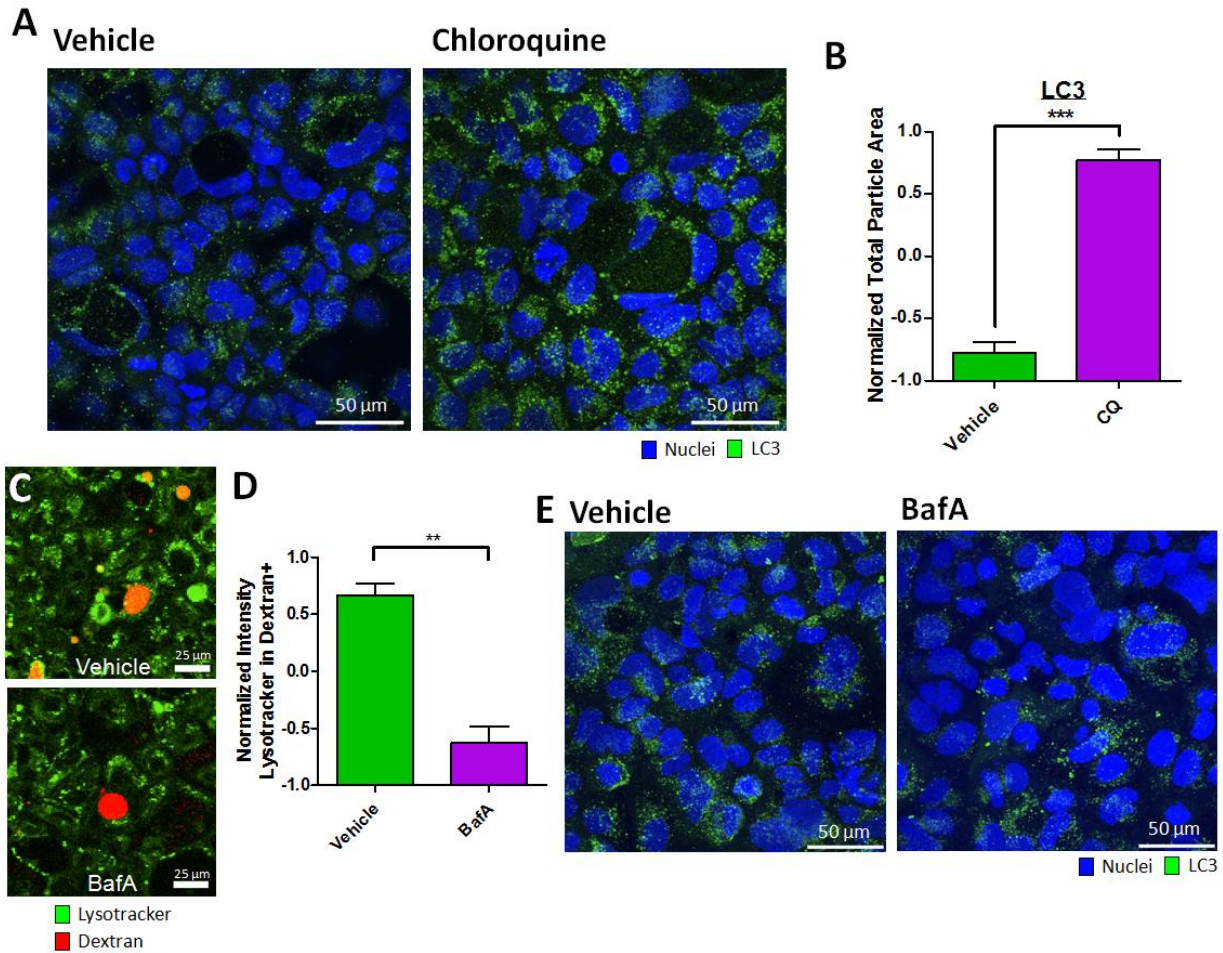


Figure 6.12 Chloroquine (CQ) and bafilomycin A1 (BafA) exert different effects on shear-induced vacuole formation. (A) Representative IF images (as maximum Z-projections) of LC3 (green) expression in cell monolayers exposed to overnight shear with culture media supplemented with vehicle or CQ. Scale bars, 50  $\mu$ m. (B) Quantification of LC3+ particles in A. (C) Representative fluorescence images of 10 kDa dextran (red) colocalization with LysoTracker (green) in cell monolayers exposed to overnight shear with culture media supplemented with vehicle or BafA. Scale bars, 25  $\mu$ m. (D) Quantification of the intensity of LysoTracker in dextran+ particles identified by image processing of C. (E) Representative IF images (as maximum Z-projections) of LC3 (green) expression in cell monolayers exposed to overnight shear with culture media supplemented with vehicle or BafA. Scale bars, 50  $\mu$ m. Error bars represent SEM from n=3 independent experiments. Data scales are normalized values derived from mean centering and variance scaling of each set of experiment. \*\* p<0.01, \*\*\* p<0.001 by t-test.

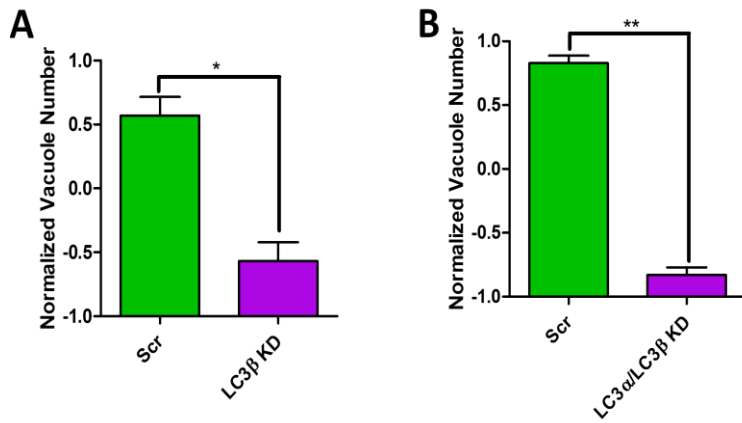


Figure 6.13 LC3 knockdown decreases shear-induced vacuole formation. Quantification of the number of vacuoles induced by overnight shear in (A) LC3 $\beta$  knockdown, and (B) LC3 $\alpha$ /LC3 $\beta$  double knockdown, compared to scramble control. Error bars represent SEM from n=3 independent experiments. Data scales are normalized values derived from mean centering and variance scaling of each set of experiment. \* p<0.05 by t-test.

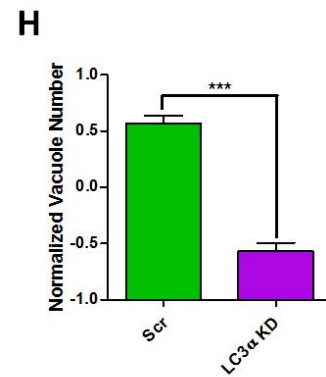
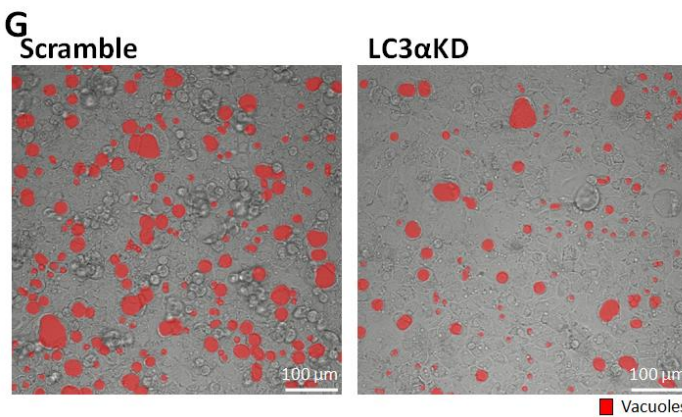
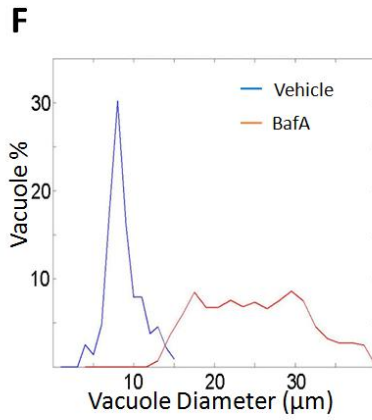
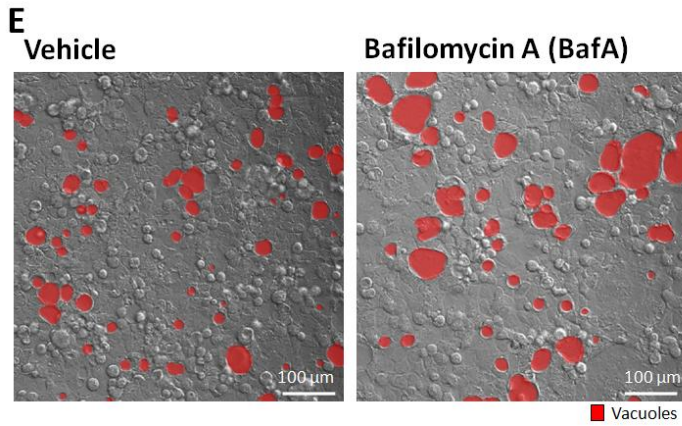
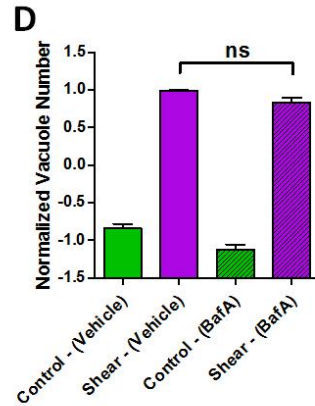
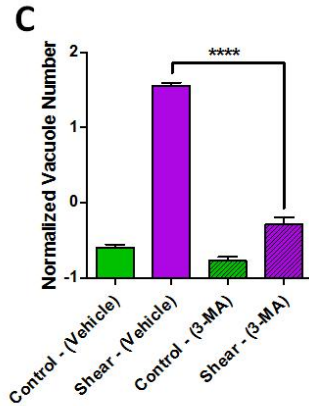
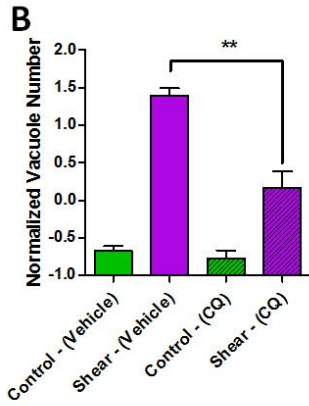
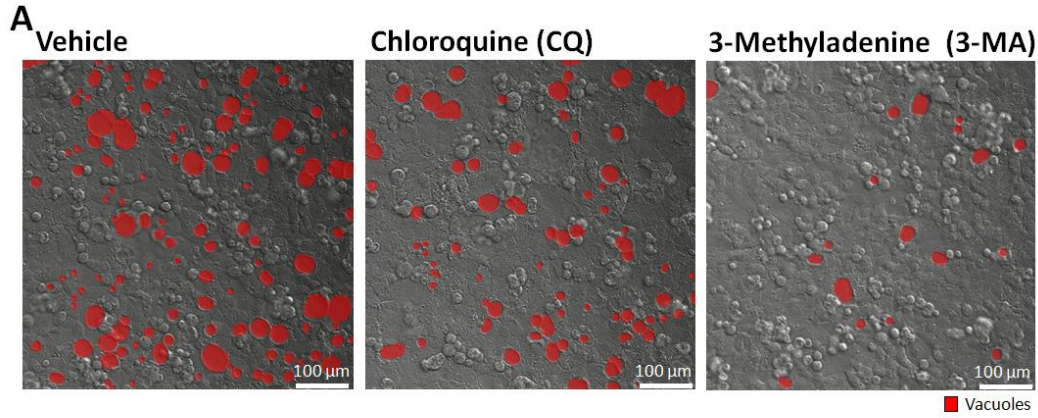


Figure 6.14 The autophagy machinery is required for shear-induced vacuole formation. (A) Representative DIC images of vacuole formation induced by shear overnight in vehicle, chloroquine (CQ), or 3-methyladenine (3-MA)-treated cell monolayers. Vacuoles are highlighted in red. (B-D) Quantification of the number of vacuoles formed resulting from shear induction overnight or static control, comparing monolayers treated with vehicle and (B) CQ, (C) 3-MA, (D) Bafilomycin A (BafA). (E) Representative DIC images of vacuole formation induced by shear overnight, comparing BafA- with vehicle-treated cell monolayers. (F) Distribution of vacuole diameter measured by image analysis of E. Data represent combination of all vacuoles from n=3 experiments (5 fields of view each). (G) Representative DIC images of vacuole formation induced by shear overnight in cell monolayers with LC3 knockdown compared with scramble control. (H) Quantification of the number of vacuoles formed in G. Error bars represent SEM from n=3 independent experiments. Data scales are normalized values derived from mean centering and variance scaling of each set of experiment. ns not significant, \*\*P<0.01, \*\*\*P<0.001, \*\*\*\* P<0.0001 by t-test. These results show that the autophagy machinery is required to produce the vacuoles, since autophagy specific drugs significantly lower the vacuole number, and that lysosomal fusion is required to remove and degrade the vacuoles, since the fusion targeted BafA dramatically increased the size of the vacuoles. The size and number of the vacuoles are determined by the flux into and out of them, which is controlled by the shear stress and lysosomal attachment respectively.

#### 6.4.4 Apical Shear Mechanosensation Depends on Microvillar Protrusions

We next turned our attention to the mechanism of mechanosensation by intestinal epithelial cells which lack the well-known mechanosensor, the primary cilium. Enterocytes in the gut epithelium develop microvilli, actin-rich protrusions located at the apical surface. Caco-2<sub>BBE</sub> cells are known to adopt an enterocyte-like state upon dense contact with neighboring cells. Microvilli have remarkable structural similarity to the stereocilia of the inner ear, a *bona fide* mechanosensor<sup>299</sup>, as outlined in chapter 5. We hypothesized that the microvilli acted as the primary sensor of fluid shear stress upstream of vacuole formation. Using a live-actin reporter to label actin-rich structures, we confirmed that Caco-2<sub>BBE</sub> cells formed microvillar protrusions upon dense confluency both in the absence and presence of shear stress (Figure 6.16A) unlike trophoblasts that do not form microvilli without shear<sup>322</sup>.

To investigate the potential for microvilli as a mechanosensor, we pursued three complementary perturbation strategies. First, we observed the shear-stress response of the parental Caco-2 line, which is less efficient at forming microvilli than the Caco-2<sub>BBE</sub> line primarily used in this study (Figure 6.15A)<sup>323,324</sup>. Parental Caco-2 cells under shear stress formed significantly fewer vacuoles compared to Caco-2<sub>BBE</sub> cells (Figure 6.15B-C). Dextran+ particles in the parental line were also decreased, correlating with the number of vacuoles (Figure 6.15D). Second, we observed the shear stress response of Caco-2<sub>BBE</sub> cells in less dense monolayers, where microvilli protrusions do not form due to a poor polarizing environment (Figure 6.15A)<sup>324</sup>. Vacuole numbers and dextran+ particles were significantly diminished in confluent monolayers that were less densely populated (Figure 6.15E-G). Third, we specifically knocked down proto-

cadherin-24 (PCDH24) in the Caco-2<sub>BBE</sub> line. PCDH24 is an essential adhesion molecule of the IMAC complex that bundles microvilli. PCDH24 downregulation is known to form an aberrantly sparse brush border in Caco-2<sub>BBE</sub> cells<sup>299</sup>. We confirmed that PCDH24 expression was downregulated in our knockdown cell line (Figure 6.16B), which was accompanied by a defective brush border with few microvilli (Figure 6.17A, Figure 6.18). Exposure to shear stress in PCDH24 knockdown cells generated significantly less vacuoles and dextran+ particles compared to the scramble control under shear (Figure 6.17B-D). Finally, we evaluated whether shear-induced LC3 upregulation is dependent on microvilli. The number of LC3+ puncta was also decreased with PCDH24 knockdown under shear compared to scramble control (Figure 6.17E-F). Taken together, these results support a necessary role of intestinal microvilli in the transduction of apical shear stress to induce vacuole formation.

Studies in inner hair cells and trophoblasts have revealed that increased calcium flux downstream of a mechanically gated ion channel is responsible for mechanotransduction<sup>322,325,326</sup>. To investigate whether microvilli-based mechanotransduction is calcium-dependent, we performed shear experiments with administration of BAPTA-AM, a cell permeable Ca<sup>2+</sup> chelator that was used in both inner hair cell and trophoblast studies. Unlike in these two cell systems, BAPTA-AM did not inhibit the shear-induced vacuole formation (Figure 6.19A). Administering ionomycin to raise intracellular calcium also had minimal effects on shear-induced vacuole formation (Figure 6.19B). Hence, unlike other mechanosensitive cell systems, shear-induced vacuole formation is not triggered by increased Ca<sup>2+</sup> flux into the cells.

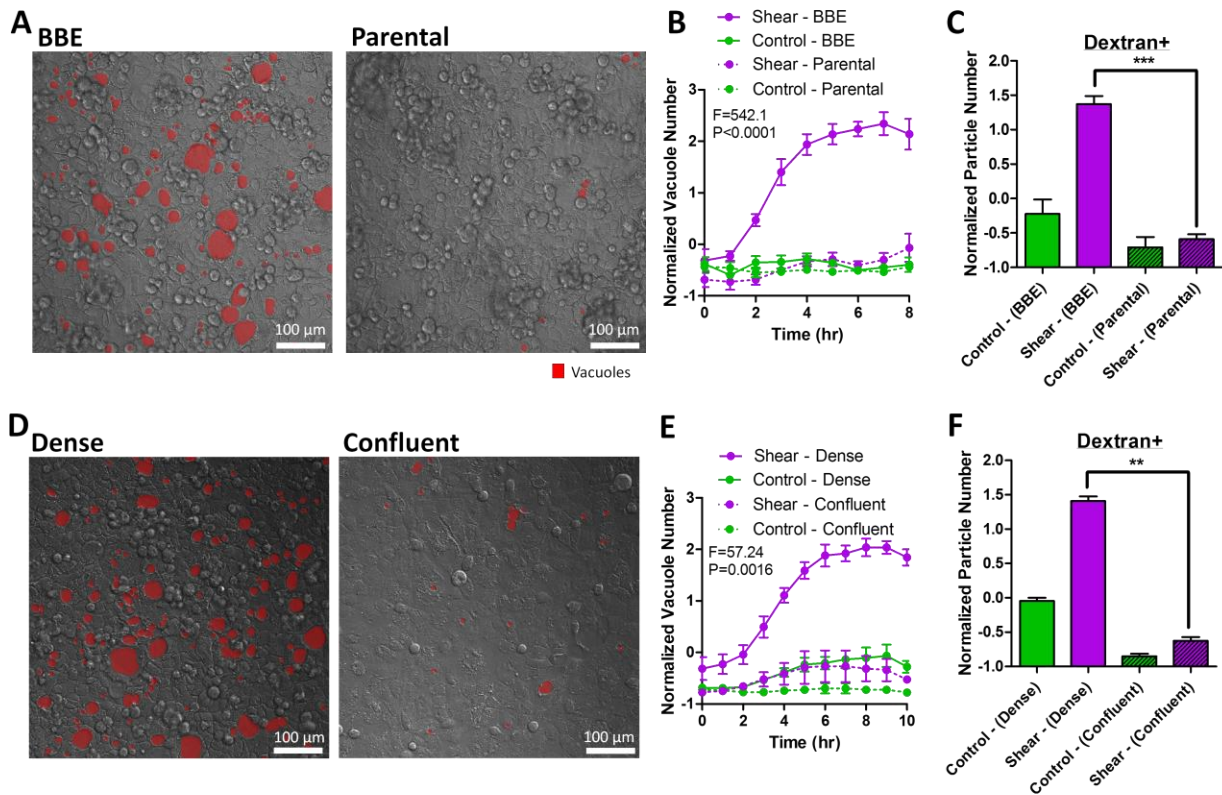


Figure 6.15 Microvilli are required for shear-induced vacuole formation. Representative DIC images of shear-induced vacuole formation overnight (A, D), comparing: (A) Caco-2<sub>BBE</sub> (control) with Caco-2 parental, and (D) dense (control) with less dense confluent plating. Vacuoles are highlighted in red. (B and E) Quantification of vacuole number as a time course of shear stress or static control, comparing conditions outlined in A and D. Statistical analysis was done by 2-way ANOVA. (C and F) Quantification of the number of dextran-positive vacuoles resulting from overnight shear induction or static control, comparing conditions outlined in A and D. Error bars represent SEM from n=3 independent experiments. Data scales are normalized values derived from mean centering and variance scaling of each set of experiment. \*\*P<0.01, \*\*\*P<0.001 by t-test. These results solidify the connection between mechanosensing by microvilli and vacuole production by removing the microvilli in two ways, with the parental cells that create fewer microvilli and through less dense seeding in which the cells produce fewer microvilli, and observing the significant decrease in vacuole number as a result.

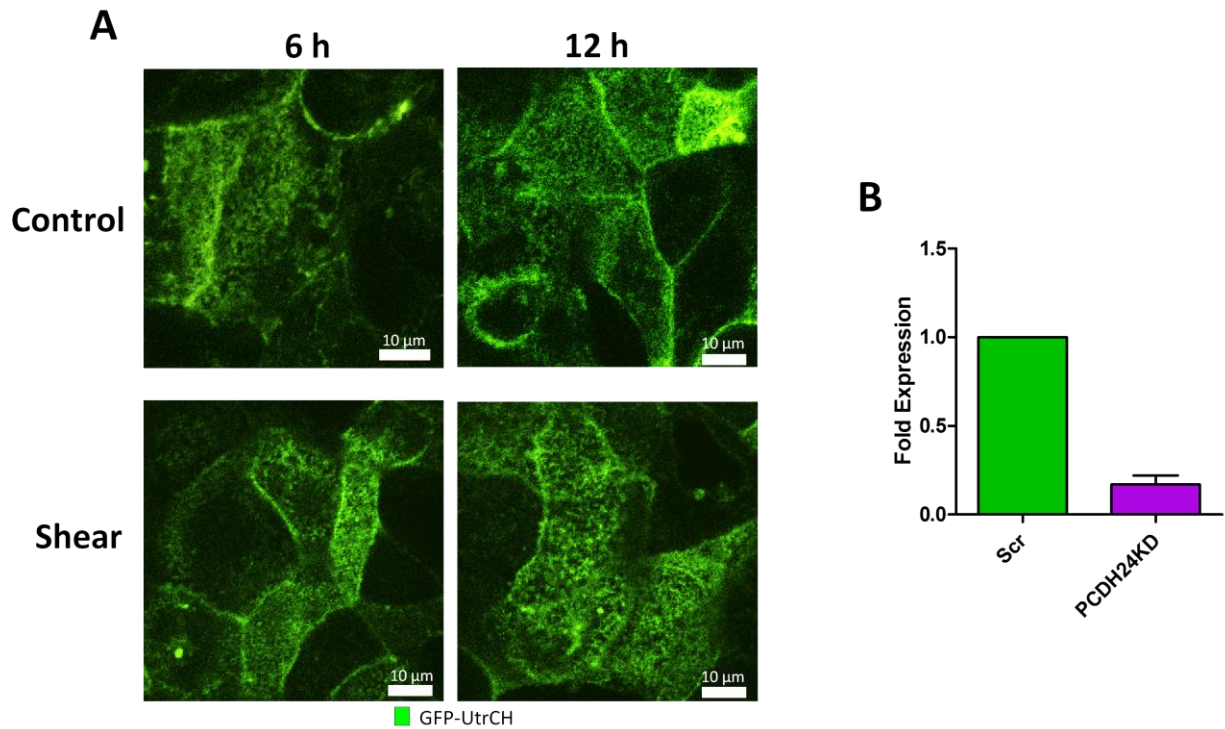


Figure 6.16 Shear does not affect microvilli formation. (A) Representative fluorescence images of cell monolayers transfected with GFP-UtrCH to visualize actin, including microvillar protrusions. Confocal image sections focused on the apical surfaces of cell monolayers exposed to shear stress or static control for the indicated times. Scale bars, 10  $\mu$ m. (B) Confirmation of PCDH24 knockdown by shRNA in Caco2<sub>BBE</sub> cells using real time RT-PCR. Fold changed compared to scramble control.

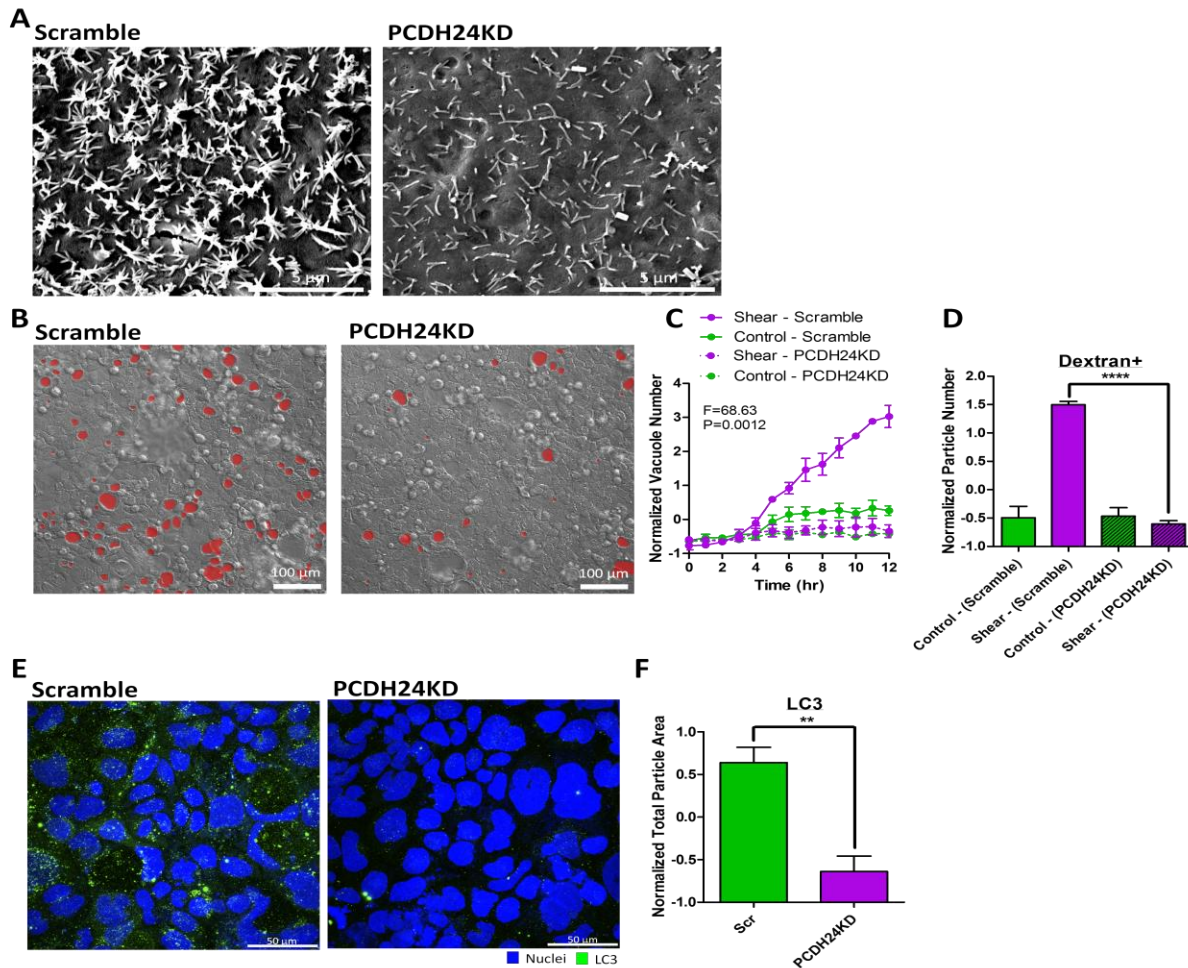
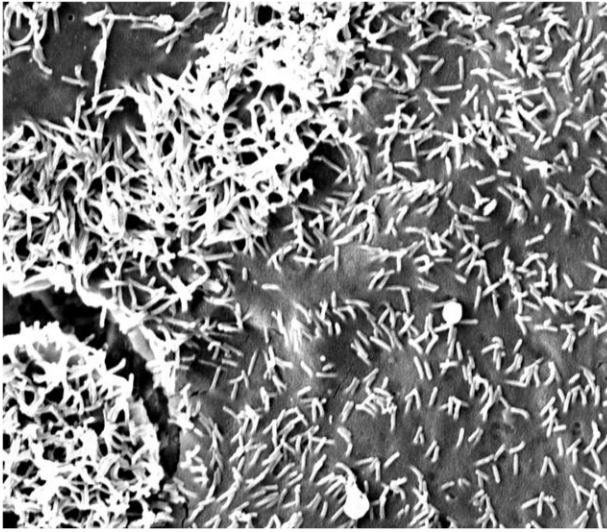


Figure 6.17 Perturbing microvilli by PCDH24 knockdown suppressed vacuole formation and autophagic trafficking. (A) Representative scanning electron micrographs of the apical surfaces of cell monolayers cultured overnight, comparing PCDH24 knockdown with scramble control. (B) Representative DIC images of shear-induced vacuole formation overnight, comparing PCDH24 knockdown with scramble control. (C) Quantification of vacuole number as a time course of shear stress or static control, comparing conditions outlined in B. Statistical analysis was done by 2-way ANOVA. (D) Quantification of the number of dextran-positive vacuoles resulting from overnight shear induction or static control, comparing conditions outlined in B. (E) Representative IF images (as a maximum Z-projection) of LC3 (green) expression induced by shear overnight, comparing PCDH24 knockdown with scramble control. (F) Quantification of LC3+ particles in E. Error bars represent SEM from  $n=3$  independent experiments. Data scales are derived from mean centering and variance scaling of each set of experiment.  $**P<0.01$ ,  $****P<0.0001$  by t-test. These results show a direct connection between mechanosensing of microvilli and parts of the autophagy machinery. Knockdown of the bundling protein, which lowers the bending stiffness, shown in Figure 5.3 to decrease the force on the membrane, results in both fewer vacuoles and less LC3 expression.

**Scramble**



**PCDH24KD**

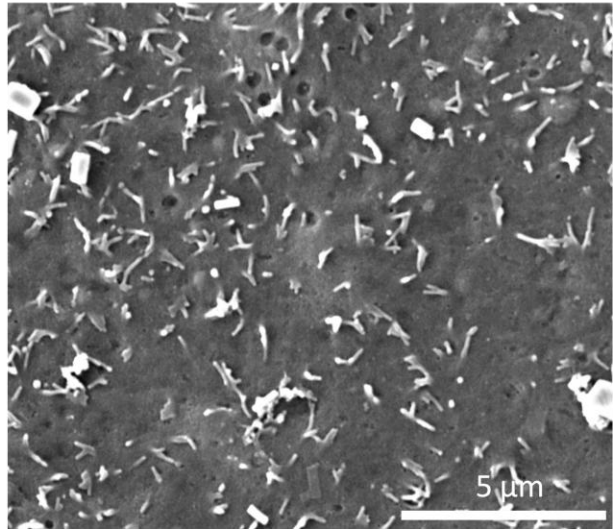
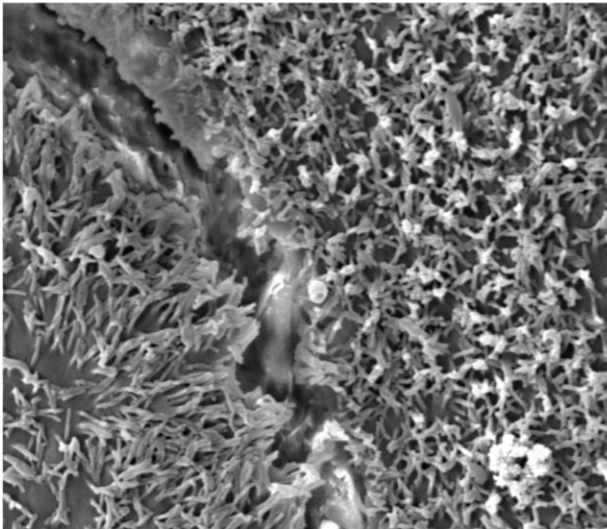
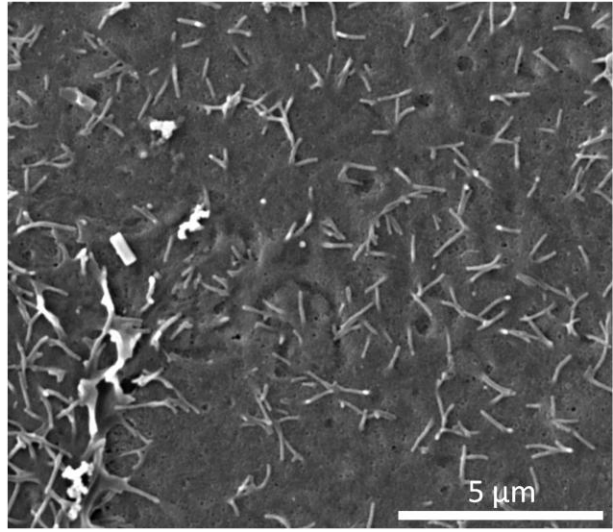


Figure 6.18 Knock down of PCDH24 perturbs microvilli formation. (A) Representative scanning electron micrographs of the apical surfaces of cell monolayers cultured overnight, comparing PCDH24 knockdown with scramble control. Scale bars, 5 μm. (B) Representative fluorescence images of cell monolayers transfected with GFP-UtrCH to visualize actin, including microvillar protrusions. Confocal image sections focused on the apical surfaces of cell monolayers cultured overnight, comparing PCDH24 knockdown with scramble control. Scale bars, 10 μm.

## 6.5 Discussion

In this study, we report that intestinal epithelial cell monolayers respond to apical shear stress by mechanosensitive microvillar protrusions. Unlike trophoblasts which respond to shear stress by forming microvilli<sup>322</sup>, our results suggest that epithelial monolayers use microvilli as a mechanosensor to induce intracellular vacuole formation via a non-canonical autophagic trafficking pathway. There is no evidence that shear stress increased endocytosis resulting from shear stress. Instead, shear-stress directs flux downstream of endocytosis into the autophagy pathway. Vacuole formation depends on central autophagy components such as LC3, and processes such as LAMP1+ lysosomal recruitment and fusion. Glycogen-containing granules are reduced by shear, consistent with studies reporting autophagy to be a central pathway for degrading glycogen stores, specifically in glycogen storage disease<sup>327,328</sup>. Taken together, we have uncovered a novel mechanism occurring in multicellular collectives, such as epithelial monolayers, that links mechanical forces to the autophagy machinery.

Although shear-induced vacuole formation shares components of the canonical autophagy pathway, our data suggests that it is actually a distinct process that is broadly classified as non-canonical autophagy. Canonical autophagy begins with phagopore formation, then maturation into autophagosomes, and ends with lysosomal fusion into autolysosomes that degrades vesicular contents<sup>329</sup>. Shear-induced vacuole formation does not end with autolysosomes that are observed as small puncta in the cell. Instead, previously uncharacterized, large vesicular structures with acidic pH are formed. These structures are distinct from swelled autolysosomes that form when downstream degradation is blocked<sup>330</sup>. Furthermore, we were not able to observe

organelles destined for degradation within vacuoles, which is characteristic of starvation-induced autophagy<sup>331</sup>. The distinctiveness of shear-induced vacuole formation from canonical autophagy is supported by the differences in CQ and BafA action, which are thought to inhibit the same autophagosome-lysosome fusion step<sup>332</sup>. In shear-induced vacuole formation, CQ inhibits a vesicular fusion step prior to vacuole formation, and BafA inhibits vacuole acidification and degradation. This mechanism is supported by larger, but less acidic vacuoles formed under BafA (Figure 6.14E-F and S9C-S9D). In turn, the accumulation of LC3 puncta caused by CQ blockage of vesicular fusion<sup>297,315-317</sup> is not observed in BafA treatment (Figure 6.14E), as flux into vacuoles is still permitted. Other LC3-dependent non-canonical autophagy pathways include LC3-associated phagocytosis resulting from immune signaling<sup>333-335</sup>, as well as entotic vacuolation<sup>336,337</sup>. Importantly, our observations in cilia-deficient but microvilli-rich intestinal epithelial cells are distinct from canonical autophagy triggered by shear forces acting on the primary cilia of kidney epithelial cells<sup>298</sup>.

The downstream mechanism by which microvilli transmit mechanical signals to autophagy components remains to be elucidated. However, unlike other protrusion-based mechanotransduction systems that trigger mechanically-gated calcium channels<sup>298,322,325,326,338</sup>, shear-induced vacuole formation is minimally affected by calcium changes. We speculate that actin-tubulin cytoskeletal cross-talk transmits apically-sensed signals to the intracellular autophagy pathway. Previous studies have demonstrated the dependency of autophagy on microtubule dynamics<sup>296,297,339</sup>, specifically tubulin acetylation that affects intracellular trafficking<sup>340,341</sup>. Cytoskeletal changes may trigger the initial recruitment and fusion of endomembrane vesicles, and

subsequent lipidation of LC3. The post-translational modification of microtubules may be a good place to start for finding a mechanistic link between F-actin-rich microvillar protrusions and vacuole formation induced by shear stress. In turn, other physical perturbations on the cytoskeleton such as tension may also induce autophagy components.

What could be the physiological relevance in shear-induced vacuole formation? The intestine is home to some 100 trillion microbes, and the apical microvilli of epithelial cells are the first line of defense against pathogens<sup>342</sup>. Engulfment and intracellular vacuolation resulting from insults to the microvilli may be a containment strategy for pathogens. An example of such containment strategy is toll-like receptor triggering of phagocytosis of microbes to be degraded by the autophagypathway<sup>334,343</sup>. As such, a significant number of autophagy genes are associated with inflammatory bowel disease<sup>284-292</sup>. Perhaps, the physical state of microvilli can serve as an additional cue for such a pathway. In addition to microbial defense, shear-induced vacuole formation may have a role in fetal and neonatal digestion. Although there is luminal motion in the adult gut, the adult mucosa is covered by mucus layers that somewhat shield epithelial microvilli<sup>344</sup>, and solid luminal contents may impose mechanical stress distinct from simple shear<sup>345</sup>. In contrast, vertebrate neonates maintain a liquid diet from milk, and their intestinal mucosa is immature, with sparse microvillar protrusions and minimal mucus, mimicking the state of Caco-2<sub>BBE</sub> monolayers<sup>346,347</sup>. Indeed, the Caco-2 line, when polarized, is known to resemble enterocytes at an immature/neonatal stage<sup>348</sup>. In neonates, dietary nutrients and immunoglobulins traverse the intestinal mucosa as macromolecules through pinocytosis of enterocytes, and are trafficked into intracellular

vacuoles<sup>349,350</sup>. Lysosomal proteases and  $\beta$ -galactosidase are highly expressed at these stages for digestion, and these enzymes are subsequently decreased further in development. The autophagy machinery may be one of the conduits of this digestive process. Bridging biological processes of microbial defense and digestion, dysregulated shear-induced autophagy in a premature gut may lead to malnutrition coupled to mucosal injury and abnormal microbial colonization, leading to devastating neonatal conditions such as necrotizing enterocolitis (NEC). Indeed, autophagy components are required for the development of NEC in both human and mouse models<sup>343</sup>. Here, we have uncovered a novel pathway by which autophagic flux can be regulated by mechanical stress, which may have significant consequences in understanding intestinal physiology and disease processes.

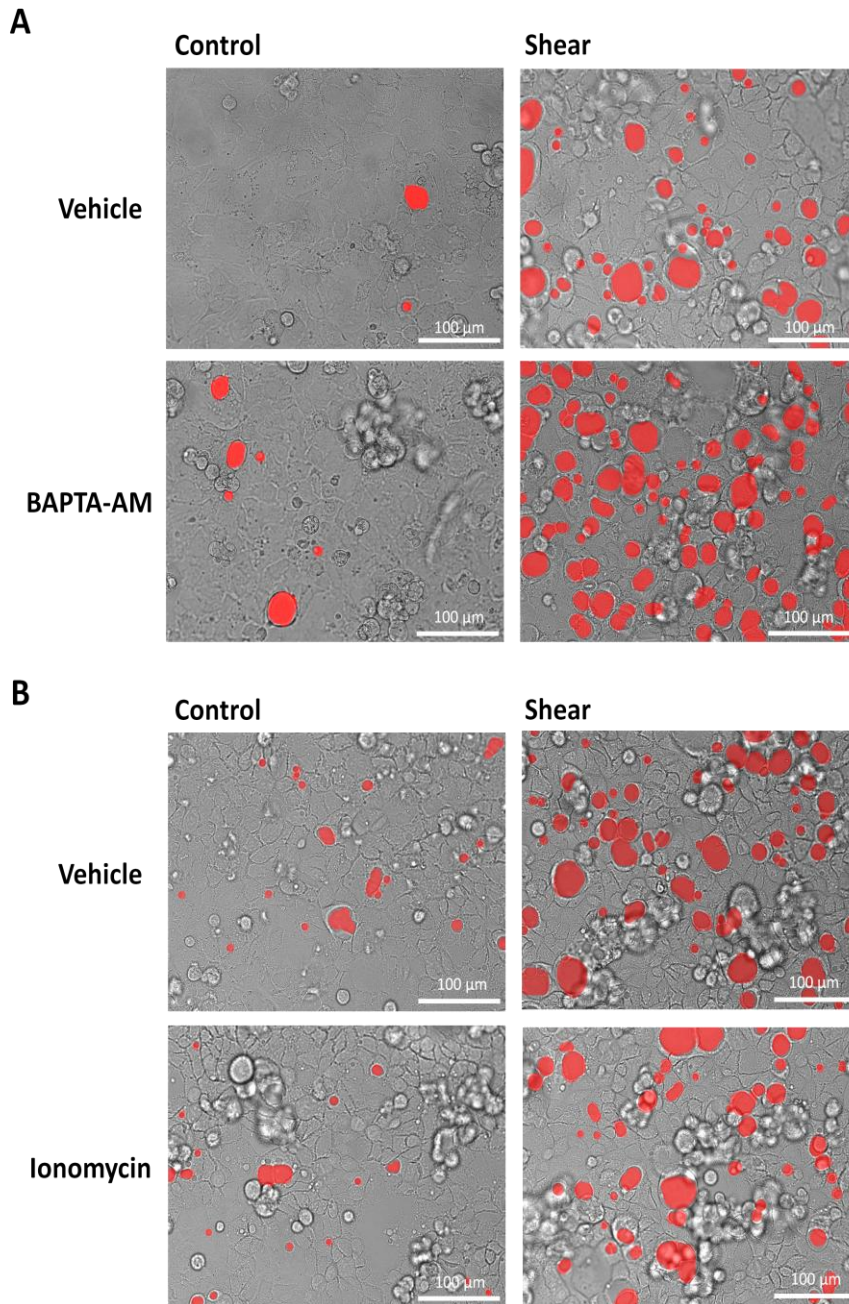


Figure 6.19 Shear-induced vacuole formation is not triggered by increased calcium flux. Representative DIC images of vacuole formation induced by overnight shear or static control, with media supplemented with vehicle or (A) 10  $\mu$ M BAPTA-AM or (B) 1  $\mu$ M ionomycin. Vacuoles are highlighted in red. Scale bars, 100  $\mu$ m.

## Chapter 7

### Future Work: Mechanosensing and Autophagy in the Gut

#### 7.1 Jamming in gut cells

Behavioral transitions within biological systems that arise from physical constraints have received treatment through analogy with phase transitions. Cells within a tissue features two such transitions, a jamming transition in which increases in density drive a shift from highly motile cells to a fairly static sheet, and a glass transition in which temperature increases have the opposite effect, driving the cells from a static state to a more motile state<sup>233</sup>. In each case, the dynamics arise from the energy of the collection of the cells in comparison to energy required to rearrange the sheet, which depends on the internal energy of each cell. A cell within a tissue has several factors contributing to its energy, which is outlined in Figure 7.1. Lisa Manning has developed a model of jamming for cells that can be described as such<sup>232</sup>. We outline this model herein.

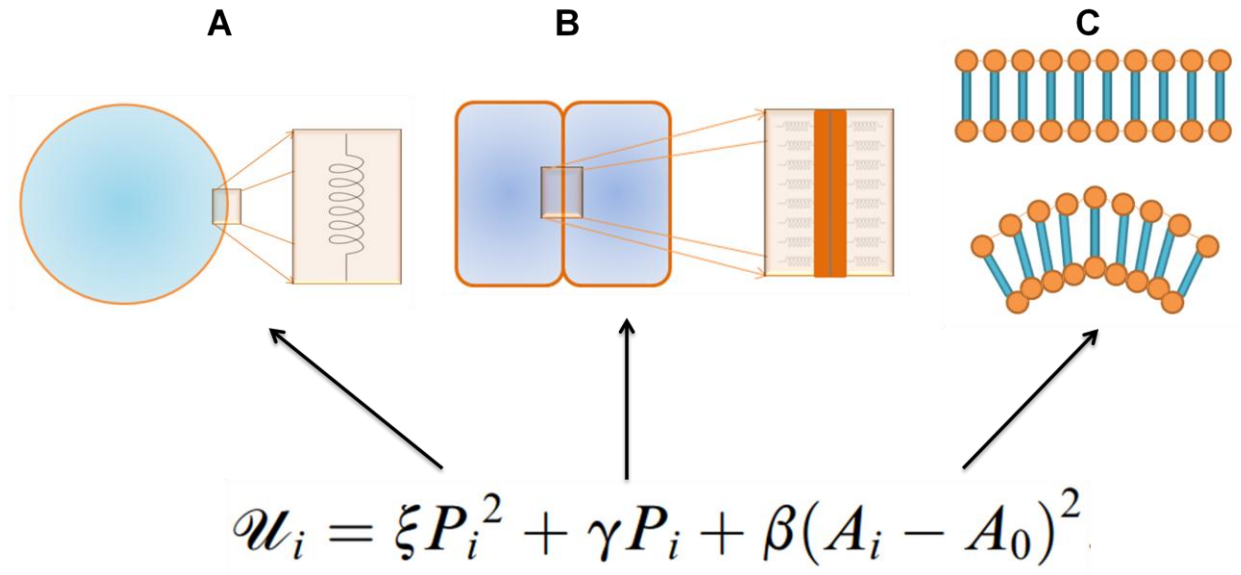


Figure 7.1 Cell energy components. A) The membrane of a cell contributes to the overall energy as a spring; a change in the perimeter results in a quadratic change in the energy. B) When cells are in contact with each other, the actin connected to the membrane acts like a spring perpendicular to the bilayer, which have some average energy stored within them. When confluent, the total perimeter of each cell contacts other cells so the number of these springs depends on the perimeter of the cell and a change in perimeter linearly changes the total energy from the springs. C) Local regions on cell membranes prefer to be flat to minimize energy, but as a whole the membrane has its lowest energy as a circle. Within a cell sheet the membranes of the cells fill all of the space, and a collection of non-overlapping circles cannot cover a region entirely so each cell is stretched in some way raising its energy. The energy in small regions of the membrane depends on the local curvature, and for minimal areas the mean curvature is zero and minimizes the energy. Increasing the mean curvature to fill the entire space in a confluent sheet increases the area and energy away from their minima. Together, these pieces use cell shape to define its energy. Equation from<sup>232</sup>.

The mechanical energy of a cell is:

$$U_i = \varepsilon P_i^2 + \gamma P_i + \beta(A_i - A_0)^2$$

With  $P$  and  $A$  the perimeter and area of the cell respectively and the subscripts  $i$  and  $0$  are the measured and optimal values respectively. The first term is a result of the spring-like membrane, which increases the energy of the cell when the perimeter is increased or stretched as a quadratic. The second term is due to the spring like actin bundles that pull inwards on the membrane, and whose number increases linearly with perimeter giving the linear dependence for this terms energy contribution. The last term is due to the difference between the internal and external walls of the cell membrane as the bilayer is bent. The optimal condition is for circular cells, but this rarely occurs in a tissue as a collection of circles does not have perfect packing density. Note that this energy equation is solely dependent on the shape of the cells. In order to move within the sheet, a cell needs to overcome the energy barrier due to its neighbors. The energy of the tissue in comparison to these energy barriers determines the frequency of cells escaping their well and finding a new optimal configuration with different neighbors. The tissue energy is controlled differently in jamming and glass transitions. In jamming, the cell density is the order parameter that determines the state of the system, and increasing the number of cells linearly increases the energy of the tissue because the total energy is the sum over all cells. Additionally the cells become more compact as the density increases which changes both the perimeter and area of the cells as polynomials. In glass transitions, temperature is typically the order parameter, though pressure can be used as well. These two directly control the energy of the sheet, and increasing either will cause an increase in shape fluctuation magnitude making sheet

rearrangements occur more frequently. Simple processes similar to jamming and glass transitions are classically described as an Arrhenius process:

$$R = \omega_0 e^{-\Delta U/\varepsilon}$$

With  $R$  the transition rate,  $\omega_0$  the escape attempt frequency,  $\Delta U$  is the energy potential separating two neighbor configurations, and  $\varepsilon = kb/T$  the scale of energy fluctuations. The average dwell time in a state is the inverse of the rate of rearrangement. The relationship between the energy of each cell and the fluctuation magnitude determines whether the dwell time function can be normalized; if dwell time is finite then the tissue is solid-like and if it is not finite then the tissue is fluid-like. Both jamming and glass transitions are more complicated than this due to intermediate states where collections of cells have correlated movement, but the concepts are similar.

Lisa Manning's experimental work with lung cells in asthmatic patients applied this phase transition framework to the study of development and disease. This work showed that the timing of the transition between unjammed and jammed states increased predicted whether a patient would develop asthma<sup>234</sup>. In asthmatic patients, the pressure on the cells is greater during early development of the lung, so pressure was varied on healthy cells to study these transitions. Cells from patients with and without asthma were collected and perpetuated. Particle image velocimetry (PIV) was used on phase contrast images to calculate the MSD and they found that increasing pressure on the cells increased migration persistence for both groups. The four point susceptibility was used to show that increased pressure decreased the lifetime of collective motion; the cells remained unjammed in high pressure. The size and lifetime

of the correlated regions are related to the neighbor rearrangement frequency, though the form of the relationship depends on the cellular energy distribution. With the distribution measured the experimental observations can be connected to the model to fit the parameters.

In our experiments, we see density dependant effects on the formation of vacuoles in response to shear stress. Below confluence, the cells don't show any response to shear stress but at confluence we see consistent production of vacuoles under shear. This suggests that there may be a jamming transition that occurs at high density. Additionally, the cells only form microvilli when they are confluent, which may affect the changes in internal energy of the cell due to shear stresses that bend them and subsequently transmit the force into the membrane. We also observe a change in migration speed under shear compared to static experiments. The effect of transmitting the force on the microvilli to the membrane could also play a role in a glass transition. To test these questions, we implemented a particle image velocimetry (PIV) algorithm to track cell movement within the sheet. We also borrowed a watershed algorithm, Seedwater Segmenter<sup>351</sup>, from David Mashburn in the Hutson lab to track the cell boundaries and calculate their energy, which connects the model of jamming directly to experiment by measuring the shape of each cell as it changes over time. The results of the two algorithms on our images are shown in Figures 7.2 and 7.3. Continuation of this approach could yield a phase transition description of the cells in response to shear stress at different densities. Such a framework may yield insight into the developmental transition or onset of disease as it has in lung cells.

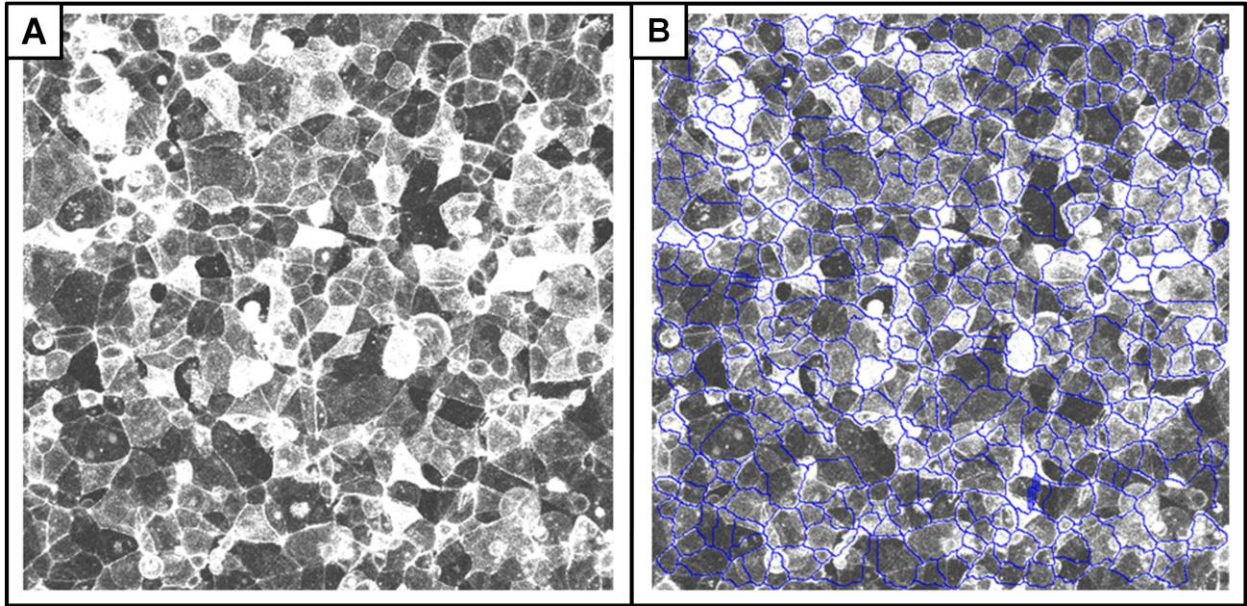


Figure 7.2 Identification of cell boundaries from fluorescent actin. A) Fluorescent images of CACO-2 cells are processed in Matlab to make the boundaries more apparent. B) The Seedwater Segmenter<sup>351</sup> is used to identify the boundaries of the cells, shown in blue. Both the preprocessing and the parameters of the segmenter need to be adjusted and improved to give more accurate boundaries. Accurate boundaries would allow direct connection of the shape based energy model and the observation of the jamming transition.

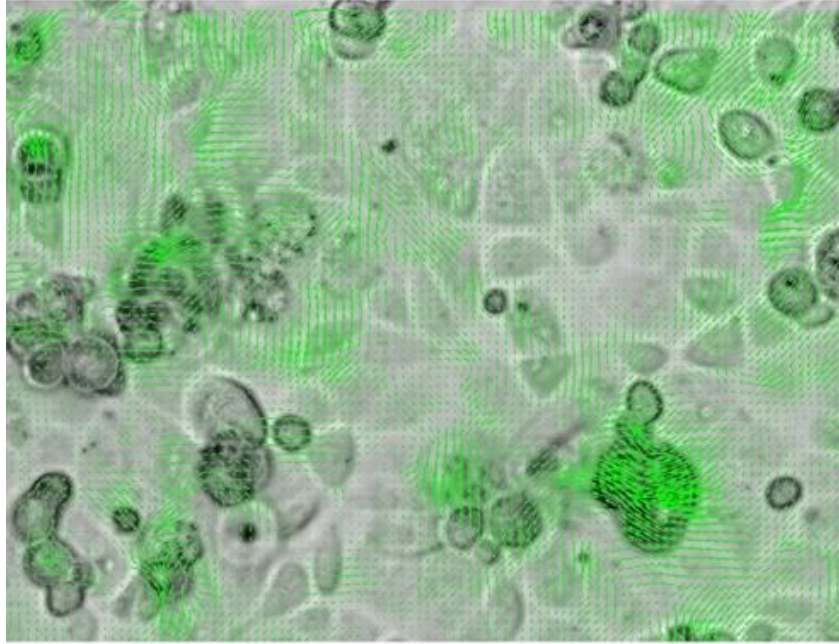


Figure 7.3 PIV analysis of CACO-2 cells under shear. Bright field images of CACO-2 cells were collected every 10 minutes and analyzed with particle image velocimetry. The magnitude of each vector represents the speed at which that region is moving. With this analysis, we can determine the size and lifetime of correlated regions to determine whether the cells are jammed or not. The analysis of the shape based energy from above can have its parameters fitted to match the correlated region size and time.

## Epilogue

We set out to study the dynamic relationship between cells and their environment. The developmental transition in *D. discoideum* in which the cells aggregate to become a multicellular organism is well studied, but the effects of receptor phosphorylation on chemotactic ability were not quantified. In our work, we used previous knowledge from literature about receptor number and phosphorylation changes over development to extend information theoretic models of chemical gradient transduction into directed motion. We found that the cells use receptor phosphorylation and number to change how they sample their environment and respond to different external chemical fields at different developmental time points. *D. discoideum's* chemotactic accuracy and ability to respond to dynamic signals was previously characterized at the beginning and end of the developmental transition. We furthered this study with imposed dynamic external chemical fields on the cells at several points in development, and found that the cells trade the ability to respond to rapid fluctuations for long term accuracy as development progresses. In the CACO-2 study, we explored the effects of shear stress on gut epithelial cells. This was an exploratory study where we found a novel mechanism to activate parts of the autophagy machinery. We found that the cells use their microvillar protrusions to sense shear stress. We showed that the cell altered fluid trafficking as a result of this stress and observed the creation of fluid filled vacuoles. We used a combination of targeted drugs, genetic manipulations, and fluorescent labels to show that the manufacture of the vacuoles included parts of the autophagy machinery and that shear stress is essential to trigger this response. We hope that mechanical sensing

will someday be as well studied and modeled as chemical sensing so that the information theoretic framework could be applied to epithelial cells' transduction networks in the same fashion as we applied it to *D. discoideum*.

## **Appendix I - Protocols**

### **1. Photolithography protocol**

Note: This is a modified protocol from Ron Reiserer and Dave Schaffer in Viibre (Vanderbilt University)

Materials:

- 1) SU-8 2XXX
- 2) Silicon wafer
- 3) Photolith mask
- 4) Blunt Syringe
- 5) NovaCure
- 6) IPA
- 7) SU-8 Developer
- 8) Edge Bead Remover
- 9) Crystallization dish
- 10) Rubylith tape
- 11) Dark Safety Glasses

Method:

- i. Turn on vacuum pump in changing area
- ii. Remove SU-8 2XXX from chemical cabinet
  - a. XXX is the expected height of the film in microns if spun at 3000 rpm
  - b. Turn on Novacure to let it heat up
- iii. Spin- coat
  - a. Remove dust from wafer with nitrogen
  - b. Make sure the spinner waste beaker is placed under the exhaust of the spinner – exhaust port is on the back of the spinner
  - c. Place wafer on center of spinner
    - i. Spin with hand to check if wafer is centered
  - d. Weigh SU-8
    - i. Write weight on excel sheet
  - e. Turn vacuum on, pour a 1.5 inch diameter circle of SU-8 on the center of the wafer
    - i. Have wipe ready to wipe bottle and catch excess resist
    - ii. Avoid getting SU-8 into threads of bottle
  - f. Weigh SU-8
    - i. Write weight on excel sheet
- iv. Program the spinner
  - a. Choose your program or select an existing one to modify

- b. Press F1 to enter program mode
- c. Press STEP to go between steps
  - i. 1<sup>st</sup> step: 10 seconds at 500 rpm (acl 5)
  - ii. 2<sup>nd</sup> step: 30 seconds at 3000 rpm (acl 10)
  - iii. I follow this exactly for SU8-2XXX to make XXXum features
  - iv. Spinning at higher rpm will create thinner layer
- d. Run the spinner
- v. Edge Bead Removal
  - a. Find a program where you can spin at 2000 rpm for 10 minutes
  - b. Fill blunt syringe with EBR
  - c. Spin wafer
  - d. Spraying a constant stream, dissolve the SU-8 around the outer edge of the wafer
    - i. Remove up to 1mm from edge
    - ii. Avoid spraying EBR on the center of the wafer
  - e. Stop spinning
    - i. Repeat c if there is still SU-8 at edge
    - ii. If bare, turn off vacuum and remove wafer
- vi. Soft Bake
  - a. Place wafer on hotplate
  - b. Let hotplate ramp itself to 95° C – sit for 5-20min (depends on SU-8, look at data sheet)
  - c. Let cool down to 40° C
  - d. Clean the spinner with a beta wipe while waiting
  - e. Remove wafer after bake and let it cool on beta wipe
- vii. Exposure
  - a. Enter program into Novacure
  - b. Select SET-UP
  - c. Enter password (1111)
  - d. Select EXPOSURE
  - e. Select DOSE and enter value
    - i. See table for value
    - ii. Remember 231 times what it says on data sheet
    - iii. 95000 for 100um thick features
  - f. Min Time - press OK
  - g. Max Time - press OK
  - h. Remove light guide and attach to stand
  - i. PUT ON SAFETY GLASSES
  - j. Run the program to be sure light hits in the 3 inch circle
    - i. Adjust height of stand if needed

- k. Dust off photomask with nitrogen – maybe clean with IPA
  - l. Place wafer on circle with mask on top—emulsion side down (brown/metal side down)
  - m. Adjust mask so that any bad spots on the wafer are covered by opaque regions of the mask – won't be exposed
  - n. Cover unused areas with Rubylith tape
  - o. \*Wear safety glasses\* Run the program using foot pedal.
  - p. Return the NovaCure light guide to the radiometer port on the NovaCure box.
- viii. Post-Exposure Bake
- a. Remove mask and place wafer on hotplate
  - b. For 100um features, set the hotplate to ramp at 2°/min (120°/hour)
  - c. Otherwise, set to 3°/min (180°/ hour)
  - d. Calculate how long it takes to reach 95° C
    - i. Add bake time from data sheet table
  - e. Set timer to total time
  - f. Set temperature to 95°
  - g. Select auto off
    - i. This turns off heat when the timer finishes
  - h. Wait until timer runs out and plate cools to 40° C
  - i. Remove wafer and let cool
- ix. Development
- a. Immersion
    - i. Pour developer into crystallization dish to cover wafer
    - ii. Swirl dish until all uncured SU-8 is removed
      - 1. This can take ~20-30 minutes for SU-8 > 50um thick SU-8
    - iii. Rinse device with IPA, dry with nitrogen
  - b. Spray: conducted in the spinner
    - i. Spray developer onto wafer, wait 30 seconds, spin off
    - ii. Repeat 4-5 times
    - iii. Wash with IPA while spinning, wait for it to dry
    - iv. Check for undeveloped SU-8
      - 1. Repeat i and iii if there is any white film on wafer or near features.
- x. Hard Bake
- a. Place device on hotplate
  - b. Set ramp to 2°/min (120°/hour)
  - c. Calculate how long it takes to reach 180° C
    - i. Add 20 minutes
  - d. Set timer to total time

- e. Set temperature to 180°
- f. Select auto off
- g. Cover device with upside-down glass crystallization dish
  - i. Have edge of dish over the edge of the hotplate so air can escape
- h. Label glass slide with name, date, and contact info and set it on or in front of hotplate
- xi. CLEAN UP
  - a. Clean spinner with acetone and IPA with beta wipes
    - i. dispose of beta wipes in hood
  - b. Put spinner waste/developer waste into waste container under bench labeled "Organic Wastes Only"
  - c. Check that exposure lamp is off and light guide is in radiometer port – don't turn off NovaCure if someone is coming in after you
  - d. Close nitrogen gas valves
  - e. Turn off vacuum pump in the entry to the clean room
- xii. Retrieve wafer when complete
  - a. Silinize wafer

## References

SyBBURE – "Module 1- Fundamentals of SU-8 Photolithography"

MicroChem- "SU-8 2000 Permanent Epoxy Negative Photoresist PROCESSING GUIDELINES FOR:

SU-8 2000.5, SU-8 2002, SU-8 2005, SU-8 2007, SU-8 2010 and SU-8 2015"

## 2. Silinization protocol

Materials:

- 1) Wafer from photolithography
  - 2) Trimethylsilane or similar
  - 3) Transfer pipette
  - 4) Glove box
  - 5) Plastic apparatus to hold wafer
  - 6) Microscope slide
  - 7) Dessicator
  - 8) Vacuum pump
- 
- i. Tape back of wafer to plastic holder
  - ii. Load wafer and transfer pipette into glove box
  - iii. Place microscope slide in dessicator
  - iv. Place 3 drops of silane onto glass slide
  - v. Place plastic apparatus in dessicator
    - a. Wafer features down
  - vi. Vacuum air out of dessicator
  - vii. Leave over night
  - viii. Remove wafer
  - ix. Wash with ethanol

### **3. PDMS pouring protocol**

PDMS pouring protocol

Materials:

- 1) Silinized wafer
- 2) Aluminum foil
- 3) 3in Petri dish
- 4) Razor blade
- 5) PDMS base and curing agent
- 6) Mixer
- 7) Scale
- 8) Dixie cup
- 9) 60° level oven
- 10) Dessicator and vacuum pump

Method:

- i. Cut aluminum foil circle using the lid of a 3in Petri dish as a guide
- ii. Place wafer in center of foil circle
- iii. Fold the edges of the circle around the wafer to form vertical edges
- iv. Crimp the foil so it will hold fluid over the wafer
- v. Place each wafer in petri dish
- vi. Weigh out 15 grams of PDMS base for each wafer to be filled in a Dixie cup
- vii. Add 1.5 grams of curing agent per wafer (10:1 base to curing agent)
- viii. Mix in the thinky mixer for 1 minute
- ix. Pour ~15 grams mixed PDMS into each wafer
- x. Stack wafers in dessicator and degass for 30 minutes
- xi. Refill dessicator slowly
- xii. Remove wafers
- xiii. Place in 60° oven for 3-4 hours (can be longer)
- xiv. PDMS will not be sticky at all when cured

#### **4. Plasma Sealing Protocol**

##### Materials:

- 1) PDMS Sheet
- 2) Razer blade
- 3) Hole punch
- 4) Scotch tape
- 5) Glass slide
- 6) 60°C Oven
- 7) Tweezers

##### Method:

- i. Remove PDMS from silicon wafer
- ii. Cut out PDMS chambers
- iii. Punch holes from the bottom, featured side
- iv. Clean both top and bottom of PDMS with scotch tape
- v. Cover microscope slide with scotch tape to prevent accidental bonding
- vi. Clean cover slip with methanol and alpha wipe and let dry
- vii. Place cover slip and PDMS chamber on tape-covered microscope slide feature side up
- viii. Place in plasma sealer and close door and air valve
- ix. Turn on vacuum and power
- x. Wait until plasma sparks then adjust air valve so that the plasma is bright pink
- xi. Leave in pink plasma for 30-60 seconds
- xii. Turn off vacuum and power
- xiii. Open air valve to let out air over ~10 seconds
- xiv. Use tweezers to pick up and flip PDMS chamber and put into contact with cover slip
- xv. Bake in 60°C oven for 3 minutes
- xvi. Remove and fill with water or buffer
- xvii. Chamber will remain hydrophilic for up to 2 weeks

## **5. Freezing and Defrosting cells Protocol**

### Materials:

- 1) Cryogenic freezing tubes
- 2) HL-5
- 3) Dicty Cells
- 4) Fetal Bovine Serum
- 5) DMSO
- 6) Dicty Incubator

### 1) Freezing Cells

- i) Grow cells in flask
- ii) Prepare freezing solution
  - (a) HL-5 with 25% fetal bovine serum, 10%DMSO
- iii) Resuspend cells in freezing solution at 5E7cell/ml
- iv) Pipette 1ml aliquots into cryogenic freezing tubes
- v) Label and place in -80°C freezer on 8<sup>th</sup> floor

### 2) Defrosting Cells

- i) Remove cells from -80°C freezer on 8<sup>th</sup> floor
- ii) Warm to room temperature
- iii) In tall Petri dish, pipette 12ml of HL-5 with appropriate antibodies
- iv) Pipette Cells into Petri Dish
- v) Label with date and put in dicty incubator
- vi) Ready to harvest in 2-3 days

## **6. Axenic Growth Protocol**

### 1) Growing Cells in Petri dish

- i. Defrost cells
- ii. Pipette contents of cell aliquot into Petri dish
- iii. Add 13ul of HL5 with appropriate antibodies
- iv. Ready to harvest in 2-3 days

### 2) Growing cells in flask

- i. Shake Petri dish with cells to suspend dead cells by sliding on surface – not in a circle
- ii. Remove all HL5 and discard
- iii. Pipette 12 ml of HL5 over the cells several times, rotating dish 30° between washes
- iv. Remove all HL5/cells with pipette then replace ~.5ml of the cell solution
- v. Pipette rest of cell solution into 125ml flask
- vi. Add 35ul of HL5 + antibodies to flask
- vii. Place on orbital shaker in Dicty incubator
- viii. Cells grown in ~2 days

### 3) Diluting cells

- i. Remove 35 ml from flask
- ii. Add 35 ml of HL5 +antibodies to flask

## 7. Development Protocol

- i. Find Cell concentration in flask
  - a. Count on hemocytometer
  - b. Cell Concentration =  $\text{Sum 5 squares} * 50,000$  (cells/ml)
- ii. Development volume =  $5E7(\text{cells}) / \text{Cell Concentration (cells/ml)}$
- iii. Pipette Development Volume of cell solution into 50ml conical tube
- iv. Centrifuge Cells at 1500rpm, acceleration 9, 20°C for 5 minutes
- v. Remove supernatant and resuspend cells in 50ml Development Buffer (DB)  
\*\*\*\*Development Clock Starts\*\*\*\*
- vi. Centrifuge Cells at 1500rpm, acceleration 9, 20°C for 5 minutes
- vii. Resuspend cells in 5ml DB
- viii. Pipette all solution into 50ml flask
- ix. Place flask on orbital shaker in Dicty incubator
- x. Wait 1 hour from when the flask goes onto shaker <not synced with development clock
- xi. While waiting make cAMP solution by putting 2ul .1M cAMP aliquot into 50ml DB
- xii. Begin pulsing after 1 hour wait
- xiii. Use Dicty pump to drop cAMP into cell solution every 6 minutes
  - a. Wait for 5:55 minutes, flow for 0:05 minutes
  - b. 3 rpm

## 8. Gradient Switching Experiment Protocol

### Dicty Gradient Switching Protocol

#### Materials:

- 1) .1mM cAMP Gradient Solution
  - 2) 10kD dextran dye
  - 3) 70kD dextran dye
  - 4) 2x Viibre pumps
  - 5) LabSmith 4 port valve
  - 6) Tygon tubing
  - 7) Peek tubing
  - 8) Tygon to peek micro fluidic adapter
  - 9) Zeiss epifluorescent microscope
  - 10) Dicty mutants (Chris)
  - 11) 2x Thumb tack
  - 12) Silinized gradient wafer
  - 13) Development pump
  - 14) Centrifuge
  - 15) Orbital Shaker
  - 16) Incubator
  - 17) 50ml conical tubes
  - 18) Eppendorf tubes
  - 19) Lab-Tek Cell Culture Chamber
- 
- i. Perform Axenic Growth of Dicty cells in 125ml flask
  - ii. Punch Peek tubing holes in top, bottom, and center (2x) inlets of 4 Gradient Chambers with blue punch
  - iii. Punch Tygon tubing hole in outlet of 4 Gradient Chambers with pink punch
  - iv. Plasma Seal 4 Gradient Chambers to cell Lab-Tek Cell Culture Chamber
  - v. Fill Gradient Chambers with Development Buffer (DB) after sealing
  - vi. Prepare Gradient Solutions
  - vii. Assemble Gradient Pumps and Valve
- 
- viii. Calibrate Viibre pumps
    - i. Fill inlet and outlet tubes with fluid then attach to pump inserts
      - a. DO NOT PULL OR PUSH THROUGH PUMP
    - ii. Connect valve outlet tubes to fluid collection reservoirs
    - iii. Run pump at 25 rpm for 30 minutes

- iv. Multiply outlet fluid volume by 2 and divide by 25 to find ul/hour/rpm
- v. Connect valve outlets to gradient chamber
- vi. Connect waste reservoir to chamber
- vii. Insert thumb tacks
- viii. Observe gradient under microscope and adjust flow rates
- ix. Stop flow.

- ix. Begin Dicty Development protocol
- x. Connect 2 Viibre pumps to control box
- xi. Connect power cable , then USB cable from controller computer to Viibre pump control box
- xii. Open Ampere
- xiii. Connect power cable and usb cable from controller computer to LabSmith control box
- xiv. Connect LabSmith control box to Labsmith breadboard
- xv. Open LabSmith software

\*\*\*\*\*Refine Pump Speed\*\*\*\*\*

- xvi. Attach Tygon outlet with waste reservoir to Gradient Chamber
- xvii. Attach Peek inlet tubes to Gradient Chamber
- xviii. Plug Gradient Chamber center inlets with thumb tacks
- xix. Run Viibre pump at 1rpm <<<<change to ul/hour
- xx. Watch gradient develop using GFP and AF568 fluorescent channels on Epi Scope through eyepiece
- xxi. Adjust pump flow so that the gradient is centered
- xxii. Stop pumps
- xxiii. Remove thumb tacks and fill center chamber with DB
- xxiv. Take 200ul of cell solution and dilute to 3E6cells/ml (~60 cells in hemocytometer)
- xxv. Add cells to middle chamber
- xxvi. Replace thumb tacks
- xxvii. Begin Viibre pumps at .1rpm
- xxviii. Repeat 16-27 so that Cells are added at 3:00, 4:30, 6:00, and 7:30 hours development time

\*\*\*\*\* Refine Pump Speed \*\*\*\*\*

- xxix. Image Cells and Gradient switch
  - i. Every 30 seconds take 20x
    - a. Bright field (250ms)
    - b. AF568 (15ms)
    - c. GFP (10ms)
  - ii. Switch Lab Smith Valve orientation 5 minutes into image acquisition

- iii. Stop acquisition after 70 minutes
  - a. 20 minutes till next time point to Refine Pump Speed

#### Calibrate Viibre pumps notes

The following steps must be performed in order: Connect two Viibre pumps to the pump controller box. Connect the power cable to the pump controller box. Connect the usb cable to the pump controller box. Open ampere using the rainbow triangle icon on the taskbar of the controlling computer. Click on controllers then manage controllers. In the pop up screen select the Quad pump and click on add controller, then click yes when prompted to add a timer and ok to confirm.

Make inlet reservoirs for each pump (2) and a waste reservoir (1) with an eppendorf tube and a 4 inch long piece of Tygon tubing by creating a hole in the top of the eppendorf tube large enough for the Tygon tubing and insert the tubing. Fill the reservoir with DI water. Connect the free end of the Tygon tubing to the inlet of the Viibre pump (can be either hole). Run the pump at full speed in the direction that draws fluid from the reservoir by clicking on the play button in ampere and dragging the slider for each pump to either the top or bottom. Remember which direction each pump needs to go to move fluid from the inlet to the outlet. Once the tube and pdms pump insert are full, water will begin to exit the outlet hole. At this time stop the pump. Cut a two foot piece of Tygon tubing for each pump. Fill each tube with one of the Gradient Solutions by inserting a syringe needle into one end and submersing the other end in the gradient solution, pulling the plunger to fill. With the syringe still in the tube, connect the opposite end to the outlet of the Viibre pump. Remove the syringe and slide the Tygon-to-peek adapter piece on to the Tygon tube and screw it into the adapter that is

connected to the valve inlet tube. Once both tubes are connected run the pumps at full speed to fill all of the peek tubing. Once several drops of fluid have emerged from the valve outlet tubes, stop the pump. Connect the valve outlet tubes to fluid collection reservoirs and run the pumps at 25rpm for 30 minutes then stop the flow. Measure the fluid in the collection reservoirs, multiply by two and divide by 25 to find the flow rate in  $\mu\text{l}/\text{hour}/\text{rpm}$ .

Connect to the peek tubing to the gradient chamber. Insert the waste reservoir tube into the gradient chamber and insert the thumb tacks into the center inlet holes. Insert the well chamber into the well chamber insert on the microscope stage. Begin pumping fluid through the chamber at  $60\mu\text{l}/\text{hour}$  (use rate found above to convert rpm to  $\mu\text{l}/\text{hour}$ ). Observe the gradient under the microscope using the GFP and Alexa568 filters to view each fluid. Adjust the flow rate so that the gradients cross in the middle of the chamber.

#### Seal gradient chambers to glass notes

Carefully remove the pdms from the silicon wafer. Cut out the intermediate sized chambers (middle column). Lay the chambers on a pdms sheet so that the punched only touch pdms (no hard surfaces). Punch the holes from the side of the pdms that was against the silicon wafer, feature side up. Use the peek tubing punch to make holes in the top, bottom, and center inlets (4 total) and the pink Tygon punch to make a hole in the outlet. Cover both sides of each chamber with scotch tape to clean off dust. Place a cover slip and three chambers feature side up on a microscope slide that is covered in scotch tape. Place slide in the center of the plasma cleaner, set the power to high and turn on the vacuum and power switches. Wait for the plasma cleaner to emit

light (~30 second wait) then use the valve on the door of the plasma cleaner to adjust the airflow, making the plasma as pink as possible. Once at the correct color, wait for 45 seconds then switch off the power and vacuum and open the air valve to allow gas back into the chamber. Once the door can be opened, remove the slide and flip each chamber onto the cover slip so that the treated sides are in contact. Place in 60° oven for ~3minutes to strengthen the bond, and then fill each chamber with DB, starting with the center inlets then the top and bottom inlets. Once filled with DB the chambers will last several days.

## References

1. Reymond, C. D., Gomer, R. H., Mehdy, M. C. & Firtel, R. A. Developmental regulation of a dictyostelium gene encoding a protein homologous to mammalian ras protein. *Cell* **39**, 141–148 (1984).
2. Wallet, V. *et al.* Dictyostelium Nucleoside Diphosphate Kinase Highly Homologous to Nm23 and Awd Proteins Involved in Mammalian Tumor Metastasis and Drosophila Development. *J. Natl. Cancer Inst.* **82**, 1199–1202 (1990).
3. Swigart, P., Insall, R., Wilkins, A. & Cockcroft, S. Purification and cloning of phosphatidylinositol transfer proteins from Dictyostelium discoideum: homologues of both mammalian PITPs and Saccharomyces cerevisiae Sec14p are found in the same cell. *Biochem. J.* **347**, 837–843 (2000).
4. Eichinger, L. *et al.* The genome of the social amoeba Dictyostelium discoideum. *Nature* **435**, 43–57 (2005).
5. Gaudet, P., Pilcher, K. E., Fey, P. & Chisholm, R. L. Transformation of Dictyostelium discoideum with plasmid DNA. *Nat. Protoc.* **2**, 1317–1324 (2007).
6. Mohamed, W., Ray, S., Brazill, D. & Baskar, R. Absence of catalytic domain in a putative protein kinase C (PkcA) suppresses tip dominance in Dictyostelium discoideum. *Dev. Biol.* **405**, 10–20 (2015).
7. Long, Y., Abad, M. G., Olson, E. D., Carrillo, E. Y. & Jackman, J. E. Identification of distinct biological functions for four 3'-5' RNA polymerases. *Nucleic Acids Res.* gkw681 (2016). doi:10.1093/nar/gkw681
8. Xue, D. M. & Hou, L. S. Shortening of the cell cycle and developmental interruption in a Dictyostelium discoideum cell line due to RNAi-silenced expression of allantoicase. *Genet. Mol. Res. GMR* **11**, 1923–1933 (2012).
9. Chen, C.-L., Wang, Y., Sesaki, H. & Iijima, M. Myosin I Links PIP3 Signaling to Remodeling of the Actin Cytoskeleton in Chemotaxis. *Sci Signal* **5**, ra10–ra10 (2012).
10. Plak, K., Keizer-Gunnink, I., Haastert, P. J. M. van & Kortholt, A. Rap1-dependent pathways coordinate cytokinesis in Dictyostelium. *Mol. Biol. Cell* **25**, 4195–4204 (2014).
11. Meier, D. *et al.* Analysis of the Microprocessor in Dictyostelium: The Role of RbdB, a dsRNA Binding Protein. *PLOS Genet* **12**, e1006057 (2016).
12. Merlot, S. & Firtel, R. A. Leading the way: directional sensing through phosphatidylinositol 3-kinase and other signaling pathways. *J. Cell Sci.* **116**, 3471–3478 (2003).

13. Willard, S. S. & Devreotes, P. N. Signaling pathways mediating chemotaxis in the social amoeba, *Dictyostelium discoideum*. *Eur. J. Cell Biol.* **85**, 897–904 (2006).
14. Rupper, A. & Cardelli, J. Regulation of phagocytosis and endo-phagosomal trafficking pathways in *Dictyostelium discoideum*. *Biochim. Biophys. Acta BBA - Gen. Subj.* **1525**, 205–216 (2001).
15. Levchenko, A. & Iglesias, P. A. Models of Eukaryotic Gradient Sensing: Application to Chemotaxis of Amoebae and Neutrophils. *Biophys. J.* **82**, 50–63 (2002).
16. Friedl, P., Borgmann, S. & Bröcker, E.-B. Amoeboid leukocyte crawling through extracellular matrix: lessons from the *Dictyostelium* paradigm of cell movement. *J. Leukoc. Biol.* **70**, 491–509 (2001).
17. Chen, X.-F., Zhang, Y., Xu, H. & Bu, G. Transcriptional regulation and its misregulation in Alzheimer's disease. *Mol. Brain* **6**, 44 (2013).
18. Lee, T. I. & Young, R. A. Transcriptional Regulation and Its Misregulation in Disease. *Cell* **152**, 1237–1251 (2013).
19. Gross, J. D., Bradbury, J., Kay, R. R. & Peacey, M. J. Intracellular pH and the control of cell differentiation in *Dictyostelium discoideum*. *Nature* **303**, 244–245 (1983).
20. Gerisch, G. in *Current Topics in Developmental Biology* (ed. Monroy, A. A. M. and A.) **3**, 157–197 (Academic Press, 1968).
21. Kawata, T. *et al.* SH2 Signaling in a Lower Eukaryote: A STAT Protein That Regulates Stalk Cell Differentiation in *Dictyostelium*. *Cell* **89**, 909–916 (1997).
22. Hohl, H. R. & Hamamoto, S. T. Ultrastructure of spore differentiation in *Dictyostelium*: the prespore vacuole. *J. Ultrastruct. Res.* **26**, 442–453 (1969).
23. Siegert, F. & Weijer, C. J. Spiral and concentric waves organize multicellular *Dictyostelium* mounds. *Curr. Biol.* **5**, 937–943 (1995).
24. Matsukuma, S. & Durston, A. J. Chemotactic cell sorting in *Dictyostelium discoideum*. *Development* **50**, 243–251 (1979).
25. Williams, J. G. *et al.* Origins of the prestalk-prespore pattern in *Dictyostelium* development. *Cell* **59**, 1157–1163 (1989).
26. Chisholm, R. L. & Firtel, R. A. Insights into morphogenesis from a simple developmental system. *Nat. Rev. Mol. Cell Biol.* **5**, 531–541 (2004).
27. wimsweden. *Altruistic, self-sacrificing amoebae that fight cheaters a challenge for Francis Collins.*

28. Shaffer, B. M. Aspects of Aggregation in Cellular Slime Moulds 1. Orientation and Chemotaxis. *Am. Nat.* **91**, 19–35 (1957).
29. Bonner, J. T. A Descriptive Study of the Development of the Slime Mold *Dictyostelium discoideum*. *Am. J. Bot.* **31**, 175–182 (1944).
30. Konijn, T. M., Barkley, D. S., Chang, Y. Y. & Bonner, J. T. Cyclic Amp: A Naturally Occurring Acrasin in the Cellular Slime Molds. *Am. Nat.* **102**, 225–233 (1968).
31. Bonner, J. T. *et al.* Acrasin, acrasinase, and the sensitivity to acrasin in *Dictyostelium discoideum*. *Dev. Biol.* **20**, 72–87 (1969).
32. Tomchik, K. J. & Devreotes, P. N. Adenosine 3',5'-monophosphate waves in *Dictyostelium discoideum*: a demonstration by isotope dilution--fluorography. *Science* **212**, 443–446 (1981).
33. Bonner, J. T. Evidence for the formation of cell aggregates by chemotaxis in the development of the slime mold *Dictyostelium discoideum*. *J. Exp. Zool.* **106**, 1–26 (1947).
34. Shaffer, B. M. Acrasin, the Chemotactic Agent in Cellular Slime Moulds. *J. Exp. Biol.* **33**, 645–657 (1956).
35. Shaffer, B. M. Integration in Aggregating Cellular Slime Moulds. *Q. J. Microsc. Sci.* **s3-99**, 103–121 (1958).
36. Shaffer, B. M. Properties of Slime-Mould Amoebae of Significance for Aggregation. *Q. J. Microsc. Sci.* **s3-98**, 377–392 (1957).
37. Cyclic 3',5'-AMP relay in *Dictyostelium discoideum* III. The relationship of cAMP synthesis and secretion during the cAMP signaling response. *J. Cell Biol.* **86**, 537–544 (1980).
38. Alcantara, F. & Monk, M. Signal Propagation during Aggregation in the Slime Mould *Dictyostelium discoideum*. *J. Gen. Microbiol.* **85**, 321–334 (1974).
39. Devreotes, P. N., Derstine, P. L. & Steck, T. L. Cyclic 3',5' AMP relay in *Dictyostelium discoideum*. I. A technique to monitor responses to controlled stimuli. *J. Cell Biol.* **80**, 291–299 (1979).
40. Gerisch, G. & Hess, B. Cyclic-AMP-Controlled Oscillations in Suspended *Dictyostelium* Cells: Their Relation to Morphogenetic Cell Interactions. *Proc. Natl. Acad. Sci.* **71**, 2118–2122 (1974).
41. McCann, C. P., Kriebel, P. W., Parent, C. A. & Losert, W. Cell speed, persistence and information transmission during signal relay and collective migration. *J. Cell Sci.* **123**, 1724–1731 (2010).

42. Devreotes, P. N. & Steck, T. L. Cyclic 3',5' AMP relay in *Dictyostelium discoideum*. II. Requirements for the initiation and termination of the response. *J. Cell Biol.* **80**, 300–309 (1979).
43. Durston, A. J. Pacemaker activity during aggregation in *Dictyostelium discoideum*. *Dev. Biol.* **37**, 225–235 (1974).
44. Shaffer, B. M. Secretion of cyclic AMP induced by cyclic AMP in the cellular slime mould *Dictyostelium discoideum*. *Nature* **255**, 549–552 (1975).
45. Kim, J., Heslop-Harrison, P., Postlethwaite, I. & Bates, D. G. Stochastic Noise and Synchronisation during *Dictyostelium* Aggregation Make cAMP Oscillations Robust. *PLOS Comput Biol* **3**, e218 (2007).
46. Loomis, W. F. Cell signaling during development of *Dictyostelium*. *Dev. Biol.* **391**, 1–16 (2014).
47. Gerisch, G., Fromm, H., Huesgen, A. & Wick, U. Control of cell-contact sites by cyclic AMP pulses in differentiating *Dictyostelium* cells. *Nature* **255**, 547–549 (1975).
48. Goldbeter, A. Mechanism for oscillatory synthesis of cyclic AMP in *Dictyostelium discoideum*. *Nature* **253**, 540–542 (1975).
49. Goldbeter, A. & Segel, L. A. Unified mechanism for relay and oscillation of cyclic AMP in *Dictyostelium discoideum*. *Proc. Natl. Acad. Sci. U. S. A.* **74**, 1543–1547 (1977).
50. Roos, W., Nanjundiah, V., Malchow, D. & Gerisch, G. Amplification of cyclic-AMP signals in aggregating cells of *Dictyostelium discoideum*. *FEBS Lett.* **53**, 139–142 (1975).
51. Pramanik, M. K., Iijima, M., Iwadate, Y. & Yumura, S. PTEN is a mechanosensing signal transducer for myosin II localization in *Dictyostelium* cells. *Genes Cells Devoted Mol. Cell. Mech.* **14**, 821–834 (2009).
52. Haviv, L., Gillo, D., Backouche, F. & Bernheim-Groswasser, A. A cytoskeletal demolition worker: myosin II acts as an actin depolymerization agent. *J. Mol. Biol.* **375**, 325–330 (2008).
53. Cell Migration: A Physically Integrated Molecular Process. Available at: <http://www.sciencedirect.com/science/article/pii/S0092867400812805>. (Accessed: 24th August 2016)
54. Sgro, A. E. *et al.* From intracellular signaling to population oscillations: bridging size- and time-scales in collective behavior. *Mol. Syst. Biol.* **11**, (2015).

55. Parent, C. A. & Devreotes, P. N. Molecular Genetics of Signal Transduction in Dictyostelium. *Annu. Rev. Biochem.* **65**, 411–440 (1996).
56. Annesley, S. J. & Fisher, P. R. Dictyostelium discoideum--a model for many reasons. *Mol. Cell. Biochem.* **329**, 73–91 (2009).
57. Brzostowski, J. A. & Kimmel, A. R. Signaling at zero G: G-protein-independent functions for 7-TM receptors. *Trends Biochem. Sci.* **26**, 291–297 (2001).
58. Brzostowski, J. A. *et al.* Phosphorylation of chemoattractant receptors regulates chemotaxis, actin reorganization and signal relay. *J. Cell Sci.* **126**, 4614–4626 (2013).
59. Hereld, D., Vaughan, R., Kim, J. Y., Borleis, J. & Devreotes, P. Localization of ligand-induced phosphorylation sites to serine clusters in the C-terminal domain of the Dictyostelium cAMP receptor, cAR1. *J. Biol. Chem.* **269**, 7036–7044 (1994).
60. Briscoe, C. *et al.* The phosphorylated C-terminus of cAR1 plays a role in cell-type-specific gene expression and STATa tyrosine phosphorylation. *Dev. Biol.* **233**, 225–236 (2001).
61. King, J. S. & Insall, R. H. Chemotaxis: finding the way forward with Dictyostelium. *Trends Cell Biol.* **19**, 523–530 (2009).
62. Bolourani, P., Spiegelman, G. B. & Weeks, G. Delineation of the Roles Played by RasG and RasC in cAMP-dependent Signal Transduction during the Early Development of Dictyostelium discoideum. *Mol. Biol. Cell* **17**, 4543–4550 (2006).
63. Kölsch, V., Charest, P. G. & Firtel, R. A. The regulation of cell motility and chemotaxis by phospholipid signaling. *J. Cell Sci.* **121**, 551–559 (2008).
64. Iijima, M., Huang, Y. E., Luo, H. R., Vazquez, F. & Devreotes, P. N. Novel mechanism of PTEN regulation by its PIP2 binding motif is critical for chemotaxis. *J. Biol. Chem.* (2004). doi:10.1074/jbc.M312098200
65. Chung, C. Y., Potikyan, G. & Firtel, R. A. Control of Cell Polarity and Chemotaxis by Akt/PKB and PI3 Kinase through the Regulation of PAKa. *Mol. Cell* **7**, 937–947 (2001).
66. Machesky, L. M. & Hall, A. Role of Actin Polymerization and Adhesion to Extracellular Matrix in Rac- and Rho-induced Cytoskeletal Reorganization. *J. Cell Biol.* **138**, 913–926 (1997).
67. Elzie, C. A., Colby, J., Sammons, M. A. & Janetopoulos, C. Dynamic localization of G proteins in Dictyostelium discoideum. *J. Cell Sci.* **122**, 2597–2603 (2009).

68. Srinivasan, K. *et al.* Delineating the core regulatory elements crucial for directed cell migration by examining folic-acid-mediated responses. *J. Cell Sci.* **126**, 221–233 (2013).
69. Funamoto, S., Meili, R., Lee, S., Parry, L. & Firtel, R. A. Spatial and temporal regulation of 3-phosphoinositides by PI 3-kinase and PTEN mediates chemotaxis. *Cell* **109**, 611–623 (2002).
70. Comer, F. I. & Parent, C. A. PI 3-kinases and PTEN: how opposites chemoattract. *Cell* **109**, 541–544 (2002).
71. Caterina, M. J., Hereld, D. & Devreotes, P. N. Occupancy of the Dictyostelium cAMP receptor, cAR1, induces a reduction in affinity which depends upon COOH-terminal serine residues. *J. Biol. Chem.* **270**, 4418–4423 (1995).
72. Faix, J., Kreppel, L., Shaulsky, G., Schleicher, M. & Kimmel, A. R. A rapid and efficient method to generate multiple gene disruptions in Dictyostelium discoideum using a single selectable marker and the Cre-loxP system. *Nucleic Acids Res.* **32**, e143–e143 (2004).
73. Manahan, C. L., Iglesias, P. A., Long, Y. & Devreotes, P. N. Chemoattractant Signaling in Dictyostelium Discoideum. *Annu. Rev. Cell Dev. Biol.* **20**, 223–253 (2004).
74. Chung, C. Y., Funamoto, S. & Firtel, R. A. Signaling pathways controlling cell polarity and chemotaxis. *Trends Biochem. Sci.* **26**, 557–566 (2001).
75. Garcia, G. L. & Parent, C. A. Signal relay during chemotaxis. *J. Microsc.* **231**, 529–534 (2008).
76. Insall, R. H., Soede, R. D., Schaap, P. & Devreotes, P. N. Two cAMP receptors activate common signaling pathways in Dictyostelium. *Mol. Biol. Cell* **5**, 703–711 (1994).
77. Mahadeo, D. C. & Parent, C. A. Signal relay during the life cycle of Dictyostelium. *Curr. Top. Dev. Biol.* **73**, 115–140 (2006).
78. Lee, S. *et al.* TOR complex 2 integrates cell movement during chemotaxis and signal relay in Dictyostelium. *Mol. Biol. Cell* **16**, 4572–4583 (2005).
79. Haastert, P. J. M. V. Chemotaxis: insights from the extending pseudopod. *J Cell Sci* **123**, 3031–3037 (2010).
80. Kriebel, P. W. & Parent, C. A. Group migration and signal relay in Dictyostelium. *Methods Mol. Biol. Clifton NJ* **571**, 111–124 (2009).

81. Das, S., Rericha, E. C., Bagorda, A. & Parent, C. A. Direct Biochemical Measurements of Signal Relay during Dictyostelium Development. *J. Biol. Chem.* **286**, 38649–38658 (2011).
82. Barra, J., Barrant, P., Blondelet, M.-H. & Brachet, P. pdsA, a gene involved in the production of active phosphodiesterase during starvation of Dictyostelium discoideum amoebae. *Mol. Gen. Genet. MGG* **177**, 607–613
83. Garcia, G. L., Rericha, E. C., Heger, C. D., Goldsmith, P. K. & Parent, C. A. The group migration of Dictyostelium cells is regulated by extracellular chemoattractant degradation. *Mol. Biol. Cell* **20**, 3295–3304 (2009).
84. Lee, K. J., Cox, E. C. & Goldstein, R. E. Competing Patterns of Signaling Activity in Dictyostelium Discoideum. *Phys. Rev. Lett.* **76**, 1174–1177 (1996).
85. Siegert, F. & Weijer, C. J. Analysis of optical density wave propagation and cell movement in the cellular slime mould Dictyostelium discoideum. *Phys. Nonlinear Phenom.* **49**, 224–232 (1991).
86. Hofer, T., Sherratt, J. A. & Maini, P. K. Dictyostelium discoideum: Cellular Self-Organization in an Excitable Biological Medium. *Proc. R. Soc. Lond. B Biol. Sci.* **259**, 249–257 (1995).
87. Pálsson, E. & Cox, E. C. Origin and evolution of circular waves and spirals in Dictyostelium discoideum territories. *Proc. Natl. Acad. Sci. U. S. A.* **93**, 1151–1155 (1996).
88. Pálsson, E. *et al.* Selection for spiral waves in the social amoebae Dictyostelium. *Proc. Natl. Acad. Sci.* **94**, 13719–13723 (1997).
89. Noorbakhsh, J., Schwab, D. J., Sgro, A. E., Gregor, T. & Mehta, P. Modeling oscillations and spiral waves in Dictyostelium populations. *Phys. Rev. E* **91**, 062711 (2015).
90. Bhowmik, A., Rappel, W.-J. & Levine, H. Excitable waves and direction-sensing in Dictyostelium discoideum: steps towards a chemotaxis model. *Phys. Biol.* **13**, 016002 (2016).
91. Driscoll, M. K. *et al.* Cell Shape Dynamics: From Waves to Migration. *PLOS Comput Biol* **8**, e1002392 (2012).
92. Schneider, I. C. & Haugh, J. M. Mechanisms of Gradient Sensing and Chemotaxis: Conserved Pathways, Diverse Regulation. *Cell Cycle* **5**, 1130–1134 (2006).
93. Holmes, W. R. & Edelstein-Keshet, L. A Comparison of Computational Models for Eukaryotic Cell Shape and Motility. *PLOS Comput Biol* **8**, e1002793 (2012).

94. Onsum, M. D. & Rao, C. V. Calling heads from tails: the role of mathematical modeling in understanding cell polarization. *Curr. Opin. Cell Biol.* **21**, 74–81 (2009).
95. Zhang, J., Guo, W.-H. & Wang, Y.-L. Microtubules stabilize cell polarity by localizing rear signals. *Proc. Natl. Acad. Sci. U. S. A.* **111**, 16383–16388 (2014).
96. Ma, L., Janetopoulos, C., Yang, L., Devreotes, P. N. & Iglesias, P. A. Two Complementary, Local Excitation, Global Inhibition Mechanisms Acting in Parallel Can Explain the Chemoattractant-Induced Regulation of PI(3,4,5)P3 Response in Dictyostelium Cells. *Biophys. J.* **87**, 3764–3774 (2004).
97. Sakurai, T., Mihaliuk, E., Chirila, F. & Showalter, K. Design and Control of Wave Propagation Patterns in Excitable Media. *Science* **296**, 2009–2012 (2002).
98. Tyson, J. J. & Keener, J. P. Singular perturbation theory of traveling waves in excitable media (a review). *Phys. Nonlinear Phenom.* **32**, 327–361 (1988).
99. Iglesias, P. A. & Devreotes, P. N. Biased excitable networks: How cells direct motion in response to gradients. *Curr. Opin. Cell Biol.* **24**, 245–253 (2012).
100. Levine, H. & Rappel, W.-J. The physics of eukaryotic chemotaxis. *Phys. Today* **66**, (2013).
101. Neilson, M. P. *et al.* Chemotaxis: A Feedback-Based Computational Model Robustly Predicts Multiple Aspects of Real Cell Behaviour. *PLOS Biol* **9**, e1000618 (2011).
102. Hecht, I. *et al.* Activated Membrane Patches Guide Chemotactic Cell Motility. *PLOS Comput Biol* **7**, e1002044 (2011).
103. Xiong, Y., Huang, C.-H., Iglesias, P. A. & Devreotes, P. N. Cells navigate with a local-excitation, global-inhibition-biased excitable network. *Proc. Natl. Acad. Sci.* **107**, 17079–17086 (2010).
104. Shannon, C. E. & Weaver, W. *The Mathematical Theory of Communication*. (University of Illinois Press, 1998).
105. Hu, B., Chen, W., Levine, H. & Rappel, W.-J. Quantifying Information Transmission in Eukaryotic Gradient Sensing and Chemotactic Response. *J. Stat. Phys.* **142**, 1167–1186 (2011).
106. Rhee, A., Cheong, R. & Levchenko, A. The application of information theory to biochemical signaling systems. *Phys. Biol.* **9**, 045011 (2012).
107. Waltermann, C. & Klipp, E. Information theory based approaches to cellular signaling. *Biochim. Biophys. Acta* **1810**, 924–932 (2011).

108. Tkačik, G. & Walczak, A. M. Information transmission in genetic regulatory networks: a review. *J. Phys. Condens. Matter* **23**, 153102 (2011).
109. Kobayashi, T. J. & Kamimura, A. Dynamics of intracellular information decoding. *Phys. Biol.* **8**, 055007 (2011).
110. Cheong, R., Rhee, A., Wang, C. J., Nemenman, I. & Levchenko, A. Information transduction capacity of noisy biochemical signaling networks. *Science* **334**, 354–358 (2011).
111. Edelman, G. M. & Gally, J. A. Degeneracy and complexity in biological systems. *Proc. Natl. Acad. Sci.* **98**, 13763–13768 (2001).
112. Wolfram, S. Universality and complexity in cellular automata. *Phys. Nonlinear Phenom.* **10**, 1–35 (1984).
113. Fuller, D. *et al.* External and internal constraints on eukaryotic chemotaxis. *Proc. Natl. Acad. Sci.* **107**, 9656–9659 (2010).
114. Shalizi, C. R., Shalizi, K. L. & Haslinger, R. Quantifying Self-Organization with Optimal Predictors. *Phys. Rev. Lett.* **93**, 118701 (2004).
115. Cover, T. M. & Thomas, J. A. *Elements of Information Theory*. (John Wiley & Sons, 2012).
116. Andrews, B. W. & Iglesias, P. A. An Information-Theoretic Characterization of the Optimal Gradient Sensing Response of Cells. *PLOS Comput Biol* **3**, e153 (2007).
117. Segota, I. *et al.* High fidelity information processing in folic acid chemotaxis of *Dictyostelium amoebae*. *J. R. Soc. Interface R. Soc.* **10**, 20130606 (2013).
118. Campos, D., Méndez, V. & Llopis, I. Persistent random motion: uncovering cell migration dynamics. *J. Theor. Biol.* **267**, 526–534 (2010).
119. Takagi, H., Sato, M. J., Yanagida, T. & Ueda, M. Functional Analysis of Spontaneous Cell Movement under Different Physiological Conditions. *PLOS ONE* **3**, e2648 (2008).
120. Pan, P., Hall, E. M. & Bonner, J. T. Folic acid as second chemotactic substance in the cellular slime moulds. *Nature. New Biol.* **237**, 181–182 (1972).
121. Korohoda, W., Madeja, Z. & Sroka, J. Diverse chemotactic responses of *Dictyostelium discoideum amoebae* in the developing (temporal) and stationary (spatial) concentration gradients of folic acid, cAMP, Ca(2+) and Mg(2+). *Cell Motil. Cytoskeleton* **53**, 1–25 (2002).

122. Srinivasan, K. *et al.* Delineating the core regulatory elements crucial for directed cell migration by examining folic-acid-mediated responses. *J. Cell Sci.* **126**, 221–233 (2013).
123. Rericha, E. C. & Parent, C. A. Steering in Quadruplet: The Complex Signaling Pathways Directing Chemotaxis. *Sci Signal* **1**, pe26–pe26 (2008).
124. Mahadeo, D. C. & Parent, C. A. Signal relay during the life cycle of Dictyostelium. *Curr. Top. Dev. Biol.* **73**, 115–140 (2006).
125. Kriebel, P. W., Barr, V. A. & Parent, C. A. Adenylyl Cyclase Localization Regulates Streaming during Chemotaxis. *Cell* **112**, 549–560 (2003).
126. Tobin, A. B. G-protein-coupled receptor phosphorylation: where, when and by whom. *Br. J. Pharmacol.* **153**, S167–S176 (2008).
127. Yu, F.-X. *et al.* Regulation of the Hippo-YAP Pathway by G-Protein-Coupled Receptor Signaling. *Cell* **150**, 780–791 (2012).
128. Premont, R. T., Inglese, J. & Lefkowitz, R. J. Protein kinases that phosphorylate activated G protein-coupled receptors. *FASEB J.* **9**, 175–182 (1995).
129. Brzostowski, J. A. *et al.* Phosphorylation of chemoattractant receptors regulates chemotaxis, actin reorganization and signal relay. *J. Cell Sci.* **126**, 4614–4626 (2013).
130. Devreotes, P. N. G protein-linked signaling pathways control the developmental program of Dictyostelium. *Neuron* **12**, 235–241 (1994).
131. Laub, M. T. & Loomis, W. F. A Molecular Network That Produces Spontaneous Oscillations in Excitable Cells of Dictyostelium. *Mol. Biol. Cell* **9**, 3521–3532 (1998).
132. Caterina, M. J., Devreotes, P. N., Borleis, J. & Hereld, D. Agonist-induced Loss of Ligand Binding Is Correlated with Phosphorylation of cAR1, a G Protein-coupled Chemoattractant Receptor from Dictyostelium. *J. Biol. Chem.* **270**, 8667–8672 (1995).
133. Manahan, C. L., Iglesias, P. A., Long, Y. & Devreotes, P. N. Chemoattractant Signaling in Dictyostelium Discoideum. *Annu. Rev. Cell Dev. Biol.* **20**, 223–253 (2004).
134. Segota, I. *et al.* High fidelity information processing in folic acid chemotaxis of Dictyostelium amoebae. *J. R. Soc. Interface R. Soc.* **10**, 20130606 (2013).
135. Klein, P. S. *et al.* A chemoattractant receptor controls development in Dictyostelium discoideum. *Science* **241**, 1467–1472 (1988).

136. Kimmel, A. R. & Firtel, R. A. Breaking symmetries: regulation of Dictyostelium development through chemoattractant and morphogen signal-response. *Curr. Opin. Genet. Dev.* **14**, 540–549 (2004).
137. Iranfar, N., Fuller, D. & Loomis, W. F. Genome-Wide Expression Analyses of Gene Regulation during Early Development of Dictyostelium discoideum. *Eukaryot. Cell* **2**, 664–670 (2003).
138. Loomis, W. F. Cell signaling during development of Dictyostelium. *Dev. Biol.* **391**, 1–16 (2014).
139. Raisley, B., Zhang, M., Hereld, D. & Hadwiger, J. A. A cAMP receptor-like G protein-coupled receptor with roles in growth regulation and development. *Dev. Biol.* **265**, 433–445 (2004).
140. Das, S., Rericha, E. C., Bagorda, A. & Parent, C. A. Direct Biochemical Measurements of Signal Relay during Dictyostelium Development. *J. Biol. Chem.* **286**, 38649–38658 (2011).
141. Fey, P., Kowal, A. S., Gaudet, P., Pilcher, K. E. & Chisholm, R. L. Protocols for growth and development of Dictyostelium discoideum. *Nat. Protoc.* **2**, 1307–1316 (2007).
142. Gorman, B. R. & Wikswo, J. P. Characterization of transport in microfluidic gradient generators. *Microfluid. Nanofluidics* **4**, 273–285 (2007).
143. Saadi, W., Wang, S.-J., Lin, F. & Jeon, N. L. A parallel-gradient microfluidic chamber for quantitative analysis of breast cancer cell chemotaxis. *Biomed. Microdevices* **8**, 109–118 (2006).
144. Keenan, T. M., Frevert, C. W., Wu, A., Wong, V. & Folch, A. A new method for studying gradient-induced neutrophil desensitization based on an open microfluidic chamber. *Lab. Chip* **10**, 116–122 (2010).
145. Bhattacharya, S., Datta, A., Berg, J. M. & Gangopadhyay, S. Studies on surface wettability of poly(dimethyl) siloxane (PDMS) and glass under oxygen-plasma treatment and correlation with bond strength. *J. Microelectromechanical Syst.* **14**, 590–597 (2005).
146. Arrio-Dupont, M., Cribier, S., Foucault, G., Devaux, P. F. & d’Albis, A. Diffusion of fluorescently labeled macromolecules in cultured muscle cells. *Biophys. J.* **70**, 2327–2332 (1996).
147. Dworkin, M. & Keller, K. H. Solubility and diffusion coefficient of adenosine 3':5'-monophosphate. *J. Biol. Chem.* **252**, 864–865 (1977).
148. Johnson, R. L., Saxe, C. L., Gollop, R., Kimmel, A. R. & Devreotes, P. N. Identification and targeted gene disruption of cAR3, a cAMP receptor subtype

- expressed during multicellular stages of Dictyostelium development. *Genes Dev.* **7**, 273–282 (1993).
149. Zhang, M., Goswami, M. & Hereld, D. Constitutively Active G Protein-coupled Receptor Mutants Block Dictyostelium Development. *Mol. Biol. Cell* **16**, 562–572 (2005).
  150. Xiao, Z., Yao, Y., Long, Y. & Devreotes, P. Desensitization of G-protein-coupled Receptors AGONIST-INDUCED PHOSPHORYLATION OF THE CHEMOATTRACTANT RECEPTOR<sub>cAR1</sub> LOWERS ITS INTRINSIC AFFINITY FOR cAMP. *J. Biol. Chem.* **274**, 1440–1448 (1999).
  151. Dormann, D., Kim, J.-Y., Devreotes, P. N. & Weijer, C. J. cAMP receptor affinity controls wave dynamics, geometry and morphogenesis in Dictyostelium. *J. Cell Sci.* **114**, 2513–2523 (2001).
  152. McCann, C. P., Kriebel, P. W., Parent, C. A. & Losert, W. Cell speed, persistence and information transmission during signal relay and collective migration. *J. Cell Sci.* **123**, 1724–1731 (2010).
  153. Nichols, J. M., Veltman, D. & Kay, R. R. Chemotaxis of a model organism: progress with Dictyostelium. *Curr. Opin. Cell Biol.* **36**, 7–12 (2015).
  154. Janetopoulos, C. & Firtel, R. A. Directional sensing during chemotaxis. *FEBS Lett.* **582**, 2075–2085 (2008).
  155. Kutscher, B., Devreotes, P. & Iglesias, P. A. Local Excitation, Global Inhibition Mechanism for Gradient Sensing: An Interactive Applet. *Sci STKE* **2004**, pl3–pl3 (2004).
  156. Takeda, K. *et al.* Incoherent Feedforward Control Governs Adaptation of Activated Ras in a Eukaryotic Chemotaxis Pathway. *Sci. Signal.* **5**, ra2 (2012).
  157. Rappel, W.-J. & Levine, H. Receptor noise limitations on chemotactic sensing. *Proc. Natl. Acad. Sci.* **105**, 19270–19275 (2008).
  158. Endres, R. G. & Wingreen, N. S. Precise adaptation in bacterial chemotaxis through ‘assistance neighborhoods’. *Proc. Natl. Acad. Sci.* **103**, 13040–13044 (2006).
  159. Zarnitsyna, V. I. *et al.* Memory in receptor–ligand-mediated cell adhesion. *Proc. Natl. Acad. Sci.* **104**, 18037–18042 (2007).
  160. Lan, G., Sartori, P., Neumann, S., Sourjik, V. & Tu, Y. The energy-speed-accuracy trade-off in sensory adaptation. *Nat. Phys.* **8**, 422–428 (2012).
  161. Andrews, B. W., Yi, T.-M. & Iglesias, P. A. Optimal Noise Filtering in the Chemotactic Response of Escherichia coli. *PLOS Comput Biol* **2**, e154 (2006).

162. Skoge, M. *et al.* Cellular memory in eukaryotic chemotaxis. *Proc. Natl. Acad. Sci.* **111**, 14448–14453 (2014).
163. Mehta, P. & Schwab, D. J. Energetic costs of cellular computation. *Proc. Natl. Acad. Sci.* **109**, 17978–17982 (2012).
164. Richards, W. A. The Phenomenology and Potential Religious Import of States of Consciousness Facilitated by Psilocybin. *Arch. Psychol. Relig.* **30**, 189–199 (2008).
165. Carhart-Harris, R. L. *et al.* Neural correlates of the psychedelic state as determined by fMRI studies with psilocybin. *Proc. Natl. Acad. Sci.* **109**, 2138–2143 (2012).
166. Carhart-Harris, R. L. *et al.* Neural correlates of the LSD experience revealed by multimodal neuroimaging. *Proc. Natl. Acad. Sci.* **113**, 4853–4858 (2016).
167. Vollenweider, F. X. & Geyer, M. A. A systems model of altered consciousness: integrating natural and drug-induced psychoses. *Brain Res. Bull.* **56**, 495–507 (2001).
168. aan het Rot, M., Zarate Jr., C. A., Charney, D. S. & Mathew, S. J. Ketamine for Depression: Where Do We Go from Here? *Biol. Psychiatry* **72**, 537–547 (2012).
169. Larkin, G. L. & Beautrais, A. L. A preliminary naturalistic study of low-dose ketamine for depression and suicide ideation in the emergency department. *Int. J. Neuropsychopharmacol.* **14**, 1127–1131 (2011).
170. Rasmussen, K. G. *et al.* Serial infusions of low-dose ketamine for major depression. *J. Psychopharmacol. (Oxf.)* 0269881113478283 (2013). doi:10.1177/0269881113478283
171. Gasser, P. *et al.* Safety and Efficacy of Lysergic Acid Diethylamide-Assisted Psychotherapy for Anxiety Associated With Life-threatening Diseases. *J. Nerv. Ment. Dis.* **202**, 513–520 (2014).
172. Olive, K. P. *et al.* Inhibition of Hedgehog Signaling Enhances Delivery of Chemotherapy in a Mouse Model of Pancreatic Cancer. *Science* **324**, 1457–1461 (2009).
173. Rottenberg, S. *et al.* Selective induction of chemotherapy resistance of mammary tumors in a conditional mouse model for hereditary breast cancer. *Proc. Natl. Acad. Sci.* **104**, 12117–12122 (2007).
174. A. Kulchitsky, V. *et al.* Cytotoxic Effects of Chemotherapeutic Drugs and Heterocyclic Compounds at Application on the Cells of Primary Culture of Neuroepithelium Tumors. *Med. Chem.* **8**, 22–32 (2012).
175. Orlando, L. *et al.* When less is better: Safety and efficacy of combination of trastuzumab and continuous low oral dose chemotherapy (HEX) as first-line

- therapy for HER2-positive advanced breast cancer (ABC)--First early results from a phase II trial on behalf of Gruppo Oncologico Italia Meridionale (GOIM). *ASCO Meet. Abstr.* **31**, 618 (2013).
176. Kerbel, R. & Folkman, J. Clinical translation of angiogenesis inhibitors. *Nat. Rev. Cancer* **2**, 727–739 (2002).
177. Dalrymple, A. *et al.* Cigarette smoke induced genotoxicity and respiratory tract pathology: evidence to support reduced exposure time and animal numbers in tobacco product testing. *Inhal. Toxicol.* **28**, 324–338 (2016).
178. Klump, K. L. Puberty as a critical risk period for eating disorders: A review of human and animal studies. *Horm. Behav.* **64**, 399–410 (2013).
179. Brom, M., Both, S., Laan, E., Everaerd, W. & Spinhoven, P. The role of conditioning, learning and dopamine in sexual behavior: A narrative review of animal and human studies. *Neurosci. Biobehav. Rev.* **38**, 38–59 (2014).
180. Griffiths, R. R. & Woodson, P. P. Caffeine physical dependence: a review of human and laboratory animal studies. *Psychopharmacology (Berl.)* **94**, 437–451
181. Björkqvist, K. Sex differences in physical, verbal, and indirect aggression: A review of recent research. *Sex Roles* **30**, 177–188
182. Bezard, E., Yue, Z., Kirik, D. & Spillantini, M. G. Animal models of Parkinson's disease: Limits and relevance to neuroprotection studies. *Mov. Disord.* **28**, 61–70 (2013).
183. Wang, Y. *et al.* TREM2 Lipid Sensing Sustains the Microglial Response in an Alzheimer's Disease Model. *Cell* **160**, 1061–1071 (2015).
184. Ruggeri, B. A., Camp, F. & Miknyoczki, S. Animal models of disease: Pre-clinical animal models of cancer and their applications and utility in drug discovery. *Biochem. Pharmacol.* **87**, 150–161 (2014).
185. Brownell, K. D. & Gold, M. S. *Food and Addiction: A Comprehensive Handbook*. (Oxford University Press, 2012).
186. Carvalho, M. J. A. & Mirth, C. K. Coordinating morphology with behavior during development: an integrative approach from a fly perspective. *Behav. Evol. Ecol.* **3**, 5 (2015).
187. de Laat, W. & Duboule, D. Topology of mammalian developmental enhancers and their regulatory landscapes. *Nature* **502**, 499–506 (2013).
188. Banting, F. G., Best, C., Collip, J. & Macleod, J. The Effect of Insulin on the Excretion of Ketone Bodies by the Diabetic Dog." *Trans. R. Soc. Can.* **16**, 3–3 (1922).

189. Wyatt, L. S., Shors, S. T., Murphy, B. R. & Moss, B. Development of a replication-deficient recombinant vaccinia virus vaccine effective against parainfluenza virus 3 infection in an animal model. *Vaccine* **14**, 1451–1458 (1996).
190. Bok, K. *et al.* Chimpanzees as an animal model for human norovirus infection and vaccine development. *Proc. Natl. Acad. Sci.* **108**, 325–330 (2011).
191. Schofield, L., Hewitt, M. C., Evans, K., Siomos, M.-A. & Seeberger, P. H. Synthetic GPI as a candidate anti-toxic vaccine in a model of malaria. *Nature* **418**, 785–789 (2002).
192. Morgan, D. *et al.* A $\beta$  peptide vaccination prevents memory loss in an animal model of Alzheimer's disease. *Nature* **408**, 982–985 (2000).
193. Russo-Neustadt, A., Ha, T., Ramirez, R. & Kesslak, J. P. Physical activity–antidepressant treatment combination: impact on brain-derived neurotrophic factor and behavior in an animal model. *Behav. Brain Res.* **120**, 87–95 (2001).
194. Kim, J.-H. *et al.* Dopamine neurons derived from embryonic stem cells function in an animal model of Parkinson's disease. *Nature* **418**, 50–56 (2002).
195. Laconi, S. *et al.* Massive Liver Replacement by Transplanted Hepatocytes in the Absence of Exogenous Growth Stimuli in Rats Treated with Retrorsine. *Am. J. Pathol.* **158**, 771–777 (2001).
196. Atala, A. Tissue engineering for the replacement of organ function in the genitourinary system. *Am. J. Transplant.* **4**, 58–73 (2004).
197. Pearce, A. I., Richards, R. G., Milz, S., Schneider, E. & Pearce, S. G. Animal models for implant biomaterial research in bone: a review. *Eur. Cell. Mater.* **13**, 1–10 (2007).
198. Henderson, V. C., Kimmelman, J., Fergusson, D., Grimshaw, J. M. & Hackam, D. G. Threats to Validity in the Design and Conduct of Preclinical Efficacy Studies: A Systematic Review of Guidelines for In Vivo Animal Experiments. *PLOS Med* **10**, e1001489 (2013).
199. Evans, H. & Mitre, E. Worms as therapeutic agents for allergy and asthma: Understanding why benefits in animal studies have not translated into clinical success. *J. Allergy Clin. Immunol.* **135**, 343–353 (2015).
200. Mak, I. W., Evaniew, N. & Ghert, M. Lost in translation: animal models and clinical trials in cancer treatment. *Am. J. Transl. Res.* **6**, 114–118 (2014).
201. Seok, J. *et al.* Genomic responses in mouse models poorly mimic human inflammatory diseases. *Proc. Natl. Acad. Sci.* **110**, 3507–3512 (2013).

202. Anonymous. Animal Welfare Act Violations at Ivy League Universities. *The Physicians Committee* (2011). Available at: <http://www.pcrm.org/research/edtraining/ivy-league/awa-violations-at-ivy-league-detailed-results>. (Accessed: 2nd November 2016)
203. Provost, P. J. *et al.* An inactivated hepatitis A viral vaccine of cell culture origin. *J. Med. Virol.* **19**, 23–31 (1986).
204. Cox, J. H. & Schneider, L. G. Prophylactic immunization of humans against rabies by intradermal inoculation of human diploid cell culture vaccine. *J. Clin. Microbiol.* **3**, 96–101 (1976).
205. Monath, T. P. *et al.* An Inactivated Cell-Culture Vaccine against Yellow Fever. *N. Engl. J. Med.* **364**, 1326–1333 (2011).
206. Tree, J. A., Richardson, C., Fooks, A. R., Clegg, J. C. & Looby, D. Comparison of large-scale mammalian cell culture systems with egg culture for the production of influenza virus A vaccine strains. *Vaccine* **19**, 3444–3450 (2001).
207. Selkoe, D. J. Translating cell biology into therapeutic advances in Alzheimer’s disease. *Nature* **399**, A23–A31 (1999).
208. Beatty, W. L., Morrison, R. P. & Byrne, G. I. Persistent chlamydiae: from cell culture to a paradigm for chlamydial pathogenesis. *Microbiol. Rev.* **58**, 686–699 (1994).
209. Materne, E.-M. *et al.* The multi-organ chip--a microfluidic platform for long-term multi-tissue coculture. *J. Vis. Exp. JoVE* e52526 (2015). doi:10.3791/52526
210. Wikswa, J. P. *et al.* Scaling and systems biology for integrating multiple organs-on-a-chip. *Lab. Chip* **13**, 3496–3511 (2013).
211. Wikswa, J. P. *et al.* Engineering Challenges for Instrumenting and Controlling Integrated Organ-on-Chip Systems. *IEEE Trans. Biomed. Eng.* **60**, 682–690 (2013).
212. Bhatia, S. N. & Ingber, D. E. Microfluidic organs-on-chips. *Nat. Biotechnol.* **32**, 760–772 (2014).
213. Kim, H. J., Li, H., Collins, J. J. & Ingber, D. E. Contributions of microbiome and mechanical deformation to intestinal bacterial overgrowth and inflammation in a human gut-on-a-chip. *Proc. Natl. Acad. Sci.* **113**, E7–E15 (2016).
214. Bjerketorp, J. *et al.* Rapid lab-on-a-chip profiling of human gut bacteria. *J. Microbiol. Methods* **72**, 82–90 (2008).

215. Dantas, G., Sommer, M. O. A., Degnan, P. H. & Goodman, A. L. Experimental Approaches for Defining Functional Roles of Microbes in the Human Gut. *Annu. Rev. Microbiol.* **67**, 459–475 (2013).
216. Kim, H. J. & Ingber, D. E. Gut-on-a-Chip microenvironment induces human intestinal cells to undergo villus differentiation. *Integr. Biol.* **5**, 1130–1140 (2013).
217. Ho, C.-T. *et al.* Liver-cell patterning lab chip: mimicking the morphology of liver lobule tissue. *Lab. Chip* **13**, 3578–3587 (2013).
218. Zhao, L. *et al.* Chemotherapy resistance research of lung cancer based on microfluidic chip system with flow medium. *Biomed. Microdevices* **12**, 325–332 (2010).
219. Huh, D. *et al.* A Human Disease Model of Drug Toxicity–Induced Pulmonary Edema in a Lung-on-a-Chip Microdevice. *Sci. Transl. Med.* **4**, 159ra147–159ra147 (2012).
220. Bhise, N. S. *et al.* Organ-on-a-chip platforms for studying drug delivery systems. *J. Controlled Release* **190**, 82–93 (2014).
221. Selimović, Š., Dokmeci, M. R. & Khademhosseini, A. Organs-on-a-chip for drug discovery. *Curr. Opin. Pharmacol.* **13**, 829–833 (2013).
222. Esch, M. B., King, T. L. & Shuler, M. L. The Role of Body-on-a-Chip Devices in Drug and Toxicity Studies. *Annu. Rev. Biomed. Eng.* **13**, 55–72 (2011).
223. Griep, L. M. *et al.* BBB ON CHIP: microfluidic platform to mechanically and biochemically modulate blood-brain barrier function. *Biomed. Microdevices* **15**, 145–150 (2012).
224. Ghaemmaghami, A. M., Hancock, M. J., Harrington, H., Kaji, H. & Khademhosseini, A. Biomimetic tissues on a chip for drug discovery. *Drug Discov. Today* **17**, 173–181 (2012).
225. Huh, D. *et al.* Reconstituting organ-level lung functions on a chip. *Science* **328**, 1662–1668 (2010).
226. Kim, H. J., Huh, D., Hamilton, G. & Ingber, D. E. Human gut-on-a-chip inhabited by microbial flora that experiences intestinal peristalsis-like motions and flow. *Lab. Chip* **12**, 2165–2174 (2012).
227. Brown, J. A. *et al.* Recreating blood-brain barrier physiology and structure on chip: A novel neurovascular microfluidic bioreactor. *Biomicrofluidics* **9**, 054124 (2015).
228. Lee, P. J., Hung, P. J. & Lee, L. P. An artificial liver sinusoid with a microfluidic endothelial-like barrier for primary hepatocyte culture. *Biotechnol. Bioeng.* **97**, 1340–1346 (2007).

229. Levesque, M. J. & Nerem, R. M. The Elongation and Orientation of Cultured Endothelial Cells in Response to Shear Stress. *J. Biomech. Eng.* **107**, 341–347 (1985).
230. Dewey, J. C. F., Bussolari, S. R., Gimbrone, J. M. A. & Davies, P. F. The Dynamic Response of Vascular Endothelial Cells to Fluid Shear Stress. *J. Biomech. Eng.* **103**, 177–185 (1981).
231. Meer, A. D. van der, Poot, A. A., Feijen, J. & Vermes, I. Analyzing shear stress-induced alignment of actin filaments in endothelial cells with a microfluidic assay. *Biomicrofluidics* **4**, 011103 (2010).
232. Bi, D., Lopez, J. H., Schwarz, J. M. & Manning, M. L. Energy barriers and cell migration in densely packed tissues. *Soft Matter* **10**, 1885–1890 (2014).
233. Bi, D., Yang, X., Marchetti, M. C. & Manning, M. L. Motility-driven glass and jamming transitions in biological tissues. *Phys. Rev. X* **6**, (2016).
234. Park, J.-A. *et al.* Unjamming and cell shape in the asthmatic airway epithelium. *Nat. Mater.* **14**, 1040–1048 (2015).
235. Crawley, S. W. *et al.* Intestinal Brush Border Assembly Driven by Protocadherin-Based Intermicrovillar Adhesion. *Cell* **157**, 433–446 (2014).
236. Ahmed, Z. M. *et al.* The tip-link antigen, a protein associated with the transduction complex of sensory hair cells, is protocadherin-15. *J. Neurosci. Off. J. Soc. Neurosci.* **26**, 7022–7034 (2006).
237. Goodyear, R. J., Forge, A., Legan, P. K. & Richardson, G. P. Asymmetric distribution of cadherin 23 and protocadherin 15 in the kinocilial links of avian sensory hair cells. *J. Comp. Neurol.* **518**, 4288–4297 (2010).
238. Claessens, M. M. a. E., Tharmann, R., Kroy, K. & Bausch, A. R. Microstructure and viscoelasticity of confined semiflexible polymer networks. *Nat. Phys.* **2**, 186–189 (2006).
239. Claessens, M. M. A. E., Bathe, M., Frey, E. & Bausch, A. R. Actin-binding proteins sensitively mediate F-actin bundle stiffness. *Nat. Mater.* **5**, 748–753 (2006).
240. Kiseleva, I. & Kamkin, A. *Mechanosensitivity and Mechanotransduction*. (Springer Science & Business Media, 2010).
241. Bitner-Glindzicz, M. *et al.* A recessive contiguous gene deletion causing infantile hyperinsulinism, enteropathy and deafness identifies the Usher type 1C gene. *Nat. Genet.* **26**, 56–60 (2000).

242. Verpy, E. *et al.* A defect in harmonin, a PDZ domain-containing protein expressed in the inner ear sensory hair cells, underlies Usher syndrome type 1C. *Nat. Genet.* **26**, 51–55 (2000).
243. Siemens, J. *et al.* The Usher syndrome proteins cadherin 23 and harmonin form a complex by means of PDZ-domain interactions. *Proc. Natl. Acad. Sci.* **99**, 14946–14951 (2002).
244. Lampasona, V. *et al.* Autoantibodies to Harmonin and Villin Are Diagnostic Markers in Children with IPEX Syndrome. *PLOS ONE* **8**, e78664 (2013).
245. Li, J., He, Y., Lu, Q. & Zhang, M. Mechanistic Basis of Organization of the Harmonin/USH1C-Mediated Brush Border Microvilli Tip-Link Complex. *Dev. Cell* **36**, 179–189 (2016).
246. Ceriani, F. & Mammano, F. Calcium signaling in the cochlea – Molecular mechanisms and physiopathological implications. *Cell Commun. Signal.* **10**, 20 (2012).
247. Denk, W., Holt, J. R., Shepherd, G. M. G. & Corey, D. P. Calcium imaging of single stereocilia in hair cells: Localization of transduction channels at both ends of tip links. *Neuron* **15**, 1311–1321 (1995).
248. Powers, R. J. *et al.* The Local Forces Acting on the Mechanotransduction Channel in Hair Cell Stereocilia. *Biophys. J.* **106**, 2519–2528 (2014).
249. Lumpkin, E. A. & Caterina, M. J. Mechanisms of sensory transduction in the skin. *Nature* **445**, 858–865 (2007).
250. Ebert, J. *et al.* Recovery of mechano-electrical transduction in rat cochlear hair bundles after postnatal destruction of the stereociliar cross-links. *Proc. R. Soc. Lond. B Biol. Sci.* rspb20100219 (2010). doi:10.1098/rspb.2010.0219
251. Codogno, P., Mehrpour, M. & Proikas-Cezanne, T. Canonical and non-canonical autophagy: variations on a common theme of self-eating? *Nat. Rev. Mol. Cell Biol.* **13**, 7–12 (2012).
252. Kim, J., Kundu, M., Viollet, B. & Guan, K.-L. AMPK and mTOR regulate autophagy through direct phosphorylation of Ulk1. *Nat. Cell Biol.* **13**, 132–141 (2011).
253. Kuroyanagi, H. *et al.* Human ULK1, a Novel Serine/Threonine Kinase Related to UNC-51 Kinase of *Caenorhabditis elegans*: cDNA Cloning, Expression, and Chromosomal Assignment. *Genomics* **51**, 76–85 (1998).
254. Randall-Demillo, S., Chieppa, M. & Eri, R. Intestinal epithelium and autophagy: partners in gut homeostasis. *Front. Immunol.* **4**, 301 (2013).

255. McKnight, N. C. & Zhenyu, Y. Beclin 1, an Essential Component and Master Regulator of PI3K-III in Health and Disease. *Curr. Pathobiol. Rep.* **1**, 231–238 (2013).
256. Russell, R. C. *et al.* ULK1 induces autophagy by phosphorylating Beclin-1 and activating VPS34 lipid kinase. *Nat. Cell Biol.* **15**, 741–750 (2013).
257. Israelachvili, J. N., Mitchell, D. J. & Ninham, B. W. Theory of self-assembly of hydrocarbon amphiphiles into micelles and bilayers. *J. Chem. Soc., Faraday Trans. 2* **72**, 1525–1568 (1976).
258. Tanida, I., Ueno, T. & Kominami, E. LC3 conjugation system in mammalian autophagy. *Int. J. Biochem. Cell Biol.* **36**, 2503–2518 (2004).
259. Nakatogawa, H. Two ubiquitin-like conjugation systems that mediate membrane formation during autophagy. *Essays Biochem.* **55**, 39–50 (2013).
260. Eskelinen, E.-L. & Kovács, A. L. Double membranes vs. lipid bilayers, and their significance for correct identification of macroautophagic structures. *Autophagy* **7**, 931–932 (2011).
261. Dancourt, J. & Melia, T. J. Lipidation of the autophagy proteins LC3 and GABARAP is a membrane-curvature dependent process. *Autophagy* **10**, 1470–1471 (2014).
262. Hernández-Zapata, E., Martínez-Balbuena, L. & Santamaría-Holek, I. Thermodynamics and dynamics of the formation of spherical lipid vesicles. *J. Biol. Phys.* **35**, 297–308 (2009).
263. Knorr, R. L., Dimova, R. & Lipowsky, R. Curvature of Double-Membrane Organelles Generated by Changes in Membrane Size and Composition. *PLOS ONE* **7**, e32753 (2012).
264. Rubinsztein, D. C., Shpilka, T. & Elazar, Z. Mechanisms of Autophagosome Biogenesis. *Curr. Biol.* **22**, R29–R34 (2012).
265. Knorr, R. L., Lipowsky, R. & Dimova, R. Autophagosome closure requires membrane scission. *Autophagy* **11**, 2134–2137 (2015).
266. Amaravadi, R., Kimmelman, A. C. & White, E. Recent insights into the function of autophagy in cancer. *Genes Dev.* **30**, 1913–1930 (2016).
267. Galluzzi, L. *et al.* Autophagy in malignant transformation and cancer progression. *EMBO J.* **34**, 856–880 (2015).
268. Zhong, Z., Sanchez-Lopez, E. & Karin, M. Autophagy, Inflammation, and Immunity: A Troika Governing Cancer and Its Treatment. *Cell* **166**, 288–298 (2016).

269. Bento, C. F., Ashkenazi, A., Jimenez-Sanchez, M. & Rubinsztein, D. C. The Parkinson's disease-associated genes ATP13A2 and SYT11 regulate autophagy via a common pathway. *Nat. Commun.* **7**, 11803 (2016).
270. Martin, D. D. O., Ladha, S., Ehrnhoefer, D. E. & Hayden, M. R. Autophagy in Huntington disease and huntingtin in autophagy. *Trends Neurosci.* **38**, 26–35 (2015).
271. Orogo, A. M. & Gustafsson, Å. B. Therapeutic Targeting of Autophagy. *Circ. Res.* **116**, 489–503 (2015).
272. Meyer, G. R. Y. D. *et al.* Autophagy in Vascular Disease. *Circ. Res.* **116**, 468–479 (2015).
273. Slutsky, N. *et al.* Decreased adiponectin links elevated adipose tissue autophagy with adipocyte endocrine dysfunction in obesity. *Int. J. Obes.* **40**, 912–920 (2016).
274. Soussi, H., Clément, K. & Dugail, I. Adipose tissue autophagy status in obesity: Expression and flux—two faces of the picture. *Autophagy* **12**, 588–589 (2016).
275. Tooze, S. A., Abada, A. & Elazar, Z. Endocytosis and autophagy: Exploitation or cooperation? *Cold Spring Harb. Perspect. Biol.* **6**, (2014).
276. Klionsky DJ, Abdelmohsen K, Abe A, Abedin MJ, Abeliovich H, Acevedo Arozena A, Adachi H, Adams CM, Adams PD, Adeli K, Adhietty PJ, Adler SG, Agam G, Agarwal R, Aghi MK, Agnello M, Agostinis P, Aguilar PV, Aguirre-Ghiso J, Airoidi EM, Ait-Si-Ali S, Akemat, Z. S. Guidelines for use and interpretation of assays for monitoring autophagy (3rd edition). *Autophagy* **12**, 1–222 (2016).
277. Mizushima, N. *et al.* Autophagy : process and function. *Cell Rep.* **7**, 2861–2873 (2014).
278. Schneider, J. L. & Cuervo, A. M. Autophagy and human disease: Emerging themes. *Curr. Opin. Genet. Dev.* **26**, 16–23 (2014).
279. Nixon, R. The role of autophagy in neurodegenerative disease. *Nat. Med.* **19**, 983–997 (2013).
280. Kenific, C. M. & Debnath, J. Cellular and metabolic functions for autophagy in cancer cells. *Trends Cell Biol.* **25**, 37–45 (2015).
281. Rubinsztein, D. C., Mariño, G. & Kroemer, G. Autophagy and aging. *Cell* **146**, 682–695 (2011).
282. Nagy, L. E., Ding, W.-X., Cresci, G., Saikia, P. & Shah, V. H. Linking Pathogenic Mechanisms of Alcoholic Liver Disease With Clinical Phenotypes. *Gastroenterology* **150**, 1756–1768 (2016).

283. Heath, R. J. & Xavier, R. Autophagy, immunity and human disease. *Curr Opin Gastroenterol* 1–12 (2010). doi:10.1002/0471143030.cb1910s42.Overview
284. Kaser, A. *et al.* XBP1 links ER stress to intestinal inflammation and confers genetic risk for human inflammatory bowel disease. *Cell* **134**, 743–756 (2008).
285. Adolph, T. E. *et al.* Paneth cells as a site of origin for intestinal inflammation. *Nature* **503**, 272–6 (2013).
286. Fritz, T., Niederreiter, L., Adolph, T., Blumberg, R. S. & Kaser, a. Crohn's disease: NOD2, autophagy and ER stress converge. *Gut* **60**, 1580–1588 (2011).
287. Abraham, C. & Cho, J. H. Inflammatory bowel disease. *N. Engl. J. Med.* **361**, 2066–78 (2009).
288. Khor, B., Gardet, A. & Xavier, R. J. Genetics and pathogenesis of inflammatory bowel disease. *Nature* **474**, 307–17 (2011).
289. Vandussen, K. L. *et al.* Genetic variants synthesize to produce paneth cell phenotypes that define subtypes of Crohn's disease. *Gastroenterology* **146**, 200–9 (2014).
290. Jostins, L. *et al.* Host-microbe interactions have shaped the genetic architecture of inflammatory bowel disease. *Nature* **491**, 119–24 (2012).
291. Kaser, A. & Blumberg, R. S. Autophagy, microbial sensing, endoplasmic reticulum stress, and epithelial function in inflammatory bowel disease. *Gastroenterology* **140**, 1738–1747 (2011).
292. Barrett, J. C. *et al.* Genome-wide association defines more than thirty distinct susceptibility loci for Crohn's disease. *Nat Genet* **40**, 955–962 (2009).
293. Yilmaz, Ö. H. *et al.* mTORC1 in the Paneth cell niche couples intestinal stem-cell function to calorie intake. *Nature* **486**, 490–5 (2012).
294. Igarashi, M. *et al.* mTORC1 and SIRT1 Cooperate to Foster Expansion of Gut Adult Stem Cells during Calorie Restriction. *Cell* **0**, 19–33 (2016).
295. Chen, Y. & Klionsky, D. J. The regulation of autophagy - unanswered questions. *J. Cell Sci.* **124**, 161–170 (2011).
296. Mackeh, R., Perdiz, D., Lorin, S., Codogno, P. & Poüs, C. Autophagy and microtubules - new story, old players. *J. Cell Sci.* **126**, 1071–80 (2013).
297. Chauhan, S. *et al.* Pharmaceutical screen identifies novel target processes for activation of autophagy with a broad translational potential. *Nat. Commun.* **6**, 8620 (2015).

298. Orhon, I. *et al.* Primary-cilium-dependent autophagy controls epithelial cell volume in response to fluid flow. *Nat. Cell Biol.* **i**, (2016).
299. Crawley, S. W. *et al.* Intestinal Brush Border Assembly Driven by Protocadherin-Based Intermicrovillar Adhesion. *Cell* **157**, 433–446 (2014).
300. Hudspeth, A. J. Integrating the active process of hair cells with cochlear function. *Nat. Rev. Neurosci.* **15**, 600–614 (2014).
301. Burkel, B. M., Von Dassow, G. & Bement, W. M. Versatile fluorescent probes for actin filaments based on the actin-binding domain of utrophin. *Cell Motil. Cytoskeleton* **64**, 822–832 (2007).
302. Sakaue-Sawano, A. *et al.* Visualizing spatiotemporal dynamics of multicellular cell-cycle progression. *Cell* **132**, 487–98 (2008).
303. Lentle, R. G. & Janssen, P. W. M. Physical characteristics of digesta and their influence on flow and mixing in the mammalian intestine: A review. *Journal of Comparative Physiology B: Biochemical, Systemic, and Environmental Physiology* **178**, 673–690 (2008).
304. Ishikawa, T., Sato, T., Mohit, G., Imai, Y. & Yamaguchi, T. Transport phenomena of microbial flora in the small intestine with peristalsis. *J. Theor. Biol.* **279**, 63–73 (2011).
305. Chi, M. *et al.* A microfluidic cell culture device ( $\mu$ FCCD) to culture epithelial cells with physiological and morphological properties that mimic those of the human intestine. *Biomed. Microdevices* **17**, (2015).
306. Kim, H. J., Huh, D., Hamilton, G. & Ingber, D. E. Human gut-on-a-chip inhabited by microbial flora that experiences intestinal peristalsis-like motions and flow. *Lab. Chip* **12**, 2165–74 (2012).
307. Sakaue-Sawano, A. *et al.* Visualizing spatiotemporal dynamics of multicellular cell-cycle progression. *Cell* **132**, 487–98 (2008).
308. Sinadinos, C. *et al.* Neuronal glycogen synthesis contributes to physiological aging. *Aging Cell* **13**, 935–945 (2014).
309. Utech, M. *et al.* Mechanism of IFN-gamma-induced endocytosis of tight junction proteins: myosin II-dependent vacuolarization of the apical plasma membrane. *Mol. Biol. Cell* **16**, 5040–52 (2005).
310. Gilbert, T. & Rodriguez-Boulan, E. Induction of vacuolar apical compartments in the Caco-2 intestinal epithelial cell line. *J. Cell Sci.* **100 ( Pt 3)**, 451–8 (1991).
311. Müller, M. *et al.* The coordinated action of the MVB pathway and autophagy ensures cell survival during starvation. *eLife* **2015**, 1–25 (2015).

312. Conibear, E. & Stevens, T. H. Multiple sorting pathways between the late Golgi and the vacuole in yeast. *Biochim. Biophys. Acta - Mol. Cell Res.* **1404**, 211–230 (1998).
313. Ravikumar, B., Moreau, K., Jahreiss, L., Puri, C. & Rubinsztein, D. C. Plasma membrane contributes to the formation of pre-autophagosomal structures. *Nat. Cell Biol.* **12**, 747–57 (2010).
314. Razi, M., Chan, E. Y. W. & Tooze, S. A. Early endosomes and endosomal coatomer are required for autophagy. *J. Cell Biol.* **185**, 305–21 (2009).
315. Mizushima, N., Yoshimori, T. & Levine, B. Methods in Mammalian Autophagy Research. *Cell* **140**, 313–326 (2010).
316. Lamoureux, F. *et al.* Blocked autophagy using lysosomotropic agents sensitizes resistant prostate tumor cells to the novel Akt inhibitor AZD5363. *Clin. Cancer Res.* **19**, 833–844 (2013).
317. Kimura, S., Noda, T. & Yoshimori, T. Dissection of the autophagosome maturation process by a novel reporter protein, tandem fluorescent-tagged LC3. *Autophagy* **3**, 452–460 (2007).
318. Oda, K. & Ikehara, Y. Weakly basic amines inhibit the proteolytic conversion of proalbumin to serum albumin in cultured rat hepatocytes. *Eur. J. Biochem. FEBS* **152**, 605–9 (1985).
319. Yoshimori, T., Yamamoto, A., Moriyama, Y., Futai, M. & Tashiro, Y. Bafilomycin A1, a specific inhibitor of vacuolar-type H(+)-ATPase, inhibits acidification and protein degradation in lysosomes of cultured cells. *J. Biol. Chem.* **266**, 17707–12 (1991).
320. Scherz-Shouval, R. *et al.* p53-dependent regulation of autophagy protein LC3 supports cancer cell survival under prolonged starvation. *Proc. Natl. Acad. Sci. U. S. A.* **107**, 18511–6 (2010).
321. Ding, Y. *et al.* TGF- $\beta$ 1 protects against mesangial cell apoptosis via induction of autophagy. *J. Biol. Chem.* **285**, 37909–37919 (2010).
322. Miura, S., Sato, K., Kato-Negishi, M., Teshima, T. & Takeuchi, S. Fluid shear triggers microvilli formation via mechanosensitive activation of TRPV6. *Nat. Commun.* **6**, 8871 (2015).
323. Peterson, M. D. & Mooseker, M. S. Characterization of the enterocyte-like brush border cytoskeleton of the C2 BBe clones of the human intestinal cell line, Caco-2. *Cell* **600**, 581–600 (1992).
324. Peterson, M. D., Bement, W. M. & Mooseker, M. S. An in vitro model for the analysis of intestinal brush border assembly. II. Changes in expression and

- localization of brush border proteins during cell contact-induced brush border assembly in Caco-2BBE cells. *J Cell Sci* **105** ( Pt 2, 461–472 (1993).
325. Goutman, J. D., Elgoyhen, A. B. & Gómez-Casati, M. E. Cochlear hair cells: The sound-sensing machines. *FEBS Lett.* **589**, 3354–3361 (2015).
326. Lange, K. Fundamental role of microvilli in the main functions of differentiated cells: Outline of an universal regulating and signaling system at the cell periphery. *J. Cell. Physiol.* **226**, 896–927 (2011).
327. Sedwick, C. The Fly Muscles in on Glycogen Autophagy. *PLoS Biol.* **11**, 1–2 (2013).
328. Nascimbeni, A. C., Fanin, M., Masiero, E., Angelini, C. & Sandri, M. The role of autophagy in the pathogenesis of glycogen storage disease type II (GSDII). *Cell Death Differ.* **19**, 1698–708 (2012).
329. Shintani, T. & Klionsky, D. J. Autophagy in health and disease: a double-edged sword. *Science* **306**, 990–5 (2004).
330. Mauvezin, C., Nagy, P., Juhasz, G. & Neufeld, T. P. Autophagosome-lysosome fusion is independent of V-ATPase-mediated acidification. *Nat Commun* **6**, 7007 (2015).
331. Kaur, J. & Debnath, J. Autophagy at the crossroads of catabolism and anabolism. *Nat. Rev. Mol. Cell Biol.* **16**, 461–472 (2015).
332. Cheong, H., Lu, C., Lindsten, T. & Thompson, C. B. Therapeutic targets in cancer cell metabolism and autophagy. *Nat. Biotechnol.* **30**, 671–8 (2012).
333. Bestebroer, J., V'kovski, P., Mauthe, M. & Reggiori, F. Hidden behind autophagy: The unconventional roles of ATG proteins. *Traffic* **14**, 1029–1041 (2013).
334. Sanjuan, M. A. *et al.* Toll-like receptor signalling in macrophages links the autophagy pathway to phagocytosis. *Nature* **450**, 1253–7 (2007).
335. Huang, J. *et al.* Activation of antibacterial autophagy by NADPH oxidases. *Proc. Natl. Acad. Sci. U. S. A.* **106**, 6226–6231 (2009).
336. Florey, O., Gammoh, N., Kim, S. E., Jiang, X. & Overholtzer, M. V-ATPase and osmotic imbalances activate endolysosomal LC3 lipidation. *Autophagy* **11**, 88–99 (2015).
337. Overholtzer, M. *et al.* A Nonapoptotic Cell Death Process, Entosis, that Occurs by Cell-in-Cell Invasion. *Cell* **131**, 966–979 (2007).
338. Praetorius, H. a & Spring, K. R. Removal of the MDCK cell primary cilium abolishes flow sensing. *J. Membr. Biol.* **191**, 69–76 (2003).

339. Geeraert, C. *et al.* Starvation-induced hyperacetylation of tubulin is required for the stimulation of autophagy by nutrient deprivation. *J. Biol. Chem.* **285**, 24184–24194 (2010).
340. Song, Y. & Brady, S. T. Post-translational modifications of tubulin: Pathways to functional diversity of microtubules. *Trends Cell Biol.* **25**, 125–136 (2015).
341. Deribe, Y. L. *et al.* Regulation of epidermal growth factor receptor trafficking by lysine deacetylase HDAC6. *Sci. Signal.* **2**, ra84 (2009).
342. Shifrin, Jr., D. A., Crawley, S. W., Grega-Larson, N. E. & Tyska, M. J. Dynamics of brush border remodeling induced by enteropathogenic *E. coli*. *Gut Microbes* **5**, 504–516 (2014).
343. Neal, M. D. *et al.* A critical role for TLR4 induction of autophagy in the regulation of enterocyte migration and the pathogenesis of necrotizing enterocolitis. *J. Immunol. Baltim. Md 1950* **190**, 3541–51 (2013).
344. Donaldson, G. P., Lee, S. M. & Mazmanian, S. K. Gut biogeography of the bacterial microbiota. *Nat. Rev. Microbiol.* (2015). doi:10.1038/nrmicro3552
345. Takahashi, T. & Sakata, T. Viscous properties of pig cecal contents and the contribution of solid particles to viscosity. *Nutr. Burbank Los Angel. Cty. Calif* **20**, 377–82 (2004).
346. Tourneur, E. & Chassin, C. Neonatal immune adaptation of the gut and its role during infections. *Clin. Dev. Immunol.* **2013**, (2013).
347. Muncan, V. *et al.* Blimp1 regulates the transition of neonatal to adult intestinal epithelium. *Nat. Commun.* **2**, 452 (2011).
348. Schnabl, K. L., Field, C. & Clandinin, M. T. Ganglioside composition of differentiated Caco-2 cells resembles human colostrum and neonatal rat intestine. *Br. J. Nutr.* **101**, 694–700 (2009).
349. Moxey, P. C. & Trier, J. S. Development of villus absorptive cells in the human fetal small intestine: a morphological and morphometric study. *Anat. Rec.* **195**, 463–82 (1979).
350. Henning, S. J. Postnatal development: coordination of feeding, digestion, and metabolism. *Am. J. Physiol.* **241**, G199–214 (1981).
351. Mashburn, D. N., Lynch, H. E., Ma, X. & Hutson, M. S. Enabling user-guided segmentation and tracking of surface-labeled cells in time-lapse image sets of living tissues. *Cytometry A* **81A**, 409–418 (2012).

